

**On the thermodynamic and kinetic
properties of bulk glass forming metallic
systems**

Dissertation

zur Erlangung des Grades

Doktor der Naturwissenschaften (Dr. rer. nat.)

der

Naturwissenschaftlich-Technischen Fakultät III Chemie, Pharmazie und
Werkstoffwissenschaften

der

Universität des Saarlandes

vorgelegt von

Zachary J. Evenson

Saarbrücken

Juni 2012

Tag des Kolloquiums: 18.10.2012

Dekan: Prof. Dr. Wilhelm F. Maier

1. Gutachter: Prof. Dr. rer. nat. Ralf Busch

2. Gutachter: Prof. Dr. rer. nat. habil. Wulff Possart

3. Gutachter: Prof. Dr. -Ing. Gerhard Wilde

Vorsitz: Prof. Dr. -Ing. Markus Stommel

Akad. Mitarbeiter: Dr. -Ing. Joachim Schmitt

Abstract

Bulk metallic glasses (BMGs) are typically formed from the rapid quenching of multicomponent metallic melts. Good BMG-forming systems are associated with a large atomic size mismatch and deep eutectic formation between the constituent elements. As such, these densely packed BMG-forming liquids can be characterized through sluggish kinetics, which impedes the nucleation and growth of crystals, as well as a low driving force for crystallization that is present in the undercooled liquid.

In this work, the equilibrium thermodynamic and kinetic properties of certain BMG-forming liquids are analyzed at temperatures near the melting point and in the deeply supercooled state near the glass transition. This includes determination of the viscosity and thermodynamic functions of the liquid. The non-equilibrium properties of the glassy state are also studied, looking at the phenomenology of structural relaxation as it relates to viscosity, enthalpy and free volume. A look at viscous flow in terms of configurational entropy and various models of the free volume is given.

Finally, the molten viscous behavior of various BMG-forming alloys is investigated at temperatures above the melting point. The kinetics in the melt at high temperatures reveals a distinctively more fragile liquid state than at low temperatures near the glass transition. This behavior is revealed to be the result of a fragile-to-strong transition in the undercooled liquid, possibly due to polyamorphism.

Zusammenfassung

Metallische Massivgläser (MMG) entstehen üblicherweise durch schnelles Abkühlen mehrkomponentiger metallischer Schmelzen. Ein großer Unterschied in den jeweiligen Atomradien und die Bildung tiefer Eutektika sind typische Kennzeichen guter MMG-bildener Systeme. Dementsprechend werden solche MMG-bildenen Schmelzen durch eine langsame Kinetik, sowie eine geringe treibende Kraft zur Kristallisation, gekennzeichnet.

In dieser Arbeit werden bei Temperaturen in der Nähe des Schmelzpunktes, sowie bei sehr tiefen Unterkühlungen nahe des Glasübergangs, die thermodynamischen und kinetischen Gleichgewichtseigenschaften bestimmter MMG-bildener Schmelzen untersucht. Es werden die Viskosität und die thermodynamischen Funktionen bestimmt. Nichtgleichgewichtseigenschaften des Glaszustandes werden auch berücksichtigt und die Phänomenologie struktureller Relaxation in Bezug auf Viskosität, Enthalpie und freies Volumen untersucht. Eine Beschreibung viskoses Fließen mittels der Konfigurationsentropie sowie verschiedener Modelle des freien Volumens werden auch diskutiert.

Es wird schließlich das viskose Verhalten verschiedener MMG-bildener Schmelzen bei Temperaturen nahe des Schmelzpunkts untersucht. Die Kinetik der Schmelze bei diesen hohen Temperaturen zeigt ein kinetisch fragileres Verhalten als es bei niedrigeren Temperaturen in der Nähe des Glasübergangs zu beobachten ist. Dies deutet auf einen Fragil-Stark-Übergang in der unterkühlten Schmelze hin, der eventuell auf Polyamorphismus beruht.

for my grandfather...

Acknowledgments

I would first like to express my sincerest gratitude to my supervisor Ralf Busch for his guidance throughout this project and for allowing me the opportunity to make these last five years at the *Lehrstuhl für Metallische Werkstoffe* some of the most challenging and productive I've had thus far. Above all, I'm thankful to have had the chance to gain invaluable practical experience and the freedom to pursue my own ideas.

My colleagues and co-workers at the LMW have been a great source of inspiration and insight for me and I would like to thank them all for their cooperation and the friendship that we've developed over the years. In particular, I am grateful for the support and training provided by Isabella Gallino, who mentored me during my first year at the department and has been a constant source of optimism. I would especially like to thank Dr.-Ing. Frank Aubertin for the many productive and insightful conversations we've had together, as well as his willingness in helping me to answer some of the great many questions that I have encountered during this project. I would like to recognize and thank Hermann Altmeyer and Jörg Eiden of the LMW technical staff for putting forth the hard work necessary to keep everything running and having the patience to help me improve my own technical competence as well. I would also like to thank Martina Stemmler for her help in carrying out the XRD measurements. It also goes without saying that the time and effort put in by our *HiWis* in casting and preparing samples is greatly appreciated.

I am thankful for also being able to have as my peers some genuinely good friends. I would like to acknowledge Jochen Heinrich, whom I have known since our year at OSU together and would like to thank him for the help and guidance he's given me towards understanding the ins and out of Germany. I am happy to have also had the chance to work with Moritz Stolpe, someone who has never failed at putting a smile on my face or leading an interesting conversation. I am very thankful for the friendship I've had with Will Hembree over these past years and consider him a close companion. I would also like to thank Shuai Wei for the many insightful discussions we've had together in our collaborations and I wish him all the best in his scientific endeavors.

My stay in Germany would not have been possible without the encouragement

and guidance of Prof. Christian Stehr of Oregon State University. Prof. Stehr enabled me to make the first steps towards continuing my graduate education in Germany and I am indebted to him for his years of support. My deepest gratitude also goes out to the many funding agencies who have provided financial support for me along the way. I would especially like to acknowledge the opportunities provided to me by the Ford Family Foundation, allowing me to carry out my undergraduate studies. Additionally, my graduate work in Saarbrücken would not have been possible without the effort put forth by the many individuals behind the AMASE Master, as well as the generous financial support provided by the Erasmus Mundus Program. I would especially like to recognize and thank Prof. Dr.-Ing. Frank Mücklich and Dr.-Ing. Flavio Soldera for their work in making this possible. Lastly, I would like to recognize the *Deutsche Forschungsgemeinschaft*, whose funding has supported a portion of this project.

My most heartfelt thanks go out to my partner, Sanja, who has shown infinite patience with me throughout this entire process. Her love and support has helped me immeasurably. Most of all though, I would like to express my deepest gratitude for the ongoing support and encouragement of my family, teachers and close friends. None of this would have been possible without them.

Z. Evenson
Saarbrücken, June 2012

Contributions and publications

The experimental results presented in Chapters 5 and 6 were collected, analyzed and interpreted by the author. A portion of the three-point beam-bending data on Vitreloy 106 and 106a were originally collected and analyzed by S. Raedersdorf [1]. The three-point beam-bending data shown in this work for Vitreloy 106 and 106a correspond to experiments and analysis that were repeated by the author. In Chapter 7, high-temperature viscosity data were taken from experiments performed by T. Schmitt [2], M. Nicola and W. Hembree [3]; the data analysis, presentation and conclusions are the author's original work. I. Gallino was responsible for assisting with and directing the experimental implementation of the calorimetric studies carried out here. The overall research direction and project administration was conducted by R. Busch.

At the time of writing this thesis, there have been five publications based on the results presented in this work:

- Z. Evenson, I. Gallino and R. Busch, The effect of cooling rates on the apparent fragility of Zr-based bulk metallic glasses, *J Appl Phys*, **107**; 123529 (2010)
- Z. Evenson, S. Raedersdorf, I. Gallino and R. Busch, Equilibrium viscosity of Zr-Cu-Ni-Al-Nb bulk metallic glasses, *Scripta Mater*, **63**; 573-576 (2010)
- Z. Evenson and R. Busch, Equilibrium viscosity, enthalpy recovery and free volume relaxation in a $Zr_{44}Ti_{11}Ni_{10}Cu_{10}Be_{25}$ bulk metallic glass, *Acta Mater*, **59**; 4404-4415 (2011)
- Z. Evenson and R. Busch, Enthalpy recovery and free volume relaxation in a $Zr_{44}Ti_{11}Ni_{10}Cu_{10}Be_{25}$ bulk metallic glass, *J Alloys Comp*, **509S**; S38-S41 (2011)
- Z. Evenson, T. Schmitt, M. Nicola, I. Gallino and R. Busch, High temperature melt viscosity and fragile-to-strong transition in Zr-Cu-Ni-Al-Nb(Ti) and $Cu_{47}Ti_{34}Zr_{11}Ni_8$ bulk metallic glasses, *Acta Mater*, **60**; 4712-4719 (2012)

Additionally, these results have been presented as contributions to various academic symposia:

- Z. Evenson, I. Gallino and R. Busch. The Effect of Cooling Rates on the Apparent Fragility of the $Zr_{58.5}Cu_{15.6}Ni_{12.8}Al_{10.3}Nb_{2.8}$ Bulk Metallic Glass. Poster presented at *RQ13, The 13th International Conference on Rapidly Quenched and Metastable Materials*; 2008 Aug 24-29; **Dresden, Germany**.
- Z. Evenson, I. Gallino and R. Busch. The Effect of Cooling Rates on the Apparent Fragility of the $Zr_{58.5}Cu_{15.6}Ni_{12.8}Al_{10.3}Nb_{2.8}$ Bulk Metallic Glass. Poster presented at *Glass and Time: Fragility of Liquids – Cause(s) and Consequences, International workshop*; 2008 Oct 08-10; **Copenhagen, Denmark**.
- Z. Evenson, I. Gallino and R. Busch. The Effect of Cooling Rates on the Apparent Fragility of the $Zr_{58.5}Cu_{15.6}Ni_{12.8}Al_{10.3}Nb_{2.8}$ Bulk Metallic Glass. Poster presented at *Materials Research Society Fall Meeting 2008*; 2008 Dec 01-05; **Boston, USA**.
- Z. Evenson and R. Busch. Relaxation Phenomena in a $Zr_{44}Ti_{11}Ni_{10}Cu_{10}Be_{25}$ BMG Alloy as Investigated with Dilatometric Methods. Poster presented at *5th International EEIGM / AMASE / FORGEMAT Conference on Advanced Materials Research*; 2009 Nov 04-05; **Nancy, France**.
- Z. Evenson and R. Busch. Enthalpy and Free Volume Relaxation in a Zr-Ti-Ni-Cu-Be Bulk Metallic Glass Alloy. Presented at *DPG Frühjahrstagung der Sektion Kondensierte Materie (SKM)*; 2010 Mar 21-26; **Regensburg, Germany**.
- Z. Evenson and R. Busch. Enthalpy and Free Volume Relaxation in a Zr-Ti-Ni-Cu-Be Bulk Metallic Glass Alloy. Presented at *International Symposium on Metastable, Amorphous and Nanostructured Materials (ISMANAM) 2010*; 2010 July 4-9; **Zürich, Switzerland**.
- Z. Evenson and R. Busch. Structural Relaxation in a $Zr_{44}Ti_{11}Ni_{10}Cu_{10}Be_{25}$ Bulk Metallic Glass. Poster presented at *International Workshop on Dynamics in Viscous Liquids*; 2011 Mar 30 - Apr 2; **Rome, Italy**.

Finally, a portion of the results presented in Section 5.1 was produced from the preliminary work that appears in the Master's thesis, "The effect of cooling rates on the glass transition of Zr-based bulk metallic glasses", by Z. Evenson (2008).

Contents

1	Introduction	1
2	From liquid metal to metallic glass	4
2.1	The metastable liquid	4
2.2	The driving force for crystallization	6
2.3	Nucleation and crystal growth	9
2.4	Viscous slowdown and structural relaxation	16
2.5	The fragility concept	20
2.5.1	The free volume model	24
2.5.2	The configurational entropy model	26
2.6	The glass transition and the fictive temperature	26
3	Current perspectives	29
3.1	Glass forming ability	29
3.2	Structure	35
3.3	Crystallization	41
4	Materials and methods	48
4.1	Theory and principles of thermomechanical analysis	49
4.1.1	Dilatometry	50
4.1.2	Three-point beam bending	51
4.2	Theory and principles of calorimetry	57
4.2.1	Differential thermal analysis	57
4.2.2	Differential scanning calorimetry	60
4.3	Measurement of thermophysical properties	63
4.3.1	The calorimetric glass transition and melting interval	64
4.3.2	Specific heat capacity	65
4.3.3	Viscosity between T_g and T_x	67
4.4	Measurement of relaxation phenomena	70
4.4.1	Enthalpy relaxation	70
4.4.2	Volumetric relaxation	71
4.4.3	Isothermal viscosity below T_g	74
5	Thermodynamics and kinetics of the equilibrium liquid	75
5.1	The kinetic glass transition in DSC	76
5.1.1	Apparent fragility	76
5.1.2	Comparison of fragility indices	84
5.2	Thermodynamic functions of the equilibrium liquid	88

CONTENTS

5.2.1	Specific heat capacity	89
5.2.2	Enthalpy	93
5.2.3	Entropy	94
5.2.4	Gibbs free energy	96
5.3	Crystallization of the equilibrium liquid	104
5.3.1	Crystallization near T_{liq}	104
5.3.2	Crystallization near T_g	109
5.4	Equilibrium viscosity	111
5.4.1	Relationship between D_η^* and D_τ^*	117
5.4.2	Free volume and configurational entropy models	121
5.5	Enthalpy and free volume	128
5.6	Summary and Conclusions	132
6	The kinetics of structural relaxation below T_g	135
6.1	Viscous flow below T_g	136
6.1.1	Phase separation	137
6.2	Enthalpy and free volume	144
6.3	The kinetics of structural relaxation	151
6.4	Summary and Conclusions	154
7	Fragile-to-strong transitions in metallic glass-forming liquids	158
7.1	Viscosity measurements in the molten state	160
7.2	Viscous behavior of the melt	165
7.3	Fragile-to-strong transition	169
7.4	Summary and Conclusions	172
8	Summarizing remarks and outlook	174
A	Alloy properties	179
B	Copyright Permissions	186
	References	187

Chapter 1

Introduction

The seminal work of David Turnbull in the 1950s brought new insight into the undercooling properties of pure metals below their thermodynamic crystallization temperatures [4–6]. No more than 10 years later Duwez and co-workers successfully undercooled a binary Au-Si alloy from the melt into the glassy state by rapidly quenching a liquid droplet into a 10 μm -thick amorphous foil [7]. This discovery subsequently led to an influx of research effort devoted towards investigations into different amorphous alloy systems, along with development of new experimental processing methods and analyses of important thermodynamic and physical properties. In 1982 Drehman, Greer and Turnbull showed that bulk glassy samples ($\varnothing \sim 0.5 \text{ cm}$) of a Pd-Ni-P alloy could be produced with cooling rates as low as 1.4 K s^{-1} [8]. Not long afterwards, several alloy systems based on La-Ni-Al [9], Zr-Ni-Al-Cu [10], Mg-Cu-Y [11] and Zr-Ti-Cu-Ni-Be [12] were shown to form bulk glassy specimens under conditions reflecting cooling rates of 100 K s^{-1} and lower.

The discovery of these new *bulk metallic glasses* (BMGs) was not only appealing from a technological point of view, but generated considerable interest from within the scientific community as well. Specifically, the greatly enhanced thermal stability of these multicomponent alloy melts with respect to crystallization allowed for more extensive studies to be carried out in the deeply undercooled liquid. The numerous investigations into the $\text{Zr}_{41.2}\text{Ti}_{13.8}\text{Cu}_{12.5}\text{Ni}_{10.0}\text{Be}_{22.5}$ (Vitreyloy 1) alloy, for example, have already given a comprehensive picture of the liquid state in terms of thermodynamic functions [13], viscosity [14, 15], diffusion [16–18] and crystallization kinetics [19, 20]. The existence of metallic glasses and the strong undercooling ability of these multicomponent metallic melts reflect a range of unique thermodynamic and kinetic properties. As such, the present work will focus on the

measurement, characterization and analysis of these properties.

The thermodynamics presented and discussed here will predominately deal with the analysis of such macroscopic properties like volume, thermal expansion, specific heat capacity, enthalpy, entropy and Gibbs free energy of equilibrium (stable and metastable) multicomponent metallic melts, as well as of the glassy, non-equilibrium state. Unfortunately, the term *kinetics* can be rather ambiguous regarding the quantities that are actually under investigation. In this work, *kinetics* will be defined to include the following:

1. **The mobility of atomic species within the equilibrium melt**, as primarily described by the temperature-dependent properties of viscosity.
2. **The set of time-dependent phenomena observed during relaxation** from the non-equilibrium, glassy state into the metastable, undercooled liquid. Mainly this will include the isothermal, time-dependent nature of macroscopic, thermodynamic quantities as they approach equilibrium, as well as the time dependence of inherently kinetic properties, such as viscosity.
3. **The kinetic glass transition** as measured during constant heating or cooling using calorimetric methods.

The work presented here is not intended to be an overview of metallic glasses as such, but rather is aimed at presenting a detailed look into macroscopic thermodynamic and kinetic quantities of the liquid state and highlighting their roles in various topics in the metallic glass community. The unifying theme of each chapter will be centered on thermodynamic and kinetic properties. Chapter 2 gives an introduction and overview of the formation of metallic glasses from the liquid melt. Chapter 3 acts as the literature review and gives an assessment of the current perspectives in the metallic glass community with regard to glass forming ability (GFA), structure and crystallization. The relevant methods of thermal analysis are introduced in Chapter 4, focusing on calorimetry and thermomechanical analysis (TMA). Chapters 5 through 7 present the experimental results and analyses of various thermodynamic and kinetic properties in select bulk metallic glass-forming systems. Chapter 5 deals with the thermodynamics and kinetics of the equilibrium liquid at high temperatures in the melt and at low temperatures in the undercooled liquid near the glass transition. In Chapter 6, the phenomenon of structural relaxation from the glassy state into the equilibrium liquid at temperatures below

the glass transition is introduced and studied. New evidence of a liquid-liquid transition in the melts of various bulk metallic glass-forming compositions is presented in Chapter 7 and the generality of the so-called fragile-to-strong transition in metallic glasses is discussed. An overall summary of the work presented here is given in Chapter 8.

Chapter 2

From liquid metal to metallic glass

Liquids and solids are both states of condensed matter. The dividing line between the two can be distinguished macroscopically by the liquid's characteristic ability to flow. Microscopically, the liquid is contrasted against many of its solid counterparts by its lack of a long-range order, or periodicity of an atomic lattice that is characteristic of a crystal. Amorphous, or non-crystalline, solids also lack long-range order. Like the atoms or molecules of a liquid, those of amorphous solids have a similar disordered structure. The term *disordered* should be regarded with some care however, as its general usage can also include liquids and solids that have localized order; e.g., short and/or medium-range ordering.

2.1 The metastable liquid

The melting point or melting temperature, T_m , of a substance is the temperature signifying the onset of the transition from the crystalline solid to a liquid. For a pure material (one-component system), the liquid and crystalline phases coexist in thermodynamic equilibrium only at this temperature; that is, T_m signifies both the melting temperature upon heating and the solidification temperature upon cooling.¹ In multicomponent systems, crystals from the solid can actually remain stable over a range of temperatures when heated above T_m . The liquidus temperature, T_{liq} , specifies the maximum temperature at which crystals can coexist in stable thermodynamic equilibrium

¹The glass transition is also technically a liquid/solid transition. However, since the glassy state does not represent thermodynamic equilibrium, it is exempt from this definition.

2.1 The metastable liquid

with the liquid. Upon cooling, the solidification process will begin at T_{liq} and end at T_m . This specific transition can be referred to by a number of terms, in particular: freezing, solidification or crystallization. As both *freezing* and *solidification* are also used to refer to the liquid-glass transition, the term *crystallization* is found to be better suited here since it refers specifically to the thermodynamic transition from the equilibrium liquid to the equilibrium crystalline solid. More importantly, crystallization refers to the most common route of liquid solidification; i.e., the nucleation and growth of crystals.

The temperature at which crystallization begins can, for a given substance, be lower than its liquidus temperature (or melting temperature, in the case of a one-component system). If the liquid is cooled below T_{liq} or T_m without crystallizing, it is said to be in *metastable equilibrium*. This process is referred to as *supercooling* or *undercooling*. The undercooled liquid is metastable with respect to the crystalline ground state, but still in equilibrium. For some substances, the crystallization temperature is very close to T_{liq} or T_m , and practically no undercooling is observed. Other substances, on the other hand, will not crystallize during the entire range of undercooling, eventually leading to a kinetic liquid-glass transition. Deep undercoolings were not observed in metals until the middle of the twentieth century [21]. In some pure metals, for example, the degree of undercooling, $\Delta T = T_m - T_x$, where T_x is the temperature at which crystallization begins, has been shown to vary from 39 to 370 K in the absence of heterogeneous nucleation sites, depending on the element [5].

In general the free energy of the system, $G(x)$, where x is a generalized phase space coordinate, can be described by the schematic curve shown in Fig. 2.1. The maxima and minima of the free energy curve are found where $dG/dx = 0$ and correspond to the various equilibria in the system with respect to x . The system is said to be "in equilibrium" when its thermodynamic properties do not change with time; this is the case for the metastable and stable equilibria of Fig. 2.1 (points **1** and **4**, respectively). The stable equilibrium at point **4** represents the global minimum of the system and corresponds therefore to its thermodynamic ground state. However, for the local minimum represented by point **1**, the system may remain stable for small fluctuations, but will eventually, given enough time, transition from point **1** to point **4**. In the unstable equilibrium state represented by point **2**, small fluctuations about this point may quickly lead to a transition to a more stable thermodynamic state. Point **3** is an example of a non-equilibrium state. At this point, the system is in a transitory state and its properties are continuously changing.

The sign of the free energy difference between states **1** and **4**, ΔG^{1-4} , shows

2.2 The driving force for crystallization

that the transformation is thermodynamically favored. However, the existence of a transformation barrier between **1** and **4** indicates that extra energy is needed in order for the transformation to take place; i.e., ΔG^{1-2} . The existence of a transformation barrier is important to nucleation theory and will be discussed further in Sec. 2.2. Where there is no barrier to transformation – for example from **3** to **4** – the free energy continuously decreases and the process may occur spontaneously.

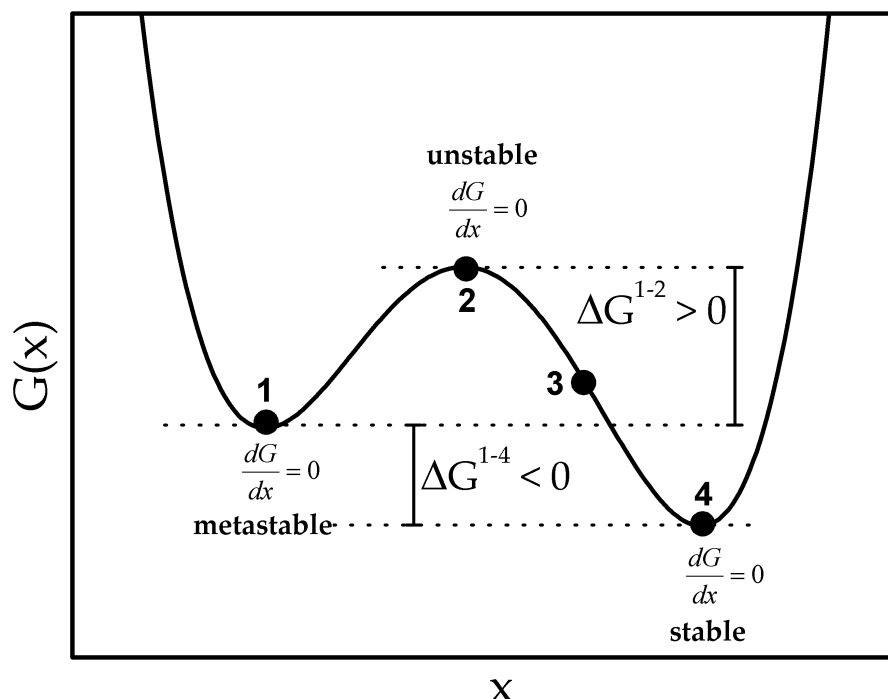


Figure 2.1: Schematic illustration of the free energy, $G(x)$, of a system, showing the transitions through various equilibria.

2.2 The driving force for crystallization

It is tempting to describe the formation of a glass as requiring a rapid quench or fast cooling from the liquid state, especially when dealing with metallic glasses. While this may be the case for simple metallic alloys whose critical cooling rates can be on the order of 10^6 K s^{-1} , novel bulk metallic glasses, such as $\text{Pd}_{43}\text{Cu}_{27}\text{Ni}_{10}\text{P}_{20}$ with a critical cooling rate of 0.10 K s^{-1} , have since refuted this preconception [22]. In fact, for many oxide and polymeric glass-formers, crystallization is the exception rather than the rule. The B_2O_3 glass-former, for example, is known not to crystallize even when the melt is seeded

2.2 The driving force for crystallization

with stable crystallites [23]. A look at the breadth of critical cooling rates for various glass-formers – from around 10^{-3} K s⁻¹ for silicate glasses to a theoretical 10^{12} K s⁻¹ for pure metals¹– brings one to the the more appropriate conclusion that as long as the crystallization event is sufficiently bypassed from the melt, a glass will form.

The crystalline state of a system at temperatures lower than T_{liq} has a lower Gibbs free energy than that of the liquid. The thermodynamic driving force for crystallization may be approximated by the difference in Gibbs free energy, ΔG , between the the metastable undercooled liquid and crystalline state. Assuming that the free energies of the liquid and crystalline states at a temperature, T , can be given by

$$\begin{aligned} G^l(T) &= H^l(T) - TS^l(T) \\ G^x(T) &= H^x(T) - TS^x(T), \end{aligned} \quad (2.1)$$

where the superscripts l and x refer to the liquid and crystalline states, respectively, the Gibbs free energy difference can be expressed by

$$\begin{aligned} \Delta G &= \Delta G^{l-x}(T) = G^l(T) - G^x(T) \\ &= (H^l(T) - TS^l(T)) - (H^x(T) - TS^x(T)) \\ &= \Delta H^{l-x}(T) - T\Delta S^{l-x}(T), \end{aligned} \quad (2.2)$$

where $\Delta H^{l-x}(T) = H^l(T) - H^x(T)$ and $\Delta S^{l-x}(T) = S^l(T) - S^x(T)$ – the differences in enthalpy and entropy, respectively, between the liquid and crystalline states. As a function of temperature, these thermodynamic functions can then be defined as

$$\Delta H^{l-x}(T) = \Delta H_f + \int_{T_{liq}}^T \Delta C_p^{l-x}(T') dT' \quad (2.3)$$

and

¹The value of 10^{12} K s⁻¹ is an estimation of the critical cooling rate for the formation of glassy bulk samples of pure metals. Experimentally, submicron droplets of a series of pure elements have been shown to undergo a glass transition with critical cooling rates on the order of 10^6 - 10^8 K s⁻¹ [24]

2.2 The driving force for crystallization

$$\Delta S^{l-x}(T) = \Delta S_f + \int_{T_{liq}}^T \frac{\Delta C_p^{l-x}(T')}{T'} dT', \quad (2.4)$$

where ΔH_f and ΔS_f are the enthalpy and entropy of fusion, respectively, and ΔC_p^{l-x} is the difference in specific heat capacity between the liquid and crystalline states. From Eqs. 2.3 and 2.4, $\Delta G^{l-x}(T)$ can now be fully expressed as

$$\begin{aligned} \Delta G^{l-x}(T) = (1 - T/T_{liq})\Delta H_f - \int_{T_{liq}}^T \Delta C_p^{l-x}(T') dT' \\ + \int_{T_{liq}}^T \frac{\Delta C_p^{l-x}(T')}{T'} dT'. \end{aligned} \quad (2.5)$$

At equilibrium $\Delta G^{l-x} = \Delta H^{l-x} - T_{liq}\Delta S^{l-x} = 0$, therefore the enthalpy and entropy difference between the liquid and the crystalline states is just ΔH_f and ΔS_f , respectively. This leads to the relation

$$\Delta S_f = \Delta H_f/T_{liq}. \quad (2.6)$$

For small undercoolings, Eq. 2.6 can be combined with Eq. 2.2 giving

$$\begin{aligned} \Delta G^{l-x} &\simeq \Delta H_f - T \frac{\Delta H_f}{T_{liq}} \\ &\simeq -\Delta S_f \Delta T. \end{aligned} \quad (2.7)$$

Therefore at T_{liq} , the slope of the ΔG^{l-x} curve is equal to the negative entropy of fusion, $-\Delta S_f$. This result is very important when considering the thermodynamic contribution to the glass-forming ability of bulk metallic glass forming melts, which will be discussed later.

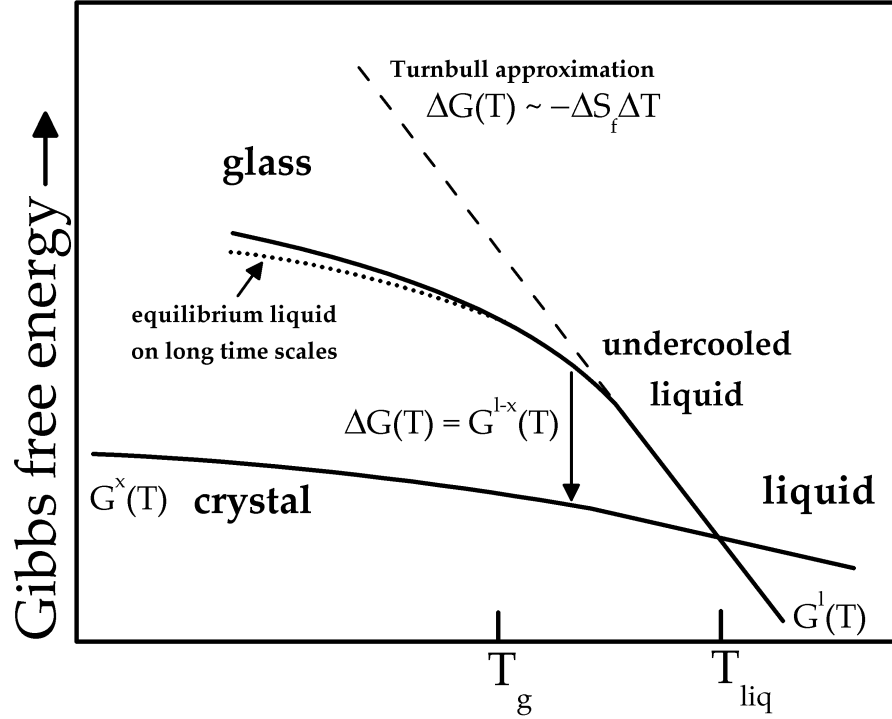


Figure 2.2: Schematic Gibbs free energy curves with respect to temperature, $G(T)$, of the liquid and crystalline state of a system, $G^l(T)$ and $G^x(T)$, respectively. At temperatures for which $T < T_{liq}$, the Gibbs free energy of the crystalline state is lower than that of the liquid, and a driving force for the crystallization process exists, approximated by $\Delta G(T) = G^l(T) - G^x(T)$.

2.3 Nucleation and crystal growth

The process of crystallization of the liquid close to T_{liq} begins with the nucleation of clusters of the stable crystal phase. The change in the free energy associated with the formation of a cluster of the solid phase is

$$\Delta G' = \Delta G_V + \Delta G_S, \quad (2.8)$$

where ΔG_V is the free energy gain for the formation of a volume of the solid phase and ΔG_S is the free energy cost of the creation of the liquid-solid interface. Since the phase transition from and undercooled liquid to a solid is thermodynamically favored, the sign of ΔG_V will be negative. The interfacial energy cost can be expressed as $\Delta G_S = \sigma A$, where σ is the interfacial energy and A is the area of the interface. The free energy of cluster formation can

2.3 Nucleation and crystal growth

then be expressed as

$$\Delta G' = -V_s \Delta G_v^{l-x}(T) + \sigma A, \quad (2.9)$$

where V_s is the volume of the cluster solid (assumed spherical) and $\Delta G_v^{l-x}(T)$ is free energy difference *per unit volume* between the liquid and crystalline states. Given a spherical cluster with volume, $V_s = \frac{4}{3}\pi r^3$ and a liquid-solid interface with surface area, $A = 4\pi r^2$, Eq. 2.9 can be rewritten as

$$\Delta G'(r) = -\frac{4}{3}\pi r^3 \Delta G_v^{l-x}(T) + 4\pi r^2 \sigma. \quad (2.10)$$

If the radius of the cluster is smaller than some critical value, r^* , the system can lower its free energy by dissolution of the solid cluster back into the liquid phase. However, if the cluster radius is larger than r^* , the cluster will grow into a stable nucleus, as every value of $r > r^*$ will result in a lower value of $\Delta G'(r)$. The free energy of cluster formation, $\Delta G'(r)$, hence has a maximum of ΔG^* at r^* . This is the critical free energy for the formation of stable crystalline nuclei in the liquid phase, and is commonly referred to as the *nucleation barrier*. By solving the equation $d\Delta G'(r)/dr = 0$, ΔG^* is found to be

$$\Delta G^* = \frac{16\pi\sigma^3}{3(\Delta G_v^{l-x})^2}, \quad (2.11)$$

with the critical radius

$$r^* = \frac{2\sigma}{\Delta G_v^{l-x}}. \quad (2.12)$$

Within the approximation of Eq. 2.7, the nucleation barrier can thus be expressed as a function of the undercooling, ΔT :

$$\Delta G^* = \frac{16\pi\sigma^3 T_{liq}^2}{3(\Delta H_f)_v^2 (\Delta T)^2}, \quad (2.13)$$

where $(\Delta H_f)_v$ is the latent heat of fusion per unit volume. Outside of the approximation, however, the free energy difference between the undercooled liquid and the crystal can only be evaluated by the integral in Eq. 2.5. There-

2.3 Nucleation and crystal growth

fore, an exact expression for Eq. 2.13 over a large temperature range would most likely involve the use of higher-order polynomial functions with several empirically determined fitting parameters.

At any given moment, the average cluster size distribution N_r ; i.e., the average number of spherical clusters per unit volume having radius r , can be given by

$$N_r = N_0 \exp\left(-\frac{\Delta G'}{kT}\right), \quad (2.14)$$

where N_0 is the total number of atoms per unit volume of the liquid and $\Delta G'$ is obtained from Eq. 2.10 for a given value of r . For $T > T_{liq}$ this expression holds over all values of r . However, for $T < T_{liq}$ this expression is only valid for $r \leq r^*$, since clusters greater than r^* are assumed to grow very quickly to macroscopic sizes and become technically nuclei, therefore leaving the liquid system.

By replacing $\Delta G'$ with the nucleation barrier, ΔG^* , from Eq. 2.11, the number of clusters per unit volume with the critical radius, N_r^* , can then be expressed as

$$N_r^* = N_0 \exp\left(-\frac{\Delta G^*}{kT}\right), \quad (2.15)$$

assuming that N_r^* represents the equilibrium distribution of critical clusters. If one or more atoms is added to a critical cluster, the cluster will grow and transform to a stable nucleus. The rate that these clusters transform into nuclei is known as the *homogeneous nucleation rate* and is given by

$$I(T) = A\nu \exp\left(-\frac{\Delta G^*}{kT}\right), \quad (2.16)$$

where A is a dynamical pre-factor and ν is the cluster growth rate. Since there is no back-flux from (super)critical clusters – atoms will only attach to the clusters, and not detach – ν can also be interpreted as the attachment frequency of atoms to the clusters. This attachment frequency is usually taken as being proportional to the atomic mobility of the liquid; i.e., the atomic diffusivity, D . In first approximation this can be quantified macroscopically by the relation $D \propto 1/\eta$, where η is the shear viscosity [25].

The exact value of the pre-factor A is a source of much contention. In some

2.3 Nucleation and crystal growth

introductory texts, the physical relevance is handled cursorily and the product $A\nu$ is stated simply to be on the order of $\sim 10^{40} \text{ m}^{-3}\text{s}^{-1}$ [26, 27]. In other more in-depth treatments, a derivation of the product is provided, usually relying on the Stokes-Einstein equation,

$$D = \frac{kT}{3\pi\eta a_0}, \quad (2.17)$$

to give a description of the atomic mobility of the melt, where a_0 is the diameter of the diffusing spherical particles and can be taken as the average atomic diameter [21]. Since the experimentally determined values for A can differ greatly from theoretical predictions [21], it is usually left as a material-specific fitting parameter. Despite this, Eq. 2.16 nevertheless identifies the relevant parameters for nucleation; that is, the thermodynamic probability of cluster formation, given by the height of the nucleation barrier, ΔG^* , and the dynamical or kinetic contribution, given by the atomic mobility expressed by the product of ν and A , incorporating the viscosity, η .

The growth velocity of the crystal-liquid interface at a given temperature can be expressed as [28]

$$u(T) = \frac{f}{a_0} D \left[1 - \exp\left(-\frac{\Delta G^{l-x}}{RT}\right) \right], \quad (2.18)$$

where f is the fraction of sites on the crystal-liquid interface where atoms are preferentially added or removed. For materials where $\Delta S_f < 2R$, f is taken to be of the order unity and does not vary significantly with undercooling [28]. Similar to Eq. 2.16, the expression for the growth velocity of nuclei contains a thermodynamic, as well as a kinetic contribution. In this case, it is the Gibbs free energy difference, ΔG^{l-x} . At low undercoolings the diffusivity is high and ΔG^{l-x} is small; however, since ΔG^{l-x} appears in the exponential term, it will dominate the growth rate at high temperatures. At lower temperatures; i.e., higher undercoolings, the Gibbs free energy difference will increase, though the overall growth rate, $u(T)$, will decrease due to the slowing down of the liquid kinetics. At these temperatures the kinetic term $D \propto 1/\eta$ will dominate the growth rate, since η will rise exponentially (see Sec. 2.5), much greater than the change in ΔG^{l-x} .

Schematic curves of the nucleation rate, $I(T)$, and growth rate, $u(T)$, are shown in Fig. 2.3. While thermodynamics may favor the creation and growth of nuclei over the entire temperature range of the undercooled liquid, a max-

2.3 Nucleation and crystal growth

imum nevertheless appears in each curve and is the result of the dramatic slowdown of the liquid kinetics as the melt is undercooled. In this particular example, the nucleation and growth rates show very little overlap, which is characteristic of a high glass-forming ability (see Sec. 3.1).

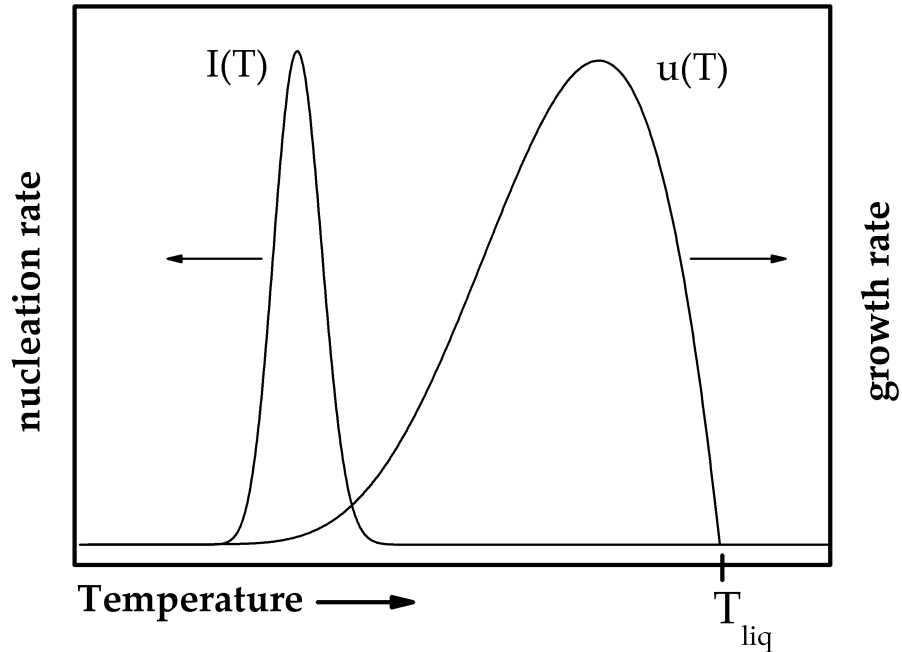


Figure 2.3: Schematic curves for the nucleation rate, $I(T)$, and growth rate, $u(T)$, of an undercooled liquid. As the system is undercooled, the liquid kinetics becomes slower, causing a notable decrease in both $I(T)$ and $u(T)$.

Assuming that the crystal growth and nucleation rates remain constant in time, for a given temperature, the volume fraction, X , crystallized in a time, t , may be modeled using the Johnson-Mehl-Avrami-Kolmogorov (JMAK) expression [29–33]

$$X(t) = 1 - \exp\left[-\frac{\pi I u^3 t^4}{3}\right], \quad (2.19)$$

where, for small values of X , this equation may be approximated as

$$X(t) \approx \frac{\pi}{3} I u^3 t^4. \quad (2.20)$$

In this way, the time to isothermally crystallize a certain volume fraction, X , can be calculated by solving Eq. 2.20 as follows:

2.3 Nucleation and crystal growth

$$t = \left(\frac{3X}{\pi I u^3} \right)^{\frac{1}{4}}. \quad (2.21)$$

If the onset of crystallization, t_x , is the desired quantity, one must consider an approximation for X that assumes a just-detectable volume fraction of crystallites. This concentration is given as 10^{-6} by Ref. [28]. Since the onset time for crystallization, t_x , depends on the nucleation rate, I , and growth velocity, u , it is reasonable to assume that the expression in Eq. 2.21 will resemble in some way the schematic curves shown in Fig. 2.3. That is, the behavior of the onset crystallization time with temperature should be shaped by both thermodynamic and kinetic factors. This is shown schematically in Fig. 2.4.

The onset time for crystallization is represented by the dashed line in Fig. 2.4 as a function the undercooling from the liquidus temperature, T_{liq} . The most relevant parameters determining the crystallization time are also shown as schematic curves; namely, the nucleation barrier (solid curve) and the viscosity (gray curve). The minimum in the crystallization time can be thought of as occurring at the temperature where simultaneously the kinetics (viscosity) of the melt is the fastest and the thermodynamic barrier to crystallization the lowest. At low undercoolings the melt mobility is high, promoting diffusion of atoms and growth of crystals; however, the nucleation barrier remains a significant hindrance to the formation of nuclei. Conversely, the nucleation barrier is lowered with increasing undercooling, yet the drastic rise in viscosity kinetically impedes the crystallization.

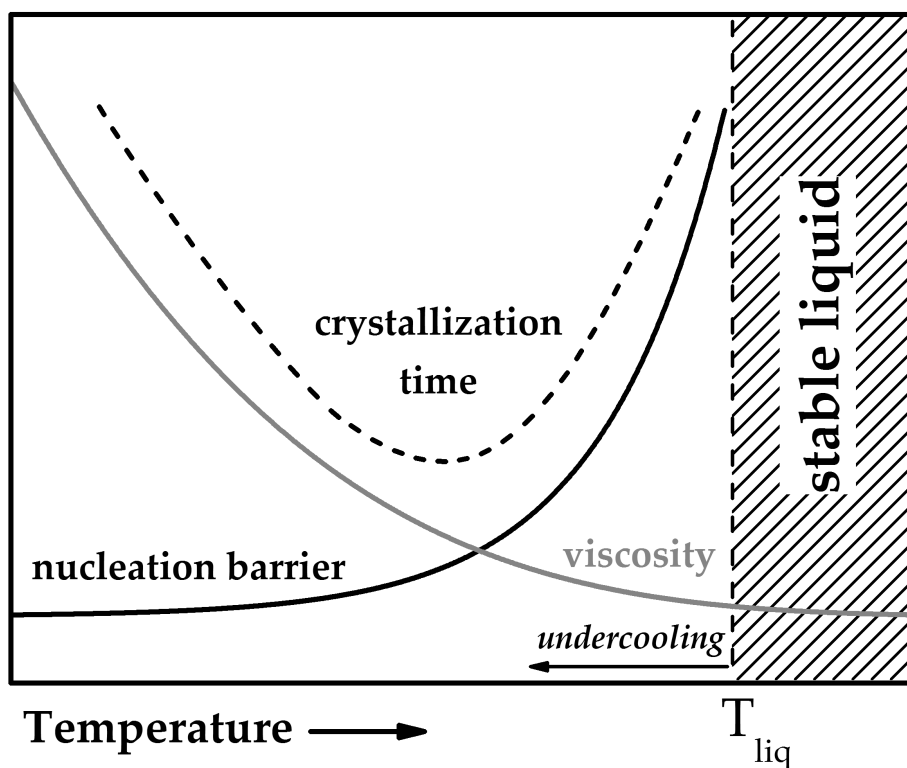


Figure 2.4: Schematic representation of the onset time for crystallization as a function of the undercooling (dashed curve). Also depicted are schematic representations of the nucleation barrier (black curve) and viscosity of the undercooled liquid (gray curve).

Typically, the logarithm of the onset time for crystallization is plotted as a function of temperature, with the temperature axis being the ordinate and $\log(\text{time})$ the abscissa. This is shown schematically in Fig. 2.5. The isothermal time for a phase transformation can be illustrated as in Fig. 2.5 and is referred to as an isothermal *time-temperature-transformation (TTT) diagram*. Two example glass-formers are represented by the solid and dotted curves in the TTT-diagram of Fig. 2.5, showing the characteristic "nose" shapes of the onset crystallization times. Schematically, the dotted curve is representative of a better glass-former, as the nose of the crystallization occurs at much longer times. A critical cooling rate for glass formation, R_c , can hence be defined as the minimum cooling rate required to bypass the formation of crystals and reach the glassy state (gray area). In this diagram the glass transition temperature, T_g , is schematically shown to decrease with increasing time. This is a result of the fact that T_g occurs at lower temperatures for slower cooling rates (see Sec. 2.6).

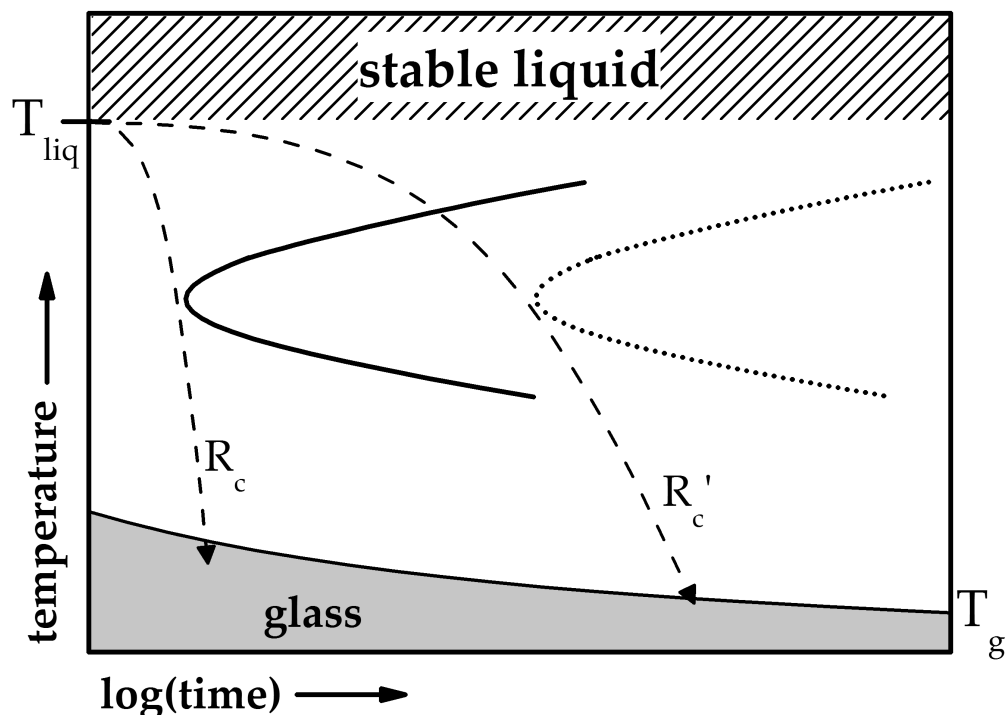


Figure 2.5: Schematic time-temperature-transformation (TTT) diagrams for two model glass-forming systems (solid and dotted curves) and their corresponding critical cooling rates (dashed curves), R_c and R'_c , respectively. The glassy region is depicted in gray.

2.4 Viscous slowdown and structural relaxation

Solidification of the metastable liquid can occur in two different ways. As was discussed in Sec. 2.3, crystallization of the liquid can occur at temperatures below T_{liq} through nucleation and growth of crystals. This process is marked by a *discontinuous* change in the extensive properties, like volume or enthalpy, of the material as the temperature is lowered (refer to path **1** of Fig. 2.6a). However, transition into the vitreous state can occur if crystallization is bypassed during undercooling. This *continuous* transformation in the volume or enthalpy is shown as path **2** in Fig. 2.6a. Monitoring the course of other physical properties of the liquid during undercooling, one would also observe the distinct transitions into the glassy and crystalline states. Path **1** (dashed line) of the schematic specific heat capacity curve in Fig. 2.6b

2.4 Viscous slowdown and structural relaxation

shows the crystallization occurring at T_{liq} , assuming no undercooling¹. If the undercooled liquid region (dotted line) remains stable with respect to crystallization, the glass transition occurs with decreasing temperature, and the specific heat capacity drops (path **2**) due to the loss in translational and reorientational degrees of freedom. The specific heat capacity of the glassy state is slightly greater, but nearly identical, to that of the crystalline state. Experimentally, the difference in specific heat capacity between the glassy and crystalline states exhibits a pronounced maximum near 0 K, due to the excess density of vibrational states at lower energies [34]. For metallic glasses the low-temperature effect has been explained as being primarily due to the localization of electrons, originating from long-range atomic disorder [35, 36].

Perhaps more outwardly indicative of the vitrification process is the dramatic increase in viscosity or relaxation time as the liquid is undercooled. Figure 2.6c shows a schematic representation of these properties along the solidification path (**2**) to a glass. The increase in viscosity or relaxation time of a liquid during undercooling reflects the inherent slowing-down of the kinetics as the glass transition is approached. Following an instantaneous drop in temperature, the liquid will take some time to equilibrate to its new state. This is known as *structural relaxation* and the characteristic time associated with it is referred to as the *structural relaxation time*, or *relaxation time*, in general. The relaxation time of the liquid is intimately connected to its viscosity, and the two quantities can be described in terms of the Maxwell relation

$$\eta = \tau G_{\infty}, \quad (2.22)$$

where G_{∞} is the high-frequency, or instantaneous, shear modulus. In the equilibrium liquid this relaxation time can be in the vicinity of 10^{-9} s, while near the glass transition increase to values on the order of 10^2 s [23]. In a similar manner the viscosity of an undercooled liquid can rise from around 10^{-1} Pa s near the melting point (for some dense metallic liquids the melt viscosity can be as great as 10 Pa s [19]) to around 10^{12} Pa s at the glass transition. When the liquid falls out of equilibrium at T_g , the timescales for structural relaxation increase even further; that is, the metastable, equilibrium liquid can only be reached from the glassy state during long-time annealing. This is shown schematically by the dashed line as path **3** in Fig. 2.6. At these temperatures the glass will effectively behave as a liquid only when observed

¹The drop in specific heat capacity depicted in Fig. 2.6b at T_{liq} is technically of zero width and infinite height and does not represent a discontinuous change like that of the volume or enthalpy.

2.4 Viscous slowdown and structural relaxation

on long time scales.

The structural relaxation of a glass below T_g can be described through the time-dependent change of many physical properties. This phenomenon is also known as *aging*. Path **3** in Fig. 2.6a shows, for example, how the volume or enthalpy of the glass will decrease during structural relaxation as the denser state of the equilibrium liquid at that temperature is attained. Accordingly, the viscosity of the glass will increase as the excess volume is annealed out (Fig. 2.6c). The increase in the specific heat capacity during structural relaxation, as shown by path **3** in Fig. 2.6b, appears here as the extrapolation of the specific heat capacity of the undercooled liquid to lower temperatures. In other words, the specific heat capacity of the glass will, given sufficient annealing time, eventually reach that of the metastable supercooled liquid, when observed on a long time scale [37].

2.4 Viscous slowdown and structural relaxation

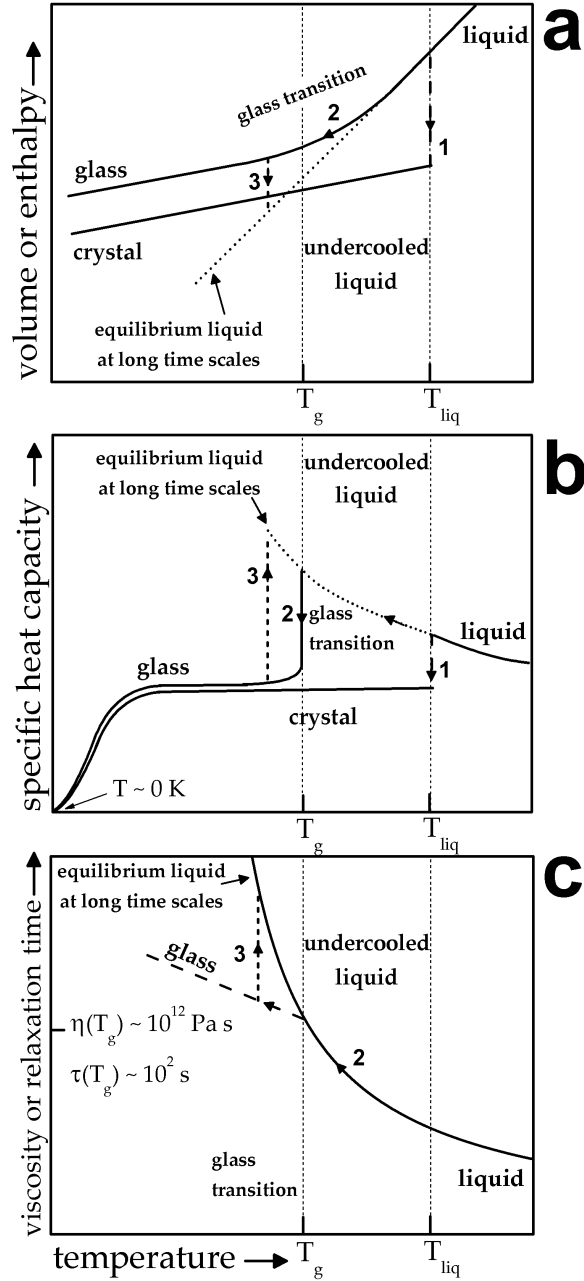


Figure 2.6: Schematic diagram showing the change in (a) volume or enthalpy, (b) specific heat capacity and (c) viscosity or relaxation time of a glass-forming substance with temperature. During undercooling, solidification can occur either (1) discontinuously through crystallization or (2) continuously by the transition into the glassy state. Below T_g , structural relaxation into the metastable, supercooled liquid will occur when observed on long time scales (3), resulting in a change of many physical properties with time.

2.5 The fragility concept

The viscosity or relaxation time of liquids can vary in different ways as T_g is approached during undercooling. For some liquids, the kinetics (viscosity or relaxation time) can be described linearly within a given temperature range using a $\ln(f)$ vs $1/T$ plot (Fig. 2.7). The viscosity or relaxation time of such glass-formers can be described by an Arrhenius equation of the form

$$f(T) = f_0 \exp\left(\frac{Q}{RT}\right), \quad (2.23)$$

where $f(T)$ represents viscosity, η , or relaxation time, τ , and f_0 the pre-exponential factors, η_0 or τ_0 , which give the theoretical infinite-temperature limits for η and τ , respectively. The commonly accepted values for these factors are $\tau_0 \sim 10^{-14}$ s, which is on the order of the inverse Debye frequency, and is thought to correspond to the characteristic time for quasi-lattice vibrations [38]; and $\eta_0 = hN_A/v_m$, where h is Planck's constant, N_A is Avogadro's number and v_m is the atomic volume [39]. The expression for η_0 was introduced by Eyring [40] as the lower bound for viscosity, under the assumption that the shortest timescale for atomic collisions in the liquid is $h/(kT)$. For many metallic glass-formers, the value of η_0 is very close to 4×10^{-5} Pa s [41–44]. The interchangeability of the η and τ in the expression in Eq. 2.23 is a result of the Maxwell relation shown in Eq. 2.22. Using the Maxwell relation, a quick comparison of the values of τ_0 and η_0 gives an instantaneous high-frequency, shear modulus, G_∞ , of $\sim 10^9$ GPa, which is in agreement with measurements of the instantaneous shear modulus ($\sim 10^9 - 10^{10}$ GPa) on a number of inorganic and metallic glasses [45, 46].

In Eq. 2.23, Q represents an apparent activation energy that is related to structural relaxation and viscous flow [40]. For oxide glass-formers like SiO_2 and GeO_2 , the values of the equilibrium viscosity over a large temperature range are well fitted by the above equation.¹ As shown in Fig. 2.7a, the slope of this curve

¹The apparent activation energy for viscous flow, Q_η , of SiO_2 , for example, correlates well with the molar energy required to break the oxide bonds, and this was thought to be the primary mechanism of viscous flow for such oxide glasses [47]. New theories, however, have found some success in using a model of line defects that better describes this behavior [48].

$$Q = R \left(\frac{d \ln(\eta, \tau)}{d(1/T)} \right), \quad (2.24)$$

is constant over the entire temperature range and gives the apparent activation energy Q .

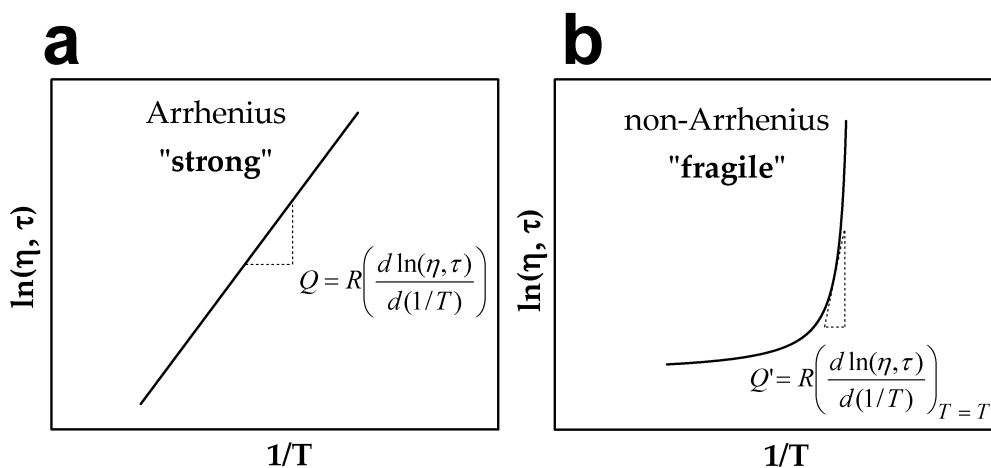


Figure 2.7: Schematic Arrhenius-plots of typical (a) *strong* and (b) *fragile* liquids.

For other classes of liquids, the viscous slowdown during undercooling can be so pronounced, that even a 10% decrease in the temperature can lead to an increase in the viscosity or relaxation time of around 10 orders of magnitude [23]. The kinetic properties of such liquids are thus not able to be described over a wide temperature range using Eq. 2.23 (dotted curve in Fig. 2.7b). However, if the temperature range is not too great, Eq. 2.23 can be used to describe the apparent activation energy, Q' at a temperature T' as

$$Q' = R \left(\frac{d \ln(\eta, \tau)}{d(1/T)} \right)_{T=T'}. \quad (2.25)$$

The curves in Figs. 2.7a-b each depict one end of the spectrum of liquid behavior, representing ideal Arrhenius and non-Arrhenius forms, respectively. The classification of liquids according to this behavior has been popularized in recent decades by researchers such as C. A. Angell [49]. In Angell's *fragility* scheme, liquids can be described by how much their kinetic descriptors; i.e., η and τ , deviate from pure Arrhenius behavior. Liquids showing large departure from the Arrhenius law of Eq. 2.23 over a large temperature range are

2.5 The fragility concept

said to be *fragile*, whereas more Arrhenius-like liquids are classified as *strong*. The degree of deviation from Arrhenius behavior is also an indicator for the sensitivity of the liquid kinetics to temperature change. Thus far, it appears that every type of liquid fits somewhere along the strong/fragile spectrum. Many oxide glass-formers fit the pattern of strong glasses, while glass-formers characterized by van der Waal interactions, for example, behave more fragile.

The non-Arrhenius behavior of glass-formers had been observed by Vogel as early as 1921 [50], and by 1926 two other researchers (Fulcher [51] and Tammann [52]) had independently published the same form of the three-parameter equation for viscosity

$$\eta(T) = A \exp\left(\frac{B}{T - T_0}\right), \quad (2.26)$$

which has now come to be known as the Vogel-Fulcher-Tammann equation, or simply VFT-equation. By utilizing the same exponential pre-factors as in Eq. 2.23, this equation can thus be rewritten as

$$f(T) = f_0 \exp\left(\frac{D^*T_0}{T - T_0}\right), \quad (2.27)$$

where the parameter B has been replaced by the product D^*T_0 , where D^* is referred to as the *fragility parameter*¹, and quantitatively describes the degree of departure from Arrhenius behavior [23]. Using this convention, the most fragile glass-formers have a fragility of around 2, whereas the strongest are on the order of 100. The VFT temperature, T_0 , is the temperature at which the barriers with respect to flow would approach infinity.

A convenient way of comparing viscosity or relaxation time over a wide temperature range of many glass-formers (usually with large variations in fragility) is shown in the so-called "Angell-plot" in Fig. 2.8 [49]. This is similar to the Arrhenius-plot in Fig. 2.7, only the inverse-temperature axis is scaled by T_g .

The expression in Eq. 2.27 has the advantage of being able to describe the experimental data over a wide temperature range. However, it has been shown that the VFT-equation breaks down for experimental data fitting over very large ranges of viscosity or relaxation times [53]. Moreover, if the data col-

¹Originally given by Angell as D , the fragility parameter was modified by Busch et al.[41] to D^* , as to distinguish it from the diffusion coefficient.

2.5 The fragility concept

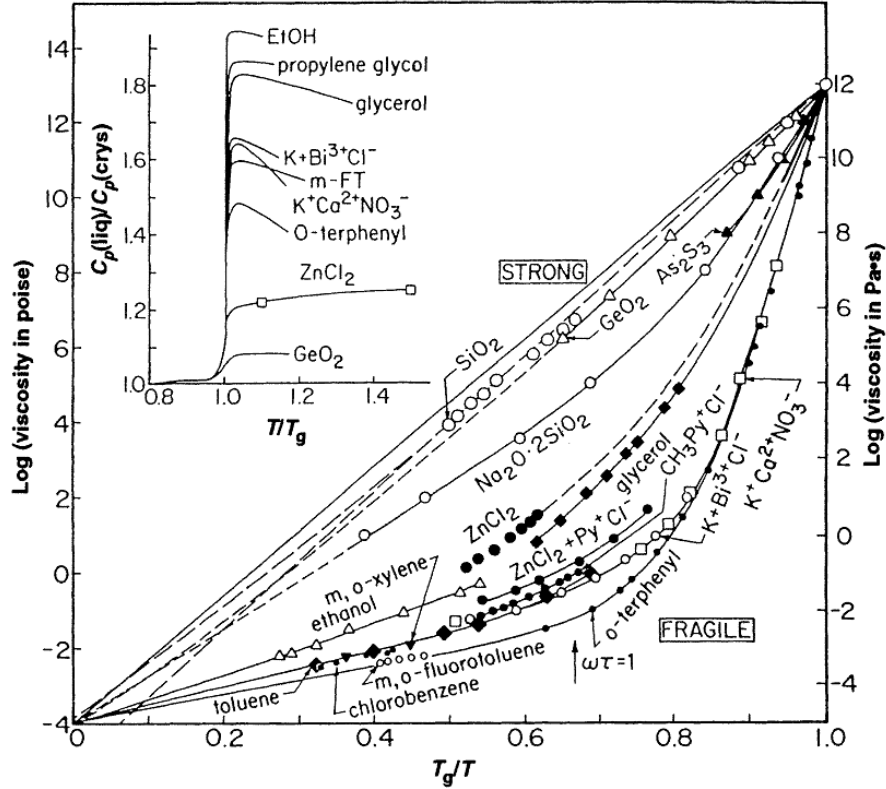


Figure 2.8: Angell-plot taken from Ref. [23].

lection is limited only to a certain temperature range (e.g. close to T_g), the values of the parameters obtained from fitting will depend strongly on the data range in question. A more common measure of fragility is the dimensionless *steepness index* or *m-fragility* and is given by

$$m = \left. \frac{d \log_{10}(\eta, \tau)}{d(T_g/T)} \right|_{T=T_g}. \quad (2.28)$$

The above expression closely resembles Eq. 2.25 and hence reflects the value of the apparent activation energy at T_g . For a perfectly Arrhenius system where the activation energy is described by Eq. 2.24, the value of m is equal to 16. In general, given that the VFT-equation is valid for the data range in question, the parameters m and D^* can be related by

$$m = 16 + 590/D^*. \quad (2.29)$$

It can be inferred from Eqs. 2.27 and 2.28 that, in the case of purely Arrhenius behavior, the fragility parameter D^* approaches infinity, while T_0 approaches zero.

2.5.1 The free volume model

An early attempt by Scott in 1960 to characterize the structure of an ideally simple liquid was through the dense random packing of hard spheres [54, 55]. However, even earlier this so-called *hard sphere model* was a useful and not altogether unreliable way of describing the atomistics of many liquid thermo-physical properties, e.g. viscosity [40, 56–58]. An important application of this led to the concept of the *free volume*, which has since become ubiquitous in the glass community.

In a series of publications from 1948 to 1954, Fox and Flory examined the relationships between molecular weight, viscosity and temperature on various polystyrenes and polyisobutylenes [56, 59–61]. They suggested that the viscosity could be expressed as a general function of the free volume, or the volume of the "holes" between these polymer segments, as well as the temperature [56].

Labeled as "free-space" by Doolittle in 1951 [57], this volume, v_f , was defined as the difference between the specific volume, v , and occupied or van der Waals volume, v_0 , at a given temperature. A phenomenological model of the equilibrium viscosity of glass forming substances was formulated in terms of the free volume by Doolittle

$$\eta(T) = \eta_0 \exp\left(\frac{bv_0}{v_f}\right), \quad (2.30)$$

where v_f is the average free volume per atom of the equilibrium liquid and the parameter b is a material specific constant of order unity. The term bv_0 represents the critical volume necessary for viscous flow. Building on the work of Fox and Flory, Bueche [62], Williams et al. [63], and Cohen and Turnbull [58] assumed a linear relation between the free volume and temperature while implicitly redefining the occupied volume in Eq. 2.30, v_0 , as the molecular, or atomic volume, v_m :

$$v_f = v_m \alpha_f (T - T_0), \quad (2.31)$$

where α_f can be approximated as the difference between the volumetric ther-

2.5 The fragility concept

mal expansion coefficients of the liquid and the glass, $\alpha_f = \alpha_{liq} - \alpha_{glass}$ [63, 64]. In this model of the free volume viscous flow occurs as a result of random density fluctuations that allow for diffusion of individual atoms without change to the local free energy [65]. In other words, viscous flow is attributed not to energy barriers, but rather to the re-distribution of free volume. Assuming now that T_0 is the temperature at which the free volume of the equilibrium liquid would vanish and viscous flow no longer be possible, it becomes immediately apparent that by substituting Eq. 2.31 for the free volume in Eq. 2.30, the VFT equation (Eq. 2.27) is recovered with the relation

$$\alpha_f = \frac{b}{D^*T_0}. \quad (2.32)$$

For approximatively hard sphere-like systems; i.e., those with mainly van der Waals bonding, Cohen and Turnbull noted that the b -parameter of Eq. 2.30 was around 60 - 80% of the molecular volume [58]¹. Additionally it was also shown in that same work that this parameter was a lot smaller – on the order of $0.1v_m$ – for some liquid metallic species; this point will be revisited later in this work.

In an extended model of the free volume by Cohen and Grest [66] the equilibrium liquid is partitioned into cells, whose free energy is a function of the cell volume. Each cell behaves then either liquid-like - capable of diffusive motion, or solid-like - capable of only oscillatory motion. Taking the Cohen and Grest expression for the free volume,

$$v_f = \frac{k}{2s_0} \left(T - T_q + \sqrt{(T - T_q)^2 + \frac{4v_a s_0}{k} T} \right), \quad (2.33)$$

and inserting it into Eq. 2.30 yields the parameters $bv_m s_0 k^{-1}$, T_q and $4v_a s_0 k^{-1}$. In this newer model of the free volume, v_f does not vanish at T_0 . Instead, the free volume remains greater than zero at all temperatures and only vanishes when $T = 0$. The viscosity, therefore, would not diverge and remain well defined for all temperatures.

¹Cohen and Turnbull give these values in terms of $\gamma v^*/v_m$, where γ is a constant and v^* is the critical volume for flow. It can be shown with relatively minimal work that $b = \gamma v^*/v_m$; the necessary relations are given in Ref. [58].

2.6 The glass transition and the fictive temperature

2.5.2 The configurational entropy model

Another phenomenological model of the equilibrium viscosity, based on the thermodynamic functions of the undercooled liquid, is the Adam-Gibbs entropy model for viscous flow [67]

$$\eta(T) = \eta_0 \exp\left(\frac{C}{S_c(T)T}\right), \quad (2.34)$$

where $S_c(T)$ is the configurational part of the entropy of the equilibrium liquid and the parameter C can be understood as a free energy barrier per particle for cooperative rearrangements. In this view, the viscous slowdown occurring during undercooling of the liquid is due mainly to the decrease in configurational entropy, $S_c(T)$. In other words, as the glass transition is approached during cooling, local potential energy barriers increase, such that fewer and fewer configurations are available to the system.

In the viewpoint from which the Adam-Gibbs equation was formulated, the mechanism of viscous flow is based on cooperative rearrangement of groups of particles. This notion of cooperative rearrangement, however, was already implicit in the free volume theories of Hirai and Eyring in 1958 [68, 69]. As the free volume decreases with progressive undercooling, viscous flow must occur through collective elemental processes; i.e., cooperative rearrangement.

The constant C of Eq. 2.34 is proportional to the height of the potential energy barrier to be crossed by the cooperatively rearranging region. The configurational entropy, $S_c(T)$, is not constant and adds an additional temperature dependence to the expression in Eq. 2.34. Assuming that $S_c(T)$ can be expressed in a similar integral form as in Eq. 2.4, it can be shown that the Adam-Gibbs equation will have the same functional form of the VFT equation [70]. In this light, the VFT fragility parameter, D^* , can be seen as being proportional to the potential barrier height, given by C , and inversely proportional the number, or density, of the configurational states, given by $S_c(T)$.

2.6 The glass transition and the fictive temperature

From a thermophysical point of view, the most accurate definition of a *glass* is a non-crystalline solid exhibiting the phenomenon of a glass transition [71].

2.6 The glass transition and the fictive temperature

Although the glass transition is well known to manifest itself through distinct changes in various physical properties, researchers like Angell, for example, prefer to describe the glass transition more generally as a "falling out of equilibrium" due to the continuous slow-down in one or more degrees of freedom [23]. The glass transition can thus be seen as being caused by a time scale that is longer than the time scale on which the system is being observed [72].

Upon undercooling from the liquid, a unique structural configuration is frozen into the glassy state as the liquid falls out of equilibrium during the glass transition. The temperature associated with the glass transition is a unique function of the cooling rate, q_C [73]. The only unambiguous definitions of the glass transition temperature are those that are determined during cooling and depend only on the cooling rate [72]. The concept of a characteristic glass transition temperature as being a unique function of the cooling rate was proposed by Tool [74] in 1946 as the fictive glass transition temperature. A distinct temperature is defined, on cooling, that is directly associated with the limiting value of the quantity measured to fall out of equilibrium at the glass transition. This temperature is known as the limiting fictive temperature, or T'_f , and is defined as the glass transition temperature as measured on cooling [73]. Figure 2.9a shows a schematic representation of the enthalpy, H , during the formation of a glass during undercooling. Geometrically, T'_f is defined from a point well into the glassy region. It is the temperature of intersection on the equilibrium H–T curve with a line drawn through the point of interest inside the glassy state having a slope equal to that of the glass curve. T'_f is usually determined from a differential scanning calorimeter (DSC) up-scan using the definition put forth by Moynihan [73]:

$$\int_{T^*}^{T'_f} (C_p^e - C_p^g) dT_f = \int_{T^*}^{T'} (C_p - C_p^g) dT. \quad (2.35)$$

The curves C_p^e and C_p^g represent the heat capacities belonging to the equilibrium liquid and glassy states, respectively. T^* is any temperature above the glass transition where $C_p = C_p^e$, and T' is a temperature well below the glass transition and into the glassy state where $C_p = C_p^g$. This construction is shown schematically in Fig. 2.9b. T_f^i is determined here graphically by matching the area underneath the curve with that of a rectangle defined by C_p^e and C_p^g . The heating rate, q_H , is intentionally left ambiguous, as T_f^i depends only on the cooling rate, q_{Ci} .

2.6 The glass transition and the fictive temperature

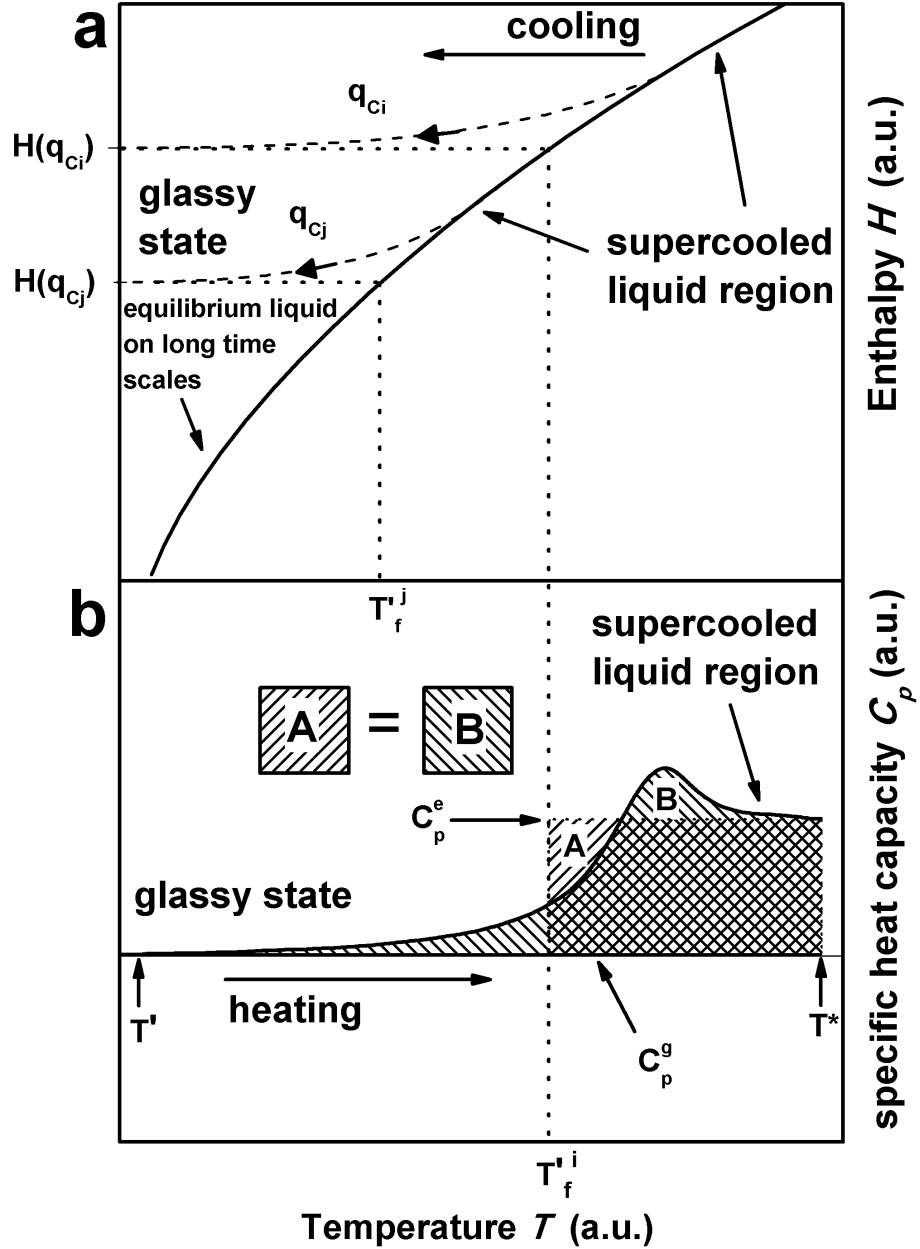


Figure 2.9: (a) Schematic plot showing enthalpy, H , versus temperature, T , during the formation of different glassy states, $H(q_{Ci})$ and $H(q_{Cj})$ by undercooling with rates q_{Ci} and q_{Cj} , respectively, where $q_{Ci} > q_{Cj}$. The corresponding limiting fictive temperatures, T_{fi}' and T_{fj}' are shown as projections (dotted lines) of the glass curve (dashed lines) onto the equilibrium liquid line (solid line) such that $T_{fi}' > T_{fj}'$. (b) Schematic of the specific heat capacity, C_p , versus temperature, T , during heating of the glass that was previously cooled from the liquid state with a rate q_{Ci} . The determination of T_{fi}' is also shown here [75].

Chapter 3

Current perspectives

3.1 Glass forming ability

The glass forming ability (GFA) of a particular liquid system is most readily reflected in its critical cooling rate, R_c (see Fig. 2.5). With a lower critical cooling rate more time is available for processing or casting of the liquid, due to the longer times needed for crystallization. It therefore follows from this that the critical casting thickness, D_c , must be inversely proportional to the critical cooling rate and can also be used as a measure of the GFA. However, the ultimate practicality of these metrics is somewhat debatable, as R_c , for example, is only accurately determined under controlled cooling conditions and must be estimated in the cases where R_c is high. Furthermore, the presence of a container wall (e.g. mold or crucible wall) will drastically effect the measured value of R_c . In a similar fashion, the determination of D_c will be highly dependent on the casting method and mold geometries used.

For this reason, many researchers have explored the use of differing metrics to estimate the GFA of BMG forming systems based on the relationships between transition temperatures like T_{liq} and T_g [76]. However, since the scope of this work centers on the liquid thermophysical properties, the focus on the GFA here will be given in terms of the relevant kinetic and thermodynamic properties of the liquid system.

The importance of simple parameters such as transition temperatures in estimating GFA was presented by Turnbull in 1969 [25]. Turnbull, considering a monatomic system, argued that the nucleation and growth rates of the underlying crystalline state are strongly dependent on the reduced temperature, $T_r = T/T_m$, and the undercooling, $\Delta T_r = (T_m - T)/T_m$. Thus, considering

the approximation from Eq. 2.7, it was shown that

$$\begin{aligned} I(T) &\propto \frac{1}{(\Delta T_r)^2} \\ u(t) &\propto \Delta T_r, \end{aligned} \tag{3.1}$$

leading to the conclusion that the GFA should scale as the *reduced glass transition temperature*, $\Delta T_{rg} = T_g/T_m$. Turnbull showed that, for values of $\Delta T_{rg} \geq 2/3$, the peak in the nucleation frequency was sharpened, lowered and shifted to higher values of the undercooling. Given the simple approximations employed by Turnbull, this ratio has nevertheless shown itself to be a good indicator of GFA; this is evidenced in the comprehensive list of metallic glass-forming systems found in Ref. [77]. However, as sole predictor of GFA, this criterion has been shown to fail in many cases [78]. Alternatively, it was shown by Inoue et al. [79] that, for a number of BMG forming alloys, the width of the supercooled liquid region as measured by a DSC/DTA up-scan, $\Delta T_x = T_x - T_g$, where T_x is the onset temperature of crystallization, correlated well with the critical cooling rate. This criterion has been referred to as the *thermal stability* and is traditionally linked with high GFA compositions. However, in their investigations on the Zr-based Vitreloy series, Waniuk et al. [80] showed that, surprisingly enough, the ΔT_x values tended to be the largest for the poorest of these glass formers (with the GFA based on R_c). This was attributed to decomposition and phase separation occurring upon heating, which was not present during cooling from the melt. The increased timescale of the decomposition process at lower temperatures thus leads to an enhanced apparent thermal stability, given by the increased value of ΔT_x .

While many metrics may exist for predicting the GFA of a liquid system, it is ultimately the understanding of the thermodynamic and kinetic factors behind glass formation that identifies the physically relevant mechanisms. The role of deep eutectics was identified early as a deciding thermodynamic indicator of a high GFA [7, 81]. Since these liquids tend to remain compositionally homogeneous over a wide temperature range and have low melting temperatures, kinetic arrest occurs earlier, facilitating glass formation (this also associated with a high value of T_{rg}) [81, 82]. It was also noticed that a strong degree of interaction between the elements; i.e., a highly negative heat of mixing, ΔH_{mix} , was very favorable to glass formation as well [82]. Alongside this, Greer [83] also remarked that, in reference to the newly discovered Vitreloy alloy series, the addition of an element with a large difference in atomic

3.1 Glass forming ability

radius (in this case, beryllium) would favor glass formation by resulting in a denser packed liquid state. Thus gave rise to the term *confusion principle*, which describes the general presumption that, by effectively mixing elements with a large size mismatch, crystal formation becomes kinetically frustrated, due to the inability, or *confusion*, of the constituent atoms in finding a viable crystal structure.

The observed criteria for good glass formation were given by Inoue [84] as basic mechanisms for stabilization of the supercooled liquid, which were summarized into three empirical rules: (1) multicomponent systems consisting of three or more elements; (2) significant difference in atomic size ratios above about 12% among the three main constituent elements; and (3) negative heats of mixing among the three main constituent elements.

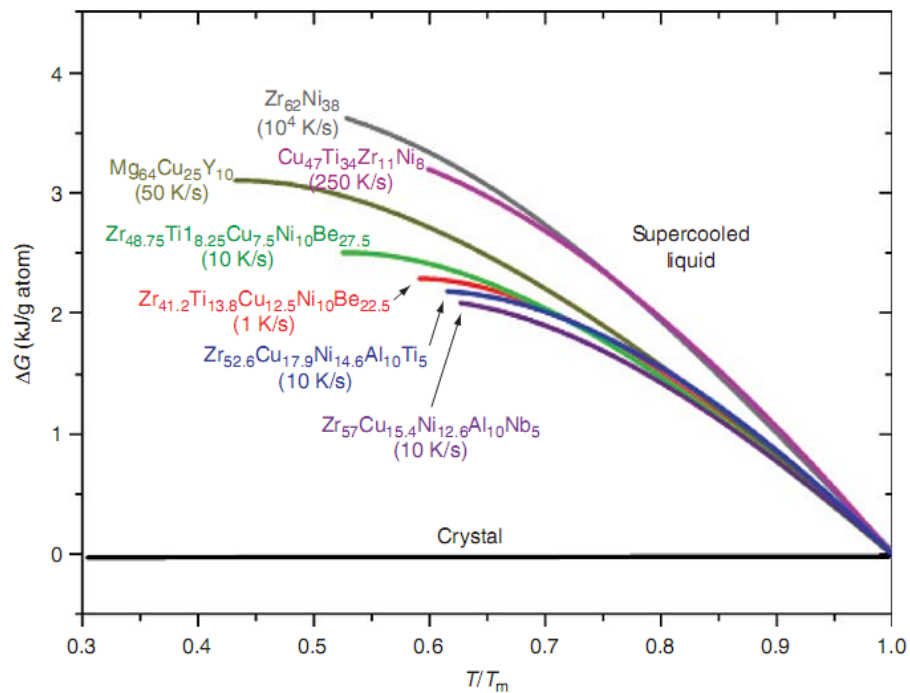


Figure 3.1: Gibbs free energy difference between the liquid and crystalline state of select BMG-forming systems, taken from Ref. [85]. The critical cooling rates are also indicated here.

Inoue postulated that the fulfillment of these criteria generally led to an increase in the degree of a dense random packed structure, which increased the difficulty of atomic rearrangements. As a consequence of this, atomic diffusivity should drastically slow down resulting in a highly viscous metallic melt, in

which the nucleation and growth of crystals is significantly suppressed. Masuhr et al. [19] showed this was indeed the case for Vitreloy 1, where the shear viscosity of the liquid was measured to be around three orders of magnitude larger than that of the individual metallic constituents.

From a thermodynamic perspective, Busch [20] compared the difference in Gibbs free energy between the liquid and crystalline states for a series of BMG compositions and noticed that, in general, the better glass formers have a much lower driving force for crystallization in the undercooled liquid. This is reproduced in Fig. 3.1. Kinetically, there also seemed to be a correlation between the fragility of the liquid and its GFA. In particular, Busch also showed that the fragility parameter, D^* , was usually higher (~ 20) amongst those multicomponent glass-formers with a high GFA (Fig. 3.2).

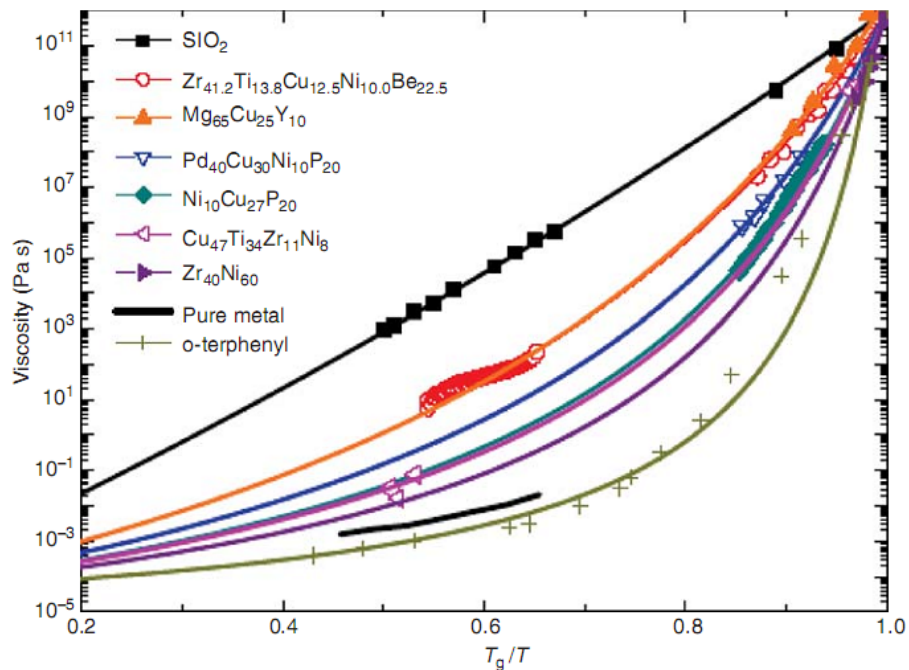


Figure 3.2: Angell plot comparing the viscosities of different glass forming systems. Taken from Ref. [85].

This strong liquid behavior of these glass formers fits well into the picture of densely packed, kinetically sluggish metallic systems. Moreover, the effect of the number of components on the kinetic fragility was determined by Shadwospeaker et al. [86], for a series of Zr-based and Ni-Nb-based alloy systems. Figure 3.3 shows the marked increase in fragility parameter as the number of components is increased from that of simple binary systems, like Zr-Ni, to

5-component systems like Zr-Ti-Cu-Ni-Be.

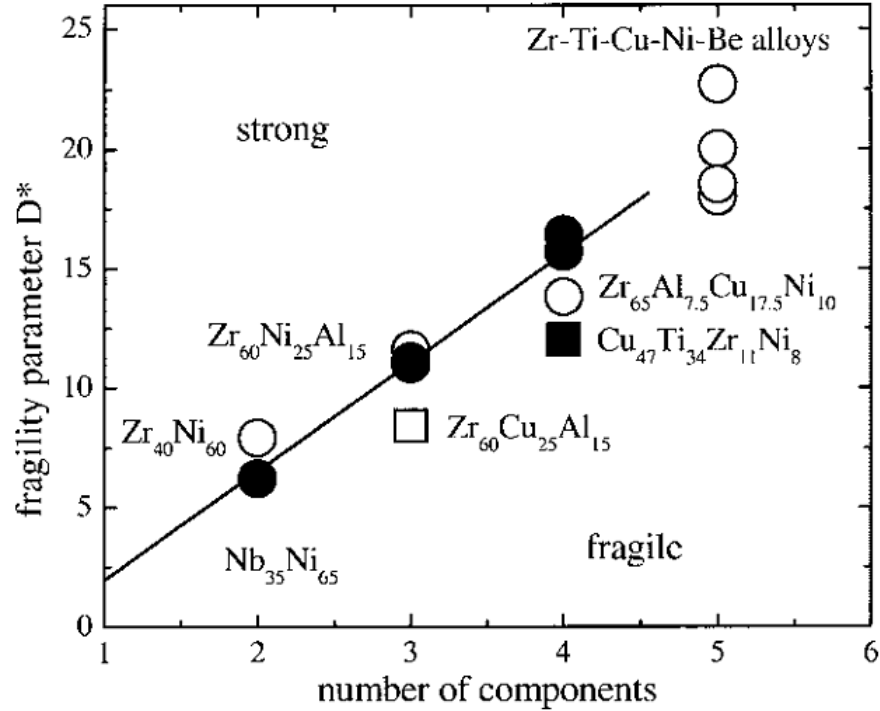


Figure 3.3: Plot of the kinetic fragility parameter, D^* , versus number of components for different glass forming systems [86].

Busch et al. [85] concluded that the GFA of a given BMG composition usually correlates well with its kinetic fragility; i.e., the stronger the liquid, the better its GFA. While this is indeed the case for many Zr-based glasses and has also been established for kinetically strong glass formers like Mg-Cu-(Y, Gd) [42, 87, 88] and Ca-Mg-Zn-Cu [89, 90], there are exceptions that deserve mentioning. In particular, the composition $\text{Pd}_{43}\text{Cu}_{27}\text{Ni}_{10}\text{P}_{20}$ currently has the lowest critical cooling rate ($R_c = 0.10 \text{ K s}^{-1}$) of all the metallic glass formers, yet has a surprisingly low fragility parameter of $D^* = 10.3$ [91]. From a thermodynamic viewpoint, however, this composition also has a very low driving force for crystallization – even lower than Vitreloy 1 (see Fig. 3.4) [92].

Given these considerations, it now becomes clear that there is no one definitive deciding factor on GFA. While kinetically strong, highly viscous melts are definitely advantageous, glass formation is ultimately decided by suppressing the formation and growth of the underlying crystalline state. However, it appears that pure thermodynamic considerations are similarly insufficient.

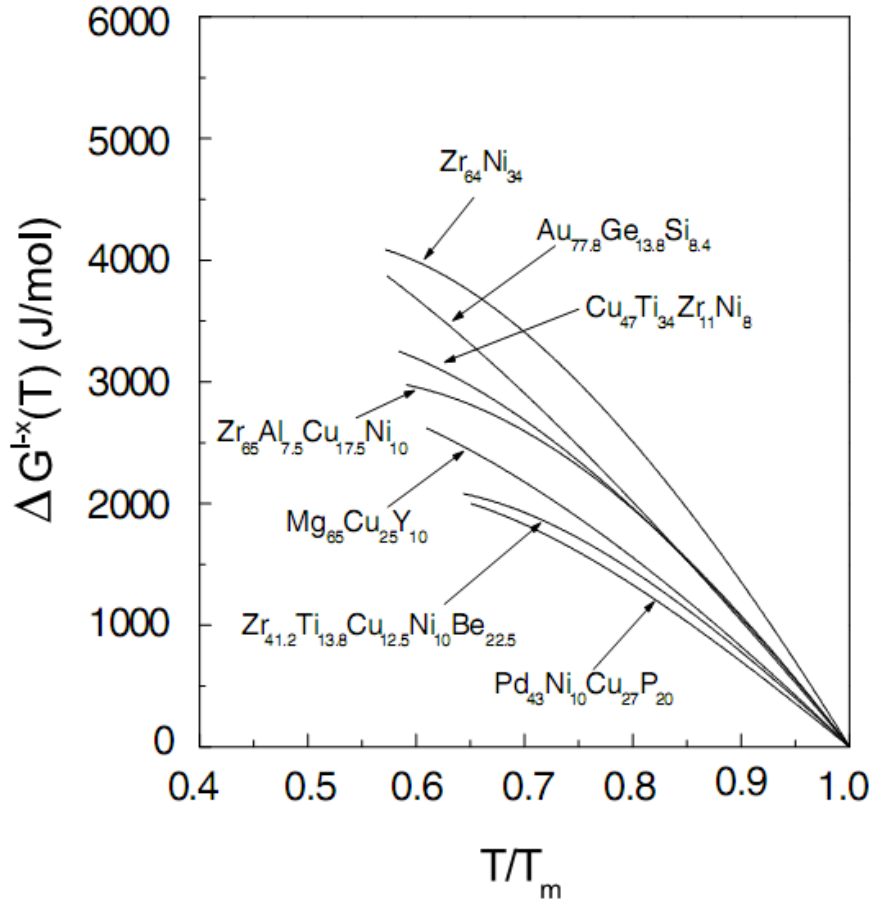


Figure 3.4: Gibbs free energy difference between the liquid and crystalline states as a function of the undercooling for various BMG forming systems [92]. The $\text{Pd}_{43}\text{Cu}_{27}\text{Ni}_{10}\text{P}_{20}$ composition is shown here as having the smallest driving force for crystallization in comparison with the other BMG glass forming liquids.

Consider the case of the bulk glass forming Cu-Zr system, for example. It was shown that there exist a few compositions in this system, for which the thermodynamic driving force for crystallization may favor the formation of competing crystalline phases, yet bulk glassy samples are nevertheless attained [93]. In that work, Li et al. provide experimental evidence that the deciding factor towards glass formation of those particular compositions was ultimately the density of the glassy phase. That is, the GFA was highest for those compositions where the density change between the glassy and crystalline states was minimal, providing evidence of especially dense packing¹.

¹It should be noted, however, that the authors in that study used the bending angles of

That work is just one of many that highlight the underlying structural facet of metallic glasses. From a thermophysical viewpoint, many of the characteristics of multicomponent metallic melts – e.g. strong liquid behavior, high viscosity and low entropy of fusion – are thought to originate from pronounced order, or structure, in the liquid state [20].

3.2 Structure

The modern idea of order in metallic melts originates from the hypothesis of Frank, who in 1952 [95] postulated that the then recently reported undercooling abilities of pure metals by Turnbull et al. [4–6] originated from a high interfacial energy, σ , between the liquid and underlying crystalline phase (see e.g. Eq. 2.11 of Sec. 2.2). Frank predicted that the interfacial energy would be high due to pronounced icosahedral short-range order in the melt. Due to its five-fold rotational symmetry, which is incompatible with the translational symmetry of normal crystalline phases, an icosahedral cluster, for example, would not be able to form a crystal without great energy cost. Additionally, the icosahedral ordering scheme suggested by Frank – one atom surrounded by twelve others – is a more energy efficient packing scheme than dense packed fcc or hcp structures with the same number of atoms. The formation of an icosahedral atomic cluster from the undercooled melt through intermediate polyhedra is illustrated schematically in Fig. 3.5.

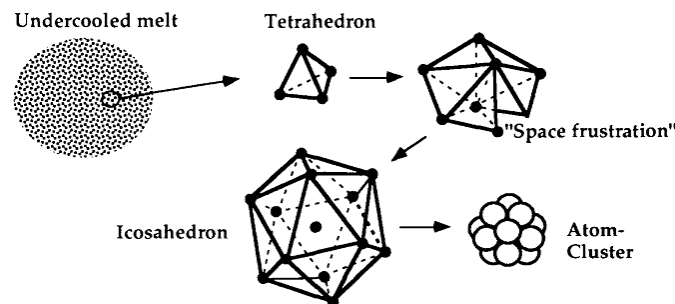


Figure 3.5: Schematic illustration of the formation of an icosahedral atomic cluster from the undercooled melt after Ref. [96].

Hayes et al. in 1978 [97] presented strong evidence of chemical ordering in a cantilevers as a measure of the density. In doing so, they failed to take into account a few factors that could influence the degree of bending, such as the relative thermal stabilities of the supercooled liquid regions of each Cu-Zr composition and the final grain size of the resulting crystal microstructures. Further critique is given in Ref. [94].

binary Pd-Ge metallic glass using synchrotron x-ray scattering. That work also highlighted the deviation from the ideal model of dense random packing of hard spheres (see Bernal [55]) due to this ordering, especially for metal-metalloid pairings. Not long afterwards, Gaskell [98, 99] developed a simple structural model for metal-metalloid glasses, in which dense random packed structures were obtained by allowing the metalloid to occupy various polyhedral sites around each metal atom. In 2003, Miracle et al. [100] explored the concept of topologically ordered atomic configurations, or clusters, having a high local packing efficiency. Similar to the ideas of Gaskell, Miracle suggested that tetrahedral and octahedral clusters, for example, can have high local packing fractions if the interstice is filled (Fig. 3.6). However, as Miracle points out, these particular clusters are unlikely to exist in metallic glasses, as they require solutes that are much smaller than what is typically present in such alloys. Based on the consideration of the radius ratio of the solute atoms to solvent atoms, R , Miracle postulated that more likely cluster configurations are capped trigonal prismatic and icosahedral.

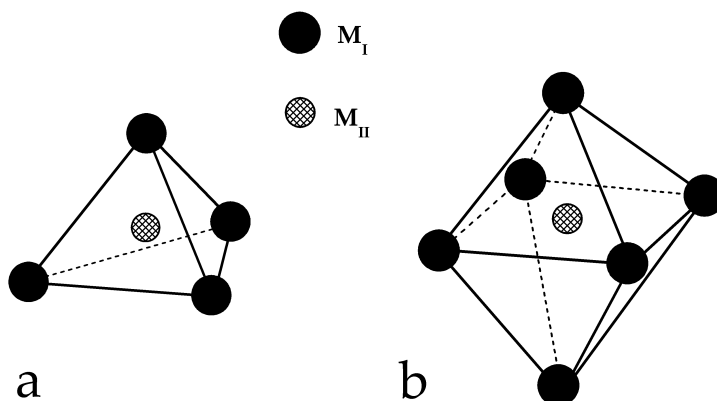


Figure 3.6: Schematic illustration of (a) tetrahedral and (b) octahedral interstitial filling of atomic clusters. M_I (filled circles) and M_{II} (hatched circles) correspond to the different atomic species.

Although these simple geometric models never went beyond nearest-neighbor considerations, they nevertheless provided the basic framework for further structural models of short-range order (SRO) and eventually medium-range order (MRO) in metallic glasses. Going beyond the efficient packing SRO model, the question arises of how to effectively fill 3-dimensional space beyond

the nearest neighbors. The consideration of the MRO is thus the question of the higher-order liquid structure based on these SRO units.

In 2004, Miracle [101] introduced a structural model for metallic glasses extending well beyond the nearest-neighbor shell. In this model, efficiently packed solute-centered atomic clusters represent the local SRO structural elements (e.g. icosahedral SRO), while the extended MRO structure is realized by placing these efficiently packed spherical clusters onto fcc or hcp lattice-like sites (see Fig. 3.7). Although based only on topological considerations; i.e., atomic size ratios, Miracle's model has nevertheless had much success at predicting the GFA of many alloy systems [101–104]. Building on the ideas of Miracle, Ma et al. [105] proposed a similar model of the MRO where the local SRO clusters are further ordered onto larger icosahedral or icosahedral-like "extended clusters".

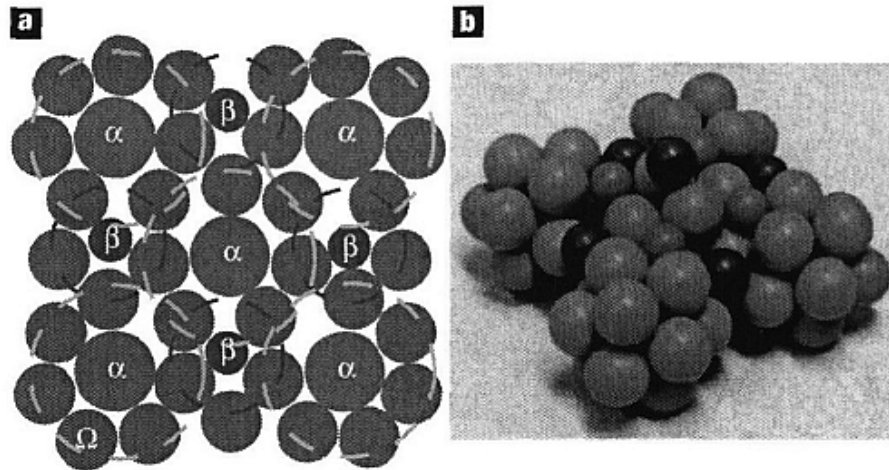


Figure 3.7: 2D and 3D models of extended medium-range order (MRO) clusters based on short-range order (SRO) icosahedral structural units. Image taken from Ref. [101].

The case for pronounced order in metallic glasses has been examined to a great extent and much experimental evidence has been brought to light, thanks in part to the development of electrostatic/electromagnetic (ESL/EML) levitation techniques [106–109] and also in part to the advancement of transmission electron microscopy (TEM) techniques using electron diffraction [110–115]. Aside from direct observations of SRO and MRO using microscopy and various scattering techniques, studies focusing on the measurement of thermophysical properties such as viscosity and density have also provided supporting evidence.

Within the context of structural relaxation below T_g , Egami [116] proposed that atomic SRO be separated into two different phenomena: topological short-range order (TSRO) and chemical short-range order (CSRO). In TSRO only the topological configurations of the atoms are taken into account; that is, only the changes in the interatomic distances, regardless of the atomic species, are considered. Changes in the TSRO are directly reflected in the increase of density, for example, during relaxation below T_g . CSRO describes the type of SRO in which only the ordering due chemical interactions between individual atomic species is taken into account. Changes to CSRO are considered to be primarily responsible for changes to the magnetic properties [116]. In general, however, the changes to any physical property during structural relaxation below T_g are thought to be affected by both the TSRO and CSRO [117].

In a series of publications, van den Beukel and co-workers [117–120] examined the changes to properties such as length, Young’s modulus and viscosity during isothermal annealing below T_g of Fe-Ni-B metallic glasses. It was concluded in those works that the TSRO contribution to structural relaxation is irreversible and slower than that of the CSRO and is described by a single activation energy, Q , which is usually observed in viscosity measurements below T_g (see e.g. Eq. 2.25 of Sec. 2.5). The CSRO contribution, on the other hand, is reversible and is best described by a range of activation energies. In two further publications, van den Beukel and Sietsma et al. [121, 122] showed that the kinetic glass transition as measured using DSC can be modeled well using a defect annihilation model of the free volume. A better model of the experimental DSC data is obtained when considering the additional effects of CSRO [122].

Using ESL techniques, Ohsaka et al. [107] measured the specific volume of Vitreloy 1 from well above the liquidus temperature down into the glassy state. It was shown that this particular alloy in its liquid state has a specific volume that is approximately 3% less than that of the ideal volume, reflecting the presence of chemical attractions between the constituent elements, leading to a negative excess volume and greater density than expected. In 2007, Busch et al. [123] measured the melt viscosity of that same alloy using concentric shear cell rheometry and gave evidence of a liquid-liquid transition from a kinetically strong to a kinetically fragile melt. More specifically, as the temperature was increased throughout the liquidus region, the viscosity of the kinetically strong melt remained quite high, at which point the viscosity decreased around two orders of magnitude (see Figs. 3.8 and 3.9) into a more kinetically fragile state. When the fragile liquid was further cooled, the high-viscosity liquid behavior was only reestablished at temperatures well below the liquidus temperature. Furthermore, pronounced non-Newtonian,

shear thinning behavior was noticed in the strong liquid, which then vanished upon entering the kinetically fragile state.

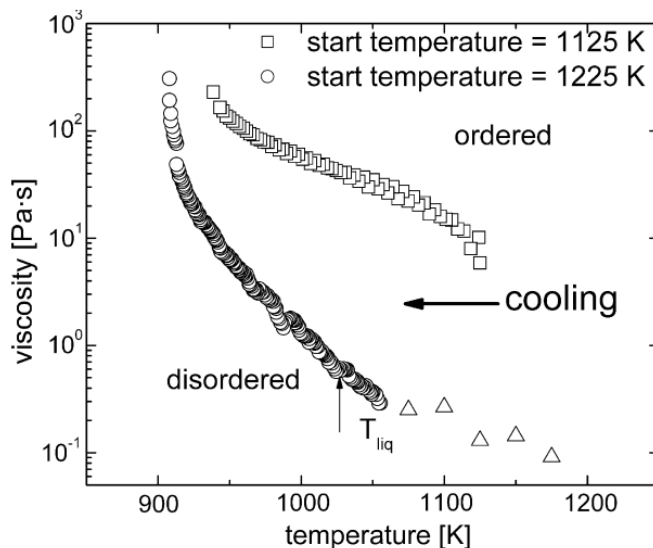


Figure 3.8: Viscosity of the ordered (open squares) and disordered (open circles and open triangles) liquid states of Vitreloy 1 on cooling from the melt. Taken from Ref. [123].

It was proposed that the observed viscosity effects in the Vitreloy 1 melt can be well explained within the established SRO and MRO models of metallic glasses. Way [124] hypothesized that the observed shear thinning behavior was the result of the destruction of the MRO clusters. Upon further shearing, the MRO clusters would break down into SRO clusters as depicted in Fig. 3.10.

Returning to Frank's hypothesis of icosahedral SRO, it is essential to note the experimental work that has taken place towards verifying this particular premise. It was shown in 1993 by Holland-Moritz et al. [106] that quasicrystal-forming¹ Al-Cu-Co and Al-Cu-Fe alloys have a much lower nucleation barrier, ΔG^* , for the icosahedral quasicrystalline phase than for the regular crystalline phase. This established indirect evidence of pronounced icosahedral SRO in the melt. In 2002 and 2003 the first direct evidence of icosahedral SRO was given by Schenk et al. [108] and Kelton et al. [109]. Using neutron scattering

¹Quasicrystals are quasi-periodic crystalline structures that lack translational symmetry but have a five-fold icosahedral point group symmetry. As such, they will diffract electrons like a regular single crystal. Further details can be found in the now much-publicized work of Shechtman et al. [125].

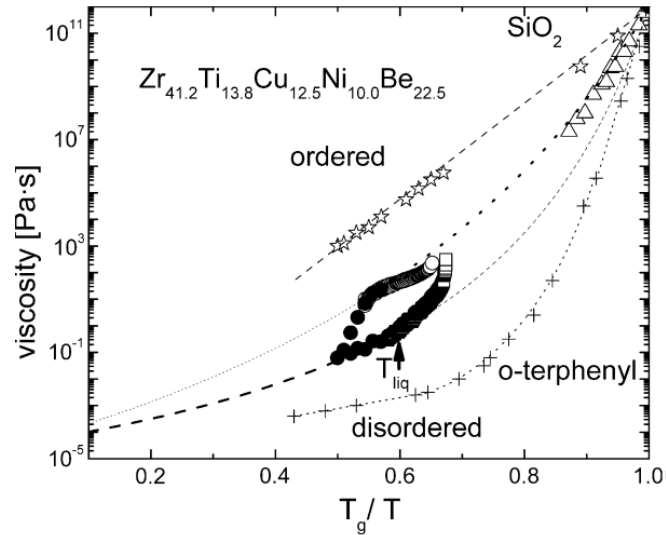


Figure 3.9: Angell-plot of the viscosity of the Vitreloy 1 liquid (open squares and open circles), showing the fragile-to-strong transition. Taken from Ref. [123].

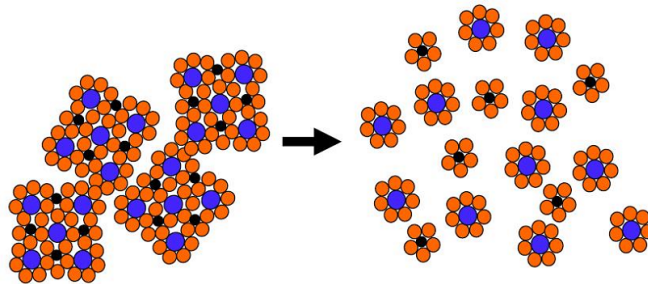


Figure 3.10: Schematic illustration of the breakdown of MRO clusters into SRO elements after Ref. [124].

techniques, Schenk studied bulk melts of several pure transition metals and showed that, from well above T_{liq} to very deep undercoolings, icosahedral SRO is present in the melt and becomes more pronounced with undercooling. Similar results in the Ti-Zr-Ni system were reported by Kelton, who showed that pronounced icosahedral SRO in the melt lowered the interfacial energy for formation of the metastable icosahedral quasicrystalline phase, which was even shown to be the preferred path to solidification over the stable C14 Laves phase.

Finally, in light of this new evidence, the old question of crystallization takes on a new face. On the one hand, the existence of pronounced icosahedral SRO in the melt should promote good GFA due to the structural incompatibility

between icosahedral clusters and an atomic lattice. However, the existence of a quasicrystalline or stable crystalline phase with local icosahedral symmetry (e.g. Frank-Casper phase [126]), would actually work to reduce the nucleation barrier and ultimately lower the GFA. Similarly, it has been argued that the relatively poor GFA of some binary metallic glasses based on early and late transition metals (e.g. W-Fe, Mo-Co and Nb-Ni) is due, in part, to the similarity between the local liquid structure and underlying crystalline phase [127]. On the other hand, since icosahedral SRO does not dominate in all BMG alloys (e.g. Ca-Mg-Zn glasses [104]), other efficiently packed cluster geometries may actually help to increase the liquid-crystal interfacial energies and increase GFA.

Given these structural considerations, it is interesting now to reexamine the trend of strong liquid behavior and high GFA. In particular, if a high melt viscosity is indicative of pronounced SRO (icosahedral or otherwise), the GFA of an alloy could actually decrease, due to the similar configurations of the liquid and crystalline states. ESL undercooling studies on the Al-Co system by Schroers et al. [128] showed that the maximum undercooling was dominated by the structure of the phase primarily solidifying from the melt. The decagonal (D) quasicrystalline phase was observed to be the primary phase solidifying from the melt, with an interfacial energy smaller than that of the crystalline β -phase. While pronounced SRO may work to hinder the nucleation and growth of crystals, a low interfacial energy between the melt and (quasi)crystal, σ , can also be an important factor affecting the GFA.

3.3 Crystallization

Kim and Busch et al. [129] gave the first report of experimental data on the crystallization of a BMG forming system (Vitreloy 1) covering the entire temperature range from the melt down to the glassy state. The resulting isothermal TTT diagram, recorded using containerless high-temperature high-vacuum electrostatic levitation (HTHVESL) techniques, exhibits the characteristic nose shape at around 100 s (Fig. 3.11). Those results also showed thermal evidence of phase separation prior to multi-stage crystallization at temperatures below the nose of the TTT diagram.

The extensive studies performed on the Vitreloy 1 alloy revealed a rather complex path to crystallization. For example, it was shown through calorimetric and thermomechanical analysis [14], as well as small angle neutron scattering and TEM [130] that Vitreloy 1 exhibits a modulated chemical decomposition process; i.e., phase separation, preceding primary crystallization into Cu-Ti

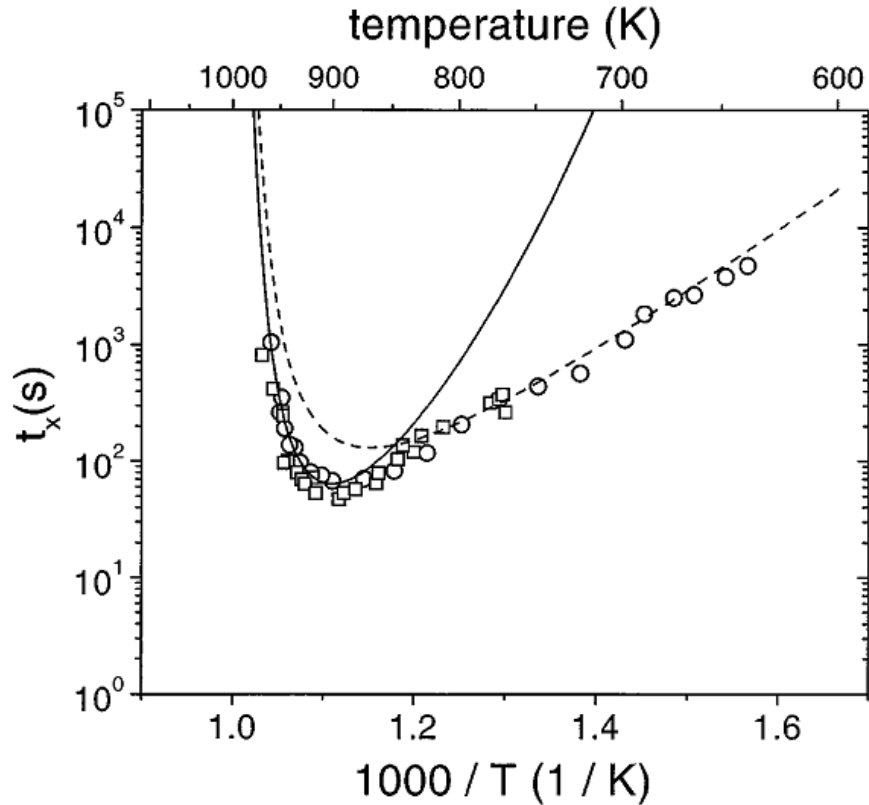


Figure 3.11: Isothermal time-temperature-transformation (TTT) of Vitreloy 1 reproduced from Ref. [19], with experimental data from Ref. [129].

rich nanocrystals during isothermal annealing around T_g . Furthermore, field-ion micrographs by Busch et al. [131] showed that this alloy, when slowly cooled from the melt, undergoes phase separation on a length scale on the order of 20 nm.

With regards to the Zr-Ti-Ni-Cu-Be system in general, many researchers have noticed marked distinctions between the isothermal crystallization behaviors of the high and low temperature regimes [80, 129, 130, 132–134]. In particular it was shown that, for annealing temperatures below the nose of the TTT-diagram, crystallization, in general, proceeds in multiple steps, usually being preceded by pronounced phase separation and the formation of a quasicrystalline phase [129, 133, 134]. As the annealing temperature is increased, most of the alloys in this system were shown to crystallize in one rapid event [134], which is also the case for temperatures above the nose of the TTT diagram [129].

These results illustrate the decisive role that different times scales can play in

3.3 Crystallization

the crystallization of multicomponent melts. While rapid quenching from the melt may avoid the onset of decomposition and phase separation, annealing from below the nose of the TTT diagram and in the vicinity of T_g may show pronounced changes in certain thermophysical properties before the onset of crystallization. Waniuk et al. [14] showed that the isothermal viscosity of Vitreloy 1 at annealing temperatures around T_g can increase, over a very long time scale, in orders of magnitude from its initial equilibrium value (see Fig. 3.12). This deviation from equilibrium was attributed to phase separation and primary nanocrystallization, eventually resulting in another metastable state. This state is thought to be most likely composed of nanocrystals embedded in an amorphous matrix having a different composition than before.

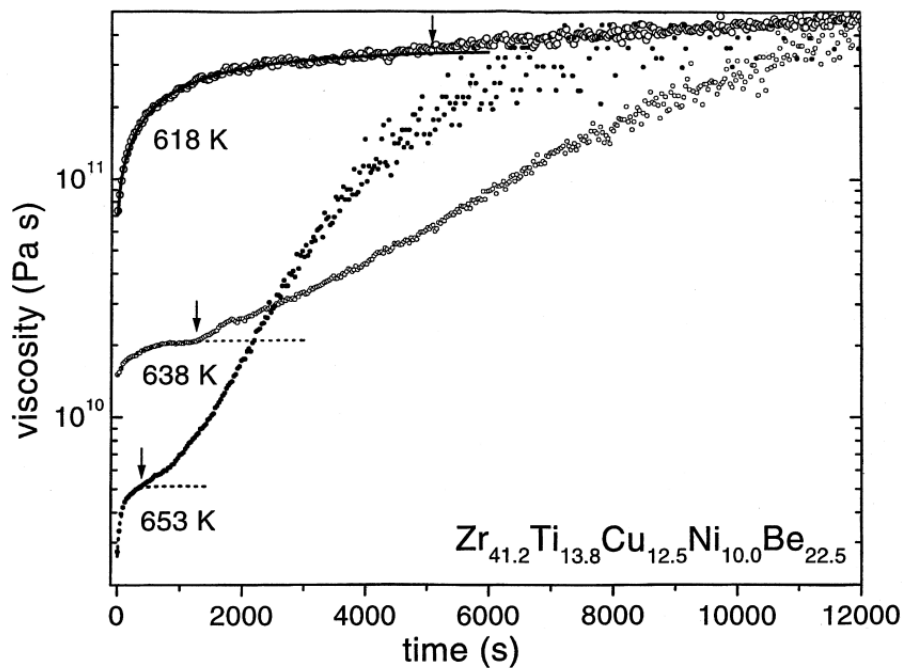


Figure 3.12: Isothermal viscosity as a function of time at temperatures below T_g for Vitreloy 1, taken from Ref. [14]. The beginning of phase separation and primary crystallization is indicated by the arrows.

It is important to note here that structural relaxation below T_g is not a precursor to crystallization as such, but rather brings the glassy structure closer to that of the equilibrium liquid [135]. However, as shown in Fig. 3.12, if the melt has a tendency to phase separate, this can contribute to reduced thermal stability by lowering the nucleation barrier in comparison with the homogeneous equilibrium liquid. Furthermore, as discussed in Sec. 3.2, if the equilibrium liquid and crystalline states share structural similarities (i.e.

3.3 Crystallization

icosahedral SRO), relaxation can increase the amount of chemical SRO, thus also potentially lowering the nucleation barrier.

Another characteristic of BMG-forming melts is the transition from nucleation-controlled to diffusion and growth-controlled crystallization. By repeating numerous isothermal crystallization experiments on Vitreloy 1, Schroers et al. [136] showed that, for temperatures above the TTT nose, the onset time for crystallization exhibited a very large scatter, reflecting the statistical nature of the nucleation process. In contrast, isothermal crystallization times below the TTT nose were reported to be rather invariant, which was attributed to a diffusion-controlled process preceding nucleation. Similar behavior was reported later by Schroers et al. [137] in the $\text{Pd}_{43}\text{Ni}_{10}\text{Cu}_{27}\text{P}_{20}$ melt. Adapting the droplet isolation technique from Turnbull et al. [6], it was shown that, at high temperatures, nucleation can be well modeled as a steady-state process, with one nucleation event triggering further events. For low temperatures, it was shown that the growth of crystals solely dominates the crystallization process over the entire sample; this model, however, requires the existence of a large number of pre-existing nuclei.

That seemingly amorphous samples of metallic glass can already contain a number of quenched-in nuclei from the melt was reported by Schroers et al. [138] in examination of the critical heating rate of Vitreloy 1. In contrast to its relatively low critical cooling rate (1 K s^{-1}), Vitreloy 1 was shown to have a critical heating rate of around 200 K s^{-1} ; that is, for heating rates above 200 K s^{-1} , samples could be heated from the glassy state directly into the melt, showing no recalescence from crystallization. It was proposed that the pronounced asymmetry between critical heating and cooling rates is due to the fact that nuclei formed during cooling experience different growth rates than those formed during heating. The nucleation and growth rate curves for most BMG-forming alloys resemble the schematic curves shown in Fig. 2.3. Since the maxima in the nucleation and growth curves are separated by a relatively large temperature range, the majority of nuclei that form during cooling will not experience high growth rates. However, upon heating, a large number of nuclei will form at the temperature where the nucleation rate has a maximum; these will then grow rapidly upon further heating when exposed to the maximum in the growth rate.

This scenario was also discussed by Angell [139] who pointed out that the TTT-curve determined in most crystallization studies actually represents a combination of nucleation and growth. The nose of the TTT curve for the pure nucleation process, argues Angell, would be shifted to shorter times; much faster cooling rates would therefore be required to obtain a completely non-

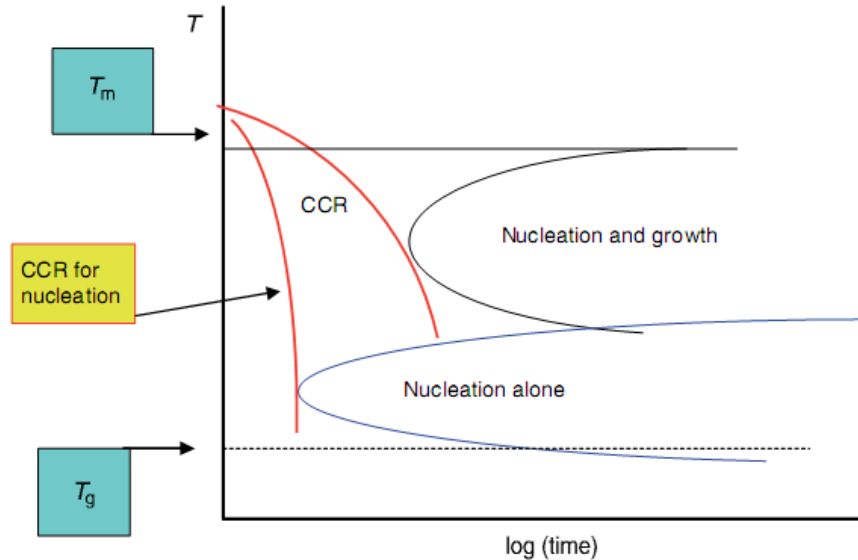


Figure 3.13: Schematic TTT-diagrams from after Ref. [139], showing the critical cooling rate (CCR) for transformations corresponding to pure nucleation (blue curve) and a combination of nucleation and growth (black curve).

nucleated glass (see Fig. 3.13). Given these considerations, it is apparent that quenched-in nuclei can play an important role in metallic glass crystallization, which may normally not be the case in oxide glasses and polymeric systems [21, 139].

In the temperature range above the nose of the TTT-diagram, the nucleation probability may be low but the maximum in the growth rate will result in rapid crystallization once an overcritical nucleus is formed. It is for this reason that heterogeneous nucleation sites; e.g., crucible surfaces or sample impurities, can become a limiting factor in the GFA of metallic melts. In certain metallic systems this can be mitigated by, for example, immersing the melt in a molten oxide flux. By processing the $\text{Pd}_{40}\text{Ni}_{40}\text{P}_{20}$ melt in a flux of molten B_2O_3 , Kui, Greer and Turnbull [140] were able to form glassy samples on the order of 1 cm with cooling rates as low as 1 K s^{-1} . These results were similar to a previous paper published by Drehman, Greer and Turnbull [8], in which glassy samples of the same alloy were obtained with roughly the same dimensions by first chemically etching the ingots such as to remove surface impurities. It was concluded by Sun et al. [141] that the mechanism of action of the B_2O_3 flux was to (1) isolate the melt from the crucible, thus avoiding heterogeneous nucleation caused by the crucible wall, and (2) to deactivate surface impurities by trapping them from the melt due to the lower interfacial

tension between the impurities and the flux.

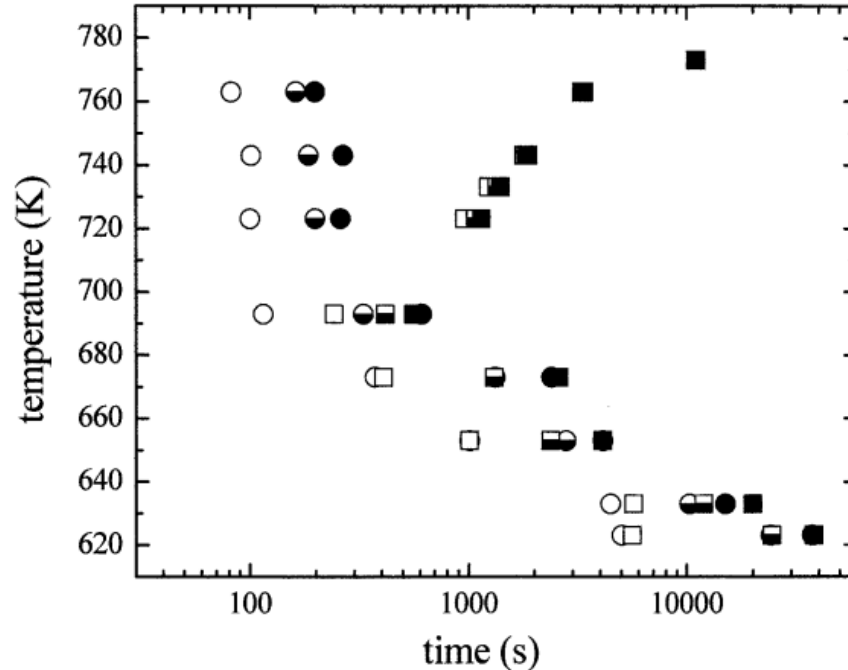


Figure 3.14: Isothermal TTT-diagram of $\text{Pd}_{43}\text{Ni}_{10}\text{Cu}_{27}\text{P}_{20}$ reproduced from Ref. [142]. The square and circle symbols correspond to samples that were processed with and without a B_2O_3 flux, respectively.

The advantage of fluxing certain BMG-forming melts was shown quantitatively in a TTT-diagram by Schroers et al. [137, 142, 143] for the $\text{Pd}_{43}\text{Ni}_{10}\text{Cu}_{27}\text{P}_{20}$ system (see Fig. 3.14), whereby fluxing of the melt with B_2O_3 led to a maximum increase in an order of magnitude in the isothermal time to crystallization as measured near the nose of the TTT-diagram. Additionally, optical micrographs confirmed that the B_2O_3 passivated surface heterogeneities and that nucleation in the fluxed samples occurred in the sample bulk [142].

Removal of surface nucleation sites with B_2O_3 is only practical in those metallic melts whose constituents do not have a lower oxide formation free energy, ΔG^o , than that of boron. Zr-based BMGs, for example, would react with the flux since $\Delta G_B^o = -650$ kJ/g-atom at, for example, 1200 K, whereas $\Delta G_{\text{Zr}}^o = -850$ kJ/g-atom at the same temperature [144]. Similar criteria would exclude Mg-based BMGs as well. However, since ΔG^o is relatively high in noble metals, the GFA of such alloy systems based on Pt and Pd has generally been shown to be enhanced through B_2O_3 fluxing techniques

[43, 140, 143, 145–147].

Interestingly enough, it appears that heterogeneous influences from the crucible wall play a less decisive role in the crystallization of some Zr-based BMGs near the liquidus temperature. The isothermal crystallization times for Vitreloy 1, for example, were measured to be roughly the same when using containerless ESL techniques as during processing in high-purity graphite crucibles (see Fig. 3.11) [19, 129, 148]. Furthermore, studies on particulate reinforced $\text{Zr}_{57}\text{Cu}_{15.4}\text{Ni}_{12.6}\text{Al}_{10}\text{Nb}_5$ showed the existence of a nanocrystalline interfacial layer formed on cooling between the BMG melt and a metal particulate (in this case, tungsten) [149]. The fact that the crystalline interface did not grow larger than 100 nm reflects the strong kinetic nature of these BMG melts, giving them an inherent resistance to the effects of heterogeneous nucleation sites. This should not, however, understate the detrimental effect that the presence of oxygen has on the GFA of most Zr-based BMG alloys [150, 151].

In light of the discussion given in this section, it becomes clear that an accurate description of the crystallization kinetics over the entire range of the undercooled liquid can involve many complicating factors. Since the GFA is ultimately a reflection of the melt's ability to resist crystallization and vitrify, knowledge of the crystallization kinetics; i.e. the TTT-diagram, is certainly useful for practical applications where production and processing are concerned. Additionally, TTT-diagrams can be calculated from nucleation and growth rates (Sec. 2.3) using experimentally determined thermophysical data. Therefore, it may seem tempting to use already existing kinetic and thermodynamic data as a model for the crystallization kinetics and infer the GFA from the calculated critical cooling rate. However, as these models only consider the *homogeneous* nucleation rate, their applicability to processing conditions where heterogeneous effects must be taken into consideration are limited [147].

Chapter 4

Materials and methods

The experimental methods discussed in this chapter are all found within the field of *thermal analysis*. Thermal analysis comprises the area of measurement techniques whereby a substance is subjected to a controlled temperature program and the resulting physical changes of that substance are recorded as a function of temperature and time. These physical changes are able to be detected through a change or variation of a given measurement signal that is output on the experimental apparatus. Often this measurement signal can be of direct use to observe a physical transition in the substance. For example, a sudden change in length or volume can be indicative of a phase transformation. Other times further data analysis may be needed to calculate specific quantities from the measurement signal by use of an established physical relation; this is the case, for example, when calculating viscosity through the deflection, or change in length, of a thin beam.

This chapter will be devoted to first introducing and laying the basic theoretical framework for various thermal analytical techniques. These techniques belong to the methods of *thermomechanical analysis* and *calorimetry*. The bulk of the theoretical background is taken from the texts of Refs. [152], [153] and [154], and will be the topics of the next two sections. The final two sections of this chapter deal with the practical application of these theories to the measurement and characterization of various physical properties and phenomena in metallic glass systems.

4.1 Theory and principles of thermomechanical analysis

Thermomechanical analysis (TMA) can be regarded as one of the simplest forms of thermal analysis. The TMA setup, in its most basic form, consists of a sample holder of a material with known thermal expansivity over the desired temperature range (preferably one with a very small thermal expansion coefficient; e.g., fused silica), a furnace for delivering the desired thermal program to the sample and a way of recording the change in sample length, ΔL , with temperature, T , and/or time, t .

Normally a fused-silica loading rod, or *probe*, is brought into physical contact with the sample and ΔL is determined through the change in position of the probe. The probe design is varied to suit the type of measurement to be carried out. For example, a probe with a rounded head is standard for thermal expansion measurements while a flat-headed probe with a cylindrical tip having a small cross-section is used to measure the penetration into the material as it softens. For flexural, or deflection, measurements of thin beams, a wedge-shaped head is appropriate. Schematics of these different probe geometries are shown in Fig. 4.1. The linear displacement of the probe is measured by means of a transducer, in most cases by a linear variable differential transformer (LVDT). In almost all TMA designs, a force can be delivered to the sample through varying the mass or load provided at the top of the loading probe. If the load remains constant throughout the duration of the measurement, the technique can be described as *Static Force Thermomechanical Analysis* or *sf-TMA*.

The desired temperature program is delivered to the sample through heating of the surrounding furnace. The sample temperature, $T_S(t)$, is then recorded by means of a thermocouple, ideally placed as close as possible to the sample without coming into contact with it (see Figs. 4.2 and 4.3). The furnace temperature, $T_F(t)$, is varied by means of a proportional-integral-derivative controller (PID controller), such that the measured sample temperature is as close as possible to the desired temperature.

The different thermomechanical techniques used in this work are outlined below in Secs. 4.1.1 and 4.1.2.

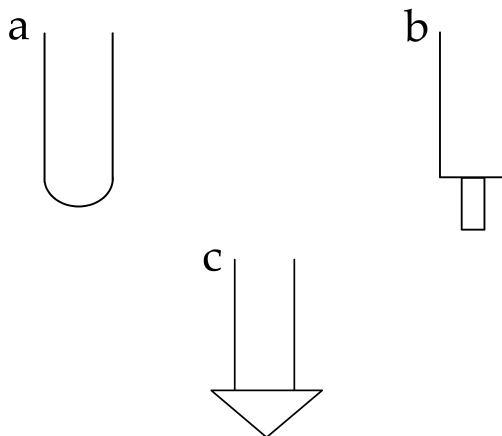


Figure 4.1: Schematic showing the various geometries of TMA loading probes for use in (a) thermal expansion, (b) penetration or (c) beam deflection measurements.

4.1.1 Dilatometry

Dilatometry involves the measurement of the change in length, ΔL , of a sample during a given heating program, $T(t)$. The TMA apparatus can be fitted with various types of probe geometries as in shown Fig. 4.1 to suit the desired measurement. In most dilatometric measurements, the rounded, hemispherical probe geometry is employed (Fig. 4.1a). A schematic of the TMA apparatus for use with dilatometric measurements is shown in Fig. 4.2.

In dilatometry a sudden change in the sample length can indicate the onset of a phase transition, such as solid-state phase changes or the solid-liquid transition. Should no abrupt phase transition occur over a certain temperature interval, the change in length of the sample, ΔL , can be estimated by

$$\Delta L = L_0 \alpha_L \Delta T, \quad (4.1)$$

where L_0 is the original length of the sample, α_L is the linear thermal expansion coefficient and ΔT is the temperature interval. In Eq. 4.1 it is assumed that α_L remains constant throughout ΔT . In general, the linear thermal expansion coefficient can be evaluated as

4.1 Theory and principles of thermomechanical analysis

$$\alpha_L = \frac{1}{L_0} \frac{dL}{dT}. \quad (4.2)$$

Equation 4.1 can then be integrated in the temperature interval from T_1 to T_2 to obtain

$$\Delta L = L_0 \int_{T_1}^{T_2} \alpha_L dT. \quad (4.3)$$

Assuming isotropic thermal expansion, the volumetric thermal expansion coefficient, α_V , can be approximated as

$$\alpha_V \approx 3\alpha_L. \quad (4.4)$$

4.1.2 Three-point beam bending

Flexure, or deflection, measurements of thin beams can be performed in the TMA using the type of setup shown schematically in Fig. 4.3. A beam, supported at each end by sharp edges, is subjected in the center to a constant force provided by a fused silica loading probe with a wedge-shaped head, and the corresponding deflection of the beam is measured.

Given a beam of mass m and Young's modulus E , this beam will deform under its own weight when placed between two rigid supports at a distance L from each other (Fig. 4.4a). The load on the beam due to its own mass is considered a continuous load and the maximum beam deflection, u , under this load is given by beam theory [155] as

$$u = \frac{5mgL^3}{384EI_c}, \quad (4.5)$$

where g is the gravitational acceleration constant and I_c is the beam's cross-sectional moment of the inertia, which is dependent on the beam geometry. Figure 4.5 shows a schematic cross-section of a rectangular bending beam, for which the cross-sectional moment of inertia is $I_c = \frac{bh^3}{3}$, where b is the base of the beam and h is the height, or thickness.

Considering now a concentrated load of mass M placed at the center of the beam, $L/2$ (Fig. 4.4b), the maximum deflection due to this load is calculated

4.1 Theory and principles of thermomechanical analysis

as

$$u = \frac{MgL^3}{48EI_c}. \quad (4.6)$$

The total deflection of the beam is now just the sum of Eqs. 4.5 and 4.6

$$u = \frac{gL^3}{48EI_c} \left(M + \frac{5m}{8} \right). \quad (4.7)$$

In 1906 Trouton [156] established an empirical relationship between the deflection, u , deflection rate, \dot{u} , Young's modulus, E , and coefficient of viscous traction, λ , for viscoelastic materials. It was reported by Trouton that the relationship between u and E is the same as the relationship between \dot{u} and λ , namely

$$\begin{aligned} u &\Rightarrow \dot{u} \\ E &\Rightarrow \lambda. \end{aligned} \quad (4.8)$$

Furthermore, given that λ is related to the viscosity, η , as

$$\lambda = 3\eta, \quad (4.9)$$

Eq. 4.7 can be expressed in terms of η as

$$\eta = \frac{gL^3}{144\dot{u}I_c} \left(M + \frac{5m}{8} \right). \quad (4.10)$$

The mass of the beam can be formulated as $m = \rho AL$, where A is the beam's cross-sectional area and ρ is its density. Eq. 4.10 can then be rewritten as

$$\eta = -\frac{gL^3}{144\nu I_c} \left(M + \frac{\rho AL}{1.6} \right), \quad (4.11)$$

where the beam midpoint deflection rate is now expressed as $\nu = -\dot{u}$. This equation was used by Hagy to evaluate glass viscosities in the range from 10^7 to 10^{14} Pa s using the beam-bending method [157], which has since become a NIST standard [158].

4.1 Theory and principles of thermomechanical analysis

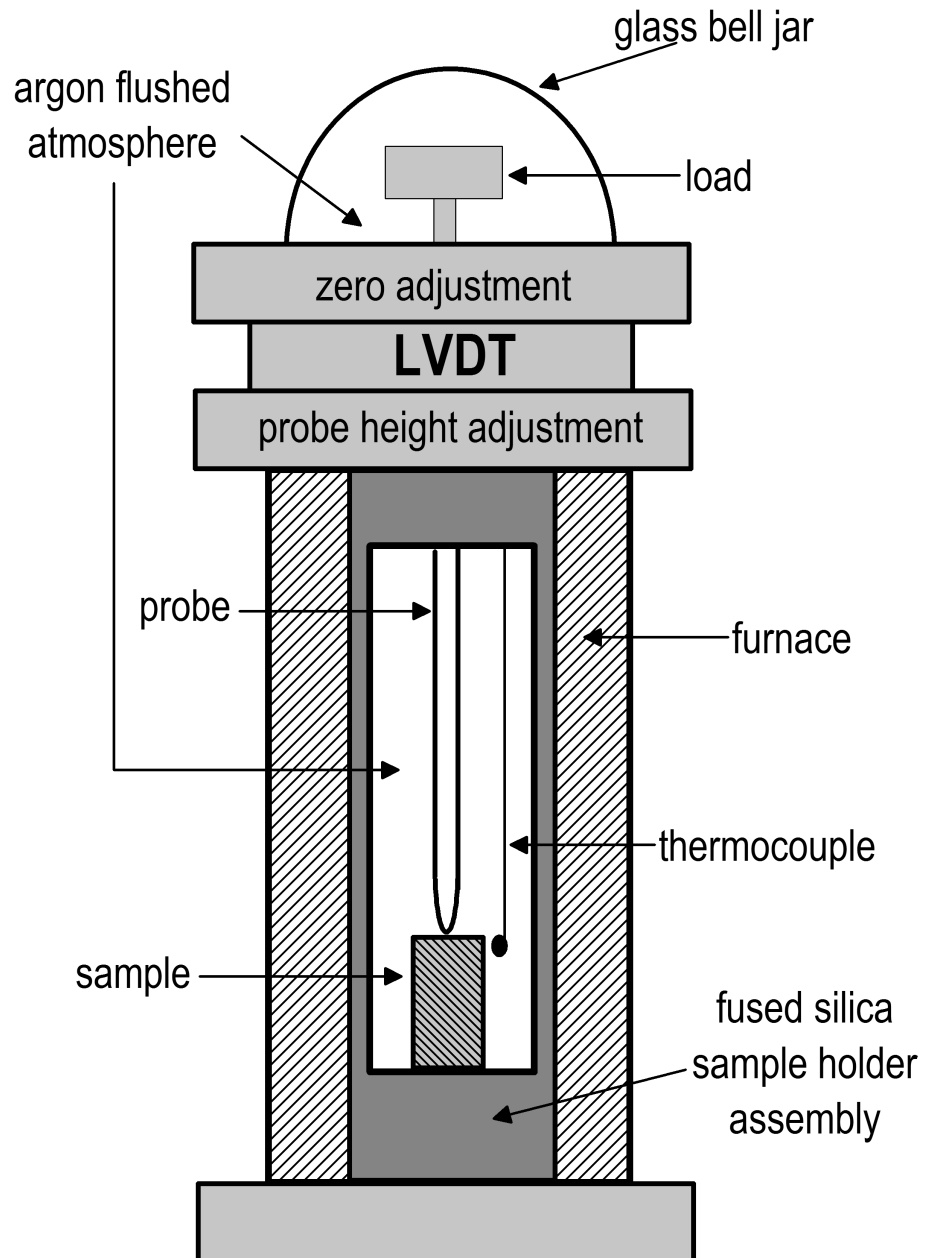


Figure 4.2: Schematic representation of a typical dilatometer TMA setup with rounded probe head.

4.1 Theory and principles of thermomechanical analysis

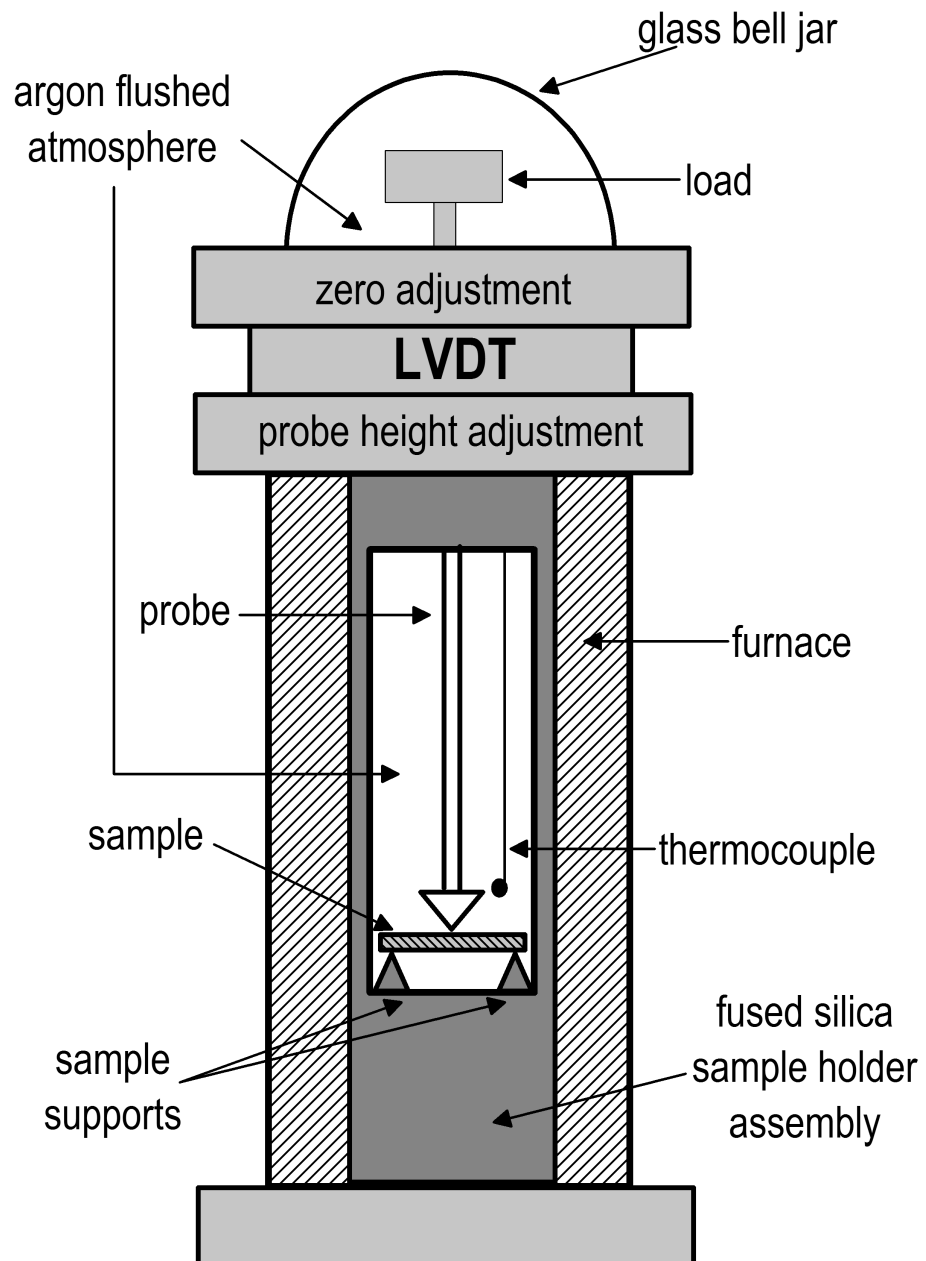


Figure 4.3: Schematic representation of a three-point beam bending setup used in TMA with a wedge-shaped probe.

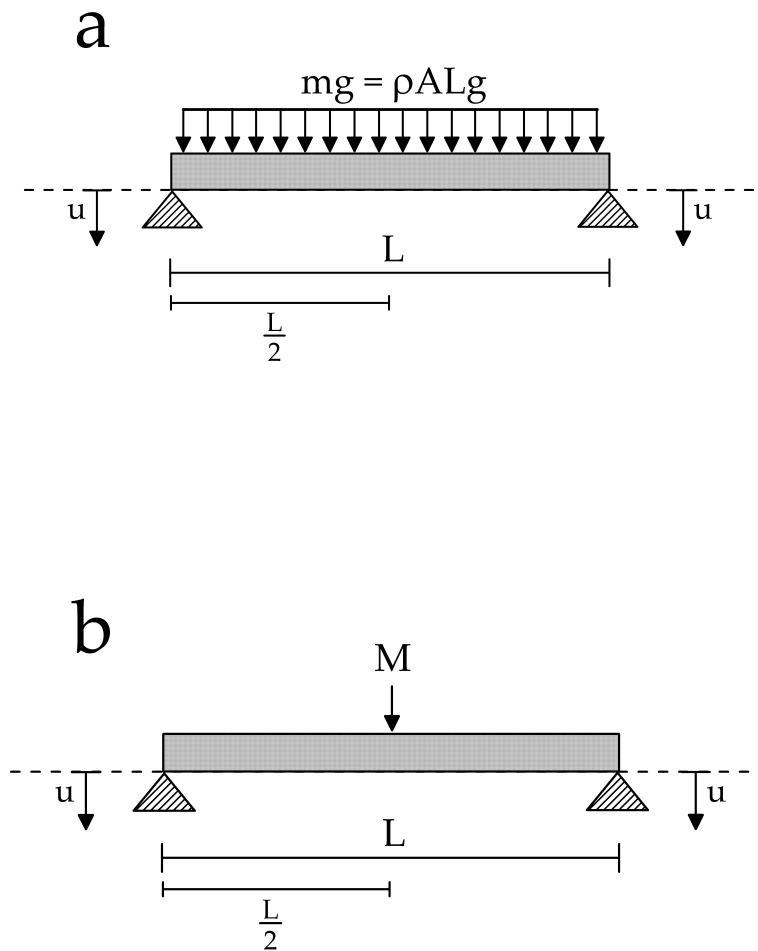


Figure 4.4: Schematics of simply supported bending beams in the case of (a) a continuous load that is the weight of the beam itself, mg , and (b) a central load, M , located at $L/2$. The mass of the beam can be expressed as $m = \rho AL$, where ρ is the beam density, A , the cross-sectional area and L is the beam length. The dashed line shows the bending axis of the beam.

4.1 Theory and principles of thermomechanical analysis

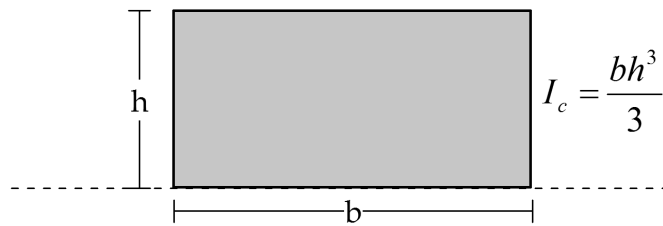


Figure 4.5: Area cross-section of a rectangular bending beam with base b and thickness, or height, h . The bending axis is shown by the dashed line.

4.2 Theory and principles of calorimetry

In this section the method of thermal analysis known as *calorimetry* is introduced, focusing specifically on the techniques of differential thermal analysis (DTA) and differential scanning calorimetry (DSC). The practical application of these techniques to the measurement of various thermophysical properties and phenomena is discussed in Secs. 4.3 and 4.4.

Calorimetry is the measurement of the heat of reactions or physical changes. Heat, Q , cannot be measured directly, however changes in heat, ΔQ , can be determined by changes in temperature, ΔT . This relationship is described by the heat equation

$$\Delta Q = mc\Delta T, \quad (4.12)$$

where m is the mass of the sample being heated and c is the specific heat capacity in units of $\text{J kg}^{-1}\text{K}^{-1}$. Through the above equation, the definition of the specific heat capacity is made clear; namely, that it is a physical property of a substance that characterizes the heat change necessary, per unit mass, to change the temperature by a certain amount.

According to Eq. 4.12, the heat exchanged is the result of a temperature difference, ΔT , between two bodies. In calorimetry, this temperature difference is measured and used to determine the amount of heat being exchanged. This is referred to as *heat flow*, and is usually described by derivative of the heat with respect to time, $dQ/dt = \dot{Q}$.

4.2.1 Differential thermal analysis

Differential thermal analysis (DTA) refers to the calorimetric measurement technique whereby identical heat flow is provided to both a sample and reference (usually empty) and the temperature difference between the two is recorded as a function of time or temperature. An example of this is shown schematically in Fig. 4.6a during a linear heating program throughout the melting point, T_m , of a given substance. Since the reference is empty in this example, no thermal effects appear in the temperature curve of the reference, T_R . At the onset of melting, however, the sample temperature, T_S , remains constant as the applied temperature is increased. The heat introduced into the system does not raise T_S , but is rather the required heat for the solid-liquid phase transition; i.e., the latent heat of fusion.

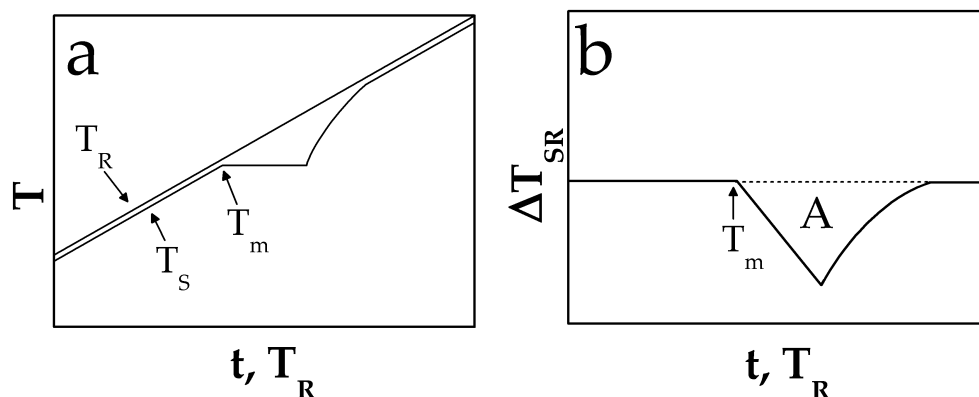


Figure 4.6: (a) Schematic temperature curves during linear heating of a sample, T_S , and empty reference, T_R . The constant value of T_S at T_m reflects the latent heat required for melting. (b) Temperature difference between the sample and reference, ΔT_{SR} , which is the recorded DTA measurement signal. The heat of fusion is proportional to the area of the melting peak, A .

In classic DTA, the thermal program, $T(t)$, is delivered to the sample and reference through the furnace. Thermocouples having good thermal contact with the undersides of the sample and reference crucibles measure the temperatures T_S and T_R , respectively. A schematic representation of a classic DTA setup with free standing measurement crucibles is given in Fig. 4.7.

The DTA output signal corresponds to the temperature difference between the sample and reference, $\Delta T_{SR} = T_S - T_R$, and is displayed in units of μV ; i.e., the voltage difference between the two thermocouples (see Fig. 4.6b). The heat of reaction, or fusion in this case, can be noted schematically in Fig. 4.6b by the area, A , under the melting peak beginning at T_m .

The measured signal, ΔT_{SR} , is related to the heat flow rate to or from the sample, \dot{Q} , through Newton's law

$$\Delta T_{SR} = R\dot{Q}, \quad (4.13)$$

where R is the thermal resistance. By using the differential form of Eq. 4.12

$$\begin{aligned} \Delta Q &= (m_S - m_R)(c_S - c_R)\Delta T_{SR} \\ \frac{dQ}{dt} &= (m_S - m_R)(c_S - c_R)\frac{dT}{dt}, \end{aligned} \quad (4.14)$$

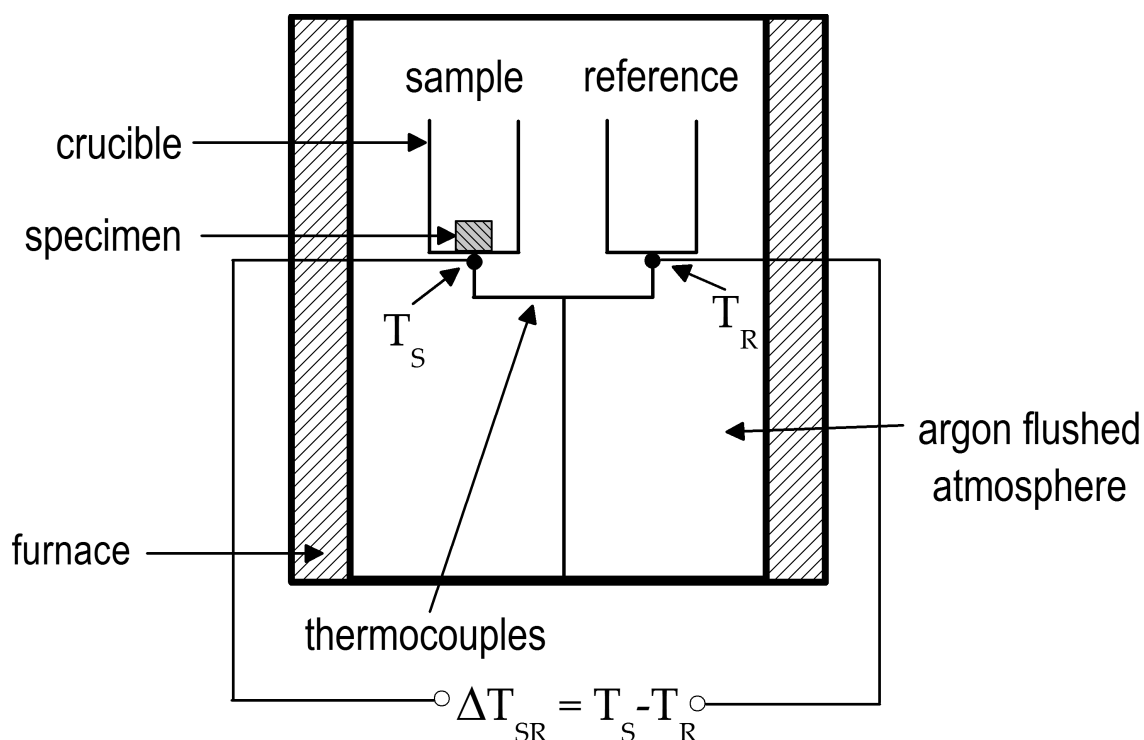


Figure 4.7: Schematic of a classic DTA experimental apparatus.

where m_S , m_R , c_S and c_R are the masses and specific heat capacities of the sample and reference, respectively, Eq. 4.13 can be rewritten as

$$\Delta T_{SR} = (m_S - m_R)(c_S - c_R)R \frac{dT}{dt}. \quad (4.15)$$

In the case of an empty reference crucible, Eq. 4.15 simplifies to

$$\Delta T_{SR} = m_S c_S R \frac{dT}{dt}. \quad (4.16)$$

The signal is therefore dependent on the heating rate, dT/dt , the thermal resistance, and the mass and specific heat capacity of the sample. The thermal resistance depends heavily on both the instrument and physical properties of the sample and sample holder, which makes heat-flow analysis using classic DTA semi-quantitative at best. However, enthalpies of transformation can be determined quantitatively by integration of the endo- or exothermic measurement peaks (e.g. in Fig. 4.6b). Calibration of the DTA using standard

4.2 Theory and principles of calorimetry

materials of known melting temperatures and enthalpies are used to determine a calibration constant, which is the proportionality constant between the experimentally determined enthalpy of transformation and the peak area under the measurement signal. In other words, integrating the measured peak between temperatures T_1 and T_2 yields

$$\Delta H = -K \int_{T_1}^{T_2} \Delta T_{SR} dT = -KA, \quad (4.17)$$

where ΔH is the enthalpy of transformation, A is the peak area of the measurement signal, ΔT_{SR} , and K the proportionality constant¹. It is necessary to take into account the sample holder material, measurement atmosphere and heating rate when performing a calibration of the DTA, as the measurement signal is influenced by these factors as well.

4.2.2 Differential scanning calorimetry

Differential scanning calorimeters can be typed into two basic categories: *heat-flux DSC* and *power compensation DSC*. Common to both types of these DSCs is that the measurement signal is directly proportional to the heat flow, \dot{Q} .

Also known as *calorimetric DTA* or *Boersma-type DTA* [153, 154], the heat-flux DSC belongs to the class of *heat-exchanging calorimeters*. Heat-exchanging calorimeters operate by delivering a defined exchange of heat to be measured symmetrically between the surroundings (furnace) and the sample and reference. Amongst the heat-flux DSCs, the design of the particular measuring system will determine the heat exchange path. A schematic of the variant discussed here is given in Fig. 4.8. In this example, a disk of good thermal conductivity (flux plate) provides the main heat flow from the furnace to the sample and reference. It is worthwhile to note that in this disk-type heat-flux DSC there is an influence from the changes in sample temperature on the reference temperature due to the thermally conducting disk. Due to this asymmetry, this particular type of heat-flux DSC cannot be classified technically as a true differential calorimeter [152]. Care must therefore be taken when interpreting measurement curves where, for example, the emissivity of

¹The minus sign in Eq. 4.17 indicates that a positive enthalpy of transformation will correspond to a negative peak area, since historically the measurement signal in classic DTA is recorded with endothermic events in the negative ordinate direction. However, as almost all modern DTA analysis software is capable of using the *endotherms up* convention, the minus sign can be dismissed here if necessary.

4.2 Theory and principles of calorimetry

the crucible material begins to effect the measurement signal at higher temperatures (as is the case for Al_2O_3).

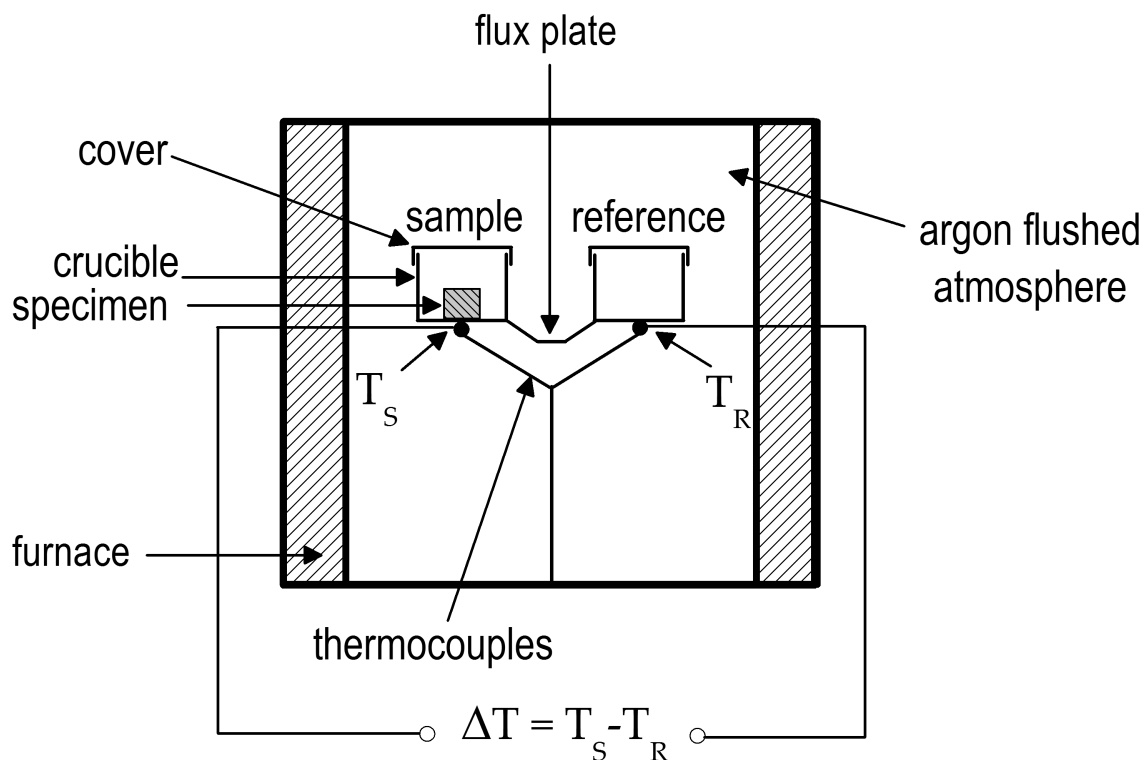


Figure 4.8: Schematic of a heat-flux DSC with the disk-type measuring system. The flux plate provides the heat exchange between the furnace and sample. The output signal, however, is still proportional to ΔT_{SR} , as in classic DTA.

In heat-flux DSC, the temperature difference between the sample and reference, ΔT_{SR} , is the original measurement signal and the measured heat flow, \dot{Q} , is assigned to this signal through various calibrations such that

$$\dot{Q} = -K\Delta T_{SR}. \quad (4.18)$$

Similar to Eq. 4.13, the calibration constant, K , is dependent on the thermal resistance, R , which in classic DTA is heavily influenced by both the instrument and physical properties of the sample and sample holder. In heat-flux DSC, R is a property only of the flux plate itself, thereby reducing the uncertainty inherent in classic DTA. The corresponding measured heat flow to the sample is therefore more representative of the true heat flow to the sample. Given these considerations, analytical descriptions of the functional principle

4.2 Theory and principles of calorimetry

of heat-flux DSC are available and classified as such:

Zeroth Approximation The DSC is represented by a simple linear model, assuming constant heat flow rates (steady-state) and taking into account only the thermal resistance between the furnace and sample. Furthermore, it is assumed that there is no asymmetry in heat flow rates to the sample and reference and that the sample and measured temperatures are equal.

First Approximation Non-steady-state conditions are taken into account, where ΔT_{SR} does not remain constant in time. These are the conditions of phase transformations and reactions, manifesting themselves as endo- or exothermic peaks in the measurement curve.

Higher-Order Approximations These approximations address the issues of thermal resistance between the thermocouples and measurement crucibles, heat flow asymmetry and heat leak from the measurement chamber.

A more detailed discussion of these approximations can be found in Ref. [152]. The same calibration procedures for classic DTA apply to heat-flux DSC as well.

Power-compensated DSC belongs to the class of *heat-compensating calorimeters* and is considered, in contrast to the heat-flux DSC, to be an "active" calorimeter [154]. Power-compensated DSC is especially unique in that it operates on what is referred to as the *null principle*; that is, the sample and reference temperatures are constantly kept equal ($\Delta T_{SR} = 0$) through increasing or decreasing the heating power, $\Delta P = P_S - P_R$, delivered to the sample and reference. To realize this, the sample and reference chambers are constructed each of an identical microfurnace and placed inside of a thermally insulated block. Each furnace contains a thermocouple and a heating element. A schematic diagram of this is given in Fig. 4.9.

In the case of identical thermal symmetry; i.e., steady-state conditions, T_S and T_R are equal. In the case of a reaction or other thermal event where the heat capacity of the sample changes, $T_S \neq T_R$ and the heating power, ΔP , is varied to compensate. The measured heat flow, \dot{Q} , is directly proportional to the heating power and is given in units of mW on the DSC. Due to the null principle in power-compensated DSC, there is no thermal resistance, R , and Eq. 4.16, can be expressed as

4.3 Measurement of thermophysical properties

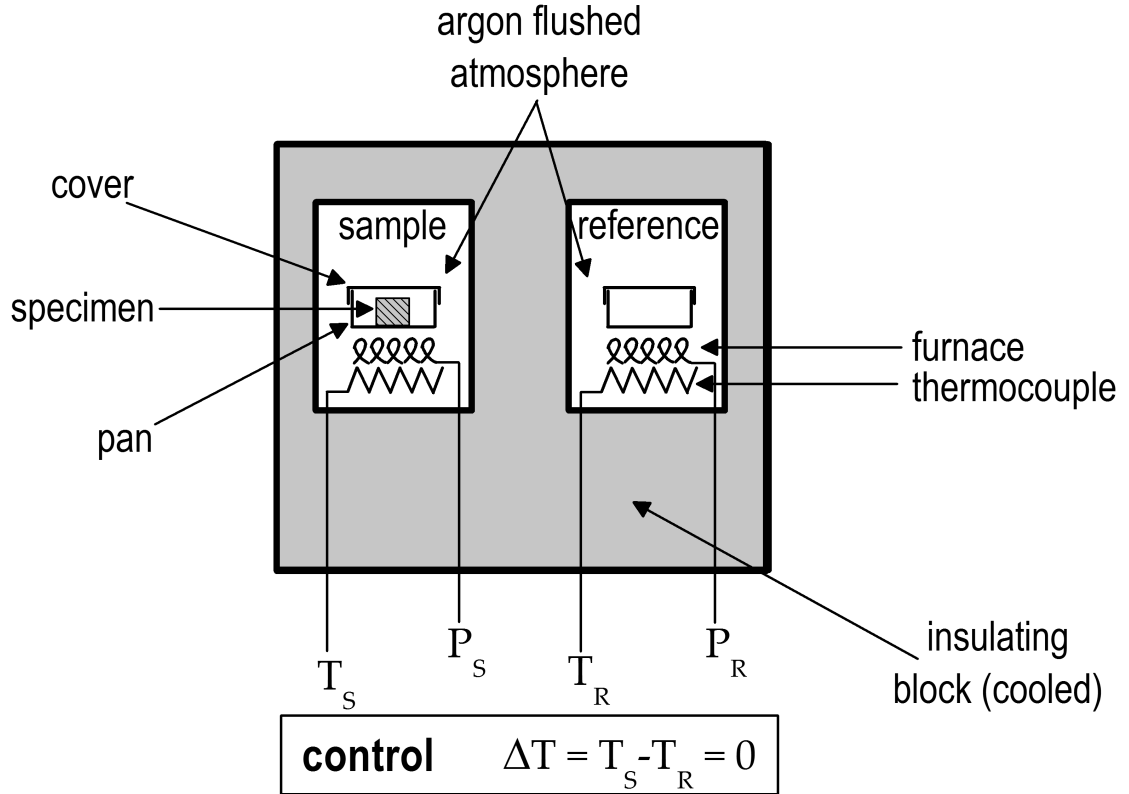


Figure 4.9: Schematic of a power-compensated DSC. The temperatures of the sample and reference, T_S and T_R , respectively, are kept equal by varying the delivered heating power, $\Delta P = P_S - P_R$.

$$\dot{Q} = mc \frac{dT}{dt}. \quad (4.19)$$

As with all other calorimetric techniques discussed here, calibrations with standard reference materials are needed in order to ensure accuracy of the measured heat flow. Similar to classic DTA and heat-flux DSC, these calibrations should take into account the measurement atmosphere, heating rate and pan material.

4.3 Measurement of thermophysical properties

In this section the experimental principles introduced in Secs. 4.1 and 4.2 are applied to the measurement and characterization of various thermophysical

4.3 Measurement of thermophysical properties

properties and phenomena in the metallic glass systems investigated in this work. Where necessary, the relevant technical specifications of the measurement apparatuses are given along with calibration information.

4.3.1 The calorimetric glass transition and melting interval

Calorimetric investigations of the Zr-based metallic glass samples in the range of their glass transition temperatures were carried out in a power-compensated DSC of the type discussed in Sec. 4.2.2. A water-cooled, Perkin-Elmer Diamond DSC was used for measurements ranging from 323.15 to 973.15 K (50 to 700 °C). For Zr-based BMGs, this range encompasses the glass transition, supercooled liquid region and crystallization events. For each desired heating rate, temperature and heat flow calibrations of the Diamond DSC were carried out according to the melting transitions of In, Zn and the $\beta - \alpha$ transition of K_2SO_4 . Measurements of all calibration materials were performed in sealed Al pans under a constant flow of ultra high-purity ($\geq 99.9999\%$) Ar-gas at 20 mL min^{-1} , with the exception of K_2SO_4 , which was measured using Cu pans.

For calorimetric measurements on the $\text{Au}_{49.0}\text{Cu}_{26.9}\text{Si}_{16.3}\text{Ag}_{5.5}\text{Pd}_{2.3}$ BMG, a Perkin-Elmer HyperDSC 8500 fitted with a three-stage Intracooler III cooling system was used. Due to the relatively low glass transition temperature of this alloy (~ 400 K), an active cooling mechanism is needed for accurate DSC measurements close to ambient temperatures and below. The effective operating temperature range of the DSC 8500 with the Intracooler III is 173.15 to 1023.15 K (-100 to 750 °C). For measurements in the temperature range from 243.15 to 773.15 K, temperature and heat flow calibrations were performed according the melting transitions of *n*-Decane, In, Sn and Zn. These calibrations were carried out in sealed Al pans under a constant flow of high-purity N_2 -gas at 30 mL min^{-1} . In order to avoid possible reaction between this BMG alloy and the Al measurement pan, the melting interval was measured in the DSC 8500 using high-purity covered Al_2O_3 pans. Separate calibration profiles were carried out using these pans according to the melting transitions of In, Sn and Zn. The gas and flow rate parameters were not changed.

For investigation of the melting interval of metallic glass alloys at temperatures higher than 973.15 K, a NETZSCH STA 449/C/6/MFC/G Jupiter Differential Thermal Analyzer was used with a TG-DSC sample carrier system based on the heat-flux DSC design explained in Sec. 4.2.2. The measurement crucible material was chosen as to avoid unwanted chemical reaction between the sample melt and the crucible. In the case of Zr-based BMGs, the samples were enclosed in crucibles of graphite and measured in an atmosphere

4.3 Measurement of thermophysical properties

of high-purity ($\geq 99.998\%$) Ar-gas at a purge gas flow rate of 50 mL min^{-1} and a constant protective Ar-gas flow rate of 20 mL min^{-1} . The DTA was calibrated for the desired heating rate according to the melting temperatures and enthalpies of: In, Sn, Bi, Zn, Al, Ag, Au and Ni.

4.3.2 Specific heat capacity

High precision measurements of the specific heat capacity were performed using the power-compensated Perkin-Elmer DSC, taking into consideration the particular alloy and temperature ranges mentioned in Sec. 4.3.1. In order to derive a suitable method of measurement, the relationship between heat flow, \dot{Q} , and specific heat capacity, C_p , must first be analyzed.

In general, the change in heat flow measured with the DSC can be expressed as

$$\Delta\dot{Q} = (m_S - m_R)(c_S - c_R)\dot{T}, \quad (4.20)$$

where $\dot{T} = dT/dt$. In the case of an empty reference, only the measured heat flow to the sample, \dot{Q}_S , is considered and

$$\dot{Q}_S = m_S c_S \dot{T}. \quad (4.21)$$

However, in practice, $\dot{Q}_S \neq m_S c_S \dot{T}$, but instead there exists an additional heat flow term, \dot{Q}_0 , that is present in the measured sample heat flow and corresponds to the zero-line value of the empty measurement pans themselves. The measured sample heat flow can thus be rewritten as

$$\dot{Q}_S = m_S c_S \dot{T} + \dot{Q}_0. \quad (4.22)$$

It is now necessary to consider the heat flow into a sample of an already known specific heat capacity. This will be referred to here as the "Reference", and is not to be confused with a "reference", which is a part of the DSC/DTA experimental setup. The heat flow into the Reference sample can be expressed in a similar manner to Eq. 4.22:

$$\dot{Q}_{Ref} = m_{Ref} c_{Ref} \dot{T} + \dot{Q}_0, \quad (4.23)$$

where c_{Ref} is the known, literature value of the specific heat capacity of the

4.3 Measurement of thermophysical properties

Reference sample. By subtracting the zero-line contribution of the empty pans, \dot{Q}_0 , and comparing Eqs. 4.22 and 4.23, the heating rate falls out and the relation

$$\frac{\dot{Q}_S - \dot{Q}_0}{\dot{Q}_{Ref} - \dot{Q}_0} = \frac{m_S \cdot c_S}{m_{Ref} \cdot c_{Ref}}, \quad (4.24)$$

is obtained. The expression in Eq. 4.24 can then be solved for the specific heat capacity of the sample, c_S , giving

$$c_S = \frac{\dot{Q}_S - \dot{Q}_0}{\dot{Q}_{Ref} - \dot{Q}_0} \cdot \frac{m_{Ref}}{m_S} \cdot c_{Ref}. \quad (4.25)$$

Rewriting Eq. 4.25 in terms of molar specific heat capacities as a function of temperature, $C_p(T)$, yields

$$C_p(T)_S = \frac{\dot{Q}_S - \dot{Q}_0}{\dot{Q}_{Ref} - \dot{Q}_0} \cdot \frac{m_{Ref} \cdot \mu_S}{m_S \cdot \mu_{Ref}} \cdot C_p(T)_{Ref}, \quad (4.26)$$

where μ refers to the molar (or gram-atomic) mass.

Equation 4.26 gives the necessary parameters and measurement quantities for a determination of the specific heat capacity of a given substance. There are, however, varying methods of obtaining the relevant measurement quantities; i.e., the heat flow, \dot{Q} .

In the "classical" procedure, the DSC is operated in continuous scanning mode and the heat flow curves of the empty pans, Reference and sample are used directly in Eq. 4.26 to determine the specific heat capacity. The accuracy of this method is, however, highly dependent the reproducibility of the DSC baseline between each run.

In the so-called "step-method" the sample is first heated to a temperature, T_1 , and held there isothermally for a certain amount of time, Δt , until the signal equilibrates. This results in a step of the measured heat flow to the sample

$$\dot{Q} = \dot{Q}_{\dot{T} \neq 0} - \dot{Q}_{\dot{T} = 0}. \quad (4.27)$$

This procedure is then repeated over the desired temperature interval in tem-

4.3 Measurement of thermophysical properties

perature steps of ΔT . In order to minimize experimental error, it is necessary to use the same measurement pan during each run. The measurement order: *empty pans–Reference–sample* is generally employed, with minimal movement of the measurement pan during changing of the sample being favored. The step-method is most accurate when the temperature interval, ΔT , is the smallest. Figure 4.10 schematically shows the temperature–time and heat flow response curves of an example step-method measurement.

In Fig. 4.11 schematic DSC heat flow curves of a sample, empty measurement pan and sapphire reference standard are shown in response to the temperature steps of Fig. 4.10a. In this example the sample has a much lower specific heat capacity than that of the sapphire standard at these temperatures, which is shown by the relative heights of their respective response curves.

4.3.3 Viscosity between T_g and T_x

Viscosity measurements at temperatures near the glass transition were carried out in a vertical NETZSCH TMA 402 using the three-point beam bending technique discussed in Sec. 4.1.2. For these experiments the TMA was calibrated using the loading probe geometry shown in Fig. 4.1c for a heating rate of 0.833 K s^{-1} in an atmosphere of high-purity ($\geq 99.998\%$) Ar-gas. The melting transitions of In and Zn, as well as the $\beta - \alpha$ transition of K_2SO_4 were used as calibration reference temperatures.

Rectangular beams with cross-sectional areas between 1.0 and 2.0 mm^2 and lengths of approximately 13 mm were cut from the glassy master specimens and heated with a constant rate throughout the glass transition and into the undercooled liquid region. Heating with a constant rate through the glass transition allows access to the equilibrium liquid in the region between T_g and T_x , the onset of crystallization. By using TMA to measure the midpoint deflection rate of the beam, ν , Eq. 4.11 can be used to evaluate the viscosity as a function of temperature, $\eta(T)$. As the viscosity decreases between T_g and T_x the deflection of the beam will accordingly become greater and greater as the material softens. The maximum deflection allowable in the TMA apparatus was determined to be $2500 \mu\text{m}$. However, it was observed that deflections near the maximum limit can cause slippage of the beam from the sample supports. Since the load applied to the probe, as well as the beam's thickness, both greatly affect the degree of beam deflection, these two parameters should be adjusted as to avoid beam slippage. For the Zr-based BMGs investigated here, it was found that a load of 5 g (0.049 N) and a beam thickness of 1 mm was sufficient.

4.3 Measurement of thermophysical properties

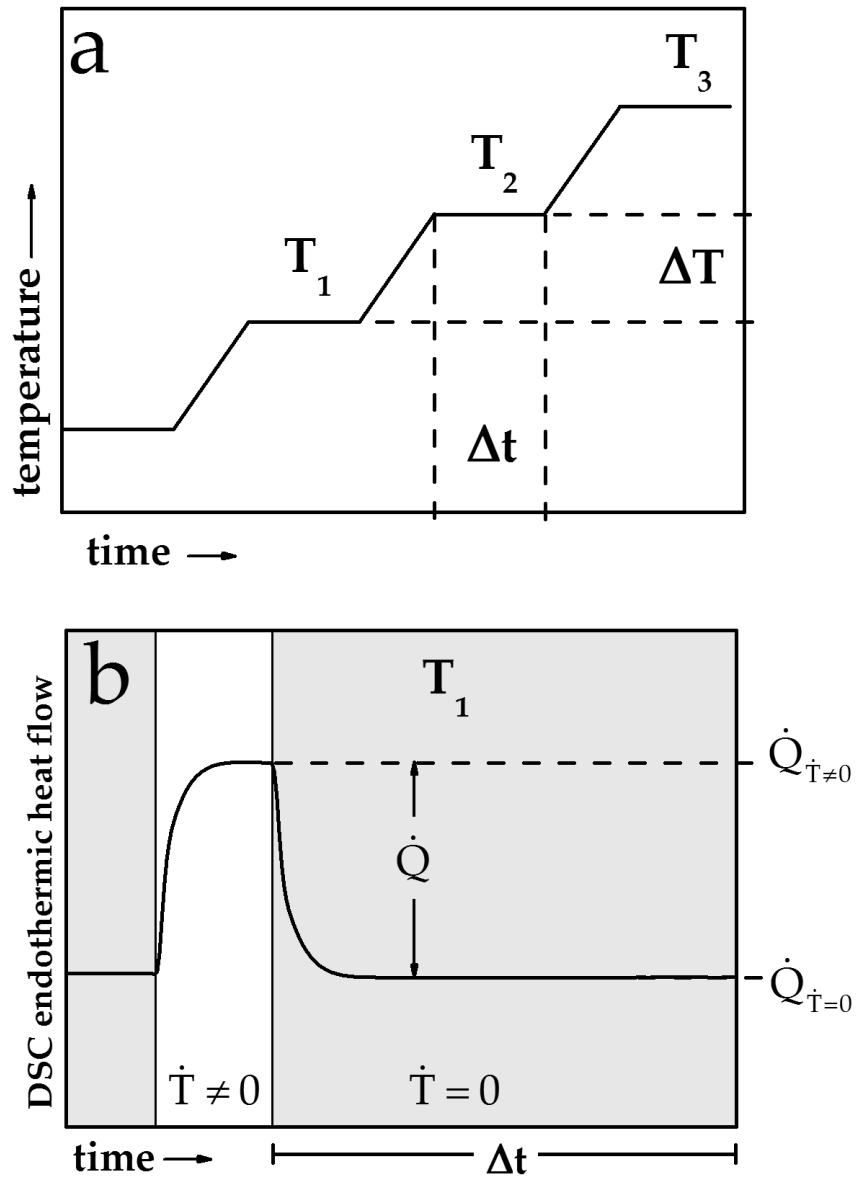


Figure 4.10: (a) Schematic temperature–time curve of the specific heat capacity measurement method utilizing isothermal steps. The step size, ΔT , is shown here along with the isothermal holding time, Δt . (b) Schematic response curve of the DSC heat flow signal to one of the temperature steps shown above. The isothermal intervals are shown in gray.

4.3 Measurement of thermophysical properties

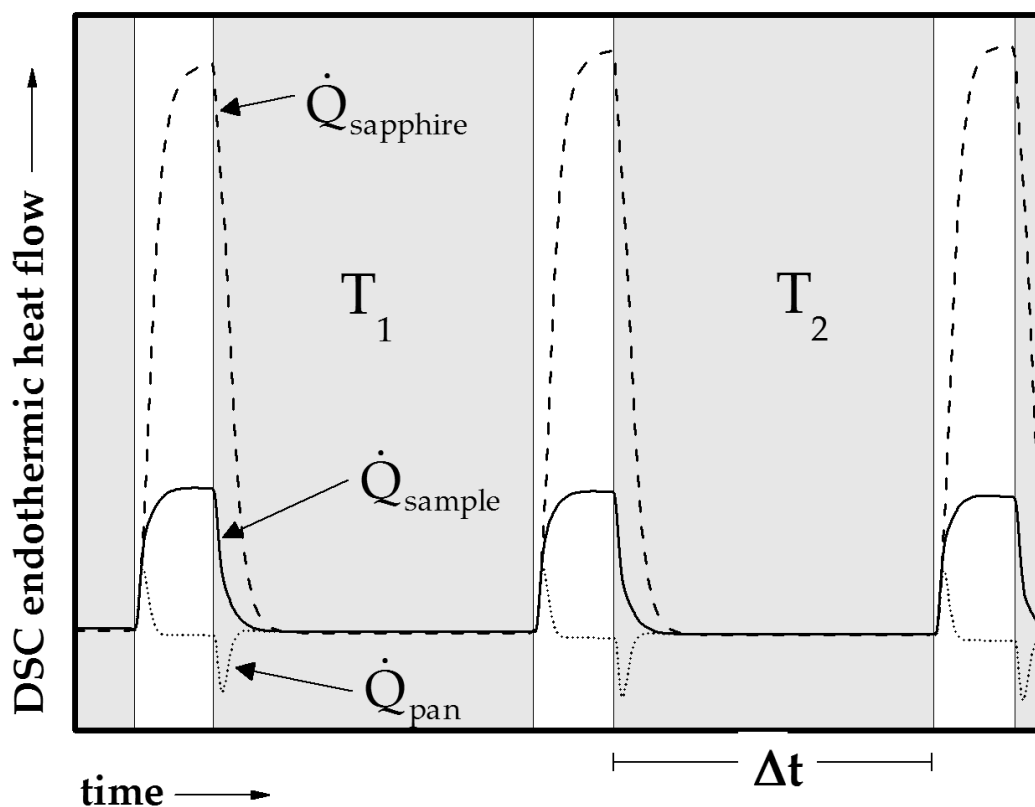


Figure 4.11: Schematic DSC heat flow curves of the sample (solid line), empty measurement pan (dotted line) and sapphire standard (dashed line) during a step-wise specific heat capacity measurement. Δt is the isothermal holding time (gray intervals).

4.4 Measurement of relaxation phenomena

In this section the procedures for measurement of structural relaxation phenomena below T_g are described. During the relaxation process a signal, $\Phi(t)$, is recorded at a constant annealing temperature over a generally long period of time. The measurement signal will begin at an initial value, Φ_0 , and relax in time until gradually reaching an equilibrium value, Φ_{eq} . This is shown schematically in Fig. 4.12.

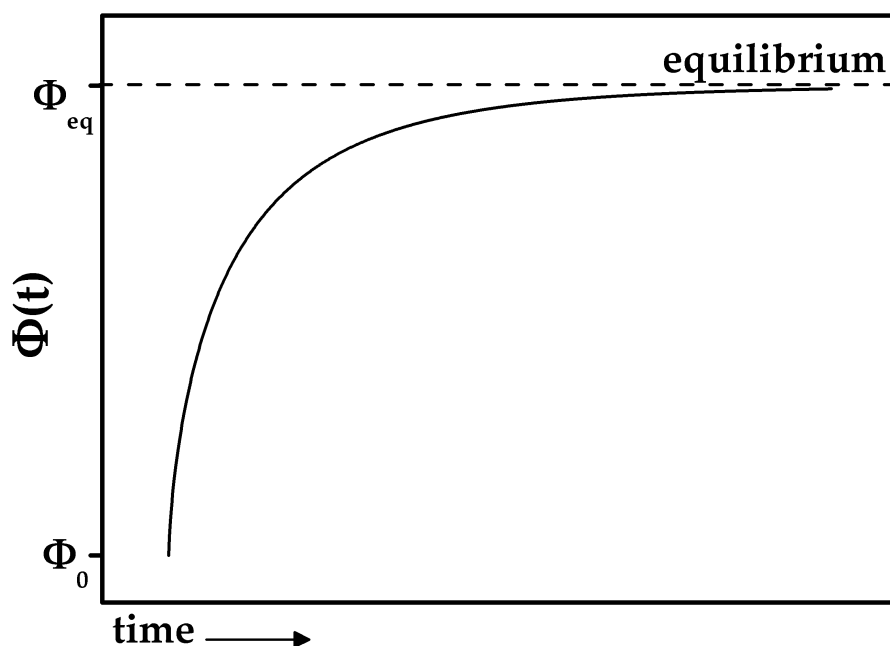


Figure 4.12: Schematic representation of a relaxation signal, $\Phi(t)$, measured at a constant temperature below T_g .

The sections below focus on the measurement of different relaxing macroscopic properties: enthalpy, $H(t)$; volume, $V(t)$; length, $L(t)$; or viscosity, $\eta(t)$.

4.4.1 Enthalpy relaxation

Enthalpy relaxation was carried out in a power-compensated DSC by first heating a sample, cooled with a rate q_C from the supercooled liquid, to the desired annealing temperature with the same heating rate, $q_H = q_C$, before the onset of the calorimetric glass transition, and then holding isothermally for a certain amount of time. At each annealing temperature the samples were held for various times. The maximum annealing time at each tempera-

4.4 Measurement of relaxation phenomena

ture was chosen to be long enough to completely relax the samples and ensure relaxation into the equilibrium liquid, while at the same time avoiding crystallization. After completion of the anneal the samples were cooled to room temperature with a certain rate and then subsequently heated with the same rate throughout the glass transition, where the enthalpy recovery was measured. Figure 4.13 a schematic of the determination of the enthalpy recovery, ΔH_r , of a sample annealed below T_g . By taking the area between the DSC scans of the annealed sample, $(dQ/dt)_a$, and the unrelaxed sample ($q_H = q_C$), $(dQ/dt)_u$, the enthalpy recovery can be determined as

$$\Delta H_r = \int_{T^*}^{T'} \left[\left(\frac{dQ}{dt} \right)_a - \left(\frac{dQ}{dt} \right)_u \right] A dT, \quad (4.28)$$

where T^* is a temperature from within the glassy state and T' is a temperature in the supercooled liquid region where $(dQ/dt)_a = (dQ/dt)_u$. Using the constant $A = \mu m^{-1} q_H^{-1}$, where μ is the gram-atomic mass of the sample and m is the sample's mass in mg, the value of ΔH_r is determined in units of J g-atom⁻¹.

4.4.2 Volumetric relaxation

For dilatometric measurements, the TMA was calibrated for the heating rates of 0.0833, 0.4167 and 0.8333 K s⁻¹ using the loading probe geometry shown in Fig. 4.1a. The melting transitions of In and Zn, as well as the $\beta - \alpha$ transition of K₂SO₄ were used as calibration reference temperatures.

As the sample relaxes during the isothermal anneal below T_g , the frozen-in excess volume will decrease, as shown schematically in Fig. 2.6a. Assuming that this relaxation occurs isotropically, the change in sample length can be used as an approximation for the overall volume change (see Eq. 4.4). In order to accurately measure the reduction in volume due solely to structural relaxation, and not viscous flow due to shearing of the sample, care must be taken to apply as little force as possible onto the sample surface during the dilatometric measurements. To this end, it is first necessary to determine the amount of force delivered by the LVDT itself.

As soon as the sample surface comes into physical contact with the tip of the probe, the probe is pushed upwards and the LVDT delivers a minuscule – but not entirely negligible – amount of force in the exact opposite direction; i.e., normal to the sample's loading face. This force is provided by means of a support spring within the LVDT assembly. Assuming that the restoring force

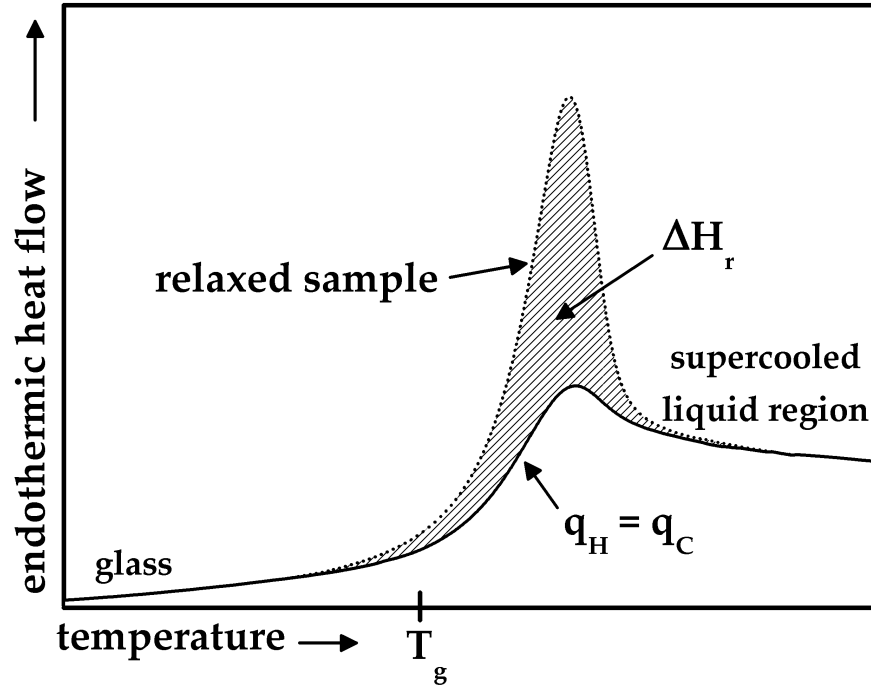


Figure 4.13: Schematic DSC heat flow curves of an unrelaxed sample where $q_H = q_C$ (solid curve) and a sample annealed for a certain time below T_g (dotted curve). The hatched area between the annealed curve and the unrelaxed curve corresponds to the enthalpy recovery, ΔH_r , and is equal to the enthalpy that was relaxed during isothermal annealing.

exerted by the spring can be described by Hooke's Law

$$\mathbf{F} = -k\mathbf{x} \quad (4.29)$$

where k is the spring constant and \mathbf{x} is the displacement vector of probe, the value of k can be determined empirically by measuring the pure displacement of the probe with no sample under it. Small samples with masses ranging from 150-300 mg were added consecutively onto the TMA loading platform, such that after the addition of each mass, m_i , the probe was displaced by an amount x_i . The total force applied to the spring, F_{tot} , is then just the sum of the individual forces exerted by each mass, or

$$F_{tot} = \sum_i F_i = g \sum_i m_i. \quad (4.30)$$

4.4 Measurement of relaxation phenomena

The total force on the probe, F_{tot} , is plotted against the total displacement, x_{tot} , and shown in Fig. 4.14. The spring constant, k , was determined through a linear fit of the data to be 11.6 N m^{-1} .

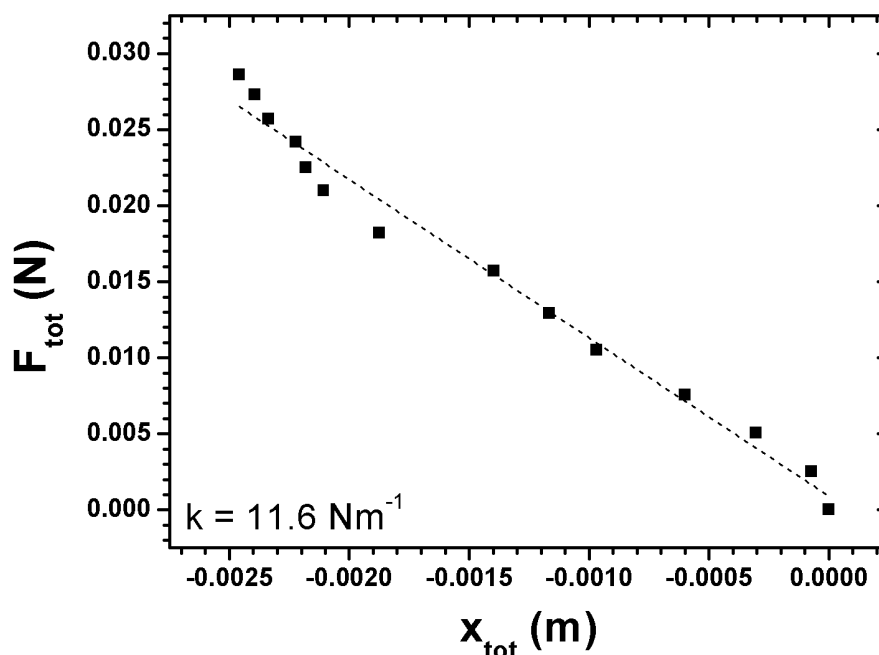


Figure 4.14: Total force, F_{tot} , as a function of displacement, x_{tot} , measured for the TMA over the entire operable range of the LVDT. The spring constant was calculated to be $k = 11.6 \text{ N m}^{-1}$.

This procedure was carried out over the entire operable range of the LVDT. In order to determine the force from the LVDT applied to the sample surface, it is now only necessary to record the vertical displacement of the loading probe due to the contact with the sample.

Rectangular samples with dimensions of approximately $2 \times 2 \times 8 \text{ mm}$ were cut from glassy master specimens and used for the dilatometric measurements. The glassy samples, previously cooled with a rate q_C , were heated with the same rate to the desired temperatures and then held isothermally where the length relaxation was directly measured. The load on the sample's surface from the spring-loaded LVDT was calculated in these experiments to be $0.20 \pm 0.04 \text{ mN}$.

4.4.3 Isothermal viscosity below T_g

At temperatures below the glass transition, the equilibrium liquid can be accessed through isothermal annealing of the sample. Beams with rectangular cross-sections between 0.2 and 1.0 mm² and lengths of approximately 13 mm were cut from the glassy samples and the three-point beam-bending technique discussed in Sec. 4.1.2 was used to measure the viscosity in the vicinity of the glass transition. In contrast to technique discussed in Sec. 4.3.3 where viscosity was measured at a constant heating rate throughout the glass transition, the glassy samples here were heated to temperatures below T_g and then held isothermally until fully relaxed into the equilibrium liquid.

In order to increase signal-to-noise ratio, the deflection of the beam should be as large as possible, such that scatter is minimized during long-time measurements. To achieve the greatest possible deflection while remaining within the measurable range of the apparatus, the applied load was kept constant at 0.01 kg and the cross-section of the beams varied, depending on the expected viscosity at a given temperature.

Chapter 5

Thermodynamics and kinetics of the equilibrium liquid

In this chapter the experimental methods introduced in Chapter 4 will be used to describe the equilibrium liquid of various BMG compositions in terms of their thermodynamic functions and kinetic properties. A look at calorimetric techniques used to characterize the kinetic glass transition will be given, focusing on the use of DSC (Sec. 4.2) to determine the liquid fragilities of Vitreloy 106 and 106a by employing differing heating rates. It should be mentioned that a portion of the results presented in Sec. 5.1 were adapted from the preliminary work appearing in the Master's thesis, "The effect of cooling rates on the glass transition of Zr-based bulk metallic glasses", by Z. Evenson (2008).

Determination of the specific heat capacity of the equilibrium liquid will be presented alongside with the various derived thermodynamics functions; e.g., enthalpy, entropy and Gibbs free energy, for the Zr-based Vitreloy 1b and Au-based $\text{Au}_{49.0}\text{Cu}_{26.9}\text{Si}_{16.3}\text{Ag}_{5.5}\text{Pd}_{2.3}$ compositions. Additionally the crystallization of the equilibrium liquid of $\text{Au}_{49.0}\text{Cu}_{26.9}\text{Si}_{16.3}\text{Ag}_{5.5}\text{Pd}_{2.3}$ will be analyzed and interpreted in terms of isothermal and continuous cooling time-temperature-transformation diagrams as well as activation energies for crystallization.

The viscosity of the equilibrium liquid in the vicinity of T_g using continuous heating as well as isothermal techniques in the TMA will be presented for the Vitreloy 1b, 106, 106a, 105 and 101 compositions (see Appendix A) as well as the $\text{Au}_{49.0}\text{Cu}_{26.9}\text{Si}_{16.3}\text{Ag}_{5.5}\text{Pd}_{2.3}$ BMG. The equilibrium viscosity data in the case of Vitreloy 1b will be described using the Cohen and Turnbull

[58] and Cohen and Grest [66] models of the free volume. Additionally, an interpretation of the free volume based on the equilibrium viscosity model of Adam-Gibbs [67] will be proposed along with analysis of the free volume and enthalpy functions of the equilibrium liquid.

Finally, previously published data on the Vitreloy 1 BMG liquid [123] will be analyzed and the Adam-Gibbs model applied to a description of the free volume of the melt.

5.1 The kinetic glass transition in DSC

In calorimetric experiments, the DSC up-scan is used to determine the glass transition temperature, which is, in practice, defined during heating of the sample with a certain heating rate, q_H . The shift of the glass transition temperature with the heating rate is assumed to reflect the fragility of the material [73, 159, 160]. Furthermore, it has been experimentally shown by various researchers that the VFT fragility parameter, as introduced in Sec. 2.5, can be determined by fitting the heating rate dependence of the glass transition with Eq. 2.27 on p. 22 [13, 86, 161–164].

It is assumed that, during heating from the glassy state and into the supercooled liquid region, one can define a particular calorimetric relaxation time, τ , for each heating rate, q_H , such that

$$\tau = \frac{\Delta T}{q_H}, \quad (5.1)$$

where $\Delta T = T_g^{end} - T_g^{onset}$ (see Fig. 5.1) is the width of the glass transition as measured for that particular heating rate. Each value of τ is inversely proportional to q_H and a plot of T_g versus τ will show the kinetic shift of the glass transition, where lower glass transition temperatures are measured for slower heating rates. The kinetic fragility parameter D_τ^* can then be determined from a fit of this shift to Eq. 2.27.

5.1.1 Apparent fragility

The convention of using the same heating rate, q_H , as that of an immediately preceding cooling rate, q_C , from the supercooled liquid region, has been adopted by many investigators, [159, 161, 165] but is still not considered standard amongst all researchers in this field. The glass transition temperature

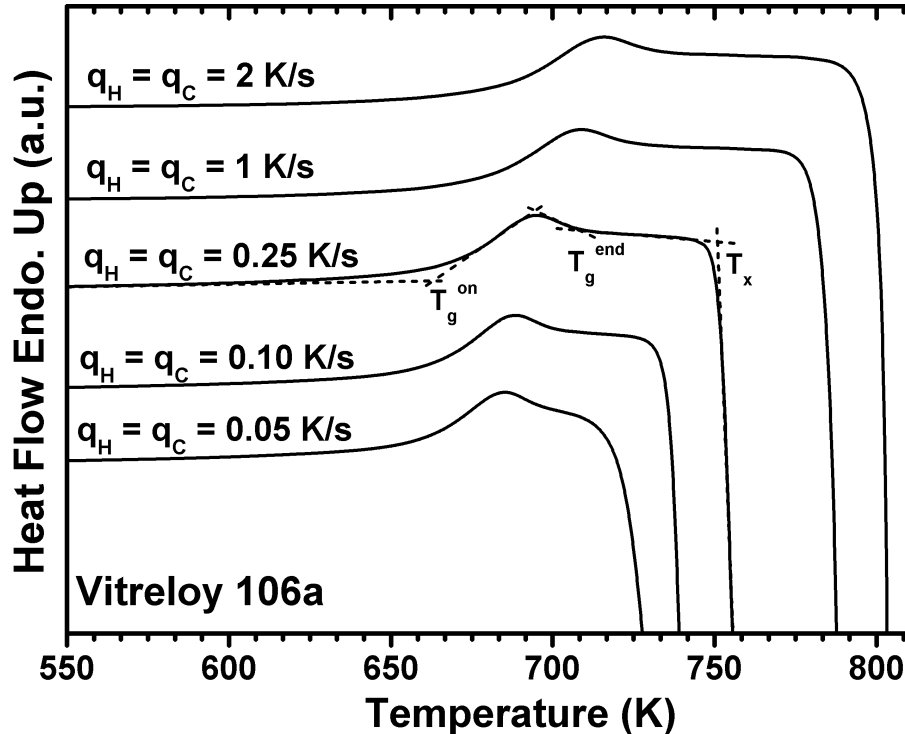


Figure 5.1: DSC heat flow curves of the Vitreloy 106a alloy showing the glass transition shift for the same heating and cooling rates; q_H and q_C , respectively. Included are the definitions of the onset and end of the glass transition, as well as the onset of the crystallization event - T_g^{onset} , T_g^{end} and T_x , respectively. Curves were translated along the vertical axis for easier comparison [75].

as measured on heating, however, can vary greatly depending on whether or not the convention $q_H = q_C$ is kept. Furthermore, if $q_H \neq q_C$, this will lead to different apparent values of D_τ^* being obtained for the same material. The onset temperature of the glass transition, as measured on heating, is not only dependent on the heating rate, but is also sensitive to the initial structural state "frozen-in" to the glass during cooling from the liquid [72]. As such, it is important to assess the effect of the material's structural state on the measurement of the glass transition during heating. Furthermore, since the shift of the onset temperature of the glass transition with the heating rate reflects the fragility of the material, an accurate measurement of this temperature is necessary in order to determine the correct fragility.

The glass transition and crystallization events for the Vitreloy 106 ($Zr_{57}Cu_{15.4}Ni_{12.6}Al_{10}Nb_5$) and Vitreloy 106a ($Zr_{58.5}Cu_{15.6}Ni_{12.8}Al_{10.3}Nb_{2.8}$) BMGs were observed in DSC up-scans for various combinations of heating and cool-

5.1 The kinetic glass transition in DSC

ing rates. Figure 5.1, for example, shows the kinetic glass transition shift of the Vitreloy 106a alloy where $q_H = q_C$. Three distinct regions are seen here – the onset of the glass transition, T_g^{onset} , the supercooled liquid region and the onset of the crystallization event, T_x . For slower heating rates the glass transition is observed at lower temperatures. The onset of crystallization is also heating rate dependent, as nucleation is a thermally activated process.

Figure 5.3 shows DSC up-scans for the Vitreloy 106a alloy as each sample, cooled with a different rate, was scanned through the glass transition with the same rate, $q_H = 2 \text{ K s}^{-1}$. These DSC up-scans show a pronounced change in the heat flow profile for samples with different thermal histories. For slower cooling rates the enthalpy recovery on re-heating is progressively larger. Data obtained from these DSC experiments show that the measured onset temperature for a given heating rate can vary depending on the cooling rate used. The inset of Fig. 5.3 shows the apparent shift in the measured value of T_g^{onset} with different cooling rates and how the measured value of T_g^{onset} for a given heating rate can vary – in some cases as much as 9 K – according to the cooling rate used.

For each set of data corresponding to a unique cooling rate, the VFT parameters D^* and T_0 are calculated by plotting the measured value of T_g^{onset} versus τ and then fitting with Eq. 2.27. In Fig. 5.2 a set of data is shown, in which the shift of T_g^{onset} with increasing heating rate is plotted after cooling with one cooling rate; e.g., the open circles represent the onsets for heating with five different rates ($q_H = 0.05, 0.10, 0.25, 1$ and 2 K s^{-1}) after cooling them all with 1 K s^{-1} . The data show an increase in the apparent kinetic fragility parameter for slower-cooled samples. In Table 5.1 the apparent fragilities and VFT temperatures calculated for both alloys are compared. The trend of an increasing value of D_τ^* with decreasing q_C is clearly observed for each alloy.

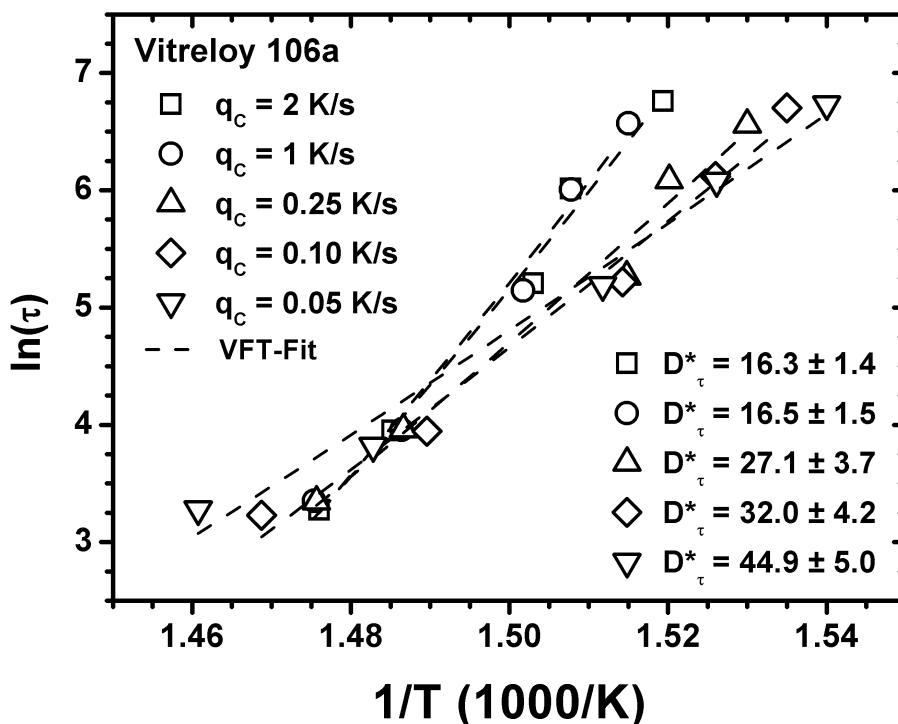


Figure 5.2: Increase in the apparent fragility, D^* , for samples of Vitreloy 106a pre-treated with slower cooling rates. Each data set represents a different cooling rate q_{Ci} (symbols). Also shown are the VFT fits (dashed lines) to the measured values of T_g^{onset} , as well as the values of D_τ^* obtained from fitting. Similar behavior is also observed in the Vitreloy 106 alloy (see Table 5.1). The error bars for the experimental data are on the order of the symbol size [75].

q_C [K s ⁻¹]	Vitreloy 106a		Vitreloy 106	
	D_τ^*	T_0 [K]	D_τ^*	T_0 [K]
2	16.3	464.5	21.9	426.2
1	16.5	462.7	21.5	429.2
0.25	27.1	384.9	31.4	367.4
0.10	32.0	356.9	36.7	338.6
0.05	44.9	301.4	50.4	285.6

Table 5.1: Apparent kinetic fragilities, D_τ^* , and VFT temperatures, T_0 , for the Vitreloy 106a and Vitreloy 106 alloys. These values were calculated from fitting each data set representing a unique cooling rate with Eq. 2.27. As the cooling rate decreases, the apparent fragility is seen to increase [75].

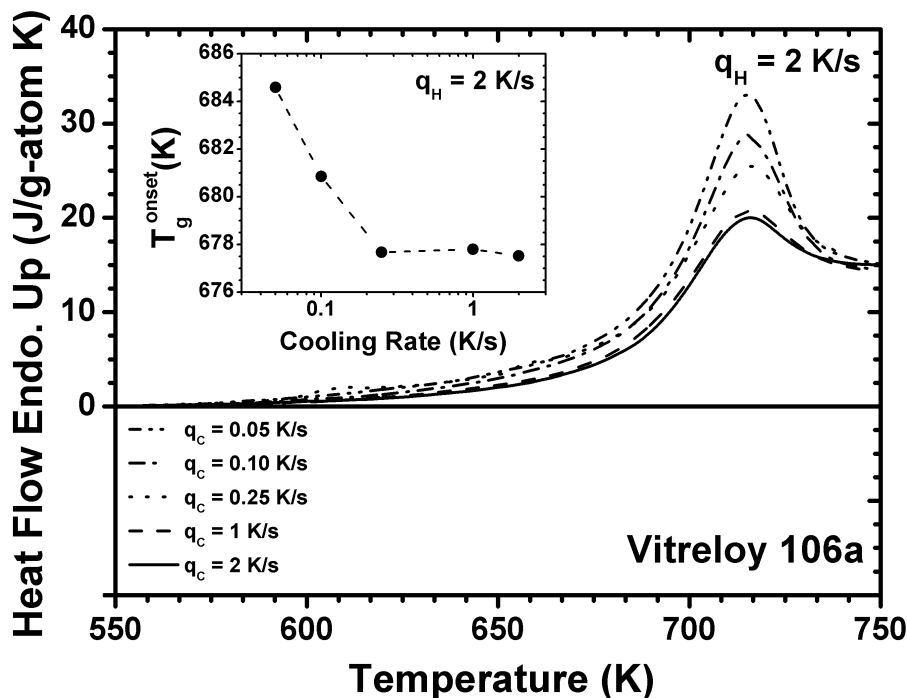


Figure 5.3: DSC up-scans of the Vitreloy 106a alloy heated through the glass transition with a rate of $q_H = 2 \text{ K s}^{-1}$, where each curve corresponds to a unique pre-treatment with a cooling rate q_{Ci} . For slower cooling rates the enthalpy recovery on re-heating is progressively larger. An apparent shift in the glass transition temperature is also seen (inset), corresponding to effect of enthalpy recovery on the measurement of T_g^{onset} . The dashed line in the inset is used to guide the eye [75].

The enthalpic state of each sample is determined by an analysis of the fictive temperature, T_f' , as defined by the enthalpy-matching procedure of the Moynihan method (see Fig. 2.9). Figure 5.4 compares the values of T_g^{onset} and T_f' in the Vitreloy 106a alloy for different cooling rates as well as the case of equal heating and cooling rates. For a given pair of heating and cooling rates, the difference between T_g^{onset} and T_f' is smallest where $q_H = q_C$; in other words, in DSC scans where the heating and cooling rates are equal, T_g^{onset} is approximately equal to T_f' . The slope of each fit to the data is indicated here. The value of the slope corresponds to the correlation between T_g^{onset} and T_f' . A value close to 1 would correspond to perfect linear correlation, whereas a value close to 0 would indicate no correlation.

The results presented here show that kinetic phenomena resulting from the sample's thermal history below T_g^{onset} will manifest themselves during the glass transition and also play a role in determining the glass transition tem-

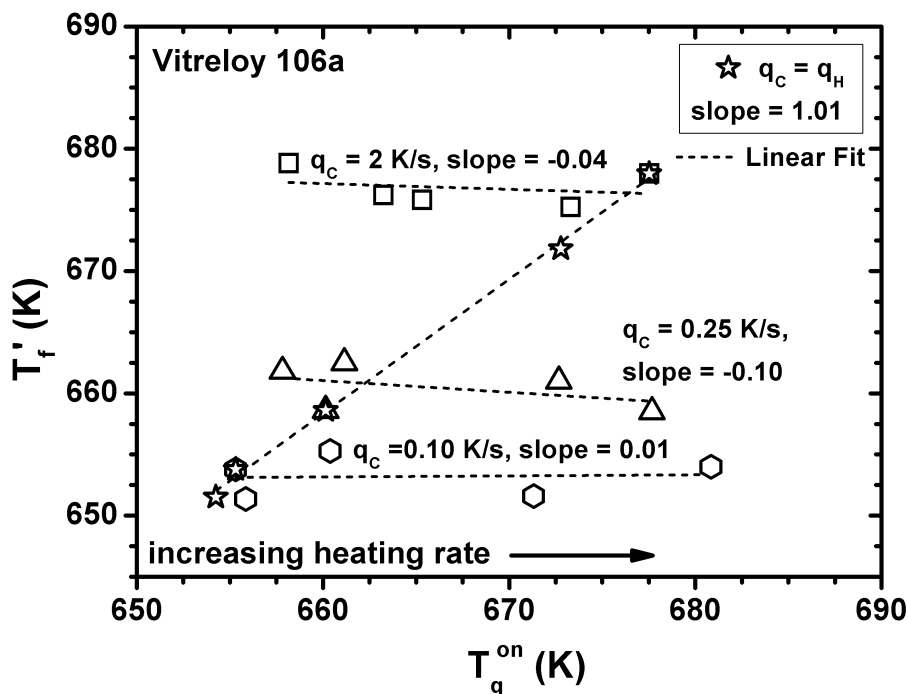


Figure 5.4: Comparison of T_g^{onset} and T_f' for the Vitreloy 106a alloy. Each point represents (T_g^{onset}, T_f') for a unique heating and cooling rate pair. Shown are the datasets for three different cooling rates: $q_C = 2 \text{ K s}^{-1}$, $q_C = 0.25 \text{ K s}^{-1}$ and $q_C = 0.10 \text{ K s}^{-1}$ (square, triangle and hexagon symbols, respectively), as well as the case where $q_C = q_H$ (starred symbols). The data are fitted with a linear regression (dashed lines) and the slope values for each fit are shown. The direction of increasing heating rate is also indicated here. The error bars for the experimental data are on the order of the symbol size [75].

perature. This is demonstrated in Fig. 5.3, where the measured value of T_g^{onset} is observed to apparently increase with greater enthalpy recovery as slower cooling rates are used and the heating rate is kept constant at 2 K s^{-1} . In Fig. 5.5 the DSC heat flow profile for the Vitreloy 106a alloy is shown, exemplifying different kinetic phenomena in the glass transition region. More specifically, if the heating rate is greater than the previous cooling rate ($q_H > q_C$), this will lead to enthalpy recovery during re-heating, whereas if the heating rate is slower than the previous cooling rate ($q_H < q_C$), this will lead to relaxation in the vicinity of the glass transition during re-heating.

Since the measured value of T_g^{onset} is subject to variation, depending on the cooling rate used, it is important to assess the consequences of this when calculating fragility using the method described earlier in this section. In

5.1 The kinetic glass transition in DSC

Fig. 5.2 the effect of various cooling rates on the kinetic fragility, D_{τ}^* , of the Vitreloy 106a alloy is shown. The data show that, for samples pretreated with slower cooling rates, the apparent fragility can increase considerably – e.g. from 16.3 to 44.9 in the case of Vitreloy 106a. This behavior was also observed in the Vitreloy 106 alloy (Table 5.1). From these data it can be seen that the effect of different cooling rates on the measurement of T_g^{onset} can drastically affect the calculated value of D_{τ}^* , or the apparent fragility, and result in misleading conclusions.

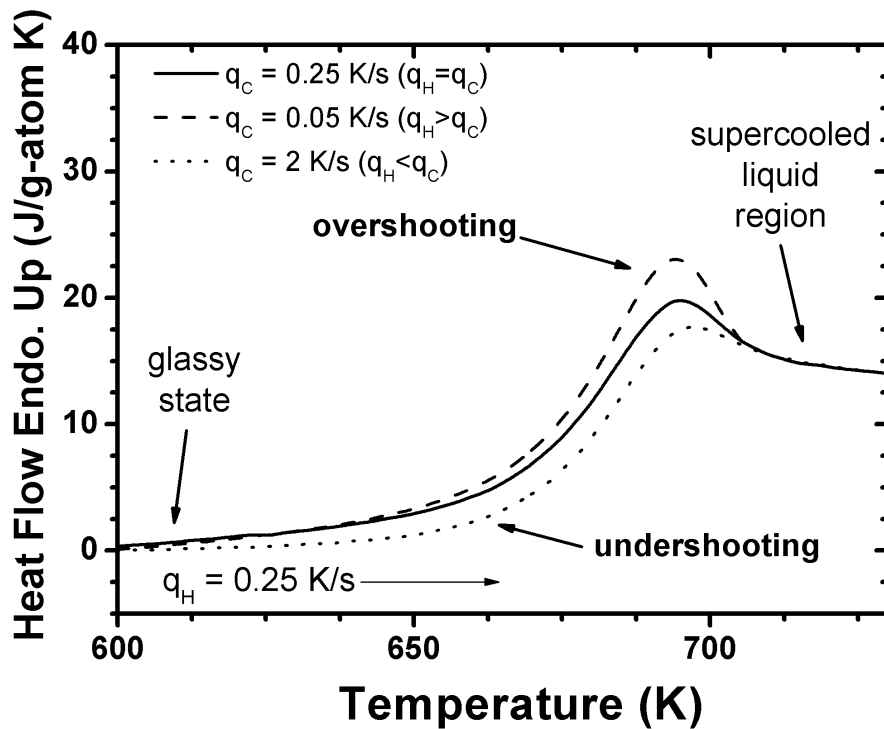


Figure 5.5: DSC heat flow curves of the Vitreloy 106a alloy representing different kinetic phenomena in the glass transition region. The unrelaxed sample (solid line) is formed by cooling from the supercooled liquid region and then re-heating with the same rate ($q_C = q_H$). When the heating rate is greater than the cooling rate ($q_H > q_C$) the heating curve will overshoot the equilibrium liquid value due to enthalpy recovery (dashed line). When the heating rate is slower than the cooling rate ($q_H < q_C$) the heating curve will show undershooting behavior (dotted line), which is attributed to relaxation at temperatures below the glass transition. After the glass transition, however, all three curves are in metastable equilibrium in the supercooled liquid region [75].

It therefore stands to reason that in order to obtain an accurate value for D_{τ}^* ,

5.1 The kinetic glass transition in DSC

it is necessary to first obtain an accurate value for T_g^{onset} . To accomplish this one must be able to associate the value of T_g^{onset} , measured at a certain heating rate, with the correct structural state of the sample. In other words, the glass transition temperature on heating is measured (T_g^{onset}) and compared with the glass transition temperature that occurred upon cooling of the sample, which was defined as the limiting fictive temperature, T_f' , in Sec. 2.6.

As the thermal history of the sample can affect the measurement of T_g^{onset} , T_f' is normally taken as the glass transition temperature, since T_f' is representative of the actual structural state of the sample (i.e. the glass transition temperature on cooling). However, the supercooled liquid region in metallic glasses can range from around 80 - 100 K to virtually non-existent [86, 164, 166, 167]. Since the value of T_f' is dependent on an accurate extrapolation of the supercooled liquid region to lower temperatures, as determined with the method described in Sec. 2.6, measurements of T_f' are limited where little or no supercooled liquid region is present. Furthermore, since T_f' reflects the structural state of the sample, enthalpy relaxation or recovery will lead to greater or lower fictive temperatures, respectively, which may differ greatly from the glass transition temperature observed on heating (see e.g. Fig. 5.4).

The values of T_g^{onset} and T_f' shown in Fig. 5.4 correlate with each other with a near one-to-one relationship in the cases where $q_C = q_H$, indicating that these values are nearly identical. This therefore leads one to the conclusion that the measured value of T_g^{onset} is most representative of the structural state when the sample is heated and cooled with the same rate.

For the data where the cooling rate was kept constant but the heating rate was varied, the expected kinetic shift of T_g^{onset} with heating rate is observed, while T_f' remains roughly constant. This is indicated in Fig. 5.4 by the near-zero slopes of the linear fits to the data, and is consistent with the definition of the fictive temperature being dependent only on the cooling rate. In contrast to the cases where $q_C = q_H$, T_g^{onset} here is not necessarily representative of the sample's structural state, and varies (along with the heating rate) with the amount of the enthalpy relaxation or recovery present during the glass transition.

As shown in Fig. 5.4 the limiting fictive temperature, T_f' , and the measured value of T_g^{onset} are similar where $q_H = q_C$; thus, the respective values of D_τ^* for each alloy are also found here to be similar (compare in Table 5.3). Where the calculated value of D_τ^* is concerned, there is no observed fundamental distinction in taking either T_f' or T_g^{onset} as the glass transition temperature in the case of equal heating and cooling rates.

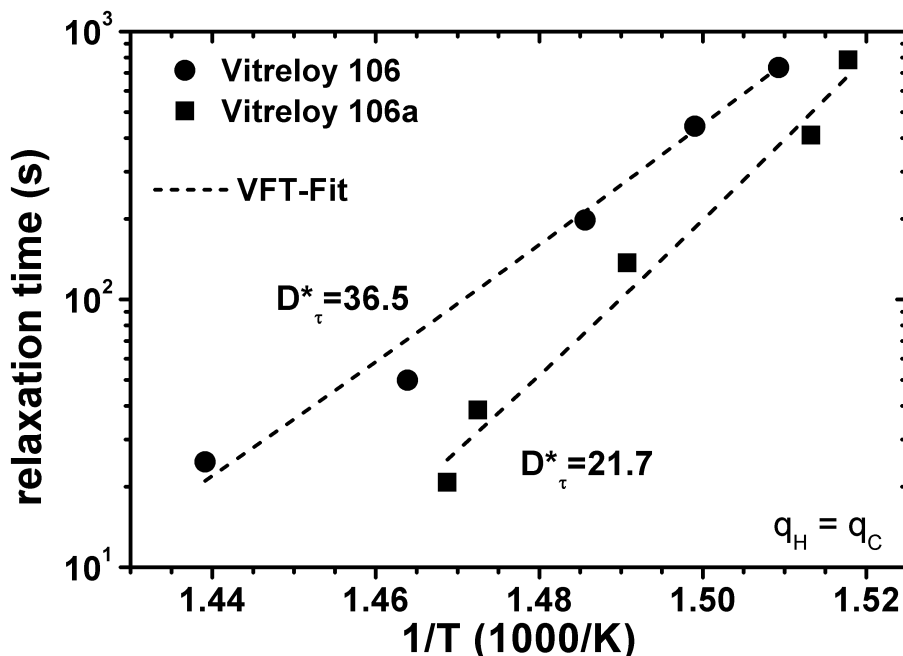


Figure 5.6: Relaxation times, τ , for Vitreloy 106 and 106a (solid circle and solid square symbols, respectively) taken from DSC experiments using Eq. 5.1. The fragilities, D_{τ}^* , calculated from fitting the experimental data to Eq. 2.27 are included here [75].

The calorimetric relaxation times from Eq. 5.1 are calculated for Vitreloy 106 and 106a for equal heating and cooling rates in the DSC and are given in Fig. 5.6. The values of the fragility parameter, D_{τ}^* , obtained by fitting the experimental data with Eq. 2.27 are given here as well as 36.5 and 21.7 for Vitreloy 106 and 106a, respectively.

In cases where the heating and cooling rates are different, T_f' and T_g^{onset} may differ substantially, indicating that the measured value of T_g^{onset} is not necessarily representative of the sample's structural state. If this is the case, the value of the kinetic fragility parameter, D_{τ}^* , calculated from the shift of T_g^{onset} may vary greatly, depending on the cooling rate used during the pre-treatment, as evidenced in Fig. 5.2 and Table 5.1.

5.1.2 Comparison of fragility indices

In Sec. 2.5 the steepness index, m , was introduced as another method of quantifying the kinetic fragility of a glass-forming liquid (see Eq. 2.28 on p. 23). Since this index is widely used as an analog to the VFT fragility

5.1 The kinetic glass transition in DSC

parameter [168], it is important to assess whether the method of determining fragility through use of Eqs. 2.27 and 5.1 is consistent with that described by Eq. 2.28.

Figure 5.7 shows a $\ln(1/q)$ vs $1/T'_f$ plot for Vitreloy 106 and 106a for the case where $q_H = q_C$. Since it was already established in the previous section that T_g^{onset} is approximately equal to T'_f in the case of equal heating and cooling rates, the limiting fictive temperature was used here instead of the onset of the glass transition only as a matter of convention after Moynihan and Angell and others [73, 163, 169].

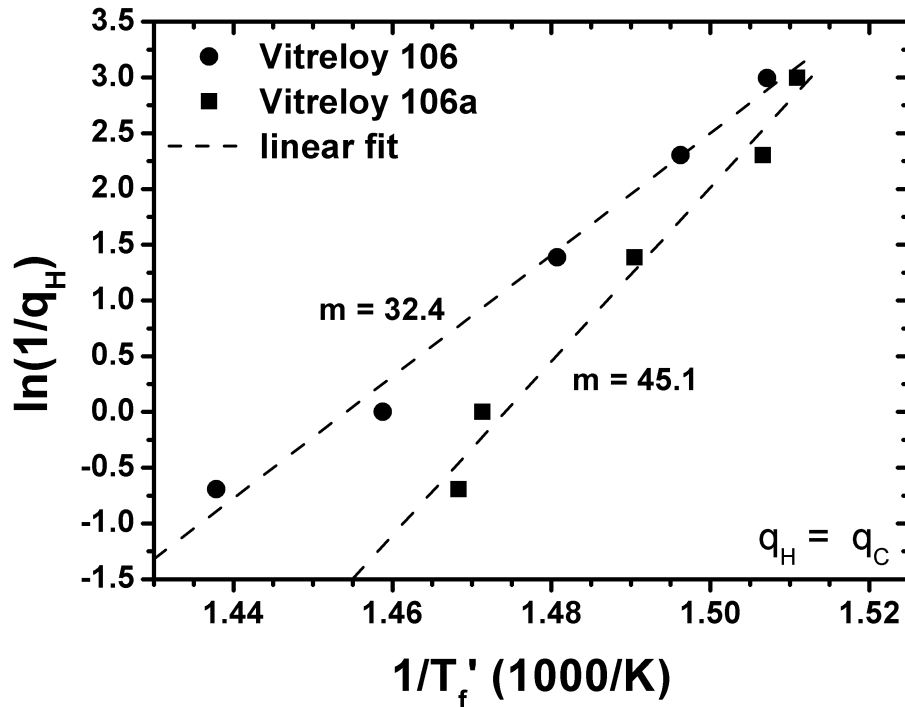


Figure 5.7: $\ln(1/q)$ vs $1/T'_f$ for Vitreloy 106 and 106a (filled circles and filled squares, respectively). The slopes of linear fits of the data (dashed lines) using Eq. 2.23 on p. 20 are proportional to the fragility as expressed by the value of m from Eq. 2.28.

Linear fits to the experimental data using Eq. 2.23 are shown in Fig. 5.7 as dashed lines, the slopes of which are proportional to the value of m in Eq. 2.28. In the plot of Fig. 5.7, these slopes have units of J g-atom^{-1} and have traditionally been interpreted as the activation energy, Q' , for the relaxation times controlling the structural relaxation from the glassy to the supercooled liquid state [73, 159]. As such, the apparent activation energy, Q' can be determined from the shift of the calorimetric glass transition temperature with the heating or cooling rate as such:

5.1 The kinetic glass transition in DSC

$$\frac{d \ln(1/q)}{d(1/T_g)} = Q'/R. \quad (5.2)$$

For Vitreloy 106 and 106a, the values of Q' are determined to be 419 and 578 kJ g-atom⁻¹, respectively.

To determine m the following equality can be employed: [160]

$$m = \frac{Q'}{\ln(10)RT_g}, \quad (5.3)$$

which can be seen as an alternative expression of Eq. 2.25 on p. 21 for $T = T_g$.

Since any value determined for T_g from a calorimetric up-scan will be highly dependent on the heating rate, the value of T_g was taken here as the temperature where the calorimetric relaxation time, τ as defined using Eq. 5.1, has a value of 200 s (further discussion on this will be given in Sec. 5.4.1) [23, 70, 160]. Using this method, the m -fragilities of Vitreloy 106 and 106a were determined to be 32.4 and 45.1, respectively.

The relationship given in Eq. 2.29 on p. 23 can be used in order to verify if the m -values determined here are in agreement with the VFT-fragility parameter, D^* . Inserting the m -values shown in Fig. 5.7 into Eq. 2.29 yields D^* -values of 35.6 and 20.2, corresponding to Vitreloy 106 and 106a, respectively. These values are in very good agreement with those determined by fitting the experimental calorimetric data to Eq. 2.27 (see Fig. 5.6). According to the results shown in Figs. 5.6 and 5.7, both methods of determining and describing fragility using DSC appear to be compatible.

The question now arises pertaining to how both the Arrhenius and VFT-equations can be used as valid descriptors of fragility for the decidedly non-Arrhenius kinetic behavior discussed in this section. At first glance, it appears obvious that the temperature range under investigation is an important consideration. Theoretically, the VFT-equation is valid for experimental data collected over all temperatures where $T > T_0$, given that the data correspond to equilibrium values and that no liquid-liquid transitions occur in this temperature range.¹ As such, a single set of invariant fitting parameters – f_0 , D_f^*

¹In practice there has been experimental evidence showing the inadequacy of the VFT-equation in describing the equilibrium viscosity of some polymeric and organic glass-formers over a wide temperature range [170–172] and recently the usefulness of the VFT-equation in general has been called into question [53].

5.1 The kinetic glass transition in DSC

and T_0 – should be sufficient to describe the data.

As was discussed in Sec. 2.5, archetypically strong liquids ($m \sim 16$) have temperature-dependent viscosities or relaxation times that are able to be well described for all temperatures where $T > 0$ with the Arrhenius-equation. In contrast to the VFT-equation, only two fitting parameters – f_0 and Q – are needed to describe the experimental data. However, in limited temperature ranges; e.g., in the vicinity of T_g , the Arrhenius-equation is able to describe any set of experimental data with as much accuracy as the VFT-equation. Data that correspond to non-Arrhenius behavior over a wide temperature range, i.e. kinetically fragile, are nevertheless able to be described with the Arrhenius-equation within a narrow temperature range, yielding an apparent activation energy, Q' (refer to Eq. 2.25), as shown in Fig. 2.7. This is the main reason why both the VFT and Arrhenius-equations succeed at fitting these data equally well.

Another important consideration is the values of the fitting constants used in the VFT and Arrhenius-equations. In order for any data fit to have physical plausibility, the values of the fitting parameters must be within reason. As discussed in Sec. 2.5, the pre-exponential factors, η_0 or τ_0 , are usually treated as fixed fitting constants with physically reasonable values. For example, the commonly accepted value range for τ_0 is $\sim 10^{-14} - 10^{-13}$ s, which has empirically been established as the limiting value of τ_0 that all data fits of experimental relaxation time data approach as $T \rightarrow \infty$ [23, 49, 173–175]. Furthermore, this range appears physically reasonable if τ_0 is viewed as a time-scale reflecting an inverse attempt frequency (after Adam-Gibbs [67]) on the order of the Debye frequency¹. However, it is implicitly understood in the definition of m -fragility from Eqs. 2.28 and 5.3 that the apparent activation energy, Q' , can only be determined when both the pre-exponential factor and Q' are left as free fitting parameters. In the case of $\ln(1/q)$ vs $1/T_f'$ data (see Fig. 5.7), this pre-exponential factor does not assume any special physical relevance and can vary over orders of magnitude in order to provide a good fit to the data.

¹The Debye frequency for a material, $\omega_D = \left(\frac{1}{V_m} 6\pi^2 v_s^3\right)^{(1/3)}$, can be estimated to be in the range of $\sim 10^{12} - 10^{14}$ s⁻¹ by assuming an atomic volume, $V_m \sim 10^{-32} - 10^{-30}$ m⁻³ and a speed of sound, $v_s \sim 10 - 1000$ m/s (material values taken from Ref. [176]).

5.2 Thermodynamic functions of the equilibrium liquid

By using the calorimetric methods described in Sec. 4.3, the thermodynamic functions of the equilibrium liquid in relation to those of the crystalline state can be accurately determined for BMG alloys. The specific heat capacity, C_p , can be evaluated directly from the DSC data using the method outlined in Sec. 4.3.2, whereas the derived functions for enthalpy, entropy and Gibbs free energy (see Sec. 2.2) require the determination of further thermodynamic quantities; e.g., the enthalpy of fusion, ΔH_f .

As well as being able to accurately measure and characterize the glass transition region (as discussed in Sec. 5.1), DSC methods can be used to determine relevant thermodynamic quantities, such as the crystallization and melting temperatures, as well as their corresponding transformation enthalpies. In the case where the melting interval lies outside of the measurable range of the DSC, this can be investigated using DTA (Secs. 4.2.1 and 4.3.1), as shown for the Vitreloy 1b alloy in Fig. 5.8.

Figure 5.8 shows the DSC and DTA traces of a glassy sample of Vitreloy 1b scanned with heating rates, q_H , of 0.416 and 0.50 K s⁻¹, respectively. The onset temperature of the glass transition, T_g^{onset} , and the beginning of the crystallization event, T_x , occur in the DSC for this heating rate at 620 and 774 K, respectively. The eutectic melting temperature, T_{eut} , is measured in the DTA at 921 K and the liquidus temperature, T_{liq} , is at 1102 K where the sample is completely molten. Taking the area of the exothermic crystallization and endothermic melting peaks shown in Fig. 5.8, the enthalpies of crystallization and fusion, ΔH_x and ΔH_f , respectively, were determined to be $\Delta H_x = -7.5$ kJ g-atom⁻¹ and $\Delta H_f = 9.30$ kJ g-atom⁻¹. The negative sign of ΔH_x indicates that crystallization is an exothermic process.

In the case of the Au_{49.0}Cu_{26.9}Si_{16.3}Ag_{5.5}Pd_{2.3} BMG, the entire glass transition and melting intervals were able to be investigated using the DSC setup discussed in Sec. 4.3.1. The DSC up-scan for Au_{49.0}Cu_{26.9}Si_{16.3}Ag_{5.5}Pd_{2.3} is shown in Fig. 5.9 for a constant heating rate of $q_H = 0.333$ K s⁻¹.

The onset of the glass transition is observed in Fig. 5.9 at 396 K, followed by multiple crystallization events beginning at 455, 504, and 560 K; these are indicated as T_{x1} , T_{x2} and T_{x3} , respectively. The melting and liquidus temperatures were determined to be $T_{eut} = 615$ K and $T_{liq} = 650$ K, with transition enthalpies of $\Delta H_x = -3.59$ kJ g-atom⁻¹ and $\Delta H_f = 5.30$ kJ g-atom⁻¹.

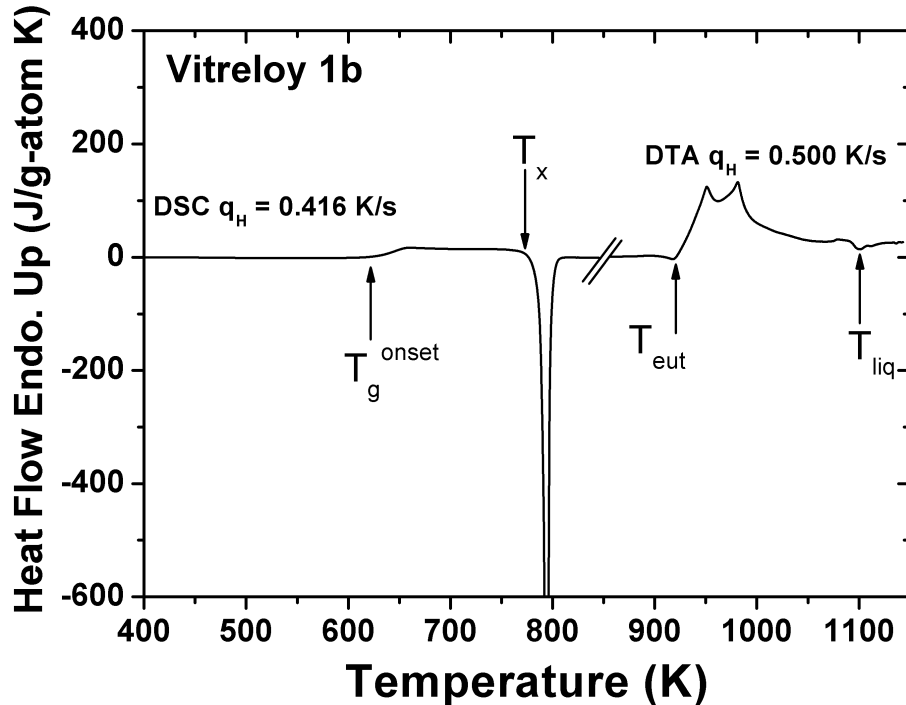


Figure 5.8: DSC and DTA thermograms of an as-cast sample of the Vitreloy 1b BMG with heating rates, q_H , of 0.416 and 0.500 K s⁻¹, respectively. T_g^{onset} (620 K), T_x (774 K), T_{eut} (921 K) and T_{liq} (1102 K) mark the onset temperatures of the glass transition, crystallization event, melting peak and liquid state respectively. The double slash at ~ 850 K separates the DSC and DTA measurement data [177].

5.2.1 Specific heat capacity

By using the step-method outlined in Sec. 4.3.2, highly accurate values of the specific heat capacity, C_p , can be determined using the DSC apparatuses described in Sec. 4.3.1. The experimentally determined values of the specific heat capacity as a function of temperature, $C_p(T)$, for the liquid, glassy and crystalline states of the Au_{49.0}Cu_{26.9}Si_{16.3}Ag_{5.5}Pd_{2.3} alloy are shown in Fig. 5.10.

The experimental values shown in Fig. 5.10 were determined for a heating rate of $q_H = 0.333$ K s⁻¹ and an isothermal holding time of 120 s. The C_p -values of the undercooled liquid in the temperature range from the liquidus temperature, T_{liq} , down to 565 K were determined by cooling at a rate of 1 K s⁻¹ and holding for 120 s in Al₂O₃ pans. These particular data points represent experiments in which the sample was not observed to crystallize during undercooling.

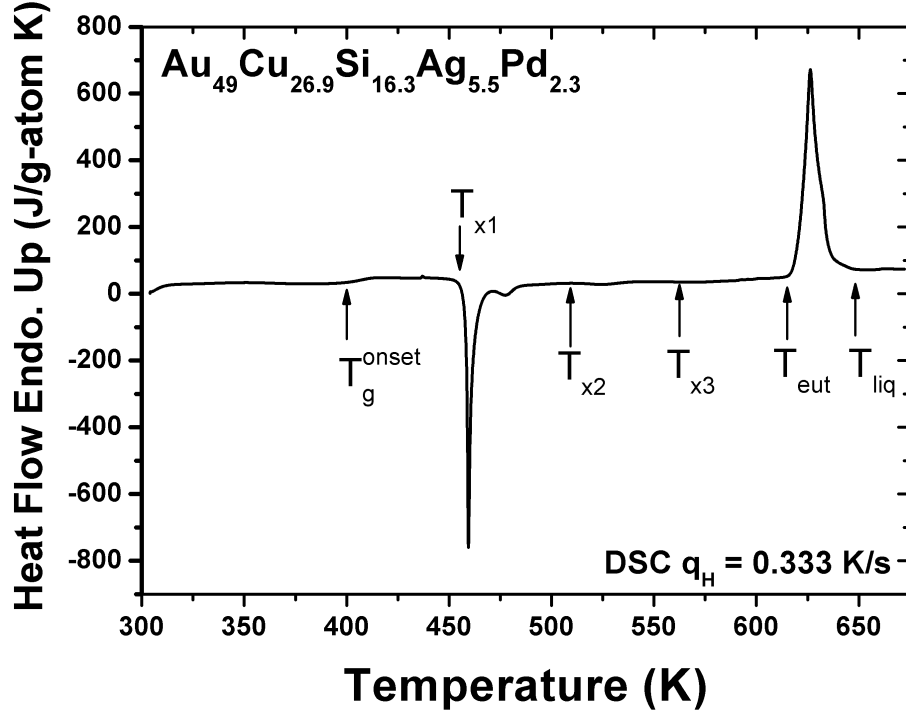


Figure 5.9: DSC thermogram of an as-cast sample of $\text{Au}_{49.0}\text{Cu}_{26.9}\text{Si}_{16.3}\text{Ag}_{5.5}\text{Pd}_{2.3}$ scanned with a heating rate of $q_H = 0.333 \text{ K s}^{-1}$. T_g^{onset} was determined at this rate as 396 K. The multiple crystallization peaks, T_{x1} , T_{x2} and T_{x3} , are shown along with the melting and liquidus temperatures, $T_{\text{eut}} = 615 \text{ K}$ and $T_{\text{liq}} = 650 \text{ K}$, respectively.

Prior to the measurements of the specific heat capacity of the crystalline state, samples of the Vitreloy 1b and $\text{Au}_{49.0}\text{Cu}_{26.9}\text{Si}_{16.3}\text{Ag}_{5.5}\text{Pd}_{2.3}$ alloys investigated here were first heated to just 5 K below T_{eut} , after the completion of all crystallization events measured in the DSC/DTA (Figs. 5.9 and 5.8). This was to ensure the complete transformation of all amorphous material in the samples.

The temperature dependence of the heat capacities for the equilibrium liquid and crystalline states far above the Debye temperature is found through fitting of the experimental data to the two equations according to Kubaschewski et al. [178]:

$$C_p^l(T) = 3R + aT + bT^{-2} \quad (5.4)$$

$$C_p^x(T) = 3R + cT + dT^2, \quad (5.5)$$

5.2 Thermodynamic functions of the equilibrium liquid

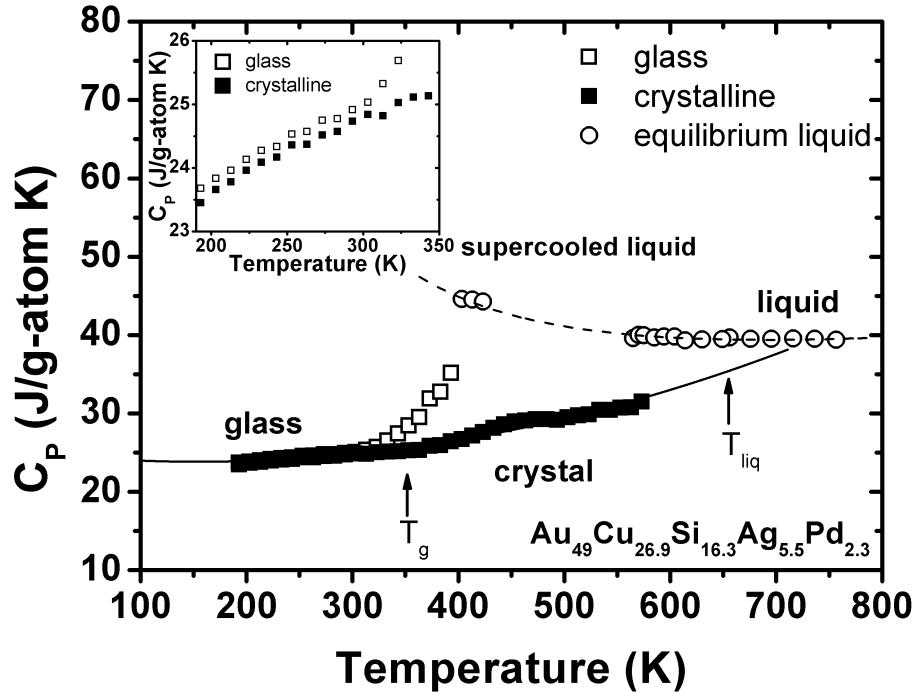


Figure 5.10: Specific heat capacity, C_p , of the glassy (open squares), crystalline (filled squares) and liquid (open circles) states of the $\text{Au}_{49.0}\text{Cu}_{26.9}\text{Si}_{16.3}\text{Ag}_{5.5}\text{Pd}_{2.3}$ BMG-forming alloy. The dashed and solid lines represent the fits to the experimental data using Eqs. 5.4 and 5.5, respectively. The specific heat capacity difference between the glassy and crystalline states is highlighted in the low-temperature range (inset).

where R is the gas constant and $C_p^l(T)$ and $C_p^x(T)$ are the specific heat capacities of the liquid and crystalline states, respectively. The fitting constants were determined here to be $a = 1.395 \times 10^{-2} \text{ J g-atom}^{-1} \text{ K}^{-2}$, $b = 2.200 \times 10^6 \text{ J K g-atom}^{-1}$, $c = -1.43 \times 10^{-2} \text{ J g-atom}^{-1} \text{ K}^{-2}$ and $d = 4.62 \times 10^{-5} \text{ J g-atom}^{-1} \text{ K}^{-3}$.

In the case where the liquid state of a BMG alloy lies outside of the measurable range of the DSC, C_p^l must be estimated using other experimentally determined thermodynamic quantities. Shown in Fig. 5.11 are the experimentally determined specific heat capacities for the amorphous (open triangles) and crystalline (filled squares) states of the Vitreloy 1b alloy. As shown earlier in Fig. 5.8, T_{liq} of this alloy was determined in the DTA as 1102 K. Therefore, the specific heat capacity of the liquid close to the melting point was approx-

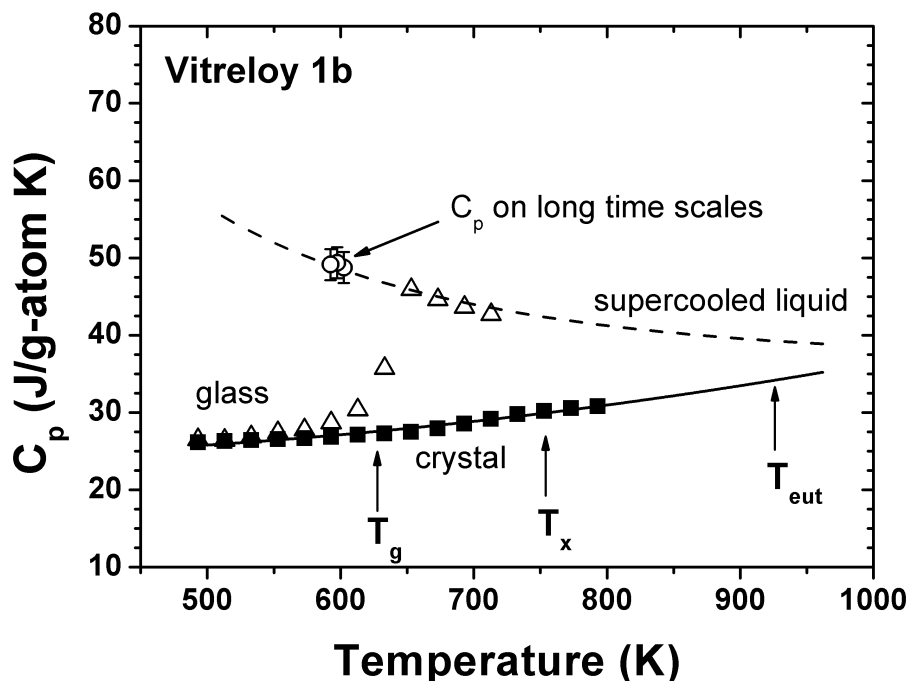


Figure 5.11: Measured specific heat capacities, C_p , of the amorphous (open triangles) and crystalline (filled squares) states of a sample of Vitreloy 1b. The equilibrium liquid on long time scales was reached through isothermal annealing and the C_p estimated from enthalpy recovery experiments (circles) (see Sec. 6.2). The dashed and solid lines are fits of the experimental data to Eqs. 5.4 and 5.5, respectively (see p. 90) [177].

imated by the difference between the experimentally determined enthalpies of fusion and crystallization; ΔH_f and ΔH_x , respectively. The difference between these two quantities represents the value of the area that lies between the specific heat capacity curves of the liquid and crystalline states in the temperature range from the crystallization to the liquidus temperature,

$$\Delta H_f - \Delta H_x = \int_{T_x}^{T_{liq}} \Delta C_p^{l-x}(T') dT', \quad (5.6)$$

where T_x is the temperature of the crystallization peak (761 K) as measured in the DSC with a heating rate of 0.333 K s^{-1} and T_{liq} is the liquidus temperature where the sample is completely molten and the Gibbs free energy of the liquid and crystal states are equal (1102 K). This method was previously used to estimate the specific heat of the liquid for the Vitreloy 1 [13] and Vitreloy 106a [164] melts as well.

5.2 Thermodynamic functions of the equilibrium liquid

Also shown in Fig. 5.11 are the specific heat capacity values as determined for long time scales at temperatures below the calorimetric glass transition (circles) using the method described in Ref. [41]. Here the difference in specific heat capacities of the glassy state, $C_p^g(T_i)$, and the equilibrium liquid, $C_p^l(T_i)$, at a temperature $T_i = T_1 + (T_2 - T_1)/2$, was approximated as

$$\Delta C_p^{(l-g)} \approx [\Delta H_r(T_1) - \Delta H_r(T_2)] / (T_2 - T_1), \quad (5.7)$$

where ΔH_r is the enthalpy of recovery measured after annealing at the specified temperature, as using the enthalpy recovery method described in Sec. 4.4.1. The values of ΔH_r are given in Sec. 6.2.

5.2.2 Enthalpy

The enthalpy difference between the equilibrium liquid and crystalline states, $\Delta H^{l-x}(T)$, is given by Eq. 2.3 on p. 7. The constant of integration in this expression is the experimentally determined enthalpy of fusion, ΔH_f , and corresponds to the enthalpy difference between the liquid and crystalline states at T_{liq} , where $G^l(T) = G^x(T)$. Through the analytical expressions for C_p^l and C_p^x in Eqs. 5.4 and 5.5, the experimentally determined values of the fitting constants a , b , c and d can be used to calculate the difference in specific heat capacity of the liquid and crystalline states, ΔC_p^{l-x} , which can then be integrated according to the expression in Eq. 2.3 to determine $\Delta H^{l-x}(T)$.

In Fig. 5.12 the enthalpy difference between the liquid and crystalline states of Vitreloy 1b is plotted as a function of temperature as calculated from Eq. 2.3. The enthalpy of fusion, $\Delta H_f = 9.3 \text{ kJ g-atom}^{-1}$, gives the enthalpy difference at T_{liq} . The glassy state is shown schematically as a dotted horizontal line where the residual enthalpy from the supercooled liquid is "frozen in" as the liquid vitrifies into a glass at T_g . Below T_g , the undercooled liquid at long time scales can be reached by isothermal annealing, as described in Sec. 4.4.

Figure 5.13 shows the $\Delta H^{l-x}(T)$ curve for the $\text{Au}_{49.0}\text{Cu}_{26.9}\text{Si}_{16.3}\text{Ag}_{5.5}\text{Pd}_{2.3}$ BMG. Shown here are experimental data points corresponding to ΔH_f (open square) and ΔH_x measured at heating rates of 0.0833, 0.333, 1, 1.5 and 2 K s^{-1} (open triangles). Additionally, ΔH_x was measured during undercooling at rates of 0.333 and 1 K s^{-1} (filled triangles). All measured values of ΔH_x agree very well with the independently obtained $\Delta H^{l-x}(T)$ curve calculated from ΔH_f and the specific heat fitting constants of Eqs. 5.4 and 5.5 (Appendix A). Also shown in Fig. 5.13 are the individual enthalpies of crystallization, measured with a heating rate $q_H = 0.333 \text{ K s}^{-1}$ (open circles). The values of

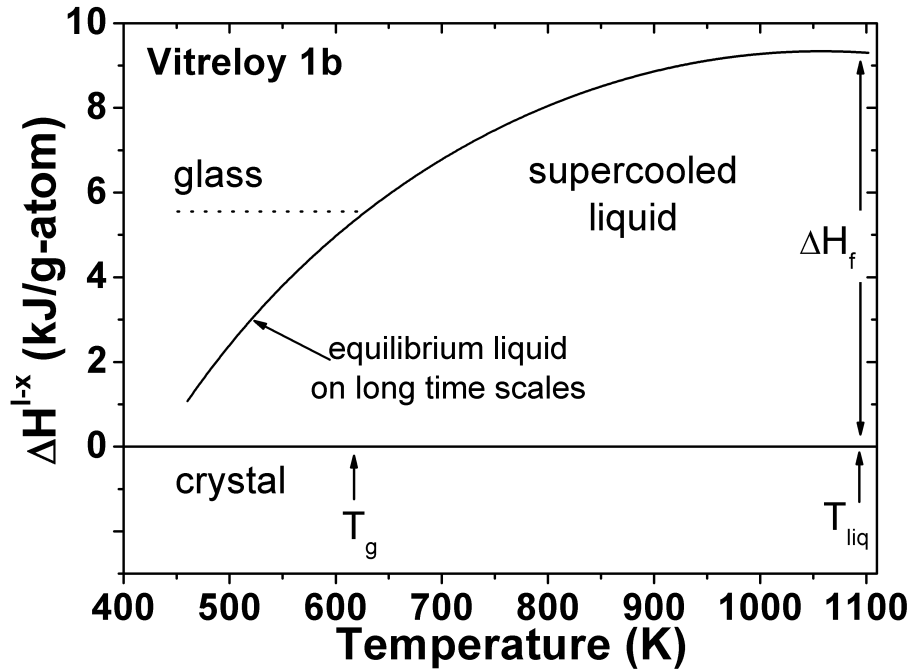


Figure 5.12: Calculated enthalpy difference, $\Delta H^{l-x}(T)$, between the liquid and crystalline states of Vitreloy 1b. The experimentally determined enthalpy of fusion is $\Delta H_f = 9.3 \text{ kJ g-atom}^{-1}$; T_{liq} was measured to be 1102 K. The glassy state is shown schematically by the dotted line beginning at T_g [177].

the crystallization onset temperatures and total crystallization enthalpy for each heating rate are given in Table 5.2.

5.2.3 Entropy

The entropy difference between the liquid and crystalline states, ΔS^{l-x} , can be calculated in a fashion similar to ΔH^{l-x} through the use of Eq. 2.4 on p. 8. In this case, the constant of integration is the entropy of fusion, $\Delta S_f = \Delta H_f/T_{liq}$. The calculated ΔS^{l-x} curves for the Vitreloy 1b and $\text{Au}_{49.0}\text{Cu}_{26.9}\text{Si}_{16.3}\text{Ag}_{5.5}\text{Pd}_{2.3}$ alloys are shown together in Fig. 5.14. The calculated values of ΔS_f are given in Appendix A. As shown schematically by the dashed lines in Fig. 5.14, residual entropy is frozen into the glassy state at T_g .

Indicated on the ΔS^{l-x} plots of Fig. 5.14 is the *isentropic* temperature, T_K . Originally introduced by Kauzmann in 1948 [179], T_K (since referred to as the Kauzmann temperature) is the apparent temperature at which the entropies

5.2 Thermodynamic functions of the equilibrium liquid

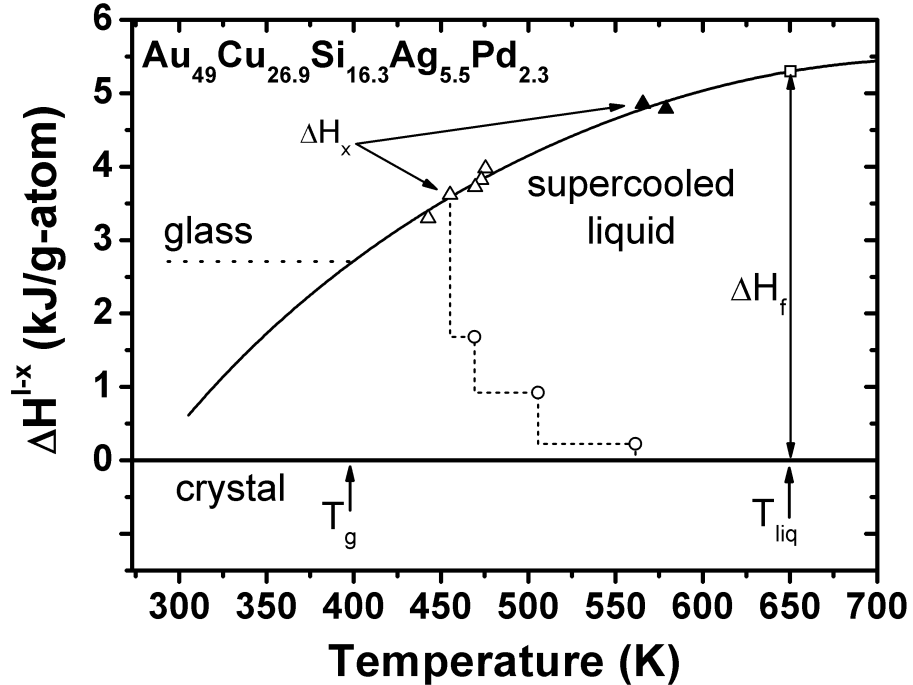


Figure 5.13: Calculated enthalpy difference, $\Delta H^{l-x}(T)$, between the liquid and crystalline states of $\text{Au}_{49.0}\text{Cu}_{26.9}\text{Si}_{16.3}\text{Ag}_{5.5}\text{Pd}_{2.3}$, showing the values of ΔH_f (open square) and ΔH_x measured during heating with different rates from the glassy region (open triangles) as well as during undercooling from the liquid (filled triangles). The transformation steps from the supercooled liquid to the crystalline state are indicated for $q_H = 0.333 \text{ K s}^{-1}$ (open circles).

of the crystal and the undercooled liquid are equal ($S^l = S^x$). It is important to note that the entropy curves in Fig. 5.14 represent both the vibrational and configurational parts of the entropy; as such, T_K marks the temperature where the *total* entropy of the undercooled liquid and crystalline states are equal. Kauzmann noticed that, if the entropies of the undercooled liquid was extrapolated to lower temperatures, it would apparently cross that of the highly ordered crystalline state. This is known as the *Kauzmann paradox* and was partially resolved by Kauzmann himself by requiring that the undercooled liquid must crystallize before reaching T_K . Another resolution of the paradox was later given by Gibbs and DiMarzio [180] by postulating the existence of an ideal, thermodynamic glass transition in the vicinity of T_K at a temperature T_2 , where the configurational entropy of the undercooled liquid would vanish. The case of whether or not there may exist a thermodynamic glass transition at these temperatures is still under heavy debate [139]. While the Adam-Gibbs entropy theory (see Sec. 2.5.2), which invokes the assumption of an Ehrenfest-

5.2 Thermodynamic functions of the equilibrium liquid

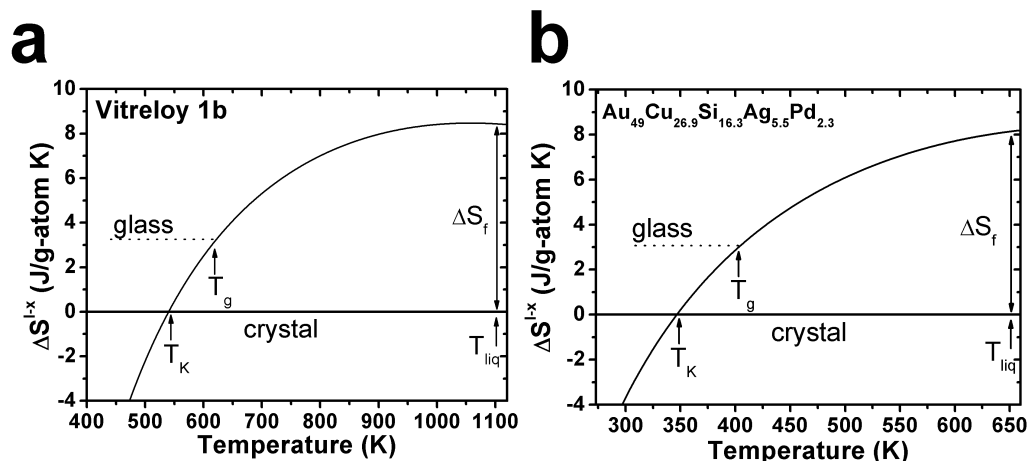


Figure 5.14: Calculated total entropy difference, $\Delta S^{l-x}(T)$, between the liquid and crystalline states of (a) Vitreloy 1b and (b) $\text{Au}_{49.0}\text{Cu}_{26.9}\text{Si}_{16.3}\text{Ag}_{5.5}\text{Pd}_{2.3}$. The Kauzmann temperatures, T_K , of each alloy were determined to be 541 and 348 K, respectively.

like glass transition at low temperatures, has found much success since its inception [67, 91, 173, 181, 182], recent experimental results in polystyrenes indicate no evidence of a thermodynamic transition at or near T_K [183, 184]. However, as pointed out by Johari [185], the absence of a thermodynamic glass transition at these temperatures need not necessarily compromise the validity of the Adam-Gibbs equation in predicting the transport properties of the liquid with the change in configurational entropy, $S_c(T)$. Further discussion of the configurational entropy of the undercooled liquid and its relation to free volume models of the equilibrium viscosity will be given in Sec. 5.4.2.

5.2.4 Gibbs free energy

The difference in Gibbs free energy between the liquid and crystalline states, $\Delta G^{l-x}(T)$, was calculated using the expression in Eq. 2.5 on p. 8. Figure 5.15 shows the calculated $\Delta G^{l-x}(T)$ curves for the Vitreloy 1b and $\text{Au}_{49.0}\text{Cu}_{26.9}\text{Si}_{16.3}\text{Ag}_{5.5}\text{Pd}_{2.3}$ alloys. Also shown are the $\Delta G^{l-x}(T)$ curves for other Zr-based bulk glass-forming liquids (see Fig. 3.1 and Ref. [85]). The specific heat fitting constants for each of the compositions can be found in Appendix A.

From the data presented in Figs. 3.1 and 5.15, a qualitative statement may be made that the driving force for crystallization, approximated by ΔG^{l-x} ,

5.2 Thermodynamic functions of the equilibrium liquid

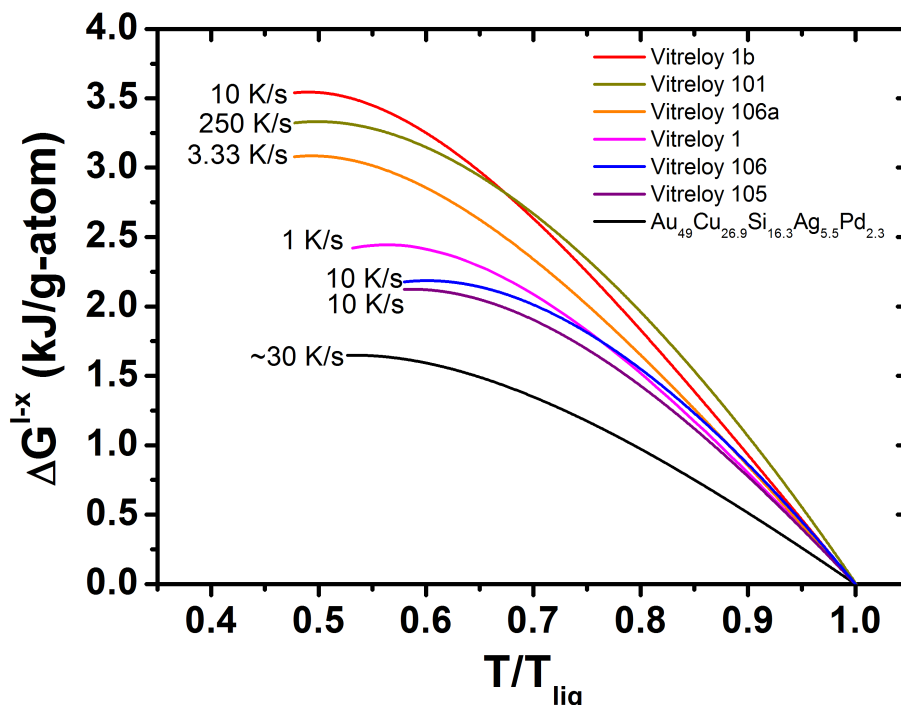


Figure 5.15: Difference in Gibbs free energy between the liquid and crystal, ΔG^{l-x} , as a function of reduced temperature, T/T_{liq} , for the Vitreloy 1b (red curve) and $\text{Au}_{49.0}\text{Cu}_{26.9}\text{Si}_{16.3}\text{Ag}_{5.5}\text{Pd}_{2.3}$ (black curve) bulk glass-forming liquids. The curves for all other compositions were reproduced from Ref. [85] and the specific heat fitting constants given in Appendix A. The critical cooling rate for each composition is indicated in units of K s^{-1} .

appears to scale with GFA, as quantified by the value of the critical cooling rate [20, 85]. This originates mainly from BMG systems having, in general, smaller entropies of fusion, ΔS_f , than conventional metallic glass-formers [20]. A small entropy of fusion indicates the tendency of these alloys to develop short-range order at the melting point and in the undercooled liquid. The entropy of fusion also gives the negative slope of the ΔG^{l-x} -curve at T_{liq} ; hence, the lower ΔS_f is, the lower the free energy difference near the melting point. Since the curves shown in Fig. 5.15 are normalized with the liquidus temperature, their true slopes aren't readily apparent. Therefore, the values of ΔS_f for each alloy are given in Fig. 5.16 (Appendix A) and plotted against the critical cooling rate, R_c . As in Fig. 5.15, the Vitreloy 1 and 101 compositions show the expected behavior; namely, that the GFA inversely scales with the Gibbs free energy difference (or entropy of fusion). However, as was discussed in Sec. 3.1, purely thermodynamic considerations, such as ΔG^{l-x} or ΔS_f , can

5.2 Thermodynamic functions of the equilibrium liquid

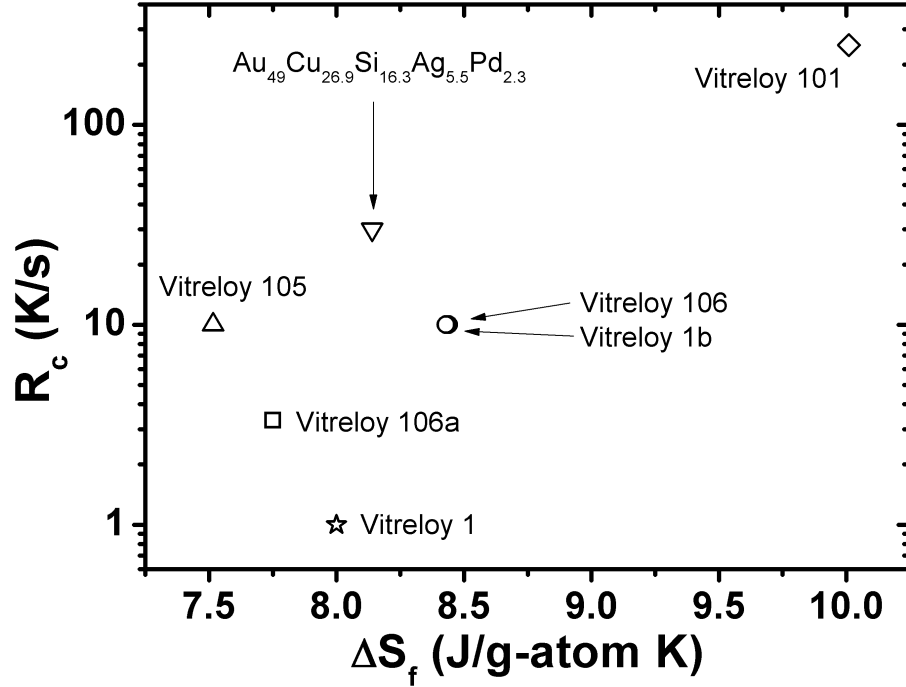


Figure 5.16: Critical cooling rate, R_c , vs. entropy of fusion, ΔS_f , for each of the BMG alloys given in Fig. 5.15.

be insufficient in accurately predicting the GFA of certain glass-forming melts. Good examples of this are the two obvious outliers in Fig. 5.15, Vitreloy 1b and $\text{Au}_{49.0}\text{Cu}_{26.9}\text{Si}_{16.3}\text{Ag}_{5.5}\text{Pd}_{2.3}$.

It should be noted that there exist some inherent limitations in approximating the driving force for crystallization with the ΔG^{l-x} curves of Fig. 5.15. Since ΔG^{l-x} only represents the measured difference in Gibbs free energy between the liquid and crystalline states (Sec. 2.2), it is not necessarily representative of the true thermodynamic driving force for nucleation. The driving force for a reaction in a given system is determined by difference in the chemical potential, $\Delta\mu$, between two states. The chemical potential is defined for a single component, i , as

$$\mu_i = \left(\frac{\partial G'}{\partial n_i} \right)_{T,P,n_j,\dots}, \quad (5.8)$$

where, formally, G' refers to the Gibbs free energy of the whole system, and G represents the *molar* Gibbs free energy. For a two-component system, in which the molar fractions of components A and B are given as X_A and X_B ,

5.2 Thermodynamic functions of the equilibrium liquid

respectively, the molar Gibbs free energy of the system and its relationship to the change in chemical potential, μ , can be expressed via the Gibbs-Duhem equation [27] as

$$G = \mu_A X_A + \mu_B X_B. \quad (5.9)$$

In Fig. 5.17 the Gibbs free energy curves of an example two-component system are shown schematically. Depicted are the Gibbs free energies of the liquid phase, L, along with two hypothetical crystal phases, α and β , as a function of the molar fraction of component B, X_B . The system is taken to be at a temperature $T < T_{liq}$; i.e., in the undercooled liquid state where the Gibbs free energies of α and β are lower than that of the liquid within a given composition range. Given a composition of, for example, $X_B = x_a$, the system can lower its free energy by crystallizing from the liquid to the α phase without a change in composition ($x_a = x_e^\alpha$). This is referred to as a *polymorphic transformation* and is indicated by the downward arrow shown in Fig. 5.17 at the composition x_a . The driving force for the polymorphic transformation is ΔG^p .

5.2 Thermodynamic functions of the equilibrium liquid

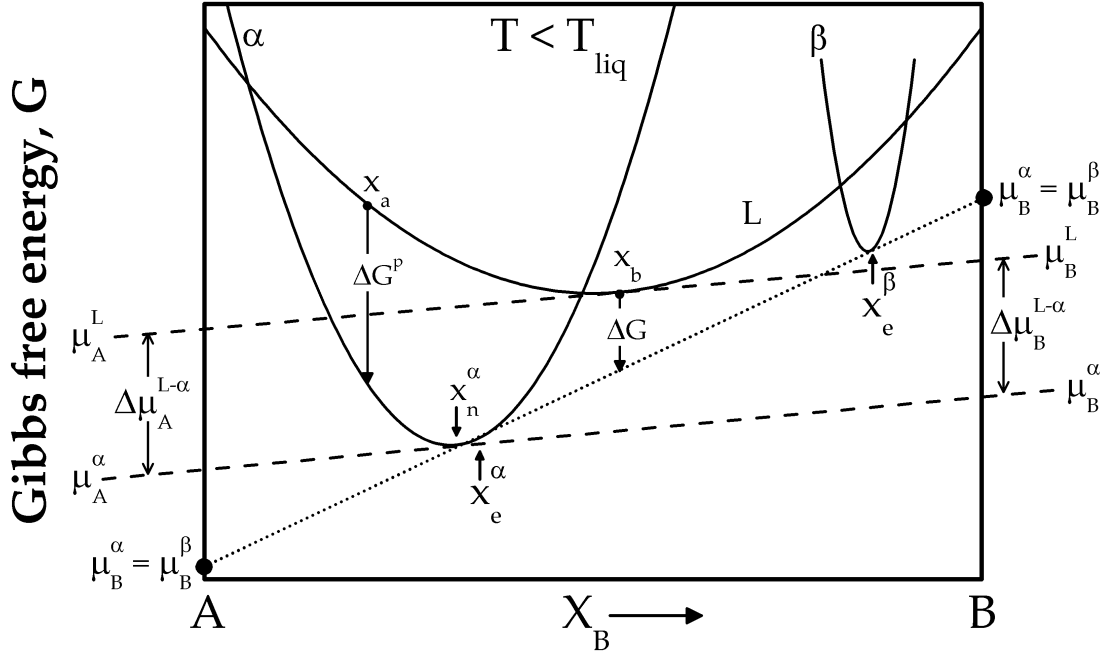


Figure 5.17: Gibbs free energy, G , as a function of molar fraction, X_B , shown schematically for a two-component system. Depicted are the free energy curves for the liquid phase, L , and two stable crystalline phases, α and β , at a temperature $T < T_{liq}$. The driving force for the polymorphic crystallization at x_a is given by the Gibbs free energy difference, ΔG^p . The dotted line gives the common tangent; i.e., equilibrium, of the α and β phases. The difference between the parallel tangents given by the dashed lines represents the maximum driving force for nucleation of an embryo of the α -phase with nuclear composition x_n^α from a liquid of composition x_b , $\Delta\mu_B^{L-\alpha} = \Delta\mu_A^{L-\alpha}$. This is larger than the driving force for the overall crystallization process at x_b , ΔG .

However, given the composition $X_B = x_b$, for example, no polymorphic driving force is present. Instead, the system can lower its free energy by an amount ΔG by crystallizing into a mixture of the α and β phases, with equilibrium concentrations x_e^α and x_e^β , respectively. The overall Gibbs free energy difference, ΔG , is indicated by the downward arrow at the composition x_b , to the equilibrium line of α and β , shown by the dotted line in Fig. 5.17. In this case ΔG is the net free energy difference of the reaction at the given temperature, but is not the driving force for nucleation of a solid phase, which has a different composition than that of the parent phase; i.e., the liquid.

In Fig. 5.17, the intercepts of tangent line taken at the point x_b in the liquid phase give the chemical potentials, μ_A^L and μ_B^L , of the atoms A and B,

5.2 Thermodynamic functions of the equilibrium liquid

respectively, for the liquid at that point. The composition of any given solid phase that results in the greatest driving force for nucleation is determined by drawing a tangent to the solid phase parallel to the tangent passing through point x_b [186–188]. For the example considered here, this condition can be expressed mathematically as

$$\left(\frac{\partial G^\alpha}{\partial X_B}\right)_{x_n^\alpha} = \left(\frac{\partial G^L}{\partial X_B}\right)_{x_b}, \quad (5.10)$$

where G^α and G^L are the molar Gibbs free energies of the α and liquid phases, respectively.

In the case of the example in Fig. 5.17, the greatest driving force for nucleation is obtained at the nuclear composition x_n^α in the α -phase. This is shown by the parallel dashed tangent lines in Fig. 5.17, giving the driving force for nucleation of an embryo of the α -phase with composition x_n^α , $\Delta\mu_B^{L-\alpha} = \Delta\mu_A^{L-\alpha}$. The initial nuclear composition is different than that of the equilibrium α -phase composition, x_e^α . For the liquid at a composition of x_b , the net change in Gibbs free energy for the crystallization, ΔG , is smaller than the change in chemical potential and, as such, should be regarded used as a lower limit to the thermodynamic driving force for nucleation.

It should be noted that, in the case of the polymorphic transformation discussed in this example, since x_a does not correspond the equilibrium α -phase composition, the polymorphic transformation does not represent the final stage of the liquid-solid transformation. Indeed, if the liquid at composition x_a is cooled fast enough, such that no long-range diffusion is allowed to occur, the liquid may transform polymorphically without composition change into the α -phase. However, if the liquid is cooled slowly enough, nucleation of embryos of the α -phase, having a different composition than that of the liquid at x_a , becomes increasingly more probable, due to long-range diffusion of the B-atoms.

Implicit in the considerations of the classical nucleation theory outlined in Sec. 2.3 is that the bulk liquid transforms to the crystalline state polymorphically, in that the crystalline phase is formed with the same composition as that of the liquid [21]. However, this has been shown not to be case with many multicomponent BMG-forming liquids, as they generally have eutectic or near-eutectic compositions, which typically result in non-polymorphic crystallization [189].

Insofar as ΔG^{l-x} can be taken as an approximation for the driving force in a

5.2 Thermodynamic functions of the equilibrium liquid

BMG-forming system, it makes sense to first examine the accuracy of the thermodynamic functions and quantities used in calculating ΔG^{l-x} . The ability to obtain accurate values of the specific heat capacity of the liquid and crystalline states is obviously of great importance. Moreover, a significant advantage is gained when the specific heat capacity of the liquid state, $C_p^l(T)$, is able to be directly measured in the DSC, as is the case with $\text{Au}_{49.0}\text{Cu}_{26.9}\text{Si}_{16.3}\text{Ag}_{5.5}\text{Pd}_{2.3}$, shown in Fig. 5.10. An even greater increase in the accuracy of the determination of $C_p^l(T)$ is gained by the ability to measure the liquid at large undercoolings, before the onset of crystallization. Furthermore, a large and stable supercooled liquid region, as measured when heating above T_g , enables the determination of C_p^l -values at temperatures that are not usually attained by undercooling conventional BMG-forming liquids¹. Most importantly, no unexpected exothermic signals were recorded in the DSC during the measurements of the liquid specific heat capacity, indicating that the liquid had not massively transformed into the crystalline state. Given these considerations, it seems valid to assume that the values of $C_p^l(T)$ determined in the DSC accurately describe the liquid state for the measured temperature ranges.

When applied to the specific heat capacity of the crystalline state, $C_p^x(T)$, the question of accuracy now pertains to whether or not this state can be considered as a suitable reference state for further thermodynamic calculations. The assumption that the crystalline state measured in the DSC corresponds to the actual equilibrium ground state of any particular BMG alloy may not always be correct. For example, the phases crystallizing from the amorphous alloy when heated above T_g may not necessarily be the same as those that are formed during cooling from the melt². An example of this is the $\text{Fe}_{80}\text{B}_{20}$ amorphous alloy, which upon annealing near T_g forms a metastable crystalline Fe_3B phase before transforming to the Fe_2B phase [190]. In other words, the phase crystallizing first from the undercooled melt may not necessarily be the one that is thermodynamically more stable, but instead be the phase with the lowest energy barrier to transition.

In Figs. 5.10 and 5.11 the values of C_p^x of the crystalline samples of Vitreloy 1b and $\text{Au}_{49.0}\text{Cu}_{26.9}\text{Si}_{16.3}\text{Ag}_{5.5}\text{Pd}_{2.3}$ were determined from the crystallized material that transformed out of the glassy state. Despite the fact that this state

¹An exception here is the $\text{Pd}_{43}\text{Cu}_{27}\text{Ni}_{10}\text{P}_{20}$ alloy, with a critical cooling rate of 0.10 K s^{-1} . $C_p^l(T)$ -values of this alloy's undercooled liquid region were obtained over the entire liquid range from T_{liq} down to T_g without crystallization intervening [91].

²This particular phenomenon has been extensively studied for the Zr-Ti-Ni-Cu-Be system [80, 129, 130, 132–134] and is thoroughly discussed for glass-forming systems in general in Chapter 8 of Ref. [21].

5.2 Thermodynamic functions of the equilibrium liquid

may not be representative of the true equilibrium state for these materials, very good agreement is noticed between the independently obtained ΔH_x -values for, e.g. $\text{Au}_{49.0}\text{Cu}_{26.9}\text{Si}_{16.3}\text{Ag}_{5.5}\text{Pd}_{2.3}$, and the ΔH^{l-x} -curve calculated using these C_p^x -values (see Fig. 5.13). This indicates that, while the population of crystalline phases may not be the same in those samples which were crystallized from near T_g and those crystallized from the undercooled liquid near T_{liq} , the differences in the specific heat capacities must be almost negligible, such as to yield values of ΔH_x that are nevertheless consistent with the calculated ΔH^{l-x} -curve. It can thus be concluded that the values obtained here for the specific heat capacities of the liquid and crystalline states are accurate enough that they lead to a sufficient description of the enthalpy difference between the liquid and crystal, and by extension, should be sufficient in calculating the Gibbs free energy difference between the liquid and crystalline states.

Another issue that arises deals with the contributing factors to GFA that are not present in the purely thermodynamic assessment given in Figs. 5.15 and 5.16. From these data, it appears clear that considering only the Gibbs free energy difference between the liquid and crystal, or similarly the entropy of fusion at T_{liq} , does not always give an accurate prediction of GFA. It then seems reasonable to also consider kinetic factors; i.e., viscosity and fragility, when looking at GFA. More specifically, melts that are very viscous in the liquid and show little change in their viscosities during undercooling (kinetically strong), will have a low growth rate of crystals (Sec. 2.3) and exhibit a high GFA. More kinetically fragile melts, however, will typically be less viscous yet exhibit a large increase in viscosity during undercooling. It is usually thought that these melts would make naturally poor bulk glass-formers [85]. However, the $\text{Pd}_{43}\text{Cu}_{27}\text{Ni}_{10}\text{P}_{20}$ composition, with a fragility parameter of $D^* = 10.3$ [91] and critical cooling rate of 0.10 K s^{-1} is an obvious exception. In such cases, it then becomes necessary to consider other factors that aren't readily apparent from a simple thermodynamic or kinetic analysis alone. For example, $\text{Pd}_{43}\text{Cu}_{27}\text{Ni}_{10}\text{P}_{20}$ [143], like most other noble-metal based BMG alloys [43, 140, 141, 145, 191, 192], can be fluxed with B_2O_3 to remove or deactivate heterogeneous nucleation sites in the melt. This can, in the case of $\text{Pt}_{57.3}\text{Cu}_{14.6}\text{Ni}_{5.3}\text{P}_{22.8}$, lead to an increase in the critical casting thickness from 6 mm to 20 mm, even though that alloy shows a large value of ΔS_f and is considered to be kinetically fragile [43].

Additionally, the liquid-crystal interfacial energy (see Sec. 2.3), σ , should be considered as also having a stabilizing effect on the undercooled liquid. High values of σ result in an increased nucleation barrier (Eq. 2.11 on p. 10) and would consequently lead to a lower nucleation rate, $I(T)$ (Eq. 2.16

5.3 Crystallization of the equilibrium liquid

on p. 11). The $\text{Pd}_{43}\text{Cu}_{27}\text{Ni}_{10}\text{P}_{20}$, $\text{Pd}_{40}\text{Cu}_{30}\text{Ni}_{10}\text{P}_{20}$ and $\text{Pt}_{57.3}\text{Cu}_{14.6}\text{Ni}_{5.3}\text{P}_{22.8}$ compositions were shown to have interfacial energies of 0.079 [137], 0.067 [193] and 0.086 J m^{-2} [43], respectively, which are all higher than that determined for Vitreloy 1 ($\sigma = 0.040 \text{ J m}^{-2}$ [19]).

Ultimately, it appears that within certain families of BMG-formers, e.g. Zr-Ti-Cu-Ni-Be or Zr-Cu-Ni-Al-Nb, correlations can be found between the GFA and certain thermodynamic or kinetic parameters. However, when comparing different BMG-forming systems with each other; e.g., Zr-Ti-Cu-Ni-Be with Pd-Cu-Ni-P, other factors need be taken into consideration. These factors can include processing methods that act to deactivate melt impurities, such as oxygen, or physical parameters, such as the liquid-crystal interface. Although the presence of oxygen has been shown to have a detrimental effect on the GFA of most Zr-based BMG alloys [150, 151], it appears that certain elements, for example aluminum, can act as a scavenger by collecting absorbed oxygen and reducing the other constituents [194]. In this way, the GFA of a given composition can be retained by increasing its intrinsic oxygen tolerance.

Although numerous criteria have been proposed to predict and describe the GFA across a variety of BMG-forming systems [78, 195, 196], they fail to address all the different factors that work to stabilize the liquid phase against crystallization and, as such, cannot satisfactorily predict the GFA and explain all of the observed data [197]. While certain criteria may appear successful by incorporating empirically validated metrics; e.g., Turnbull's reduced glass transition temperature, $\Delta T_{rg} = T_g/T_m$, their applicability is certainly not universal. A much more accurate measure of the GFA is a comprehensive knowledge of a given composition's TTT and CCT-diagrams.

5.3 Crystallization of the equilibrium liquid

The crystallization behavior of the $\text{Au}_{49.0}\text{Cu}_{26.9}\text{Si}_{16.3}\text{Ag}_{5.5}\text{Pd}_{2.3}$ undercooled liquid was studied using the DSC apparatus described in Sec. 4.3.1. Crystallization was investigated at undercoolings in the vicinity of T_{liq} , as well as in the supercooled liquid region above T_g .

5.3.1 Crystallization near T_{liq}

The times and temperatures of the onset of crystallization were determined by continuous cooling from the liquid and the data are shown in Fig. 5.18. In these experiments, samples of $\text{Au}_{49.0}\text{Cu}_{26.9}\text{Si}_{16.3}\text{Ag}_{5.5}\text{Pd}_{2.3}$ were enclosed in Al_2O_3 pans and first heated in the DSC at a rate of 0.333 K s^{-1} to a tempera-

5.3 Crystallization of the equilibrium liquid

ture of 725 K (75 K above T_{liq}); the samples were then cooled with a constant rate until the completion of crystallization on undercooling. The data points plotted in the continuous-cooling-diagram (CCD) shown in Fig. 5.18 correspond to the onset times and temperatures, (t_x, T_x) , of the single crystallization event observed during undercooling. Shown here are data (open circles) corresponding to cooling experiments performed under a constant flow of N_2 purge gas.

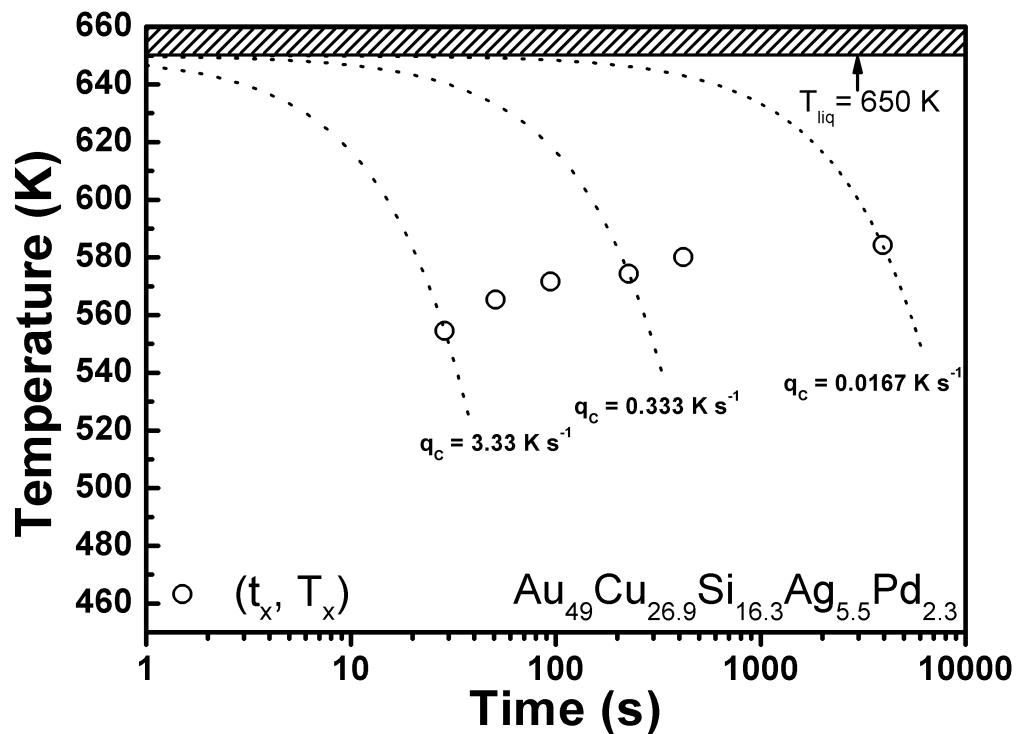


Figure 5.18: Continuous-cooling-diagram (CCD) of the $Au_{49.0}Cu_{26.9}Si_{16.3}Ag_{5.5}Pd_{2.3}$ liquid, measured for various cooling rates, q_c , using N_2 purge gases. The open circles represent the onsets of the crystallization times and temperatures, (t_x, T_x) . The dashed lines show the cooling profile in $K s^{-1}$.

The isothermal transformation times were determined in a separate set of experiments by first heating the samples in the DSC at a rate of $0.333 K s^{-1}$ to a temperature of 725 K and then cooling with a constant rate of $1 K s^{-1}$ (in an N_2 -purge) to a desired holding temperature below $T_{liq} = 650 K$. The samples were held isothermally and the resulting crystallization event

5.3 Crystallization of the equilibrium liquid

beginning at t_x recorded. Examples of the endothermic heat flow profile vs. time for these crystallization events are shown in Fig. 5.19 for three different undercooling temperatures: 564, 569 and 574 K. In this figure, the curves were manually translated along the vertical axis, in order provide better visibility. The horizontal axis begins at $t = 0$, which corresponds to the beginning of the isothermal holding time. The small exothermic peaks occurring just after $t = 0$ correspond to the heat flow equilibration of the DSC and are not to be interpreted as crystallization events.

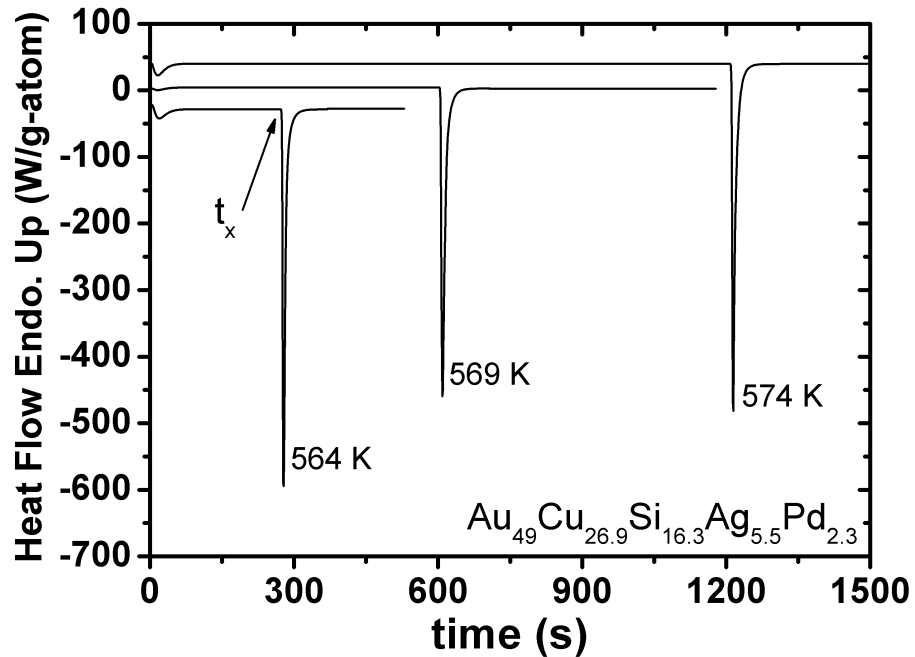


Figure 5.19: Isothermal crystallization events measured in the DSC during undercooling of the $\text{Au}_{49.0}\text{Cu}_{26.9}\text{Si}_{16.3}\text{Ag}_{5.5}\text{Pd}_{2.3}$ liquid at temperatures of 574, 569 and 564 K. These holding temperatures correspond to undercoolings of $\Delta T = 76, 81$ and 86 K, respectively, below the liquidus temperature of $T_{liq} = 650$ K. The curves were shifted along the vertical axis for better visibility.

This crystallization times and temperatures of the $\text{Au}_{49.0}\text{Cu}_{26.9}\text{Si}_{16.3}\text{Ag}_{5.5}\text{Pd}_{2.3}$ undercooled liquid are shown in the TTT-diagram of Fig. 5.20. At temperatures near T_{liq} , the data were taken from the undercooling experiments represented in Fig. 5.19. Here, the open circles correspond to the beginning of the crystallization event and the smaller filled circles indicate the end. Also shown are continuous cooling data taken from Fig. 5.18 for the cooling rates of $q_C = 3.33$ and 1 K s^{-1} (N_2 -purge, shaded circles). The data shown in the lower part of the TTT-diagram were taken from experiments performed by Fiore et al. in Ref. [198]. In these experiments, glassy samples

5.3 Crystallization of the equilibrium liquid

of $\text{Au}_{49.0}\text{Cu}_{26.9}\text{Si}_{16.3}\text{Ag}_{5.5}\text{Pd}_{2.3}$ were heated above T_g and into the supercooled liquid region with a rate of $q_C = 1.33 \text{ K s}^{-1}$ and held isothermally until completion of crystallization.

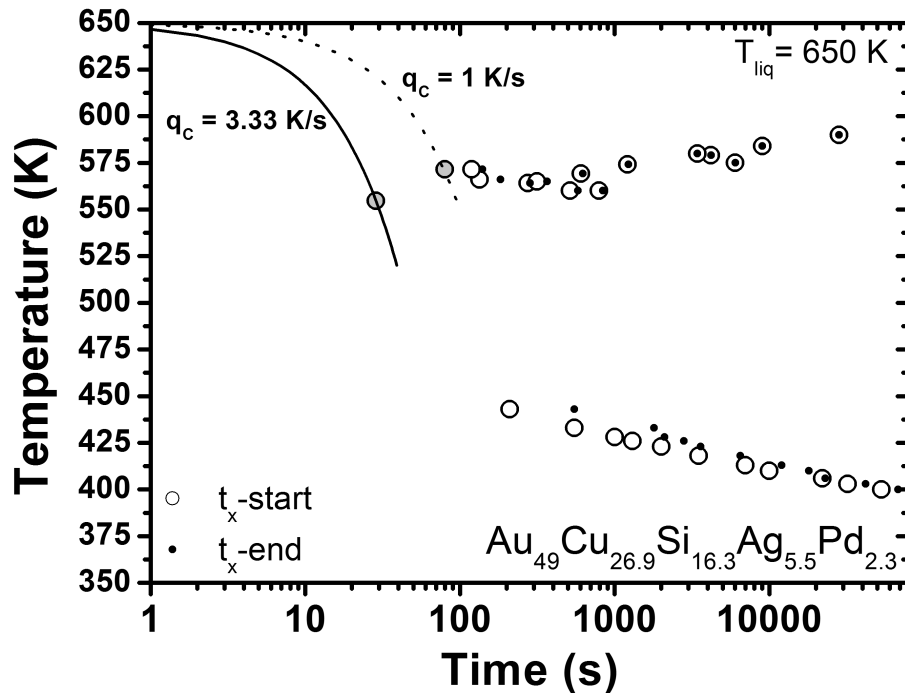


Figure 5.20: Isothermal time-temperature-transformation (TTT) diagram for $\text{Au}_{49.0}\text{Cu}_{26.9}\text{Si}_{16.3}\text{Ag}_{5.5}\text{Pd}_{2.3}$. The onset and end of the crystallization events are given by the open and filled circles, respectively. The data shown in the lower part of the diagram were taken from Ref. [198] and correspond to isothermal measurements taken in the supercooled liquid region near T_g .

It can be noticed from the data shown in Fig. 5.20 that the width of the crystallization event, Δt , varies over many orders of magnitude, depending on the crystallization temperature. More specifically, in the high temperature regime near T_{liq} , Δt remains roughly constant, $\sim 50 \text{ s}$, indicating that once crystallization in the melt occurs, it proceeds rather rapidly at these temperatures. This reflects a high value of the growth rate, $u(T)$, shown schematically in Fig. 2.3 of Sec. 2.3. This is contrasted by the larger values of Δt recorded at the lower temperatures near T_g . Here Δt increases rapidly from $\sim 300 \text{ s}$ at a temperature of 443 K to $\sim 10000 \text{ s}$ at 400 K ; this accordingly reflects a low value of $u(T)$ at these temperatures. This is in accordance with the behavior observed for the $\text{Pd}_{43}\text{Cu}_{27}\text{Ni}_{10}\text{P}_{20}$ BMG-forming liquid given in Ref. [137]. At low temperatures, growth of already present quenched-in nuclei was cited as the dominant mechanism of crystallization; whereas, at high temperatures,

5.3 Crystallization of the equilibrium liquid

spontaneous nucleation (either homogeneously or at heterogeneous nucleation sites) dominates through a stochastic processes, resulting in catastrophic crystallization of the bulk sample. However, in the experiments performed here, since the molten samples are in direct contact with the bottom of the DSC pan during undercooling, it is extremely unlikely that homogeneous nucleation was observed in the high temperature region. Crystallization was most likely initiated by heterogeneous nucleation sites on the melt-pan interface, or from impurities in the melt itself.

The undercooling limit for $\text{Au}_{49.0}\text{Cu}_{26.9}\text{Si}_{16.3}\text{Ag}_{5.5}\text{Pd}_{2.3}$ was observed in the DSC experiments shown in Figs. 5.18 and 5.20 to be at ~ 555 K, at a cooling rate of 3.33 K s^{-1} . Given the estimated critical cooling rate of this particular composition at $R_c \sim 30 \text{ K s}^{-1}$ [199], these results do not seem unreasonable. Considering the continuous cooling data given in Fig. 5.18, the minimum time for crystallization – given by the "nose" shape of the TTT-diagram – would appear to be ≤ 10 s.

However, it should be noted that the transformation times and temperatures determined in these experiments were most likely affected by the direct contact between the molten sample and the DSC pan. As such, this would work to effectively reduce the crystallization nose time and critical cooling rate estimated from Fig. 5.20. In fact, the values for R_c and isothermal crystallization times reported for alloys such as Vitreloy 106 [200], 106a [201] and 105 [200], correspond to non-contact ESL experiments, in which sample crystallization is not affected by a melt-pan interface. Only for Vitreloy 1 has it been experimentally shown that the isothermal crystallization time measured in ESL experiments are roughly on the same time scale as those measured in DTA graphite crucibles [129, 138], indicating that this particular melt shows a high resistance to the heterogeneous nucleation effects from the crucible surface. Furthermore, it was shown that molten samples of $\text{Pd}_{43}\text{Cu}_{27}\text{Ni}_{10}\text{P}_{20}$ processed in B_2O_3 show high resistance to heterogeneous nucleation effects, presumably through the B_2O_3 flux passivating surface impurities [142]. However, microstructural investigations on crystallized samples of fluxed $\text{Pd}_{43}\text{Cu}_{27}\text{Ni}_{10}\text{P}_{20}$ provide no supporting evidence for homogeneous nucleation [137], indicating that, while contributing significantly to the suppression of heterogeneous nucleation sites due to melt impurities, the B_2O_3 encapsulant itself still might act as a potential heterogeneous nucleation site.

5.3.2 Crystallization near T_g

The crystallization behavior of $\text{Au}_{49.0}\text{Cu}_{26.9}\text{Si}_{16.3}\text{Ag}_{5.5}\text{Pd}_{2.3}$ was investigated in the supercooled liquid region near T_g by scanning as-cast amorphous samples in the DSC with varying heating rates. The heat flow curves measured in the DSC are shown in Fig. 5.21 for the heating rates, q_H , of 2, 1, 1.5, 0.333 and 0.0833 K s^{-1} . In general, a minimum of three separate crystallization events – T_{x1} , T_{x2} and T_{x3} – is noticed upon heating. These are indicated in the DSC traces shown in Fig. 5.9. Below a heating rate of 1 K s^{-1} , the first crystallization event is observed to split into two separate peaks, denoted by T_{x1} and T'_{x1} . This is also seen in the DSC heat flow curves shown in Fig. 5.21, where the peak temperatures are indicated here as $T_{x,p}$. Not shown are the crystallization events corresponding to T_{x2} and T_{x3} . The onset temperatures of each crystallization event, as well as the total crystallization enthalpies, for each heating rate are listed in Table 5.2.

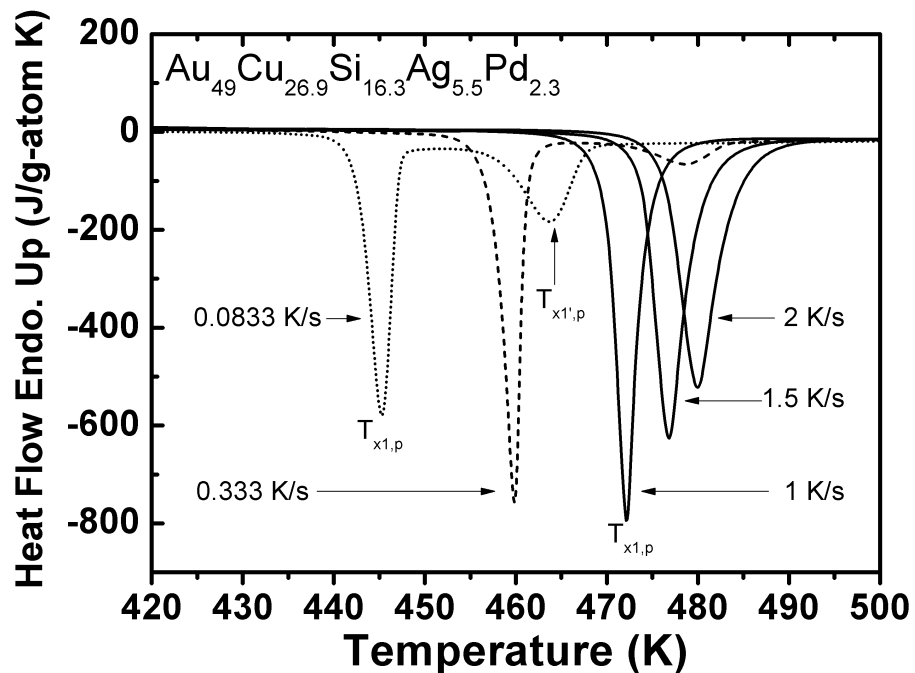


Figure 5.21: Endothermic DSC heat flow curves of $\text{Au}_{49.0}\text{Cu}_{26.9}\text{Si}_{16.3}\text{Ag}_{5.5}\text{Pd}_{2.3}$ scanned with different heating rates throughout the supercooled liquid region. Shown here is the temperature range from 420 to 500 K. For higher heating rates (solid curves), only the T_{x1} crystallization event is observed in this temperature range. For the heating rates of 0.333 and 0.0833 K s^{-1} (dashed and dotted curves, respectively), two separate events are observed at T_{x1} and T'_{x1} . Indicated here are the peak temperatures of the crystallization events, $T_{x,p}$.

5.3 Crystallization of the equilibrium liquid

	Heating rate, q_H K s ⁻¹				
	0.0833	0.333	1	1.5	2
T_{x1} [K]	442.7	455.2	469.6	473.0	475.5
T'_{x1} [K]	452.3	466.7	–	–	–
T_{x2} [K]	–	504.1	489.3	499.0	502.8
T_{x3} [K]	548.0	560.1	563.5	570.3	573.4
ΔH_x^{tot} [kJ g-atom ⁻¹]	-3.30	-3.59	-3.72	-3.82	-3.98

Table 5.2: Crystallization temperatures, T_x , and total enthalpies of crystallization, ΔH_x^{tot} , for the Au_{49.0}Cu_{26.9}Si_{16.3}Ag_{5.5}Pd_{2.3} BMG measured using DSC.

The non-isothermal crystallization kinetics of Au_{49.0}Cu_{26.9}Si_{16.3}Ag_{5.5}Pd_{2.3} were analyzed by use of the Kissinger equation [202]

$$\ln \left(\frac{q_H}{T_p^2} \right) = \frac{-Q}{RT_p} + A, \quad (5.11)$$

where q_H is the heating rate, T_p the peak crystallization temperature, Q the activation energy for crystallization and A is a constant. In this analysis, only the peak temperature of the first crystallization event, T_{x1} was considered. Shown in Fig. 5.22 are the experimental data (open squares) plotted in the Arrhenius fashion with a linear fit (dashed line). The activation energy for crystallization, Q , was determined here to be 154.7 ± 1 kJ g-atom⁻¹ (1.60 eV). In a study on this same alloy, Fiore et al. [203] performed a similar Kissinger analysis, yielding an activation energy of 162 ± 3 kJ g-atom⁻¹ (1.68 eV). These values appear reasonable, as they are comparable to the activation energy for chemical diffusion in Au-Cu alloys (~ 170 kJ g-atom⁻¹ or ~ 1.76 eV) [204].

The method of determining the activation energy for crystallization through use of the Kissinger equation of Eq. 5.11 has been applied to many BMG-forming systems [203, 205–207]. However, it should be pointed out that the results using the Kissinger analysis are strongly affected by the sample's thermal history (including the quenching rate), as well as the crystallization microstructure [21]. Furthermore, the Kissinger method does not give any useful information as to the nucleation processes and rates themselves; as such, any approach at identifying the operative mechanism of crystallization is limited to the availability of external data relating mainly to diffusion studies on binary metallic systems.

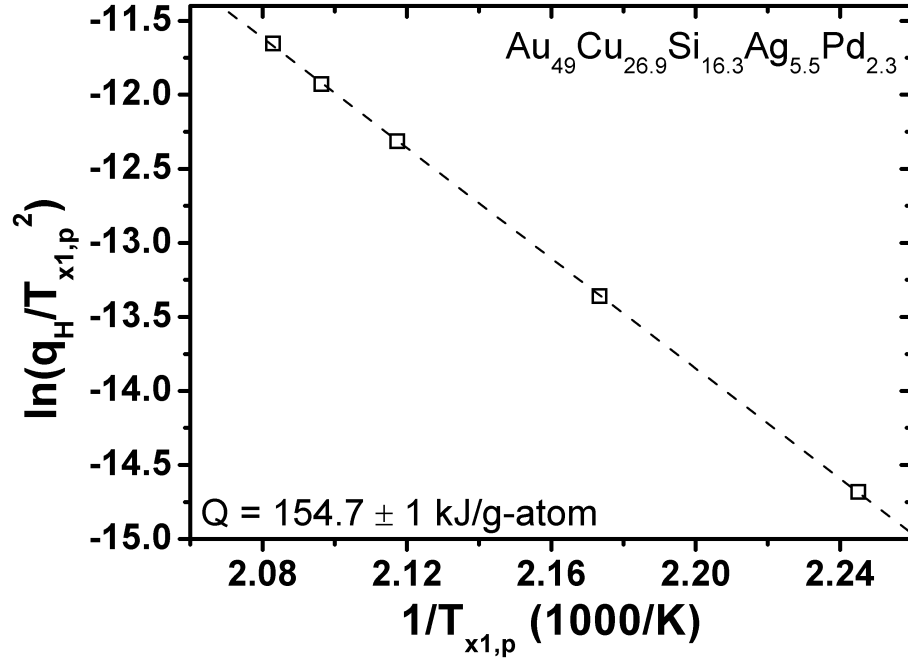


Figure 5.22: Kissinger-plot corresponding to the peak temperatures of the first crystallization event (open squares) measured in Fig. 5.21. The dashed line gives a linear fit of the data, resulting an activation energy for crystallization, $Q = 154.7 \pm 3$ kJ g-atom⁻¹ (1.60 eV).

5.4 Equilibrium viscosity

In order to determine equilibrium viscosities close to T_g , the three-point beam-bending method discussed in Secs. 4.3.3 and 4.4.3 was used. A more detailed discussion of the structural relaxation observed during isothermal viscosity measurements will be given later in Sec. 6.1. Figure 5.23 shows the experimental equilibrium viscosity data for Vitreloy 106 and 106a, and the corresponding fits to Eq. 2.27. The equilibrium viscosities were determined using the isothermal three-point beam-bending method described in Sec. 4.4.3. The determined values of the fragility parameter, D_η^* , are 35.2 and 21.0 for Vitreloy 106 and 106a, respectively. Similar experiments were performed for the Vitreloy 101 and 105 alloys, and the corresponding isothermal equilibrium viscosity data are presented in Fig. 5.24. The determined fragility parameters, D_η^* , for Vitreloy 101 and 105 are 14.9 and 18.6, respectively.

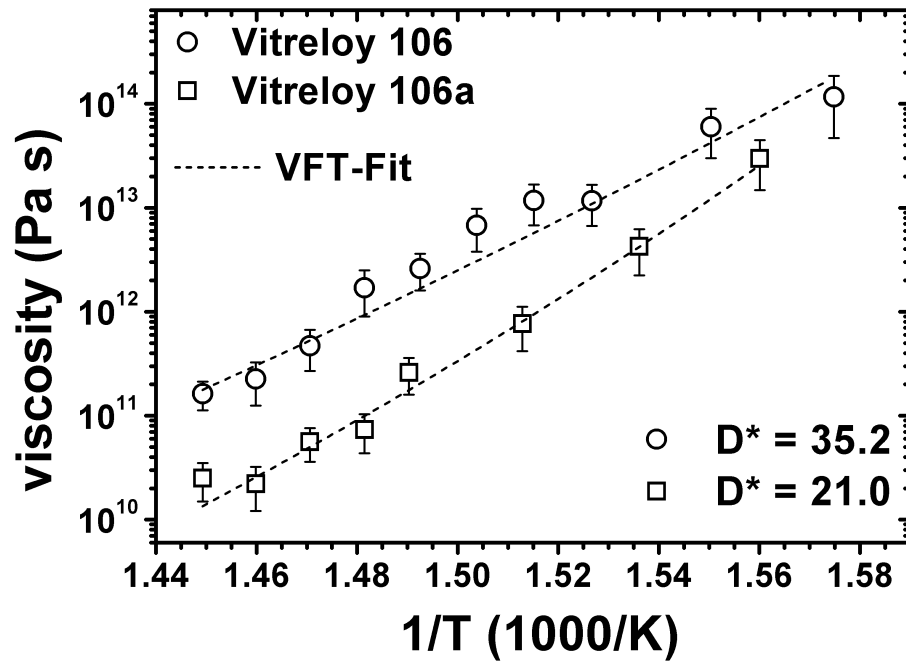


Figure 5.23: Equilibrium viscosities as a function of inverse temperature for Vitreloy 106 and 106a determined from isothermal relaxation. The fits of the experimental data to the VFT equation are included (dashed lines), as well as the fitted fragility parameters: $D_\eta^* = 35.2$ for Vitreloy 106 and $D_\eta^* = 21.0$ for Vitreloy 106a [208].

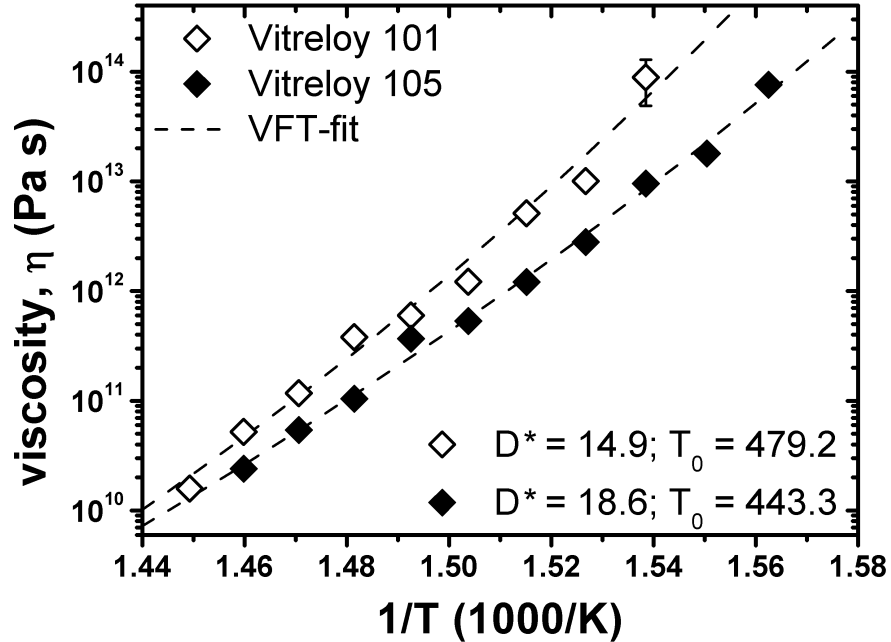


Figure 5.24: Equilibrium viscosities as a function of inverse temperature for Vitreloy 101 and 105 determined from isothermal relaxation. The fits of the experimental data to the VFT equation are included (dashed lines), as well as the fitted fragility parameters: $D_{\eta}^* = 14.9$ for Vitreloy 101 and $D_{\eta}^* = 18.6$ for Vitreloy 105 [209].

In continuous heating experiments, the viscosity of the amorphous specimens was directly determined in the TMA at temperatures corresponding to equilibrium, i.e. in the supercooled liquid region after the completion of the glass transition at T_g . Figure 5.25 shows a superposition of the endothermic heat flow profile and the measured viscosity for $\text{Au}_{49.0}\text{Cu}_{26.9}\text{Si}_{16.3}\text{Ag}_{5.5}\text{Pd}_{2.3}$, as determined in constant heating DSC and TMA experiments, respectively. The DSC heat flow curve (Fig. 5.25, top) clearly shows the onset of the glass transition, T_g , at 400 K, followed by a supercooled liquid region of ~ 40 K. The beginning of the first crystallization event is marked by T_{x1} ; the onset of the crystallization peak splitting is given as T'_{x1} . While the exact temperature of the glass transition is not as readily identifiable from the TMA data as from the DSC, the viscosity of the beam was measured to decrease by almost two orders of magnitude in the temperature range from 390 to 400 K (Fig. 5.25, bottom). The beginning of the first crystallization event was identified from the DSC data at $T_{x1} = 455.2$ K. This is manifested by a gradual rise in the apparent viscosity by about one order of magnitude from 455 to 460 K. From 460 to 465 K, the measured viscosity begins to decrease, coinciding with the end of the first crystallization peak. From this it can be deduced

that, after completion of the first crystallization event, a new equilibrium is reached, consisting of crystals embedded in an amorphous matrix.

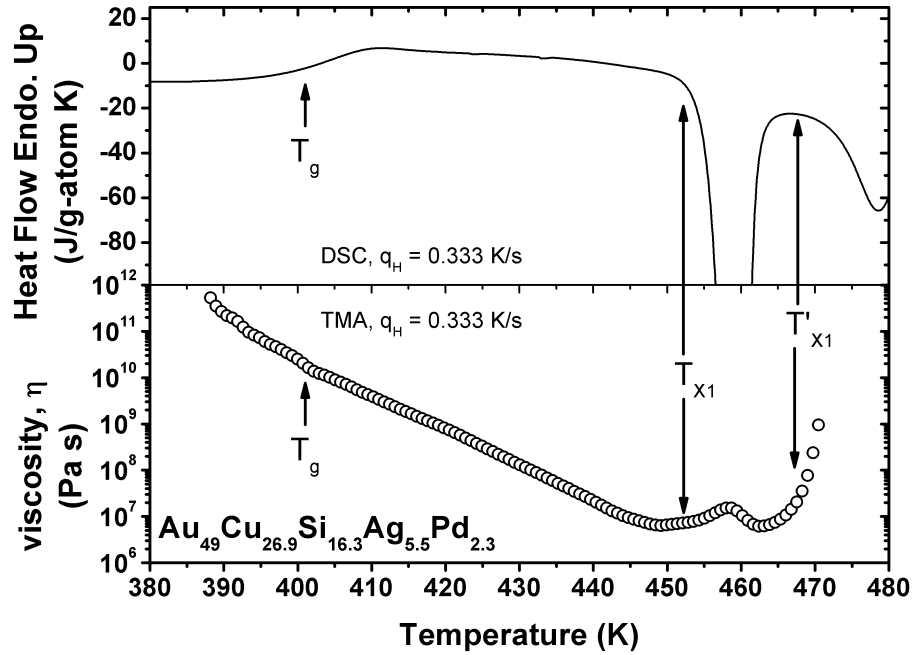


Figure 5.25: DSC heat flow profile (top) and viscosity measured in the TMA (bottom) in the vicinity of the glass transition for $\text{Au}_{49.0}\text{Cu}_{26.9}\text{Si}_{16.3}\text{Ag}_{5.5}\text{Pd}_{2.3}$ at a constant heating rate of 0.333 K s^{-1} .

As the temperature is increased, the remaining amorphous material will continue to become less and less viscous and the overall viscosity will be measured to decrease at $\sim 460 \text{ K}$. As the temperature is increased further, crystallization of most of the remaining amorphous matrix occurs, which is manifested by a sharp rise in the viscosity close to four orders of magnitude around 470 K . This appears as the onset of the split crystallization peak in the DSC curve at $T'_{x1} = 466.7 \text{ K}$ (see e.g. Fig. 5.21 and Table 5.2). Additional crystallization events were measured in the DSC at higher temperatures; however, no detectable change in the beam deflection was measured after 470 K . It can therefore be surmised that the volume fraction of the remaining amorphous matrix at these temperatures was too small as to effect any significant deflection of the beam.

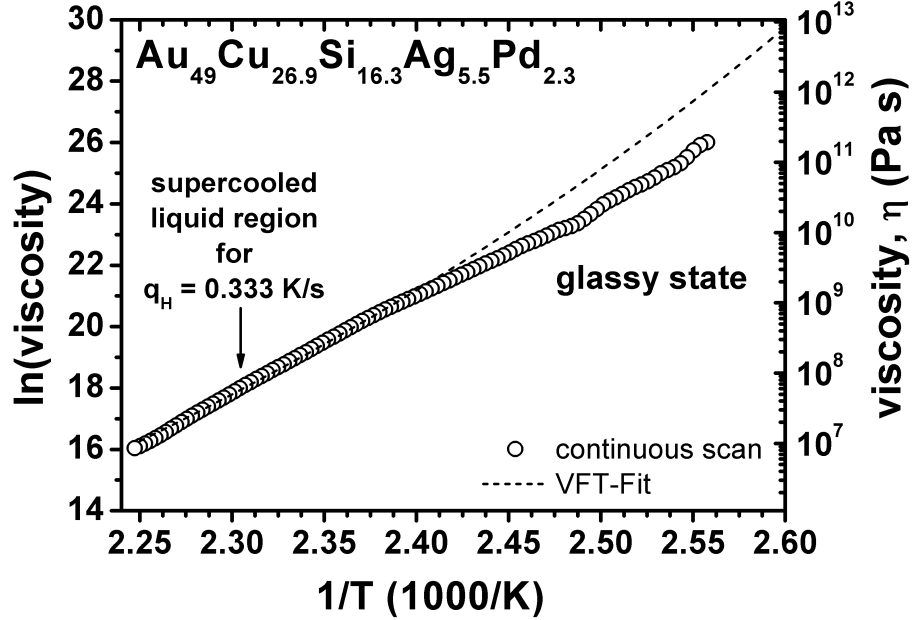


Figure 5.26: Apparent viscosities of $\text{Au}_{49.0}\text{Cu}_{26.9}\text{Si}_{16.3}\text{Ag}_{5.5}\text{Pd}_{2.3}$ as a function of inverse temperature determined with a constant heating rate of 0.333 K s^{-1} (open circles). A VFT fit to the data in the equilibrium liquid is shown with a fragility parameter, $D_{\eta}^* = 17.4$ (dashed line).

Figure 5.26 shows the results of a continuous heating viscosity measurement throughout the glass transition region for the $\text{Au}_{49.0}\text{Cu}_{26.9}\text{Si}_{16.3}\text{Ag}_{5.5}\text{Pd}_{2.3}$ BMG (open circles). A VFT-fit (Eq. 2.27) to the data corresponding to the supercooled liquid is included (dashed lines). The VFT parameters were determined here to be $D_{\eta}^* = 17.4$ and $T_0 = 267.6$. The plot in Fig. 5.27 shows the isothermal viscosity data (solid circles) taken from the Vitreloy 106a alloy as well as a continuous heating viscosity measurement (open circles). For the constant heating rate of 0.833 K s^{-1} the measured viscosity in the glassy state stays smaller than the equilibrium viscosity because of the frozen-in free volume - i.e. the isoconfigurational glassy state. As the sample is heated through the glass transition and into the supercooled liquid region, it leaves its isoconfigurational state and the measured viscosity corresponds to the equilibrium viscosity. A fit to Eq. 2.27 of both the equilibrium viscosities obtained from isothermal relaxation and continuous heating well describes both sets of data in this temperature range with a fragility parameter of $D_{\eta}^* = 21.7$.

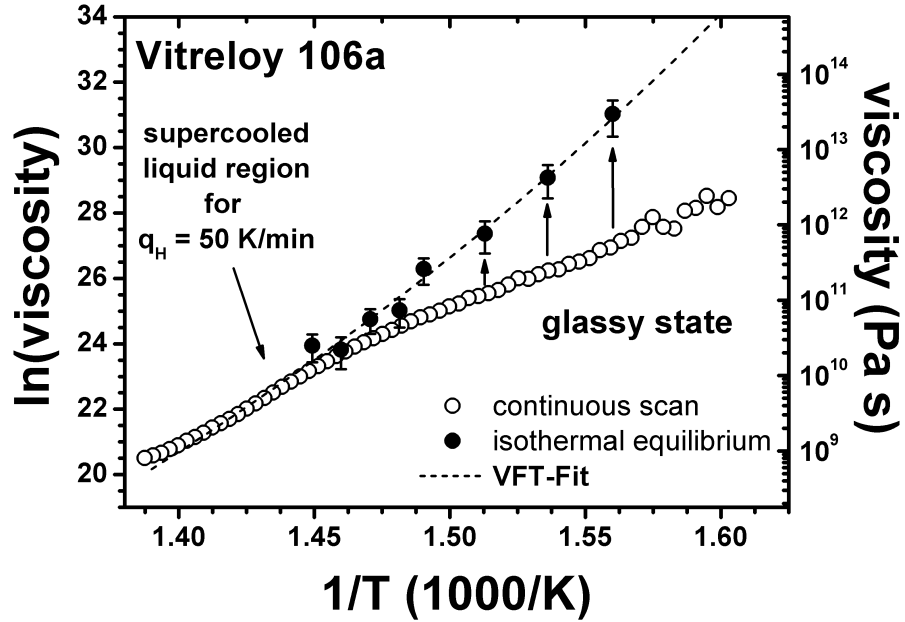


Figure 5.27: Equilibrium viscosities from isothermal relaxation experiments (closed circles) for Vitreloy 106a as a function of inverse temperature. Also shown is the measured viscosity determined with a constant heating rate of 0.833 K s^{-1} (open circles). A single VFT fit to both sets of data in the equilibrium liquid is shown with a fragility parameter, $D_\eta^* = 21.7$ (dashed line). The arrows indicate the initial isothermal relaxation pathways [208].

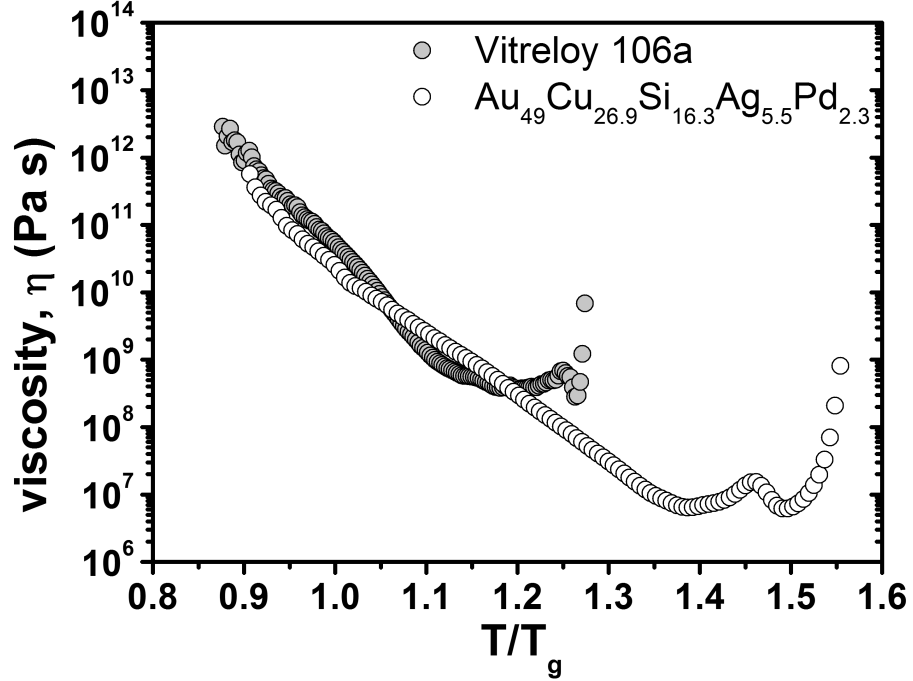


Figure 5.28: Comparison of viscosities measured in the TMA for Vitreloy 106a (shaded circles) and $\text{Au}_{49.0}\text{Cu}_{26.9}\text{Si}_{16.3}\text{Ag}_{5.5}\text{Pd}_{2.3}$ (open circles). The data are reproduced from Figs. 5.26 and 5.27.

Figure 5.28 gives a comparison the viscosities of Vitreloy 106a (shaded circles) and $\text{Au}_{49.0}\text{Cu}_{26.9}\text{Si}_{16.3}\text{Ag}_{5.5}\text{Pd}_{2.3}$ (open circles). The horizontal axis is normalized by T_g and the difference in the respective widths of each alloy's supercooled liquid region is clearly identified. Due to its greater stability of the supercooled liquid region, much lower equilibrium viscosities of $\text{Au}_{49.0}\text{Cu}_{26.9}\text{Si}_{16.3}\text{Ag}_{5.5}\text{Pd}_{2.3}$ are able to be obtained by heating above T_g . This especially large supercooled liquid region was previously unheard of in conventional metallic glass-forming alloys and is becoming of increasing interest in processing applications like blow molding or thermoplastic forming [44, 210].

5.4.1 Relationship between D_η^* and D_τ^*

In Table 5.3 the values of D_f^* and T_0 as reported in this work and from other research are shown for Vitreloy 106, 106a and $\text{Au}_{49.0}\text{Cu}_{26.9}\text{Si}_{16.3}\text{Ag}_{5.5}\text{Pd}_{2.3}$. These values were calculated either from measurement of the calorimetric relaxation time with DSC (Fig. 5.6) or from three-point beam-bending viscosity measurements using TMA (Fig. 5.23). Shown are the values of D_η^* , as well

5.4 Equilibrium viscosity

as D_τ^* calculated by using both T_g^{onset} and T_f' where $q_H = q_C$.

The agreement between the fitted values of D_τ^* and D_η^* shown in Table 5.3 for both alloys reveals that the heating rate dependence of T_g^{onset} where $q_H = q_C$, given by the value of D_τ^* , reflects to a good degree the temperature dependence of the viscosity in the supercooled liquid region, given by the value of D_η^* . These results are in accordance with earlier studies on the Vitreloy 1 BMG; namely, that the specific heat capacity and the viscosity both relax in the same temperature interval when heated with the same rate [162]. It had been established previously in work by Moynihan and others [73, 159, 163, 211, 212] that, for a number of oxide glasses, the activation energies for viscous flow and those determined from calorimetric experiments are virtually identical. It should therefore come as no great surprise that the fragility values (D_τ^* and D_η^*) determined for the above alloys are in good accord with each other.

Alloy	D_f^*	T_0 [K]	Measurement Method	Reference
Vitreloy 106	36.5	341.6	τ, T_g^{onset}	this work
...	36.3	343.3	τ, T_f'	this work
...	35.2	347.6	η - three-point beam-bending	this work
Vitreloy 106a	21.7	422.9	τ, T_g^{onset}	this work
...	22.1	420.9	τ, T_f'	this work
...	19.7	436.8	$\tau, T_g^{onset}(q_C = 1 \text{ K s}^{-1})$	[164]
...	21.0	424.3	η - three-point beam-bending	this work
Au_{49.0}Cu_{26.9}Si_{16.3}Ag_{5.5}Pd_{2.3}	16.0	250	η - parallel plate rheometry	[44]
...	19.0	not given	calculated from m -fragility, T_g^{onset}	[203]
...	17.4	267.6	η - three-point beam-bending	this work

Table 5.3: VFT fitting parameters of the alloys investigated here and in other research. The kinetic fragilities were determined by relaxation time and/or viscosity experiments and are compared here. The relaxation times, τ , were calculated using Eq. 5.1 from DSC experiments and were carried out using ($q_H = q_C$), unless otherwise indicated. There is a standard fitting error of approximately ± 2.5 associated with each value of D_f^* determined in this work.

In order to compare the degree of correspondence between the equilibrium viscosity, η (open squares), and calorimetric relaxation time, τ (shaded circles), the experimental data for Vitreloy 106 and 106a shown in Figs. 5.6 and 5.27 are reproduced in Fig. 5.29. Here, the values of η and τ are plotted in the same temperature range and a scaling of the vertical axes is determined,

such that the VFT-fits to each experimental data set are in agreement (solid curve).

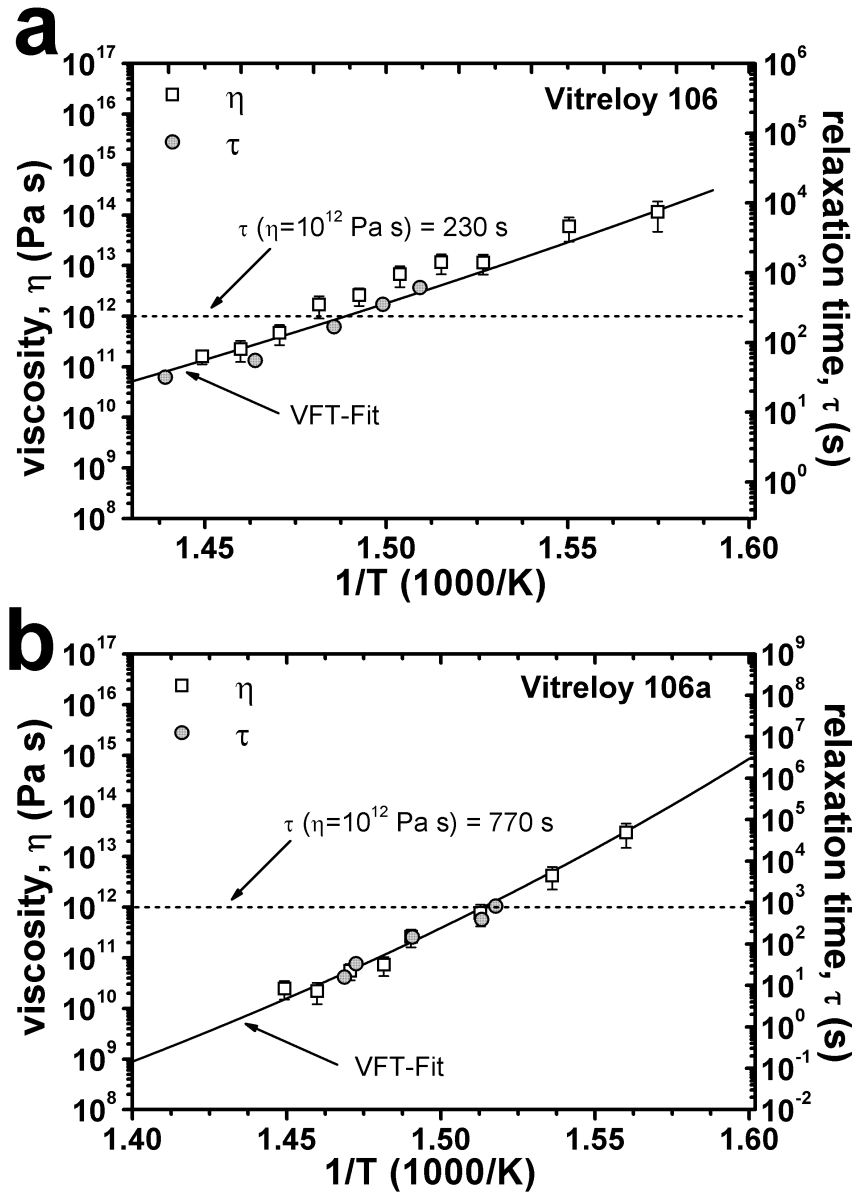


Figure 5.29: Values of the equilibrium viscosity, η (open squares) and calorimetric relaxation time, τ (shaded circles), for (a) Vitreloy 106 and (b) 106a. The scaling of the η (left axis) and τ (right axis) axes is chosen, such that the VFT-fits (solid curve) to each experimental data set are in agreement.

5.4 Equilibrium viscosity

As a common convention (suggested by Angell and others [23, 70, 160]), a value of the glass transition temperature, T_g^* , can be defined for any glass-former as the temperature where the equilibrium viscosity has a value of 10^{12} Pa s or where the structural relaxation time is on the order of 10^2 s (Angell [23] suggests more specifically 200 s). However, it should be addressed here that the use of τ in these analyses, as defined by Eq. 5.1, reflects a different "relaxation" than what was originally discussed by Angell and others. It is important to point out that the structural relaxation time of a glass-former corresponds to the characteristic time needed for the liquid to return to equilibrium after an instantaneous perturbation in temperature (see Sec. 2.4). For many polymeric and organic glass-formers, this can be probed in the frequency domain through dielectric relaxation experiments [174]. For glasses in general, however, a whole branch of phenomenology has developed around quantifying structural relaxation through calorimetric methods, i.e. in the temperature domain, most notably by using DSC up-scans [73, 159, 211, 212]. Since the value of τ in Eq. 5.1 is simply the total time of the calorimetric glass transition interval, as measured at a given heating rate, it becomes of interest whether or not this can accurately be used to quantify the structural relaxation process.

From the data presented in Fig. 5.29, it can be seen that a value of $\eta = 10^{12}$ Pa s corresponds to a τ of 230 and 700 s for Vitreloy 106 and 106a, respectively (dashed line). Here, the scaling of the equilibrium viscosity at 10^{12} Pa s apparently fits well for Vitreloy 106 at a corresponding calorimetric relaxation time of ~ 200 s. This value is somewhat higher for the more fragile Vitreloy 106a, and is more in line with some of the fragile molecular liquids mentioned in Ref. [49] where it was suggested that a more appropriate scaling viscosity be $\sim 10^{11}$ Pa s. However, it should be pointed out that the scaling of the vertical axes in Fig. 5.29 was performed according to matching of the VFT fitting parameters (D^* and T_0), which were themselves subject to inherent fitting error. Therefore, the uncertainty involved in the accuracy of the VFT-fit has to be taken into consideration when determining the corresponding value of τ for any given η -value. For example, the fitting error in the D^* -values determined for Vitreloy 106 and 106a is ± 2.5 . Taking this into consideration, it can be seen that the uncertainty in the value of τ for $\eta = 10^{12}$ Pa s is around ± 300 s.

These results are interesting, in that they show that – within experimental error – the convention of taking the total time of the calorimetric glass transition interval; i.e., τ from Eq. 5.1 on p. 76, as reflecting an intrinsic structural relaxation time, is apparently in accordance with the expectation that the structural relaxation time at T_g is on the order of 10^2 s [23, 70, 160]. As dis-

cussed earlier, in the DSC up-scan, the heating (or cooling) rate dependence of T_g is used as a measure of the activation energy for the structural relaxation time and is related to the fragility. Since τ is inversely proportional to the heating (or cooling) rate, it is expected that the fragilities as quantified by D_τ^* and m are similar. Given the evidence presented here, it also appears that the structural relaxation from the glassy state to the supercooled liquid region, as observed during constant heating in the DSC, can be reasonably quantified by the total calorimetric relaxation time defined in Eq. 5.1. That is, the value of τ is measured to be on the order of 10^2 s around the same temperature where the viscosity of the equilibrium liquid has a value of 10^{12} Pa s.

However, one should proceed with caution in interpreting these values of τ as anything other than an average calorimetric relaxation time for the glass transition interval, especially in temperature ranges far outside of that which is accessible in the DSC.

A value for the characteristic relaxation time for the glass transition can also be taken from the Maxwell relation, shown in Eq. 2.22 on p. 17. Following the convention of taking T_g^* at $\eta = 10^{12}$ Pa s in the supercooled liquid region, and an instantaneous, high-frequency shear modulus of $G_\infty \sim 10^9 - 10^{10}$ Pa (see Refs. [45, 46]), one can arrive at a characteristic relaxation time $\sim 10^2 - 10^3$ s. A recent study on a glassy Pd-Cu-Ni-P alloy shows that the characteristic Maxwell shear relaxation time at T_g^* , calculated from independent measurements of G_∞ and η , is on the order of 10^3 s [213]. These results further support the remarks by Angell [49] that the universality of the characteristic values for viscosity and relaxation time at the glass transition does not necessarily apply to all glass-formers.

5.4.2 Free volume and configurational entropy models

In Sec. 2.5.1, the free volume and configurational entropy models of the equilibrium viscosity were introduced. Here, the equilibrium viscosity of the Vitreloy 1b BMG alloy is analyzed using each of the models described in Sec. 2.5.1. More specifically, the behavior of the fitted curves of the equilibrium viscosity is analyzed in the temperature range up to T_{liq} using the free volume models of Cohen and Turnbull [58] and Cohen and Grest [66]. Additionally, the configurational entropy model of Adam-Gibbs [67] is used to describe the equilibrium viscosity and an attempt is shown to relate this to the free volume.

In the Adam-Gibbs equation for the equilibrium viscosity (Eq. 2.34 on p. 26), the quantity $S_c(T)$ is the configurational entropy of the equilibrium liquid as

5.4 Equilibrium viscosity

a function of temperature. $S_c(T)$ is that part of the total entropy, $S(T)$, that derives from all the possible sets of distinct atomic packing configurations or states available to the liquid at a temperature, T [214]. Goldstein and Stillinger refer to this as a *potential energy landscape*, the minima of which correspond to inherent structures available the system at a certain temperature [215–217].

Since $S_c(T)$ cannot be measured directly, it was common to approximate this simply as the excess entropy of the undercooled liquid over that of the crystal, $\Delta S^{l-x}(T)$; however, this has been shown in many cases to be a poor approximation [15, 92, 214, 218, 219]. Recently, it was proposed by Gallino et al. [91] that $S_c(T)$ can be approximated by assuming the same rate of decrease during undercooling as $\Delta S^{l-x}(T)$ from a fixed value of $S_c(T_m^*)$ as

$$S_c(T) = S_c(T_m^*) - \int_T^{T_m^*} \frac{\Delta C_p^{l-x}(T')}{T'} dT'. \quad (5.12)$$

This differs from many earlier approximations, in that it uses as a constant of integration not the entropy of fusion, ΔS_f , but $S_c(T_m^*)$, which is left as a fitting parameter and corresponds to a property exclusive to the liquid phase, defined arbitrarily for a fixed viscosity value of 1 Pa s. Similarly, the temperature T_m^* is the temperature in the melt where the viscosity is assumed or measured to be 1 Pa s. By using the analytical expressions for $C_p^l(T)$ and $C_p^x(T)$ given in Eqs. 5.4 and 5.5, and an approximation or measured value for T_m^* , $S_c(T)$ can be determined though fitting of the experimental viscosity data, with C and $S_c(T_m^*)$ left as fit parameters. It is assumed in the expression in Eq. 5.12 that the vibrational contribution to the total entropy of the undercooled liquid changes with approximately the same rate as the vibrational entropy of the crystal [91].

By comparing Eqs. 2.30 (p. 24) and 2.34 (p. 26) it is now possible to express the relative free volume of the equilibrium liquid in terms of its configurational entropy as

$$\frac{v_f}{v_m} = \frac{bTS_c(T)}{C}. \quad (5.13)$$

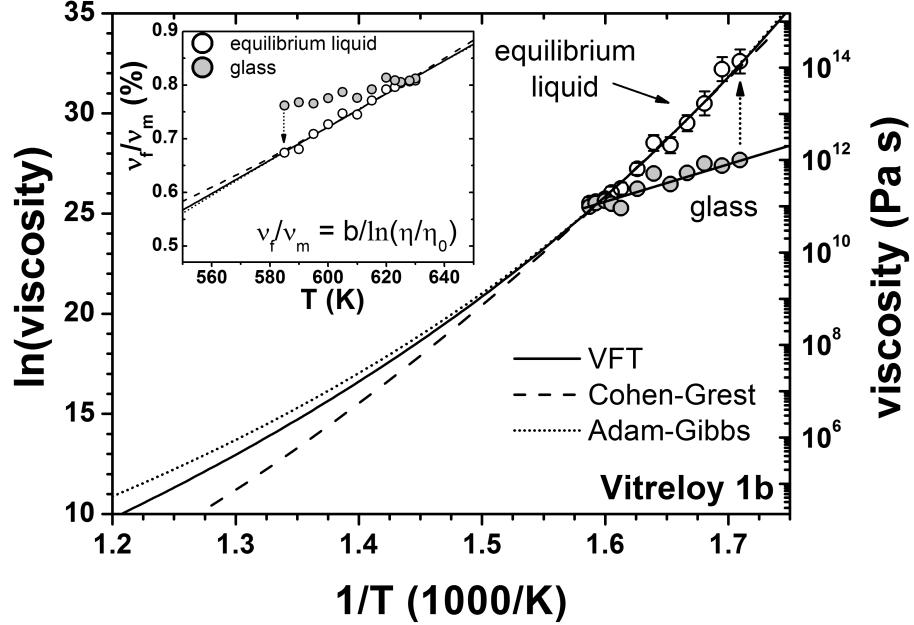


Figure 5.30: Equilibrium viscosities (open circles), as well as the viscosities of the glass immediately prior to relaxation (shaded circles) as a function of inverse temperature for the Vitreloy 1b alloy. The fits to the experimental data using Eq. 2.30 are shown as the solid, dashed and dotted lines, incorporating the expression for the relative free volume given in Eqs. 2.31, 2.33 and 5.13, respectively. Using Eq. 2.30 (inset), the relative free volumes are determined from the experimental viscosity data for the equilibrium and glassy states (see inset; open and shaded circles, respectively). The curves shown in the inset are the relative free volumes calculated from the fits shown in the main figure. The dotted arrows schematically show the path of relaxation into a more viscous amorphous state with lower free volume [177].

The equilibrium viscosity data for Vitreloy 1b (open circles) are shown in Fig. 5.30 along with the viscosities of the glassy alloy immediately before relaxation (shaded circles). A non-linear fit of the VFT-equation (Eq. 2.27) was performed to the equilibrium data (solid line), giving the fragility parameter, $D^* = 25.4$ and the VFT-temperature, $T_0 = 366.6$ K. Recall that the VFT-equation is equivalent to the Doolittle equation (Eq. 2.30) assuming the Cohen and Turnbull expression of the free volume (Eq. 2.32), as was shown on p. 25.

Additionally, a fit of the Eq. 2.30 incorporating the expression for the free volume according to Cohen and Grest (Eq. 2.33 on p. 25) was performed (dashed line), giving the fit parameters $bv_m\zeta_0k^{-1} = 5000.6$ K, $T_q = 666.6$ K and $4v_a\zeta_0k^{-1} = 160.7$ K. The b -parameter from Eq. 2.30 was calculated for

Vitreloy 1b as 0.288 using the relationship in Eq. 2.32 on p. 25, where the value of α_{liq} was taken to be the same as that for Vitreloy 1 [107]. Finally, a fit of the equilibrium viscosity data to the Adam-Gibbs equation (Eq. 2.34) is also shown (dotted line), resulting in the fit parameters $C = 320.17$ kJ g-atom⁻¹ (3.31 eV) and $S_c(T_m^*) = 18.27$ J g-atom⁻¹ K⁻¹. The configurational entropy of the Vitreloy 1b liquid, as calculated using Eq. 5.12, is shown in Fig. 5.31.

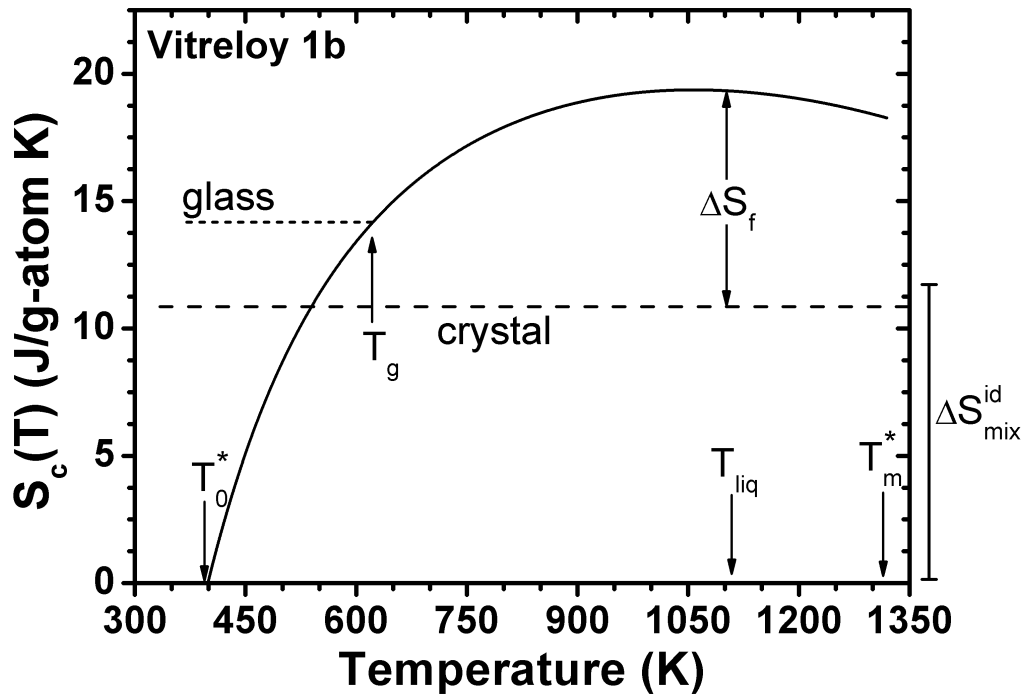


Figure 5.31: Configurational entropy as a function of temperature, $S_c(T)$, of the Vitreloy 1b undercooled liquid. Indicated here are the temperatures T_m^* , T_{liq} , T_g and T_0^* , which correspond to the temperature where the melt has a viscosity of 1 Pa s, the liquidus temperature, the glass transition temperature and the temperature where $S_c(T) = 0$, respectively.

At this point, it is worth noting that the value of $S_c(T_m^*)$ calculated here is significantly larger than the ideal entropy of mixing, ΔS_{mix}^{id} , calculated using

$$\Delta S_{mix}^{id} = -R \sum (X_i \ln X_i), \quad (5.14)$$

where R is the gas constant and X_i is the gram-atomic fraction of each individual atomic species [27]. It should also be pointed out that, in the above expression, only the random mixing of the atomic constituents is considered. That is, the ideal entropy of mixing, ΔS_{mix}^{id} , is the same for the solid, liquid and even gaseous phases of the system in question.

For Vitreloy 1b, $\Delta S_{mix}^{id} = 11.73 \text{ J g-atom}^{-1} \text{ K}^{-1}$. That $S_c(T_m^*) > \Delta S_{mix}^{id}$ implies the existence of a considerable amount of excess entropy, beyond that of the ideal mixture, present in the melt at T_m^* [91]. Furthermore, the fitted value of $S_c(T_m^*)$ is larger than the measured value for the entropy of fusion, $\Delta S_f = 8.44 \text{ J g-atom}^{-1} \text{ K}^{-1}$. However, considering that $S_c(T_m^*)$ was chosen at a temperature value significantly higher than the liquidus temperature, and that ΔS_f represents the entropy difference between the melt and a conceivably high-entropy crystalline state, the result that $S_c(T_m^*) > \Delta S_f$ is not unexpected. In fact, it was shown in previous research on the $\text{Mg}_{65}\text{Cu}_{25}\text{Y}_{10}$ BMG-forming liquid that a fit of the Adam-Gibbs equation to the experimental viscosity data was in excellent agreement with that of the VFT-equation if the configurational entropy of the melt was assumed to be greater than the entropy of fusion [42].

At low temperatures the free volume of the equilibrium liquid according to the model of Cohen and Turnbull vanishes at $T_0 = 366.6 \text{ K}$, while in the model proposed by Cohen and Grest the free volume decreases to zero only at $T = 0$, as discussed in the Sec. 2.5.1. In the model for the equilibrium free volume from the Adam-Gibbs equation for viscous flow (Eqs. 2.34 and 5.13), v_f/v_m vanishes for this alloy at a temperature of $T_0^* = 400 \text{ K}$, where T_0^* is defined in Ref. [91] as the temperature at which the configurational entropy, $S_c(T)$, vanishes in the Adam-Gibbs fit of the equilibrium viscosity data. The similarity between T_0 and T_0^* suggests the existence of a state in the equilibrium liquid at $T > 0$ with a single possible configuration; i.e., an ideal packing state, where the barriers with respect to viscous flow become infinitely large. Additionally, the value of C for this alloy of $320.17 \text{ kJ g-atom}^{-1}$ is found to be in very good agreement with the thermodynamic fragility analysis performed in Ref. [91]. That is, for Zr-based BMG systems, C compares well with the activation energy for diffusion of larger atomic species measured around the glass transition ($\sim 300 \text{ kJ g-atom}^{-1}$ [220]), indicating their crucial involvement in the cooperative rearrangements necessary for flow.

To investigate the predictive ability of each free volume model into a higher temperature range; i.e., above the melting temperature, the free volume and viscous flow for Vitreloy 1 as reported in Ref. [15] is re-visited. Equilibrium viscosity studies in the vicinity of the glass transition using a three-point

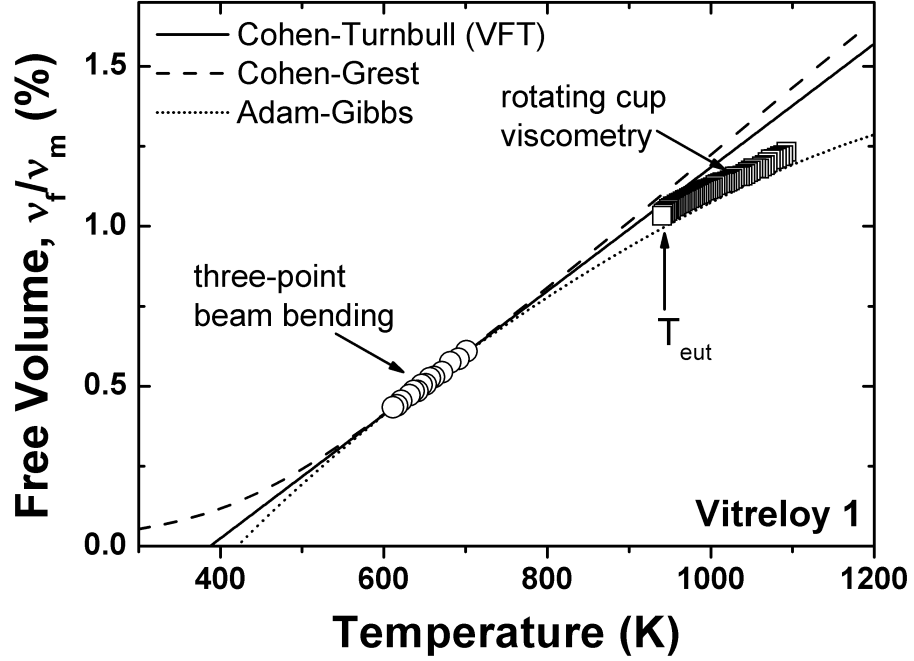


Figure 5.32: Relative free volumes of Vitreloy 1 calculated from experimental viscosity data taken in the vicinity of the glass transition (open circles) [14] and in the liquidus region (open squares) [123]. Fits of the Cohen-Turnbull (solid line), Cohen-Grest (dashed line) and Adam-Gibbs (dotted line) free volume models are shown considering only the low temperature data (open circles) [177].

beam-bending method have been performed on this particular composition [14], as well as rotating cup viscometry at temperatures into the liquid state [123]. In Fig. 5.32 the relative free volume curves for the Vitreloy 1 alloy are shown as a function of temperature, along with the experimental viscosity data taken from Refs. [14] and [123] expressed as relative free volume, in the vicinity of the glass transition (open circles) and above T_{eut} (open squares). It should be noted that Ref. [123] reports a fragile-to-strong transition for this alloy for temperatures above 1225 K, therefore only viscosity data representing the liquid state before this transition; i.e., data that represent only the kinetically strong state, were examined.

Only the low temperature viscosity data taken from three-point beam-bending experiments were considered during fitting and used to construct the relative free volume curves, similar to Fig. 5.30. By considering only the low temperature data, the fit parameters from Eqs. 2.30 (p. 24) and 2.33 (p. 25) were determined to be $bv_m\zeta_0k^{-1} = 7675.4$ K, $T_q = 453.6$ K and $4v_a\zeta_0k^{-1} = 59.9$ K, with the parameter b calculated as 0.164. This value is almost twice as

5.4 Equilibrium viscosity

much as that determined for Vitreloy 1b ($b = 0.288$), and is the result of the differences in fragility parameter, D^* , VFT-temperature, T_0 , and volumetric thermal expansion coefficient of the glassy state, α_{glass} , between these two compositions (refer to Eq. 2.32).

Non-linear fitting of Eqs. 2.27 and 2.34 was already performed for this alloy in Ref. [91], and the parameters D^* , T_0 , C and $S_c(T_m^*)$ determined to be 22.0, 387 K, 295.11 kJ g-atom⁻¹ and 19.07 J g-atom⁻¹ K⁻¹, respectively. The relative free volume curves calculated using the Cohen-Turnbull, Cohen-Grest and Adam-Gibbs models are shown as the solid, dashed and dotted lines in Fig. 5.32, respectively.

The Adam-Gibbs model of the relative free volume (dotted line) from Eq. 5.13 shows good agreement with the experimental data corresponding to the liquid state at high temperatures (open squares), even though these data were not considered for fitting. The low free volume at temperatures above the melting point is directly related to the high melt viscosity of this alloy (~ 100 Pa s), which is thought to be due to pronounced short- and medium-range order in the liquid [123]. The good predictive ability of the Adam-Gibbs model in this case lies in its dependence on the configurational entropy. This further supports a thermodynamic interpretation of the viscous behavior observed in glass-forming systems.

The entropy functions of Vitreloy 1b and Au_{49.0}Cu_{26.9}Si_{16.3}Ag_{5.5}Pd_{2.3}, $\Delta S^{l-x}(T)$, are shown in Fig. 5.14. For each alloy, the isentropic temperature, T_K , is determined to be significantly higher (~ 100 K) than the VFT-temperature, T_0 . In fact, this is the case for all BMG-forming systems investigated here (see Appendix A) and was affirmed for a number of other BMGs and non-metallic glass-formers as well [221, 222]. This gives good evidence that, at least in these multicomponent BMG-forming liquids, considerable configurational entropy must exist in the underlying crystalline state [42, 91]. That is, it appears that the undercooled liquid could still theoretically exist at temperatures below T_K , with an entropy smaller than that of the crystal. The absolute lowest temperature for glass formation, in this case, would then be the VFT-temperature, T_0 ; i.e., the temperature of vanishing free volume in the Cohen-Turnbull model [58]. It is interesting to note that, for the Vitreloy 1b alloy, it definitely appears to be the case that the excess configurational entropy over that of the entropy of fusion, ΔS_f , at T_{liq} , is roughly equal to the ideal entropy of mixing, ΔS_{mix}^{id} . This is illustrated by the horizontal dashed line in Fig. 5.31, showing the configurational entropy of the liquid, as calculated using Eq. 5.12. Assuming that the entropy of fusion mainly represents the change in configurational entropy between the liquid and crystalline states

at T_{liq} ¹, it can be inferred from these results that significant configurational entropy must already exist in the crystalline state of this alloy, which appears to approximately be equal to the ideal entropy of mixing. This is the case with so-called "high entropy alloys"; i.e., multicomponent crystalline alloys with near equimolar compositions that are intentionally designed to have a high ideal entropy of mixing [224–227].

Interestingly enough, T_0 agrees well (within ~ 35 K) with the value of T_0^* that was determined here for Vitreloy 1b (Sec. 5.4.2) and for a number of other BMG-formers as well (see Ref. [91]). Recalling that T_0^* was determined to be the temperature where the configurational entropy of the equilibrium liquid vanishes in the Adam-Gibbs fit of the equilibrium viscosity data, this suggests a link between the kinetics and thermodynamics of viscous flow. Furthermore, the similarity of T_0 and T_0^* establishes a consistency between the free volume and configurational entropy pictures of these liquids, in that the state of vanishing free volume occurs at approximately the same temperature as that of zero configurational entropy. In other words, the temperature of optimal liquid packing is equivalent to the temperature where no further configurations are available to the liquid, leading to a divergence in the viscosity. This effectively dismisses the generality that T_K must be lowest bound for the glass transition. However, this case is easily idealized for a one component system, where $T_K = T_0$, since there is no contribution of the entropy of mixing with the exception of a small contribution due to vacancies in the crystal [91].

5.5 Enthalpy and free volume

Van den Beukel and Sietsma proposed a method for quantifying the free volume in terms of enthalpy as measured using DSC [121]. This method has since been employed by several researchers, using enthalpy relaxation to examine the free volume of BMGs at temperatures below the glass transition [228–236].

In Ref. [121], a linear relationship between enthalpy and free volume is assumed to have the form

$$\Delta H = \beta' \frac{\Delta v_f}{v_m}, \quad (5.15)$$

¹Spaepen estimates the vibrational component, ΔS_{vib} , as $\sim 0.2R$ for an ideal hard sphere liquid metal [223].

where ΔH is the change in enthalpy due to the change in relative free volume, $\Delta v_f/v_m$. The proportionality constant β' therefore has the same units of enthalpy, kJ g-atom⁻¹. In the research cited in the previous paragraph, the constant β' was determined for the glassy state (this will be discussed further in Chapter 6), showing a perfectly linear relationship between the reduction in enthalpy and reduction in excess free volume. This linearity suggests a similar relationship between the equilibrium curves for enthalpy and relative free volume – ΔH^{l-x} and v_f/v_m , respectively.

This relationship is investigated for Vitreloy 1b, where v_m is taken here as the atomic volume at the liquidus temperature, 1.67×10^{-29} m³, and was previously determined for another BMG alloy with a very similar composition (Vitreloy 1) [107]. Indeed, by matching these curves, as shown in Fig. 5.33, it is seen that all three models of v_f/v_m discussed in Sec. 5.4 agree very well with the ΔH^{l-x} curve in the vicinity of the glass transition. In this temperature range the free volume and enthalpy curves appear to be linear. Within this linear regime, the value of β' for the equilibrium liquid can be estimated by $\beta'_{eq} \approx \Delta(\Delta H^{l-x})/\Delta(v_f/v_m)$ where $\Delta(\Delta H^{l-x}) = \Delta H^{l-x}(T_1) - \Delta H^{l-x}(T_2)$ and $\Delta(v_f/v_m) = v_f(T_1)/v_m - v_f(T_2)/v_m$; T_1 and T_2 mark the temperature range in which ΔH^{l-x} and v_f/v_m behave linearly (550 - 650 K). The value of β'_{eq} is estimated to be ~ 680 kJ g-atom⁻¹ (~ 7 eV).

The value of β'_{eq} reported here corresponds to the enthalpy necessary for the formation of an amount of free volume in the equilibrium liquid equal to v_m . However, flow processes in liquids usually require critical volumes that are only a fraction of v_m . Indeed, Cohen and Turnbull report the value for the critical volume to be around $0.8v_m$ for Van der Waals liquids and closer to $0.1v_m$ for pure metals [58]. In light of this, the calculated b -value of 0.288 for this alloy (see Eq. 2.32) in its undercooled state is found to be physically acceptable. Furthermore, if instead the reduced free volume, $x = v_f/(bv_m)$, is considered – thus taking into account only the critical volume necessary for flow – a reduced enthalpy of formation for free volume, $\beta_{eq} \approx \Delta(\Delta H^{l-x})/\Delta x$, of ~ 200 kJ g-atom⁻¹ (~ 2 eV) is found for the deeply undercooled equilibrium liquid from 550 to 650 K.

In Eq. 5.15 it is assumed that the enthalpy of formation for free volume remains constant with temperature. While experimental evidence indicates that this is indeed the case for the glassy state [228–236], in the equilibrium liquid, however, this formation enthalpy can be approximated as constant only in those temperature ranges where the enthalpy and free volume functions of the equilibrium liquid behave linearly - e.g. in the glass transition region in Fig. 5.33. That is, the slope of the enthalpy curve with respect to the slopes

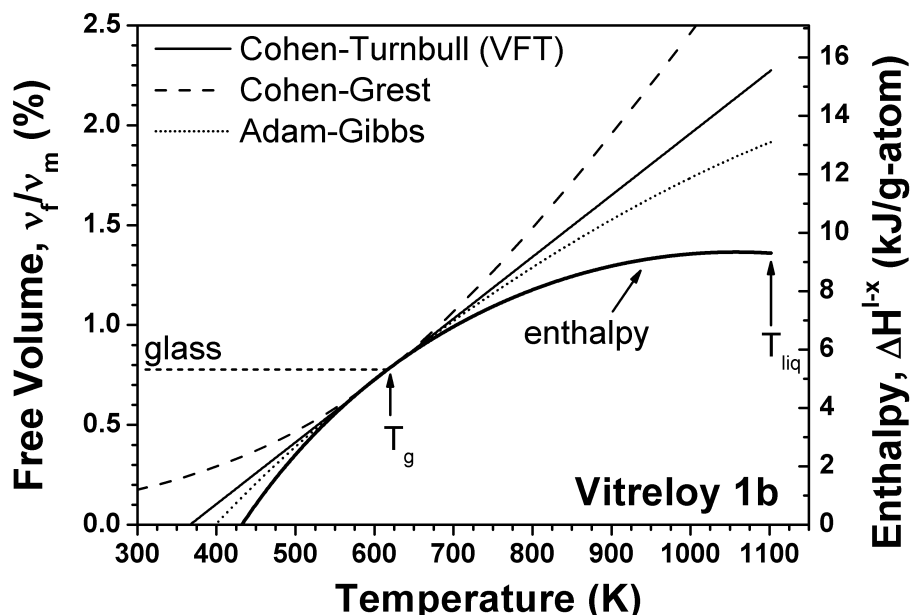


Figure 5.33: Relative free volume curves of the equilibrium liquid of Vitreloy 1b according to the models of Cohen and Turnbull, Cohen and Grest, and Adam-Gibbs (solid, dashed and dotted lines, respectively). The thick, solid line is the enthalpy difference between the liquid and crystalline states, ΔH^{l-x} , calculated from the ΔC_p^{l-x} curve and the experimentally determined value of ΔH_f . The glassy state is shown schematically by the heavy dotted line [177].

of the free volume curves remains constant throughout a given temperature range in the equilibrium liquid. In order to analyze the exact behavior of the free volume formation enthalpy over the entire temperature range of the equilibrium liquid, it is necessary to determine the instantaneous change in the slopes of the enthalpy and free volume functions.

In Fig. 5.34, the reduced enthalpy of free volume formation as the change in $\Delta H^{l-x}(T)$ with respect to the change in the reduced free volume, $x(T)$, or $\beta_{eq} = d(\Delta H^{l-x})/dx$, is calculated. Figure 5.34 shows the calculated values of β_{eq} for each of the free volume models considered here in the temperature range from the VFT-temperature, T_0 , to the melting temperature, T_{eut} . The experimental equilibrium viscosity data were taken in the vicinity of T_g and used in each free volume model; as such, the intersection of these curves at T_g is a result of that fact. In each model for β_{eq} shown in Fig. 5.34, the value increases as the temperature decreases from T_{eut} to T_0 . This is primarily a reflection of the increasing slope of the ΔH^{l-x} -curve as the liquid is undercooled below its melting point (refer to the C_p^l curve in Fig. 5.11).

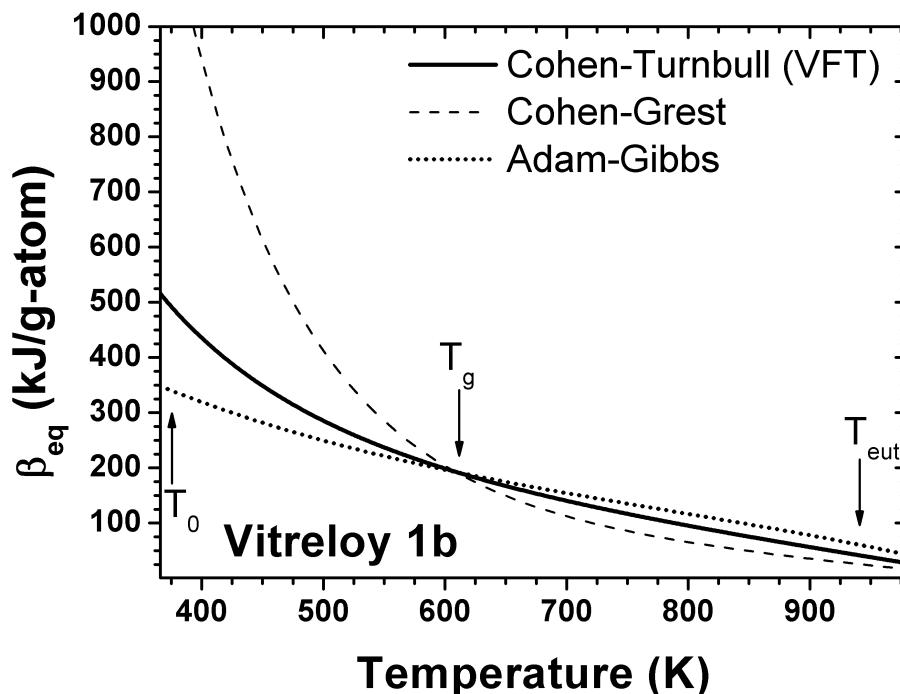


Figure 5.34: Reduced free volume formation enthalpy, β_{eq} , calculated using $\beta_{eq} = d(\Delta H^{l-x})/dx$, where $x(T)$ is the reduced free volume of the equilibrium liquid according to the free volume models given in Eqs. 2.31, 2.33 and 5.13. The solid, dashed and dotted lines represent β_{eq} calculated according to each free volume model. The temperatures indicated are the VFT-temperature, T_0 ; the glass transition temperature, T_g ; and the melting temperature, T_{eut} [177].

According to these estimations the reduced enthalpy of free volume formation in the equilibrium liquid increases from about $100 \text{ kJ g-atom}^{-1}$ ($\sim 1 \text{ eV}$) at the melting point to about $200 \text{ kJ g-atom}^{-1}$ ($\sim 2 \text{ eV}$) around T_g .

At temperatures between T_{eut} and T_g , the values of β_{eq} determined from each model are similar and comparable to experimentally determined activation enthalpies in other melts of the Zr-Ti-Cu-Ni-Be system. The activation enthalpy for diffusion of small atoms, such as beryllium, was measured to be around 1.9 eV in the undercooled liquid from $\sim 700 - 625 \text{ K}$ [237]. Similarly, in the Vitreloy 1 melt, the activation enthalpy for diffusion of the medium-sized atoms, such as nickel, was reported as 2.1 eV around T_{liq} [19]. Although the determined values for β_{eq} shown in Fig. 5.34 are somewhat lower near T_{eut} ($\sim 1 \text{ eV}$) than the activation enthalpies reported in the diffusion studies ($\sim 2 \text{ eV}$), they are not physically unreasonable and are in agreement with the hypothesis that simple diffusion governs viscous flow at high temperatures.

Below T_g , distinctions in how each model predicts the free volume change with decreasing temperature are clearly noticed. β_{eq} calculated in the Cohen and Grest model (dashed line in Fig. 5.34) increases dramatically below T_g , due to the decreasing free volume change in the liquid as the temperature is lowered. In this model, as the liquid is supercooled further below T_g , its free volume changes much less in comparison with the change in its enthalpy (see Fig. 5.33). This leads to the observed increase in β_{eq} . Mathematically, this is the result of the requirement that, in the Cohen and Grest model, $v_f > 0$ for all $T > 0$. This leads to an apparent divergence in β_{eq} for very low temperatures near T_0 .

Similar behavior of β_{eq} , though not as pronounced, is noticed in both the Cohen and Turnbull and Adam-Gibbs models (solid and dotted lines, respectively, in Fig. 5.34). As T_0 is approached in the deeply supercooled liquid, the values of β_{eq} in these cases remain well defined. At this temperature, however, the viscosity is expected to diverge. In the Cohen and Turnbull model, the viscous divergence is a result of vanishing free volume, while, in the Adam-Gibbs picture, this is due to the vanishing of the configurational entropy. One would naturally expect that, as T_0 is approached, the barriers to viscous flow would become larger and larger, thus increasing the formation enthalpy required for free volume. However, the formation enthalpies determined using the Adam-Gibbs and Cohen and Turnbull models are around 300 - 500 kJ g-atom⁻¹ ($\sim 3 - 5$ eV) near T_0 , which are not relatively large, considering that the apparent activation enthalpies for viscous flow around T_g for glass-formers with similar fragility as Vitreloy 1b are ~ 400 kJ g-atom⁻¹ (~ 4 eV) [212]. While the Cohen and Grest treatment appears to give a more reasonable behavior of β_{eq} at temperatures close to T_0 , it does not assume a dynamic divergence in the supercooled liquid, which is predicted by both the Cohen and Turnbull and Adam-Gibbs models.

5.6 Summary and Conclusions

In this chapter a fairly broad look at the kinetic and thermodynamic phenomenology of just a few BMG compositions was given. However, the cases analyzed here are not always representative of BMGs or metallic glasses in general. The alloys chosen for investigation here are among some of the best BMG-formers and have a relatively high thermal stability, i.e. resistance to crystallization, in their supercooled liquid regions. This makes it possible to heat and cool from the supercooled liquid region with a wide range of rates, while at the same time avoiding the onset or significant growth of crystals.

5.6 Summary and Conclusions

This is necessary for an accurate determination of the fictive temperature (or alternatively, T_g^{onset}) and by extension, the kinetic fragility using DSC. A high thermal stability also allows for a wider range of viscosities to be measured in the supercooled liquid (see e.g. Fig. 5.28) and also leads to greater accuracy in the determination of D_η^* . Of course, there exist many marginal glass-formers, as well as BMGs with poor thermal stabilities, in which the supercooled liquid region above T_g is practically nonexistent. Hence, any fragility analysis of such glass-formers should be interpreted with caution, as the high tendency for crystallization of the sample can no doubt lead to misleading results.

It was shown in this chapter that the thermodynamic functions of the equilibrium liquid can be calculated for a wide temperature range using experimentally determined C_p data from liquid and crystalline samples. In the case of enthalpy, there is good agreement with the independently obtained values of ΔH_x near T_g and T_{liq} and the calculated ΔH^{l-x} -curve for the $\text{Au}_{49.0}\text{Cu}_{26.9}\text{Si}_{16.3}\text{Ag}_{5.5}\text{Pd}_{2.3}$ alloy, affirming the consistency of the employed thermodynamic description of these undercooled liquids. From the calculated ΔS^{l-x} -curve, a picture of the entropy of the undercooled liquid emerges, showing values of T_K that are significantly higher than T_0 and T_0^* . This indicates the existence of a considerable amount of entropy that is present in the multicomponent crystalline mixture and that, in a highly short or medium-range ordered undercooled liquid (see Sec. 3.2), the entropy can, in fact, become lower than that of the crystal.

A look at the driving force for crystallization (Sec. 5.2.4), as approximated by $\Delta G^{l-x}(T)$ near T_{liq} , shows that the factors affecting the GFA are more complex than what simple thermodynamic considerations assume. Even taking into account kinetic factors, e.g. fragility, may not fully provide a satisfactory explanation of the GFA of certain metallic melts. In these cases, one must consider other factors, such as the B_2O_3 processing method, which is used to passivate melt impurities, or the liquid-crystal interfacial energy, which can act as a stabilizing factor by increasing the nucleation barrier.

The viscosity of the supercooled liquid region was directly determined at temperatures below T_g by isothermal annealing, as well as by heating with a constant rate to temperatures above the glass transition in the three-point beam-bending experimental apparatus. In this region the viscosity is equal to that of the equilibrium liquid. It was shown that a single VFT-fit best describes the data measured in the supercooled liquid region as well as those taken below T_g after proper equilibration (see Fig. 5.27). It was found that a calorimetric determination of the kinetic fragility (Sec. 5.1) is equivalent to the fragility determined from equilibrium viscosity data in three different

5.6 Summary and Conclusions

BMG-forming compositions (see Table 5.3). These results are in agreement with those previously published for oxide glass systems, as well as other BMGs [73, 159, 162, 163, 211, 212].

Using equilibrium viscosity data for Vitreloy 1b taken near T_g (Fig. 5.30), models of the relative free volume in the equilibrium liquid according to Cohen and Turnbull, Cohen and Grest, and Adam-Gibbs were calculated for the temperature range from 300 to 1100 K. Each model provides an excellent fit to the experimental data. Furthermore, examination of high temperature experimental viscosity data from the Vitreloy 1 BMG alloy (Fig. 5.32) revealed that the Adam-Gibbs equation for viscous flow has a good ability to predict the free volume of this alloy in the temperature region above the melting point. This supports the validity of the Adam-Gibbs model for multi-component BMG forming melts over a wide temperature range.

In Sec. 5.5, the relationship between free volume and enthalpy, as suggested by Eq. 5.15, was examined by comparing the free volume models with the enthalpy function of the undercooled liquid. The results of the analysis shown in Fig. 5.34 suggests that the reduced formation enthalpy, β_{eq} , derived from Eq. 5.15 is a function of temperature and increases from ~ 100 kJ g-atom⁻¹ (~ 1 eV) near the melting point to ~ 200 kJ g-atom⁻¹ (~ 2 eV) around the glass transition temperature.

In concluding this chapter, a brief discussion about the use of the free volume and Adam-Gibbs configurational entropy theories will be given. Goldstein [215] advocated early on the superiority of the Adam-Gibbs model over the traditional free volume model and suggested that, for temperatures in the vicinity of T_g and lower, the dynamics become sluggish because the system has to overcome local potential energy barriers in configurational space. These barriers, according to Goldstein, are large compared with the thermal energy, kT , and dominate flow at low temperatures. This is in contrast with the classic free volume model, where viscous flow occurs a result of random density re-distribution and not overcoming an activation barrier [58]. In this sense, it may seem reckless to imply, via Eq. 5.13, a direct relationship between these two seemingly contradictory viewpoints. However, the link between configurational entropy and free volume, suggested by the experimental evidence presented in Sec. 5.4.2, is an indicator that these two models share similarities and need not be mutually exclusive. Indeed, even though the shortcomings of the classical free volume theory have been well documented [66, 215, 238], this argues more for the case of an improvement to the free volume model, rather than its outright dismissal.

Chapter 6

The kinetics of structural relaxation below T_g

The following chapter looks at the phenomenology of structural relaxation below T_g in terms of enthalpy, viscosity and free volume. In contrast to the data presented in Chapter 5, which correspond to the equilibrium properties of the undercooled liquid, the data presented in this chapter will deal with the time evolution of thermophysical properties in the non-equilibrium, initially glassy state. The results presented here will focus on the structural relaxation of Vitreloy 1b below T_g as characterized through enthalpy relaxation and recovery, viscous flow and excess free volume reduction.

An analysis of the kinetics of structural relaxation will be given using the Kohlrausch-Williams-Watts (KWW) stretched exponential function [239, 240]. Relaxation processes in amorphous materials are usually found to be best described with a stretched exponential function [162, 168, 241, 242] of the form

$$\Phi(t) = \Phi_{eq} \left(1 - \exp \left[- (t/\tau)^{\beta_{KWW}} \right] \right), \quad (6.1)$$

where $\Phi(t)$ is the relaxing quantity and Φ_{eq} is the value of the relaxing quantity at equilibrium in the supercooled liquid as $t \rightarrow \infty$. Here, t is the time, τ a characteristic relaxation time and β_{KWW} is the stretching exponent parameter ($0 < \beta_{KWW} < 1$).

The structural relaxation of enthalpy, viscosity and free volume are compared in this chapter using Eq. 6.1. Additionally, a brief look at the effects of phase separation and primary crystallization of various Zr-based BMG composi-

tions is given as determined using three-point beam-bending and calorimetric methods. Alongside Vitreloy 106 and 106a, two additional BMG alloys are also investigated – Vitreloy 105 and Vitreloy 101. Finally, the relationship between enthalpy and free volume, as discussed in Sec. 5.5 of Chapter 5, is expanded upon here to include a description of the formation enthalpy for the free volume at temperatures in the glassy state of Vitreloy 1b.

6.1 Viscous flow below T_g

Heating with a constant rate through the glass transition and into the supercooled liquid region allows access to the equilibrium liquid at higher temperatures, before the onset of crystallization, as was explored in Sec. 5.4. However, at temperatures below the glass transition, the equilibrium liquid can be accessed through isothermal annealing of the sample. This is illustrated schematically in Fig. 2.6c. In Sec. 5.4, the equilibrium viscosities at temperatures below T_g were shown for a series of BMG alloys (see Figs. 5.23 and 5.24). Here, the determination of these equilibrium viscosities and the phenomenology of viscous relaxation below T_g is discussed.

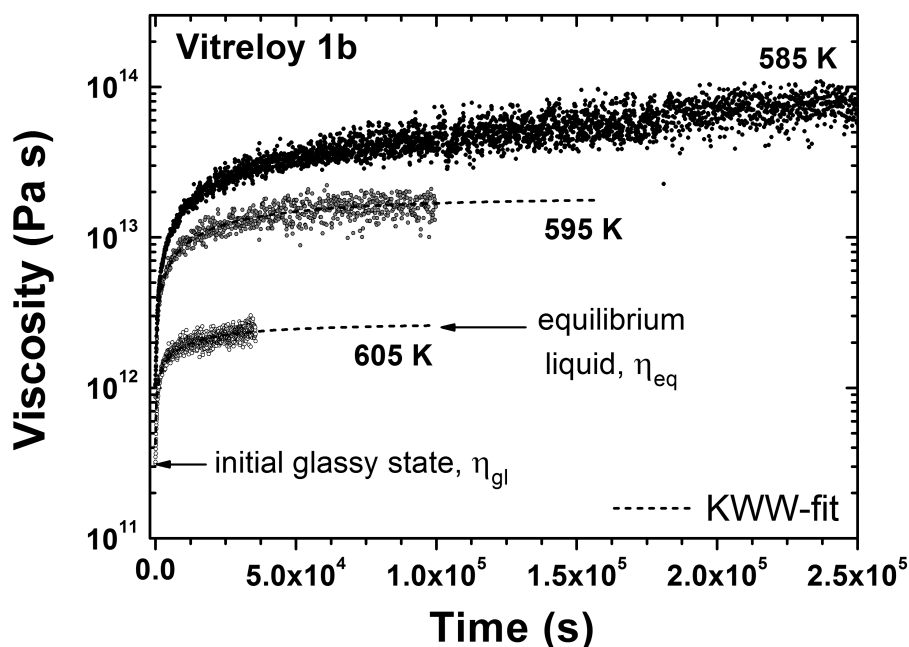


Figure 6.1: Isothermal viscosity measurements on Vitreloy 1b at three selected temperatures below T_g (585, 595 and 605 K). The relaxation from the initial glassy state into the equilibrium liquid is fitted with the stretched exponential (KWW) equation (dashed lines) [177].

The equilibrium viscosities of the Vitreloy 1b alloy were determined through measurements in the vicinity of the glass transition using the isothermal three-point beam-bending method described in Sec. 4.4.3. Figure 6.1 shows the experimental isothermal data for three selected temperatures: 585 K, 595 K and 605 K. All samples were heated to their respective annealing temperatures with a rate of 0.416 K s^{-1} and held there until equilibrium was reached. Fits of Eq. 6.1 to the measured viscosity data at selected temperatures are shown as dashed lines in Fig. 6.1. In this equation Φ_{eq} is taken to be the equilibrium viscosity, $\eta_{eq} = \eta_{gl} + \Delta\eta$, where η_{gl} is the initial viscosity of the glassy alloy before relaxation and $\Delta\eta$ is the viscosity increase during relaxation from the glassy state into the equilibrium liquid. η_{eq} therefore corresponds to the constant value reached by the KWW-fits at long times.

6.1.1 Phase separation

If annealed for sufficiently long times and/or close enough to T_g , the measured viscosity of some BMGs can show a marked departure from equilibrium. This was illustrated in Fig. 3.12 of Sec. 3.3 where it was shown that the isothermal viscosity of Vitreloy 1 at annealing temperatures around T_g can increase, over a very long time scale, in orders of magnitude from its initial equilibrium value [14]. In that work, this was attributed to phase separation and primary nanocrystallization, eventually resulting in another metastable state. This behavior is explored here for the Vitreloy 106, 106a, 105 and 101 BMGs.

Figure 6.2 shows three examples of experimentally determined viscosities of Vitreloy 106 and 106a at constant temperatures; these temperatures are 645 K, 670 K and 680 K. The glassy samples were heated in the TMA with a constant rate of $q_H = 0.833 \text{ K s}^{-1}$. The onset of the glass transition was determined for as-cast samples of Vitreloy 106 and 106a in the DSC with a heating rate of $q_H = 0.833 \text{ K s}^{-1}$ as 683 and 672 K, respectively (see Fig. 6.4)¹. In the TMA experiments, the viscosity at low temperatures (645 K) is seen to increase sharply from its initial value and approach a constant, equilibrium value at longer times. This is the relaxation of the glass into the equilibrium liquid region, similar to the viscous relaxation of Vitreloy 1b shown in Fig. 6.1. As the temperature is increased the measured viscosity

¹Note that this reported value of T_g^{onset} for as-cast Vitreloy 106 varies from that shown in Appendix A for an equal heating and cooling rate of 0.25 K s^{-1} . This discrepancy is due, in part, to the different heating rates used. Another source of error is the enthalpic release in the as-cast sample before T_g , which as discussed in Chapter 5, can complicate a correct determination of the glass transition onset.

decreases, as the overall deflection rate of the sample increases due to higher atomic mobility in the glass.

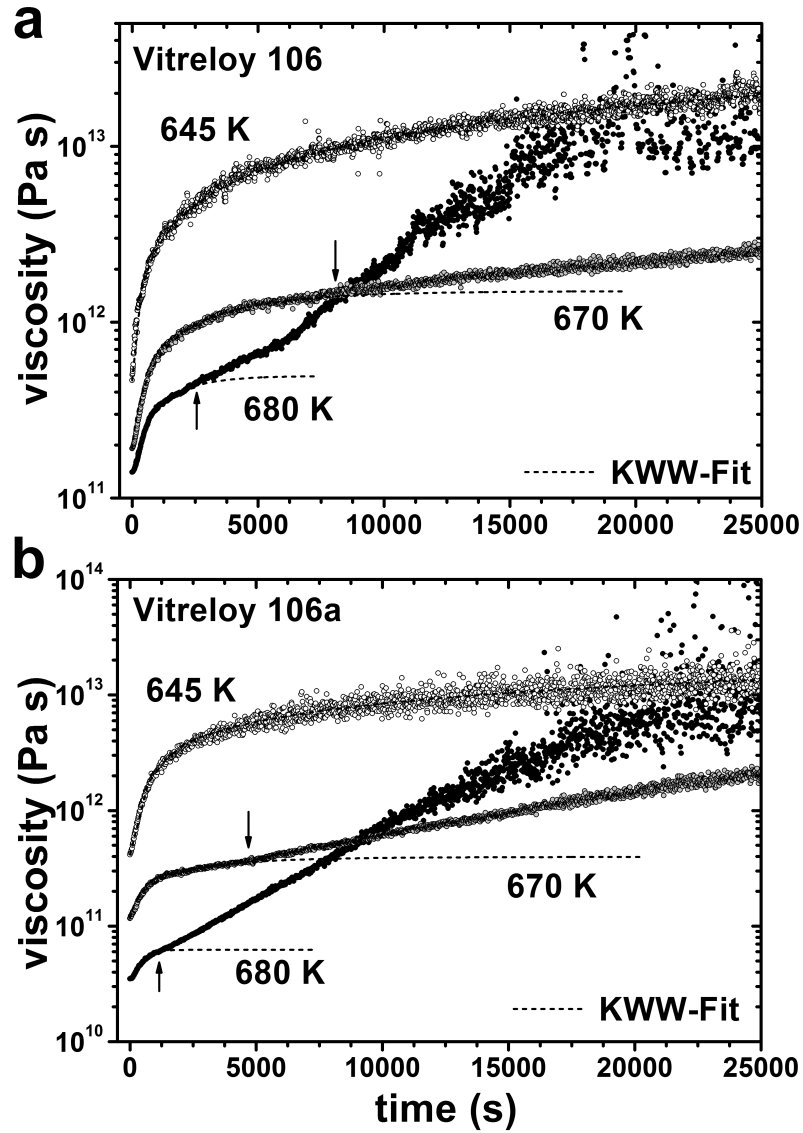


Figure 6.2: Isothermal viscosity measurements at three different temperatures for (a) Vitreloy 106 and (b) 106a. The relaxation from the glassy state into the equilibrium liquid is fitted the KWW equation (dashed lines). Arrows mark the onset phase separation [208].

In contrast to Vitreloy 1b, however, as the isothermal experiments are carried out at higher temperatures for Vitreloy 106 and 106a (670 K), the initial

relaxation of the viscosity occurs at a shorter time and is accompanied by a gradual deviation from the equilibrium value. The arrows in Fig. 6.2 indicate the onset of deviation from equilibrium. At even higher temperatures (680 K), close to or above the calorimetric glass transition, the measured viscosity of both alloys will depart from equilibrium more rapidly and undergo a sudden increase of about two orders of magnitude from around 1×10^{11} Pa s to about 1×10^{13} Pa s. For longer times the viscosity at this temperature remains virtually constant, suggesting that a new metastable equilibrium state has been reached.

Similar viscous behavior is noticed for the Vitreloy 101 and 105 BMGs and is shown in Fig. 6.3. Although Vitreloy 101 and 105 have very similar glass transition temperatures (673 and 675 K, respectively, measured using DSC at $q_H = 0.333$ K s⁻¹), they exhibit notable differences in the temperature dependence of their departures from equilibrium. This is indicated by the arrows marking the onset of phase separation seen in Fig. 6.3.

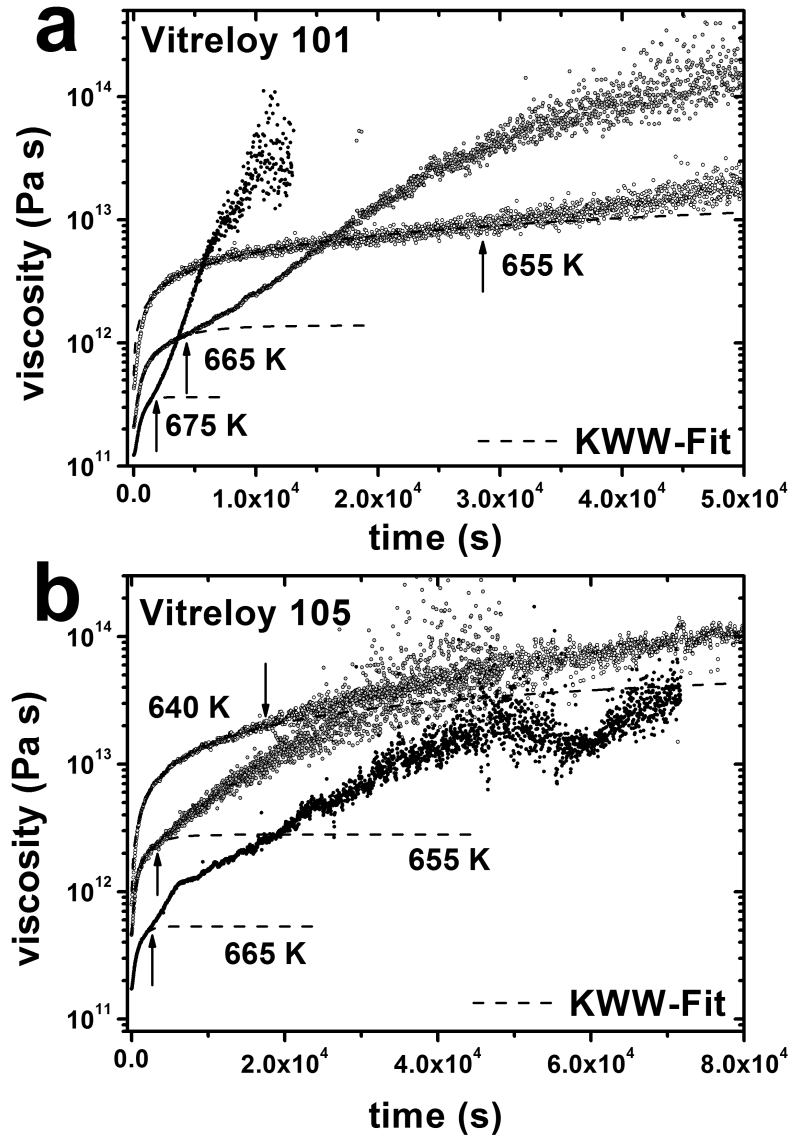


Figure 6.3: Isothermal viscosity measurements at three different temperatures for (a) Vitreloy 101 (655, 665 and 675 K) and (b) 105 (640, 655 and 665 K). The relaxation from the glassy state into the equilibrium liquid is fitted the KWW equation (dashed lines). Arrows mark the onset phase separation.

The viscosity measurements on the amorphous samples show that, in general, these alloys exhibit a complex dependence of the viscosity on temperature and annealing time. For example, in Fig. 6.2a the measured viscosity of Vitreloy 106 begins to depart from the fitted equilibrium value at around

7500 s for the isothermal measurement at 670 K and 2500 s for 680 K. At these temperatures the departures from equilibrium for 106a (Fig. 6.2b) occur earlier at around 5000 s and 1000 s, respectively. The earlier departure from the initial metastable equilibrium for 106a can be attributed to this alloy's lower glass transition temperature compared to Vitreloy 106 (see Fig. 6.4). This is also explained by the relative viscosities of these two alloys at these temperatures, which for 106a are around five times smaller than for 106, allowing for faster kinetics due to increased atomic mobility. The equilibrium viscosities determined for these alloys are obtained by fitting Eq. 6.1 only to the experimental data that were taken before the onset of the deviations from equilibrium, which occur for longer times and higher temperatures.

To investigate this behavior further, the calorimetric glass transition is investigated using DSC at a rate of 0.833 K s^{-1} after annealing the Vitreloy 106 and 106a alloys at a temperature of 680 K for 6000 s, 24 000 s and 42 000 s (Fig. 6.4). For longer annealing times, the maximum height of the glass transition, as well as the enthalpy of crystallization is seen to decrease, indicating the presence of an increasing amount crystals with increasing annealing time. The enthalpy of crystallization is measured for both alloys to decrease approximately 50% after annealing for 24 000 s. If it is assumed that this decrease in enthalpy during crystallization corresponds to the same increase in the volume fraction of crystals embedded in the amorphous matrix, the contribution of these crystals to the viscosity change observed after initial relaxation can thus be quantified with Einstein's equation for the flow of mixtures [243]

$$\eta_{eff} = \eta(1 + 2.5\xi), \quad (6.2)$$

where η_{eff} is the effective viscosity of the mixture, η the measured viscosity of the surrounding medium and ξ is the volume fraction of the crystals. It becomes apparent that a volume fraction of crystals of 0.5 would cause an increase of a factor of approximately 2.3 in the effective viscosity. The experimental observations, however, show an increase in the viscosities of both alloys of about two orders of magnitude from the initial relaxation into the equilibrium liquid region to the new metastable state attained after 24 000 s (Fig. 6.2). It is therefore concluded that the amorphous matrix must have changed its concentration to a composition corresponding to a higher equilibrium viscosity.

Furthermore, in the case of Vitreloy 106 and 106a, the onset of the glass transition is observed to shift about 10 K from the as-cast sample to the

sample annealed for 42 000 s (Fig. 6.4). Since it was already established in Sec. 5.4 that the kinetic glass transition reflects the relaxation time and the temperature dependence of the viscosity in the supercooled liquid, this shift of the glass transition to higher temperatures is consistent with the increase in viscosity of the matrix during primary crystallization observed in Fig. 6.2.

The claim that these alloys undergo decomposition and nanocrystallization during annealing is supported by results obtained in various scattering and microscopy experiments. Small-angle neutron scattering (SANS) and TEM studies on the Vitreloy 106 and 105 BMGs show a chemically homogeneous as-cast structure and the onset of decomposition and nanocrystallization at annealing temperatures below T_g [193]. Additionally, field ion microscopy, atom probe tomography, TEM and SANS experiments on Vitreloy 101 reveal an already decomposed structure in as-cast 1 mm thick plates, with further decomposition and nanocrystallization at annealing temperatures below T_g [244]. Similar studies have not been published for Vitreloy 106a; however, given that the viscosity behavior of this alloy during annealing is similar to that of Vitreloy 106, 105 and 101 (see Figs. 6.2 and 6.3), it can be assumed that this particular alloy also undergoes a similar process of decomposition and nanocrystallization.

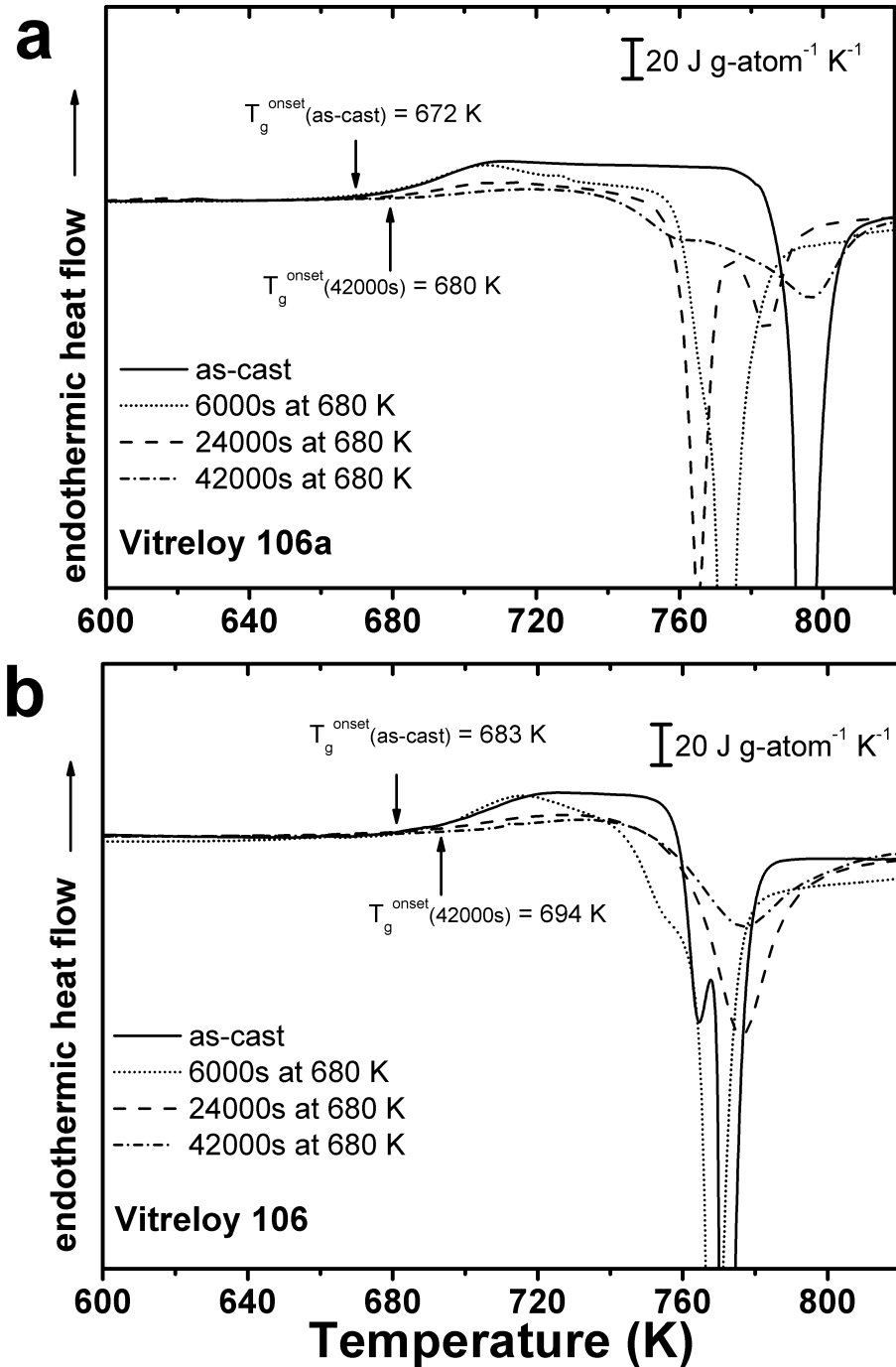


Figure 6.4: DSC up-scans with a heating of 0.833 K s^{-1} of the as-cast (a) Vitreloy 106a and (b) 106 alloys (solid lines); after annealing at 680 K for 6000 s (dotted lines), 24 000 s (dashed lines) and 42 000 s (dash-dotted lines). T_g^{onset} is the onset temperature of the glass transition [208].

6.2 Enthalpy and free volume

Besides the time dependence of the isothermal viscosity, the behavior of other thermophysical properties – enthalpy and free volume – during structural relaxation is also examined in similar relaxation experiments on Vitreloy 1b. The amount of enthalpy relaxed during annealing of glassy samples below T_g is quantified by the enthalpy recovery measurement method discussed in 4.4.1. To obtain the total reduction in free volume during relaxation, the volumetric contraction of the samples was measured isothermally in the TMA according to the method discussed in Sec. 4.4.2. If no temperature changes occur during the relaxation, conventional thermal expansion effects can be discounted and the measured reduction in volume is attributed solely to the reduction in excess free volume of the glass. Furthermore, assuming that structural relaxation occurs isotropically, the relative change in free volume of the amorphous sample, $\Delta v_f/v_m$, is given by its relative change in length, $\Delta L/L_0$ [117, 120, 245]:

$$\frac{\Delta v_f}{v_m} = 3 \frac{\Delta L}{L_0}. \quad (6.3)$$

The Vitreloy 1b alloy has not been observed to exhibit the phase separation behavior of other BMGs (see Figs. 6.2 and 6.3), and was therefore chosen for the relaxation experiments carried out here. Glassy samples of Vitreloy 1b were structurally relaxed in the DSC according to the procedure described in Sec. 4.4.1. To investigate the enthalpy and free volume changes on a long time scale, the specimens were first equilibrated in the supercooled liquid region at a temperature of 700 K and immediately cooled down to room temperature with a rate of $q_C = 0.416 \text{ K s}^{-1}$; this assured the same enthalpic state for each of the amorphous samples. In Fig. 6.5 the enthalpy recovery curves of the completely annealed samples (dotted lines) are shown after heating with the rate $q_H = 0.416 \text{ K s}^{-1}$ throughout the glass transition. The recovery curves are shown alongside a scan of the unrelaxed sample (solid line); i.e., a sample that was heated with the same rate, q_H , as that of an immediately preceding cooling, q_C , from the supercooled liquid region. It was established in Sec. 5.1 that if the convention $q_H = q_C$ is held, the measured onset temperature of the glass transition on heating, T_g^{onset} , approximates the limiting fictive temperature, T'_f . Furthermore, the amount of enthalpy recovered upon reheating annealed samples has been quantitatively shown to be equal to the enthalpy that was "lost" during the annealing process [164, 246–248].

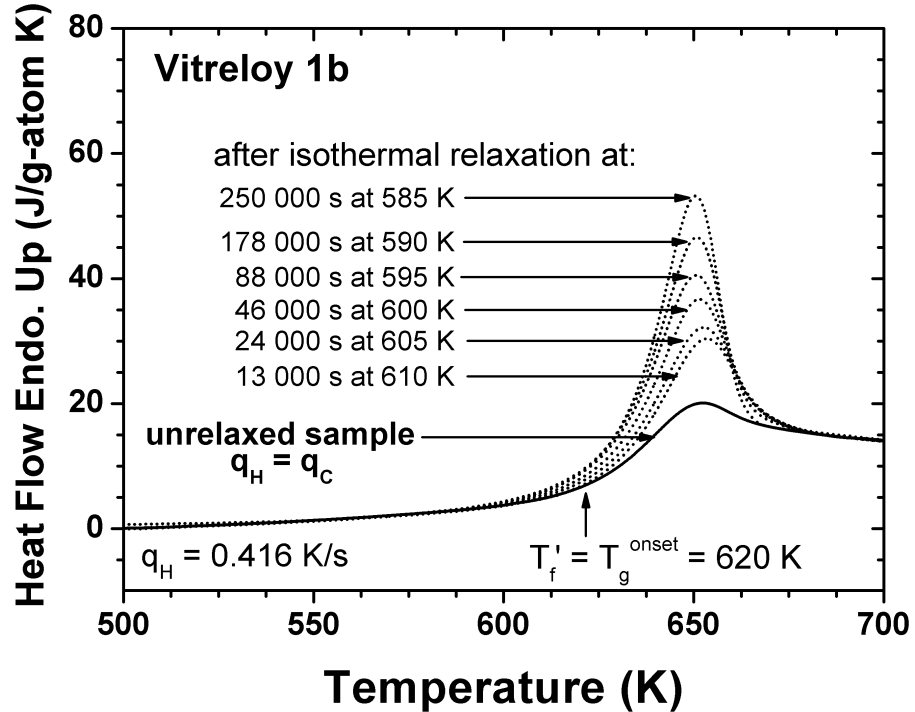


Figure 6.5: Enthalpy recovery curves of Vitreloy 1b (dotted lines) after isothermal relaxation into the equilibrium liquid at the specified temperatures. The solid line represents the curve of an unrelaxed sample; i.e., heated with the same rate, q_H , as that of an immediately preceding cooling, q_C , from the supercooled liquid region. T'_f is the limiting fictive temperature and approximates T_g^{onset} when $q_H = q_C$ [177].

The amount of enthalpy recovered, ΔH_r , is calculated, after heating throughout the glass transition, as the area between the respective recovery curve and that of the unrelaxed sample at a heating rate of $q_H = 0.416 \text{ K s}^{-1}$; this is detailed in Eq. 4.28 on p. 71. At 700 K all samples are equilibrated in the metastable, supercooled liquid region. Figure 6.6a shows the enthalpy difference between the liquid and crystalline states, as was calculated in Fig. 5.12 of Sec. 5.2.2. Figure 6.6b shows a magnification of the glassy region where the experimentally determined enthalpies of recovery, ΔH_r , calculated from the heat flow curves of the completely relaxed samples in Fig. 6.5, are plotted up from the equilibrium liquid line for each annealing temperature (filled circles).

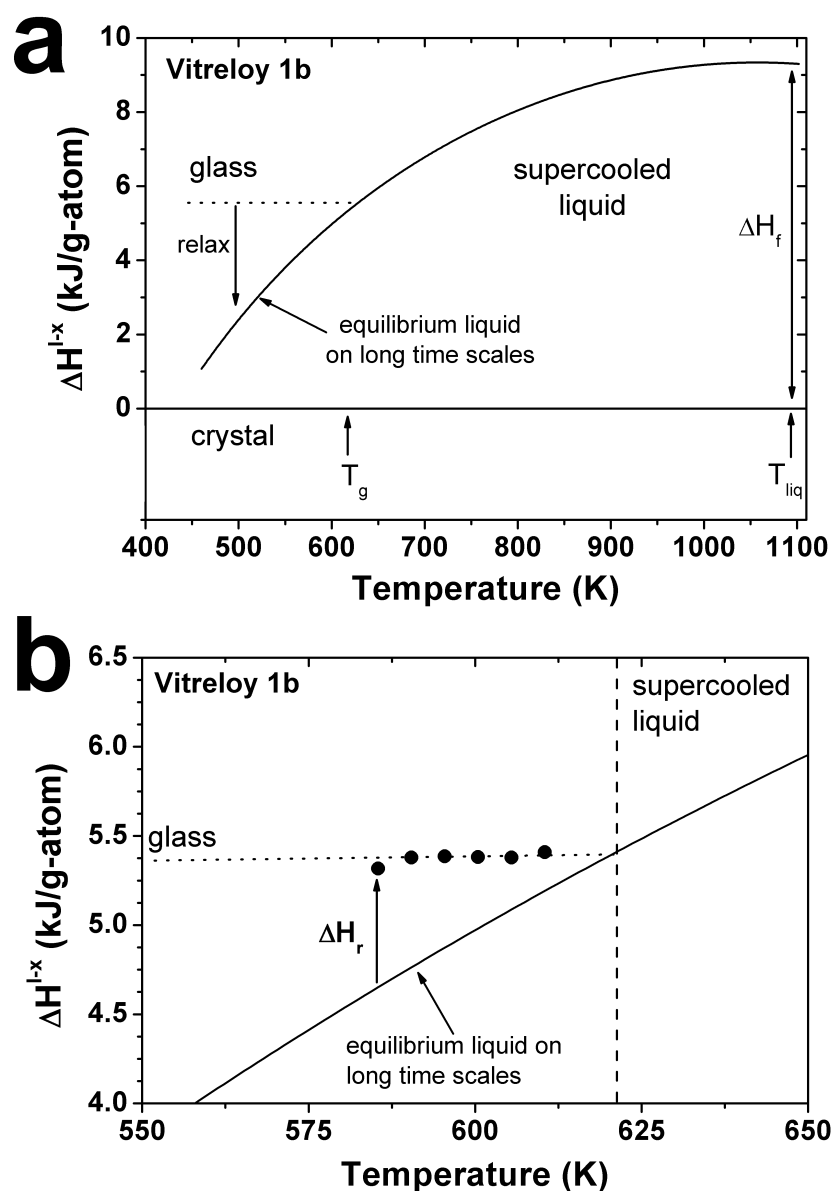


Figure 6.6: (a) Calculated enthalpy difference, ΔH^{l-x} , between the liquid and crystalline states of Vitreloy 1b. The glassy state is shown schematically by the dotted line beginning at T_g . The downward arrow schematically indicates the pathway of relaxation. (b) The experimentally determined enthalpy recoveries (filled circles) are plotted up (arrow) from the equilibrium curve (solid line). In doing so, the original enthalpic state of the glass prior to relaxation is determined for each annealing temperature [177].

In Fig. 6.7 the values of ΔH_r calculated using Eq. 4.28 are shown for various annealing times at the selected temperatures. For a given annealing temperature, the enthalpy recovery as a function of time, $\Delta H_r(t)$, approaches a constant value as the sample relaxes into equilibrium at longer annealing times. The experimental data are fitted using Eq. 6.1 and the results are given by the dashed lines in Fig. 6.7.

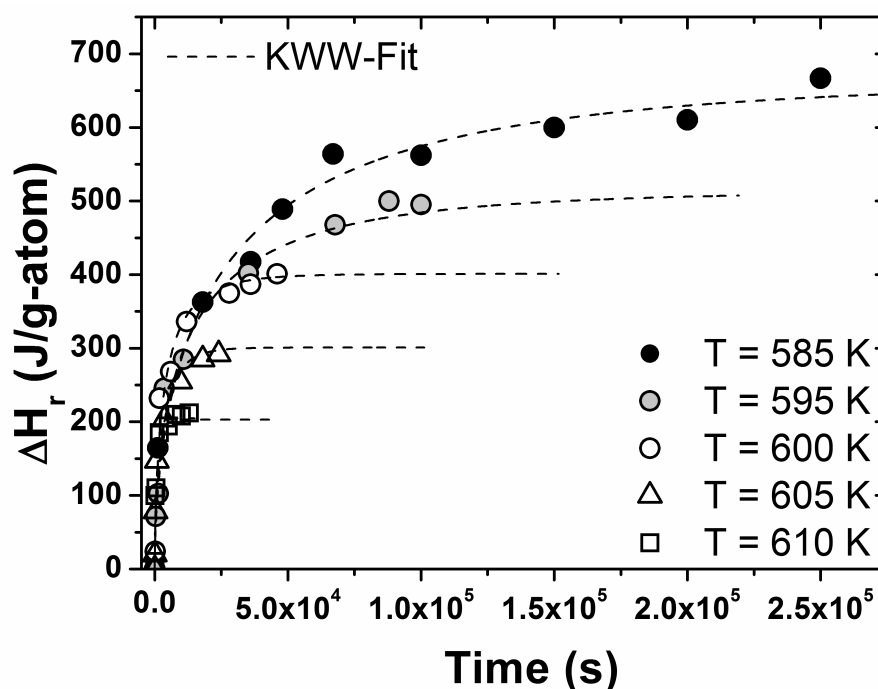


Figure 6.7: Experimentally determined enthalpies of recovery, ΔH_r , after isothermal annealing of the Vitreloy 1b BMG at various times for the temperatures shown. The dashed lines represent the fits of the KWW-equation to the experimental data. The experimental error is on the order of the symbol size [177].

Figure 6.8 shows the relative change in length, $\Delta L(t)/L_0$, of the amorphous samples as they are relaxed from the glassy state into the equilibrium liquid region during isothermal annealing at the temperatures indicated. It can be seen that, at lower temperatures, the relative changes in length are greater than at higher temperatures closer to the glass transition. The experimental data in Fig. 6.8 (open circles) are fitted with a KWW function of the form in 6.1.

The relationship between the enthalpy and free volume of the equilibrium liquid was explored in Sec. 5.5 by analyzing the calculated ΔH^{l-x} and v_f/v_m curves calculated from experimental data. Here, a linear relationship is found

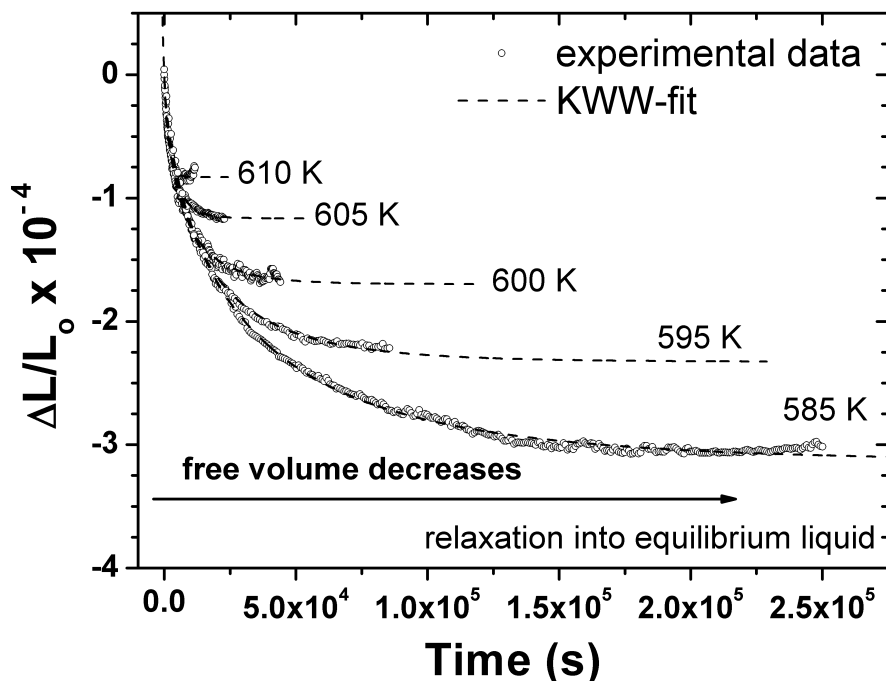


Figure 6.8: Experimental relative changes in length, $\Delta L/L_0$, of amorphous samples of Vitreloy 1b during relaxation into the equilibrium liquid for the annealing temperatures shown (open circles). The fits of the experimental data to the stretched exponential (KWW) function are also shown (dashed lines) [177].

between the amount of enthalpy recovered using DSC, ΔH_r , and the decrease in excess free volume from the glassy state using volumetric relaxation, $(\Delta v_f/v_m)_{glass}$, for each annealing temperature and is shown in Fig. 6.9. The constant β' from Eq. 5.15 on p. 128 is determined here to be 622.7 ± 20 kJ g-atom⁻¹. This result is in good agreement with similar studies performed on the quaternary $Zr_{55}Cu_{30}Al_{10}Ni_5$ BMG using direct density measurements to quantify the free volume change [228, 229]. In those studies, Ref. [228] report a value of $\beta' = 552 \pm 20$ kJ g-atom⁻¹ and Ref. [229] report a value of 718.2 kJ g-atom⁻¹.

It has been suggested that β' in Eq. 5.15 represents the formation enthalpy of an amount of free volume with the magnitude of one atomic volume [121]. In the studies on $Zr_{55}Cu_{30}Al_{10}Ni_5$ cited above, the values of β' were said to be 2-3 times greater than the formation enthalpy of a vacancy in a pure Zr crystal lattice [249]. Furthermore, Ref. [121] noted that vacancies in crystalline materials usually have a smaller volume than the atomic volume (about $0.5v_m$) due to the lattice relaxation around the vacancy; hence, a β' -

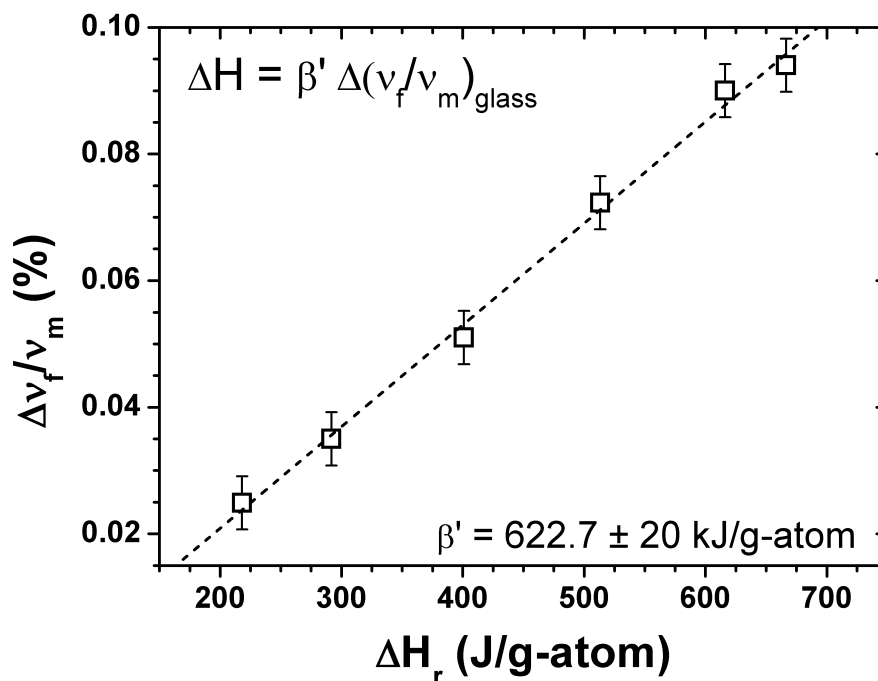


Figure 6.9: The experimentally determined values $\Delta(v_f/v_m)_{glass}$ vs. ΔH_r are shown for each annealing temperature (open squares) along with a linear fit to the data (dashed line). The proportionality constant β' was found to be 622.7 ± 20 kJ g-atom⁻¹ [177].

value corresponding to almost twice that of the vacancy formation enthalpy would be physically reasonable.

In this work, an alternative interpretation is offered based on the critical volume necessary for viscous flow (see Sec. 5.5). More specifically, if flow processes require a critical volume that is only a fraction of the atomic volume [58], then only the critical volume should be considered; i.e., bv_m , and the corresponding formation enthalpy, β' , would take on a more physically acceptable value. That is, β' would be comparable to the typical vacancy formation energies or activation energies for viscous flow (~ 2 -3 eV). Supposing now that the same critical amount of free volume is required for structural relaxation in the glass below T_g , as in the equilibrium liquid, a reduced enthalpy of formation, $\beta \sim 180$ kJ g-atom⁻¹, is calculated for the glass. This is in agreement with the value of $\beta_{eq} \sim 200$ kJ g-atom⁻¹, determined in Sec. 5.5 for the equilibrium liquid in the vicinity of T_g (see e.g. Fig. 5.34).

In Fig. 6.10 the different models of the relative free volume from Sec. 5.5

6.2 Enthalpy and free volume

are shown in the vicinity of the glass transition along with the equilibrium curve of the enthalpy, ΔH^{l-x} . The experimental enthalpy recovery data, ΔH_r , are reproduced from Fig. 6.6b (filled circles). Calculated from the viscosity data in Fig. 5.30, the relative free volumes in the equilibrium liquid, $(v_f/v_m)_{eq}$, are shown (open circles) as well as the excess free volume of the glass, $(v_f/v_m)_{glass}$, (shaded circles). Additionally, the reduction in excess free volume of the glass, $(\Delta v_f/v_m)_{glass}$, determined directly from the volumetric relaxation experiments using Eq. 6.3 on p. 144 are shown (open squares) in reference to the equilibrium v_f/v_m curves. The free volume changes reported here during isothermal relaxation are on the order of 0.05%. When compared with similar research on other BMG systems, where the reported excess free volume reduction ranges from 0.04 - 0.10% (see e.g. Refs. [228, 229, 250]), good agreement is found with the experimental results presented here.

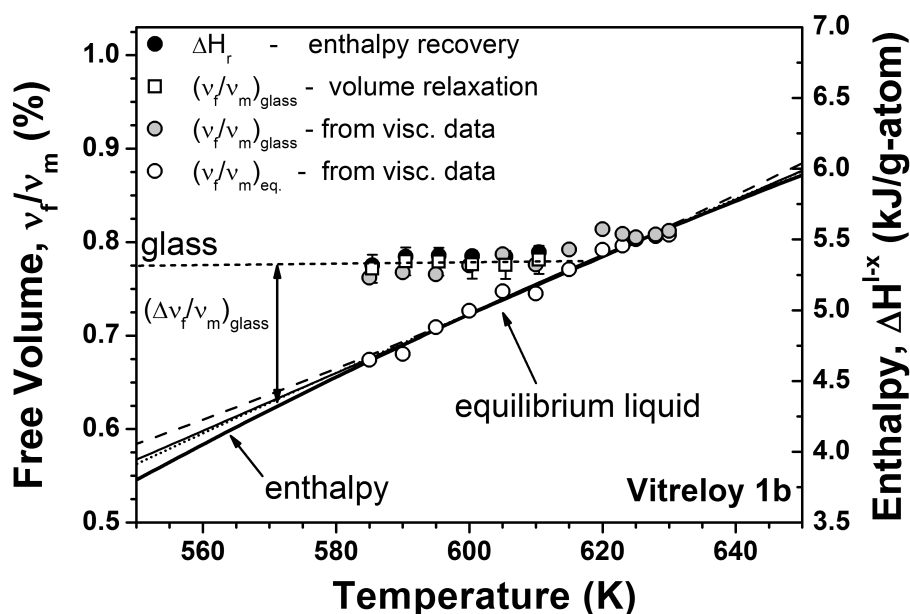


Figure 6.10: Enthalpy recoveries, ΔH_r , (dark circles) and excess free volume of the Vitreloy 1b glass, $(v_f/v_m)_{glass}$, (open squares) calculated from the changes in length during relaxation into the equilibrium liquid. The relative free volumes of the initial glassy and equilibrium states are calculated from the experimental viscosity data using Eq. 2.30 on p. 24 and shown as shaded and open circles, respectively. The relative free volume curves of the equilibrium liquid shown in Fig. 5.33 are reproduced here, as well as the calculated enthalpy difference between the liquid and crystalline states as a function of temperature. The glassy state is schematically indicated with the heavy dotted line. $(\Delta v_f/v_m)_{glass}$ glass is the excess free volume frozen into the glassy state [177].

6.3 The kinetics of structural relaxation

It has to be emphasized that each data set representing $(v_f/v_m)_{glass}$ depicted in Fig. 6.10, as well as ΔH_r , was obtained in independent measurements on the glassy samples. Additionally, remarkable agreement is found between the values of $(\Delta v_f/v_m)_{glass}$ taken from volumetric relaxation and those calculated from viscosity measurements. This is an indication that the change in viscosity during relaxation into the equilibrium liquid directly reflects the change in free volume as well as in the enthalpy.

6.3 The kinetics of structural relaxation

In this section, the experimental data presented in Secs. 6.1 and 6.2 are analyzed. Specifically, the kinetics of the structural relaxation phenomena observed in each of the investigated properties (viscosity, enthalpy and free volume) are described through the Kohlrausch-Williams-Watts (KWW) stretched exponential function shown in Eq. 6.1.

The structural relaxation of Vitreloy 1b below the glass transition temperature is quantified here, in part, by the enthalpy recovery measured upon re-heating after isothermally annealing the samples at the selected temperatures. By measuring the exothermic heat flow as a function of time directly during relaxation in the DSC, Ref. [164] showed that the amount of enthalpy relaxed during the annealing process is equal to the amount recovered upon subsequent re-heating. It was thus possible to determine the initial enthalpic state of the glassy sample at a certain temperature by calculating the enthalpy of recovery, ΔH_r , for that temperature, after complete relaxation into the equilibrium liquid, from the respective heat flow curve in Fig. 6.5 and plotting this value in the positive (endothermic) H -direction starting from the ΔH^{l-x} equilibrium curve in Fig. 6.6b. Furthermore, in Fig. 6.7 the values of ΔH_r for each annealing temperature are determined after various, increasingly longer annealing times. The data show a clear saturation of ΔH_r , and approach a constant value as the sample reaches the completely relaxed (equilibrium) state.

Structural relaxation is also quantified here by the direct measurement of the change in length of an amorphous sample during annealing (see Fig. 6.8). Using Eq. 6.3 these changes in length can be seen as being representative of a total volumetric change due to the reduction in excess free volume of the glass. The experimental data in Fig. 6.8 show very little changes in length after long annealing times. Additional optical inspection of the loading surface of the amorphous dilatometer samples after relaxation using interference contrast microscopy revealed no indentations from the TMA loading probe, giving no

6.3 The kinetics of structural relaxation

further evidence that viscous flow due to shearing of the sample was present. These results indicate that the glass sufficiently relaxes into the equilibrium liquid on long time scales and that the changes in length during relaxation are solely due to structural changes in the amorphous sample.

Isothermal measurements of the viscosity of an initially glassy sample at temperatures near the glass transition show that the Vitreloy 1b alloy, if given sufficient time, will completely relax into the metastable equilibrium liquid (see Fig. 6.1). The viscosity of the glass, as a function of time, rises sharply from its initial state and steadily approaches a constant value for long times, as seen by the fits of Eq. 6.1 to the experimental data in Fig. 6.1. This directly reflects the reduction of the excess free volume in the glass, resulting in a denser amorphous state (see e.g. Fig. 5.30). No drastic changes in the viscosity are recorded for longer times, indicating that phase separation and/or primary crystallization have not occurred during annealing of this alloy. This is in contrast to the Vitreloy 106, 106a, 101 and 105 BMGs presented in Sec. 6.1, as well as Vitreloy 1 [14], where clear deviations from stretched exponential relaxation indicate the presence of compositional changes during annealing of the glass.

The kinetics of the structural relaxation phenomena below T_g are analyzed by comparing the values of τ and β_{KWW} , taken from each type of relaxation experiment, as a function of annealing temperature. At this point the significance of the characteristic relaxation time, τ , obtained from fitting Eq. 6.1 should be discussed. Here the mean relaxation time, $\langle\tau\rangle$, is defined as

$$\langle\tau\rangle = \tau\beta_{KWW}^{-1}\Gamma(\beta_{KWW}^{-1}), \quad (6.4)$$

where Γ is the gamma function, defined as

$$\Gamma(x) = \int_0^{\infty} t^{x-1}e^{-t}dt, \quad (6.5)$$

where $x > 0$. For cases where β_{KWW} is close to unity, $\langle\tau\rangle$ and τ are approximately equal. For smaller values of β_{KWW} , $\langle\tau\rangle$ becomes greater than τ , reflecting the wider distribution of relaxation times present in the system. Therefore, the use of $\langle\tau\rangle$ is more appropriate when comparing values of τ that have different β_{KWW} values.

The data shown in Fig. 6.11 correspond the mean characteristic relaxation times, $\langle\tau\rangle$, and β_{KWW} -values (inset) obtained from fitting Eq. 6.1 to the

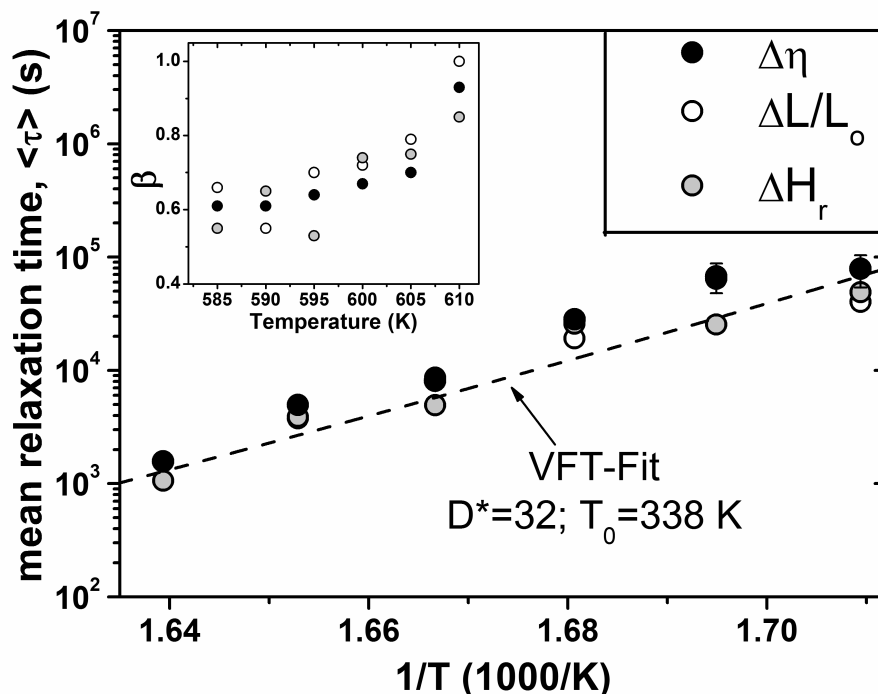


Figure 6.11: Mean characteristic relaxation times, $\langle \tau \rangle$, obtained from fitting Eq. 6.1 to the experimental data taken at various annealing temperatures below the glass transition. Shown are the relaxation times taken from fitting the change in viscosity, $\Delta\eta$ (filled circles), change in relative length, $\Delta L/L_0$ (open circles) and enthalpy recovery, ΔH_r (shaded circles). The error is on the order of the symbol size, unless otherwise given. A fit of the VFT-equation (dashed line) to the experimental data is also shown, corresponding to the parameters $D^* = 32$ and $T_0 = 338$ K. The stretching exponent parameter, β_{KWW} , reaches unity in the proximity of the glass transition (inset) [177].

experimental data in Figs. 6.7 6.8 and 6.1. In Fig. 6.11 there is very good agreement between the values of $\langle \tau \rangle$ determined at each annealing temperature for each set of data: the change in viscosity, $\Delta\eta$ (filled circles), change in relative length, $\Delta L/L_0$ (open circles) and enthalpy recovery, ΔH_r (shaded circles). This gives a direct link between each of the relaxing quantities and shows that the volumetric changes observed here during structural relaxation (Fig. 6.8) can be attributed to the changes in free volume (Figs. 6.1 and 5.30).

Furthermore, it can be seen from these results that there is a strong temperature dependence in both $\langle \tau \rangle$ and β_{KWW} . At lower annealing temperatures the characteristic time for relaxation increases while the value of β_{KWW} de-

creases (inset Fig. 6.11). As the annealing temperature approaches the glass transition, the values of β_{KWW} approach unity, indicating the presence of a purely exponential relaxation. The non-exponential behavior of the measured relaxations is clearly observed at lower annealing temperatures, suggesting a broader distribution of relaxation times. Similar non-exponential behavior was reported recently in Ref. [229] for the quaternary $\text{Zr}_{55}\text{Cu}_{30}\text{Al}_{10}\text{Ni}_5$ BMG in volume relaxation experiments and by Refs. [164] and [236] in enthalpy relaxation experiments on the Vitreloy 106a and $\text{Zr}_{45}\text{Cu}_{39.3}\text{Al}_{7.0}\text{Ag}_{8.7}$ BMGs, respectively.

The temperature dependence of the mean relaxation times shown in Fig. 6.11 was investigated with an Arrhenius-like dependence of the form $\langle\tau\rangle = \tau_0 \exp(Q/RT)$, where τ_0 is the theoretical infinite-temperature limit of the relaxation time (see Sec. 5.1) and Q is an activation energy. The results of an Arrhenius fit to these data give an apparent activation energy of around 4 eV and a value of $\tau_0 \sim 10^{-32}$ s. This value of τ_0 is unrealistically small, as τ_0 should be here $\sim 10^{-14}$ s; i.e., close to the inverse Debye frequency (see Sec. 5.1.2). Instead, a VFT-equation similar to Eq. 2.27 on p. 22, with a value of $\tau_0 = 10^{-14}$ s was used to fit the experimental data and is shown as the dotted line in Fig. 6.11. The VFT-equation provides a good fit to these data with the parameters $D^* = 32$ and $T_0 = 338$ K. This result is similar to that obtained from the volumetric relaxation times reported in Ref. [229] for the $\text{Zr}_{55}\text{Cu}_{30}\text{Al}_{10}\text{Ni}_5$ BMG.

The applicability of the VFT-equation here shows that these relaxation times reflect, to some degree, the VFT-behavior of the equilibrium undercooled liquid itself. As the temperature is lowered from T_g , the time needed for complete relaxation into the equilibrium liquid increases (Fig. 6.11). Intuitively, if the viscosity of the undercooled liquid approaches infinity at a certain temperature, then so should the characteristic structural relaxation time (τ or $\langle\tau\rangle$). Therefore, the structural relaxation time should have roughly the same temperature dependence as that of the equilibrium liquid itself. In fact, this seems to be the case here, as the VFT-parameters obtained from the equilibrium viscosity data (Fig. 5.30) are in good agreement with those obtained from the Kohlrausch relaxation times (Fig. 6.11).

6.4 Summary and Conclusions

In this chapter, structural relaxation was studied in various BMG alloys and the kinetics described using the KWW-equation of Eq. 6.1. The viscous flow and relaxation behavior of the Vitreloy 106, 106a, 101 and 105 alloys were

studied here using three-point beam-bending methods (Figs. 6.2 and 6.3). The viscosity measurements reveal that these alloys exhibit a complex dependence of the viscosity on annealing time and temperature, similar to Vitreloy 1 [14]. At longer annealing times and higher temperatures, relaxation from the glassy state into the equilibrium liquid was found to occur at shorter times and was followed by phase separation, primary crystallization and eventual relaxation into a new metastable state. The isothermal relaxation into the equilibrium liquid from the glassy state is best described by a stretched exponential fit of the viscosity, yielding equilibrium viscosity values as a function of temperature. This is in contrast to the other alloys investigated in this section, the Vitreloy 1b alloy did not exhibit pronounced deviations from its equilibrium viscosity at high temperatures or long annealing times. This is possibly an indication that noticeable phase separation does not occur for this composition within the investigated time and temperature range.

The reduction in excess free volume, $(\Delta v_f/v_m)_{glass}$, and the kinetics of structural relaxation of the Vitreloy 1b BMG alloy in the glassy state were determined at temperatures below T_g using methods of enthalpy recovery measured in the DSC and length relaxation measured in the dilatometer, as well as through measurement of the change in viscosity using a three-point beam-bending method in the TMA. It was found that the kinetics of structural relaxation can be well described with a stretched exponential function (Eq. 6.1) with β_{KWW} values approaching unity as the glass transition is approached. This is in good accordance with similar investigations of the enthalpy and volume relaxation in other Zr-based BMG systems.

The isothermal change in length of the amorphous samples during relaxation into the metastable equilibrium liquid was used directly to determine the change in the excess free volume of the glass. A linear relationship between ΔH_r and $(\Delta v_f/v_m)_{glass}$ was found in the vicinity of the glass transition and the proportionality constant determined to be 622.7 ± 20 kJ g-atom⁻¹ (~ 6.5 eV), which has been interpreted as the formation enthalpy for an amount of free volume with the magnitude of one atomic volume. Since flow processes are known to occur when a critical amount of free volume is reached ($\sim 0.1v_m$ for metallic species), the formation enthalpy necessary for this critical free volume is accordingly lower. According to the results presented here and in Chapter 5, the formation enthalpies for the critical amount of free volume needed for structural relaxation as well as for viscous flow are similar, ~ 180 - 200 kJ g-atom⁻¹ (~ 2 eV) near the glass transition. The critical volume for structural relaxation in the glassy state was determined by Taub and Spaepen [251] for a Pd-Si metallic glass to be $\sim 0.1v_m$, which is in agreement with the critical volume for flow in the equilibrium liquid given by Cohen and Turnbull

for some metallic species [58] and also reported here in Sec. 5.5 for Vitreloy 1b. Furthermore, the similarity of the formation enthalpies for the critical amount of free volume determined here for Vitreloy 1b in the glassy state and in the equilibrium liquid near T_g could indicate that similar atomic transport phenomena are involved in the glass as well as the deeply undercooled liquid. Diffusion studies on supercooled BMG-forming melts in the vicinity of T_g have shown that long-range atomic transport occurs through highly collective hopping processes, involving clusters of atoms performing thermally activated transitions into new configurations [220, 252, 253].

The values of v_f/v_m in the initially glassy state were calculated from viscosity measurements for a range of annealing temperatures using the Doolittle equation (Eq. 2.30). These values are in good agreement with the independently measured amounts of excess free volume reduction in the glass taken from the dilatometric experiments (see Fig. 6.10). Furthermore, the excellent agreement of these data with the experimentally determined enthalpy recoveries at the same annealing temperatures shows a very consistent picture of excess free volume reduction as analyzed with each of the techniques reported in this chapter.

A comparison of the mean characteristic relaxation times of each relaxing property investigated here was given in Fig. 6.11, where very good agreement was found between each set of relaxation times and β_{KWW} -values. It should be noted, however, that the similarity of these values across each measurement method is not, in general, to be expected. Indeed, it was pointed out by Johari and Aji [254], that different measurement techniques (e.g. dielectric, calorimetric or mechanical relaxation) probe different aspects of molecular and segmental diffusion, at least in polymeric and oxide glasses. As such, the relaxation times and β_{KWW} -values determined for such systems using different techniques should not necessarily be the same. However, from the evidence presented in Fig. 6.11, it can be inferred, at least within a given error range, that the similarities of τ and β_{KWW} reflect the similarity of the underlying processes governing the measured isothermal structural relaxation below T_g for Vitreloy 1b. That is, the structural relaxation, as measured through enthalpic and volumetric relaxation, as well as viscous flow, is probed similarly by each of these three techniques. The densification of the glass as it relaxes towards equilibrium directly reflects the increase in the topological short range order (TSRO), as introduced in Sec. 2.4. Similarly, this increase in TSRO is directly reflected in the exothermic process of annealing-out the excess enthalpy of the glass. The similarities of τ and β_{KWW} found in this chapter are an indicator that the kinetics of the phenomena observed here during structural relaxation are similar; i.e., relaxation occurs primarily through an

increase in TSRO resulting in an overall free volume and enthalpy reduction.

It should also be noted that the conventional concept of free volume may only provide a somewhat limited atomistic picture when applied to structural relaxation phenomena in metallic glasses. The original publication by Cohen and Turnbull on the subject [58] reported a critical volume for flow of $\sim 0.8v_m$ for van der Waal liquids and $\sim 0.1v_m$ for some metallic species. This gave the initial indications that the ideal hard-sphere model may not be completely applicable for liquid metals. Indeed, a critical volume for flow that is only 10% of the atomic volume indicates that the interatomic potential must be significantly softer than that of hard spheres. In other words, the atoms must be able to easily overcome potential energy barriers imposed by their neighbors and "squeeze" through tight spaces without free volume.

Egami points out [255] that the interatomic potentials for liquids metals are indeed far from hard-sphere systems, and argues that, since the interatomic potentials contain a harmonicity that is absent from simple Lennard-Jones systems [256, 257], negative (n -type) and positive (p -type) density fluctuations will be frozen into the glassy state. This concept is used to explain the phenomenology of structural relaxation in metallic glasses by assuming that net volumetric shrinkage occurs through the recombination of these defects [116, 255, 258–262]. However, recent positron-annihilation studies on some Zr-based BMGs [263–265] have shown that, contrary to the viewpoint put forth by Egami, excess free volume annihilates at the sample surface and contributions from the n - and p -type annihilation mechanisms are of minor importance.

From the above considerations, it becomes clear that the concept of free volume in metallic glasses is still not completely understood. One of the main drawbacks of this model is the failure to describe exactly how the free volume is distributed throughout the amorphous material (liquid or glass). Early computational models of amorphous solids suggest that large vacancies; i.e., on the order of one atomic volume, are unstable in the glassy state, leading to subsequent collapse into more densely packed arrangements [266]. The concept of randomly distributed free volume, introduced by Argon [267], has found much success when applied to describing flow and deformation in metallic glasses [268, 269]. While the hard-sphere model may not be an altogether accurate description of metallic systems, the fact that the free-volume theory can accurately describe the phenomenology of both the equilibrium and glassy properties does lend some validity to its usefulness.

Chapter 7

Fragile-to-strong transitions in metallic glass-forming liquids

In the following chapter the topic of the fragile-to-strong transition in BMG-forming melts will be covered. Recently collected experimental evidence on select BMG compositions will be presented, showing the existence of a distinctively stronger liquid state at temperatures near T_g than at high temperatures in the melt near T_{liq} . This behavior is explained in terms of a kinetic fragile-to-strong transition in the undercooled liquid, possibly due to polyamorphism and an underlying order-disorder transition.

The experimental data presented in this chapter were taken from viscosity measurements carried out close to T_g and T_{liq} . The low-temperature viscosity data, corresponding to the three-point beam-bending measurements discussed in Chapters 5 and 6, are the author's original work. The high-temperature measurements of the shear viscosity that will be introduced in this chapter were performed by M. Nicola, T. Schmitt [2] and W. Hembree [3]. The extended data analysis, discussion and conclusions correspond to the author's independent contributions to the project.

As introduced in Section 3.2, experimental viscosity measurements on Vitreloy 1 in the vicinity of T_g have determined a fragility parameter of $D^* = 22$, showing that this BMG is a moderately strong glass-former, similar to sodium silicate glasses [14, 91]. However, it was shown that this liquid retains its highly viscous, kinetically strong nature upon melting and, with increasing temperature, transforms to a more kinetically fragile system, characterized by a marked decrease in the viscosity of around three orders of magnitude (refer to Figs. 3.8 and 3.9) [123]. This liquid remains in the fragile state ($D^* \sim 10$)

until undercooled below the liquidus temperature, where the high viscosity liquid behavior is then re-established. In addition to this fragile-to-strong transition, it was also shown in those same experiments that the Vitreloy 1 melt exhibits pronounced shear thinning behavior; both effects have been attributed to the destruction and re-establishment of short and medium-range order in the melt.

In this chapter, the high-temperature melt viscosities of three non-beryllium-bearing, Zr-based BMGs, as well as one Cu-based BMG, as determined using concentric rotating cylinder viscometry will be discussed and the possibility of a fragile-to-strong transition similar to that noticed in Vitreloy 1 investigated. The compositions investigated here are: Vitreloy 106, Vitreloy 106a, Vitreloy 105 and Vitreloy 101.

The low-temperature equilibrium viscosities of each alloy were determined using the three-point beam-bending technique described in Sec. 4.4.3. The experimental data were presented in Figs. 5.23 and 5.24 of Sec. 5.4. The fragility parameter, D^* , of each alloy is given in Table 7.1 alongside other relevant thermophysical parameters. Additionally, a scaling parameter, T_g^* , is shown, which is equal to the temperature at which the equilibrium viscosity has a value of 10^{12} Pa s (see Sec. 5.4.1). The values of T_g given in this table were determined from as-cast amorphous samples that were heated in the DTA at a rate of $q_H = 0.333$ K s⁻¹. This should be taken into account when comparing these values to those listed in Appendix A.

Alloy	T_g [K]	T_{liq} [K]	D_η^*	T_g^* [K]
Vitreloy 101	676	1164	14.9	668
Vitreloy 106	670	1115	35.2	674
Vitreloy 106a	668	1140	21.0	659
Vitreloy 105	661	1125	18.6	662

Table 7.1: Thermophysical properties of the investigated BMG compositions. The values of T_g was determined from as-cast samples in the DTA at a heating rate of $q_H = 0.333$ K s⁻¹. The values of T_{liq} are given from Appendix A.

Previous analyses of the equilibrium viscosity of Vitreloy 101 using a three-point beam-bending technique were published in Refs. [91, 270]. By considering only the low-temperature viscosity data, a fragility parameter of $D^* = 20.4$ was determined [91], which differs considerably from the value

7.1 Viscosity measurements in the molten state

of 14.9 determined in this work. This discrepancy is most likely due to insufficient annealing times of the glassy samples measured in Ref. [270], giving an apparently different trend in the measured viscosity with temperature.

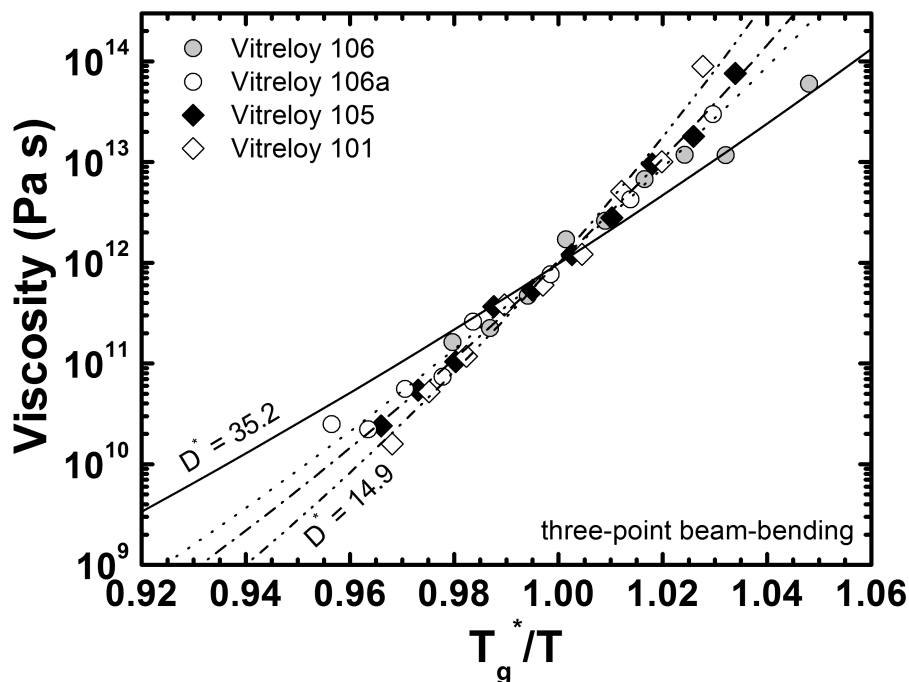


Figure 7.1: Angell-plot of the equilibrium viscosities near T_g of Vitreloy 106 (shaded circles), 106a (open circles), 105 (filled diamonds) and 101 (open diamonds). The curves represent the fits of the VFT-equation to the experimental data. The values of D^* and T_g^* determined for these alloys are listed in Table 7.1.

In Fig. 7.1 an Angell-plot (see Sec. 2.5 and Ref. [23]) is shown, comparing the experimentally determined equilibrium viscosities of Vitreloy 106, 106a, 105 and 101 in the vicinity of T_g . The curves represent VFT-fits to the experimental data. As a comparison, the fragility parameters for Vitreloy 106 and 101, $D^* = 35.2$ and $D^* = 14.9$, respectively, are indicated.

7.1 Viscosity measurements in the molten state

A large number of experimental methods have previously been employed in determining the high temperature melt viscosities of metallic glass-forming liquids: the oscillating vessel method [271], noncontact oscillating drop method [253, 272, 273], capillary flow method [274, 275] and concentric rotating cylinder viscometry [15, 19, 123, 148]. A review and comparison of the various methods used to determine liquid metal viscosities can be found in Ref. [276].

7.1 Viscosity measurements in the molten state

The melt viscosities of the Vitreloy 106, 106a, 105 and 101 BMG compositions were determined using concentric rotating cylinder viscometry. The method employed in these studies was adapted from that used to measure the melt viscosity of Vitreloy 1 [123]. The experimental setup of this particular high-vacuum high-temperature Couette concentric cylinder viscometer is described in Refs. [2, 3] and will not be discussed here.

The graphite shear cell was machined from Ringsdorff-Isographite R6710. Additional microscopy investigations revealed no infiltration of the molten Zr into this specific type of graphite [2]. Each alloy sample was first inductively heated to a temperature above T_{liq} . At this temperature, a shearing profile was applied by gradually varying the shear rate, $\dot{\gamma}$, from $\sim 50 \text{ s}^{-1}$ to $\sim 450 \text{ s}^{-1}$. The temperature was then increased in increments of 25 K, where the shearing profile was applied again. At the end of the first series of isothermal measurements, the melt was cooled back down to the initial starting temperature and the aforementioned procedure was carried out a second time.

In a detailed error analysis of the experimentally measured melt viscosities using the current viscometer setup, it was shown that bias, or systemic, error is the dominant source of error for shear rates greater than $\sim 50 \text{ s}^{-1}$ [3]. The error bars given in this work will therefore reflect the greater of the error estimates.

The results of isothermal melt viscosity measurements with varying shear rates on initially amorphous Vitreloy 106, 106a, 105 and 101 are shown in Fig. 7.2. For increasing temperatures, the viscosity of each alloy melt was measured to decrease, reflecting an increase in atomic mobility. To investigate the possible influence of the initial state of the liquid on its shear behavior, a subsequent measurement of the viscosity at each holding temperature was carried out after completion of the first set of viscosity measurements. Experimental results showed virtually no change in the measured viscosity between the first and second set of measurements.

In order to examine the shear rate dependence, if any, of the viscosity, the isothermal shearing data at each temperature were fit with a power law of the form [123, 277]

$$\eta = A\dot{\gamma}^{n-1}, \quad (7.1)$$

where A is a fit parameter and n is the shear thinning exponent. Non-Newtonian liquid behavior is characterized by $n < 1$; that is, the viscosity decreases with increasing shear rate. In the case where $n = 1$, the liquid

7.1 Viscosity measurements in the molten state

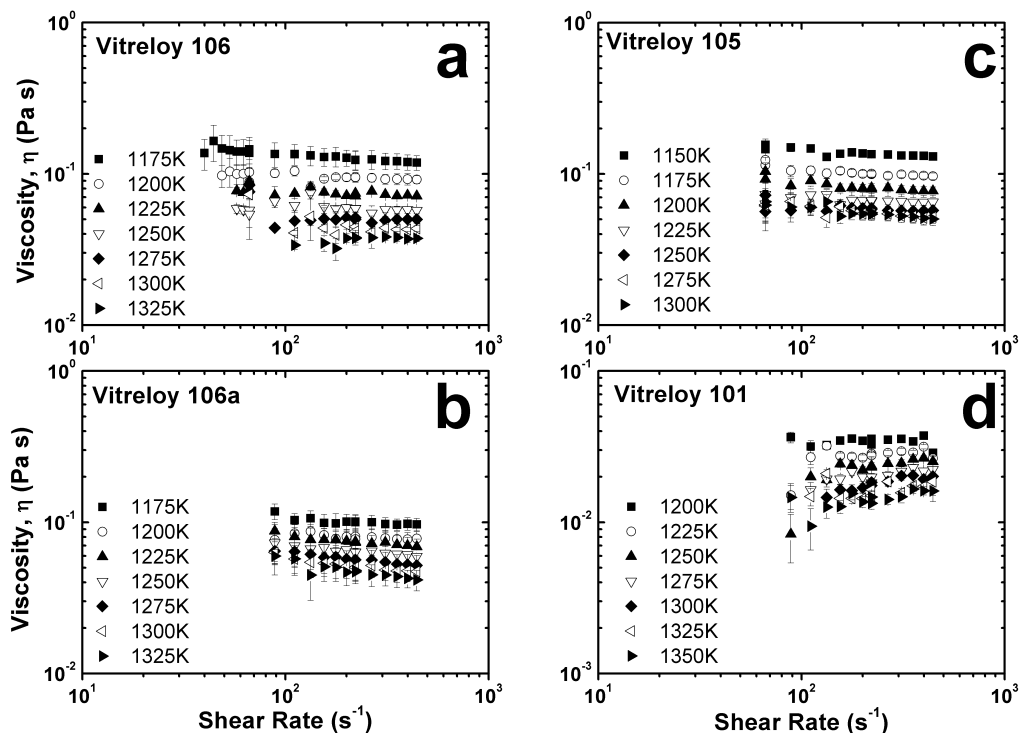


Figure 7.2: Isothermal viscosity vs. shear rate upon heating of the initially amorphous (a) Vitreloy 106, (b) Vitreloy 106a, (c) Vitreloy 105 and (d) Vitreloy 101 alloys. Measurement data were taken beginning just above T_{liq} and collected in 25 K intervals. Note the change in viscosity scale of the Vitreloy 101 composition. The error bars represent the uncertainty due to systemic error; where no bars are seen, the error is on the order of the symbol size [209].

exhibits Newtonian behavior and the viscosity has no shear rate dependence.

Figure 7.3 shows the fitted value of the shear thinning exponent, n , of each alloy for each measurement temperature. Shown for each alloy are two datasets. The 1st temperature scan (filled circles) corresponds to the first series of isothermal viscosity measurements of the initially amorphous material; the 2nd temperature scan (open circles) corresponds to the subsequent repetition of the isothermal measurements performed during the 1st temperature scan. The value of n does not decrease below 0.8 in any of the data sets plotted in Fig. 7.3. Additionally, no clear dependence of n on temperature is able to be discerned for either temperature scan nor is any significant change in n observed between temperature scans. All values of n shown for Vitreloy 101 (Fig. 7.3d) were determined to be 1.0 ± 0.3 .

7.1 Viscosity measurements in the molten state

Since volume fractions of the crystal state can remain in the melt up to T_{liq} , it is important that any viscosity measurement of the alloy melt take place at significantly high enough temperatures, such as to discount the effect of remaining crystallites on the measured melt viscosity. All measurements of the shear viscosity upon heating were carried out after the completion of the melting transition at T_{liq} . The values of T_{liq} given in Table 7.1 represent experimental values measured using the DTA setup outlined in Sec. 4.3. The melting peak of Vitreloy 106 appears to be completed at a temperature of 1115 K; however, the existence of a small exothermic jump at $T \sim 1170$ K could possibly signify the completion of melting of remaining crystalline phases. For this reason, measurements of the melt viscosity of Vitreloy 106 were started at 1175 K.

The isothermal shear viscosities shown in Fig. 7.2 upon heating of the initially amorphous samples showed no significant changes when measured a second time, after subsequent completion of the first set of measurements. Furthermore, a determination of the shear thinning exponent, n , from the isothermal melt viscosity measurements (see Fig. 7.3) showed no appreciable shear thinning in either set of measurements. Also, the values of n shown in Fig. 7.3 do not show any significant change between the first and second set of viscosity measurements. These results are in contrast to those of Vitreloy 1 (see Fig. 7.4), where pronounced shear thinning was observed during the first temperature scan, with values of n ranging from 0.4 at 1075 K and increasing to 1.0 at above 1225 K. Moreover, the shear thinning behavior of the Vitreloy 1 melt was observed to vanish ($n = 1$) after the completion of the first set of isothermal viscosity measurements [123].

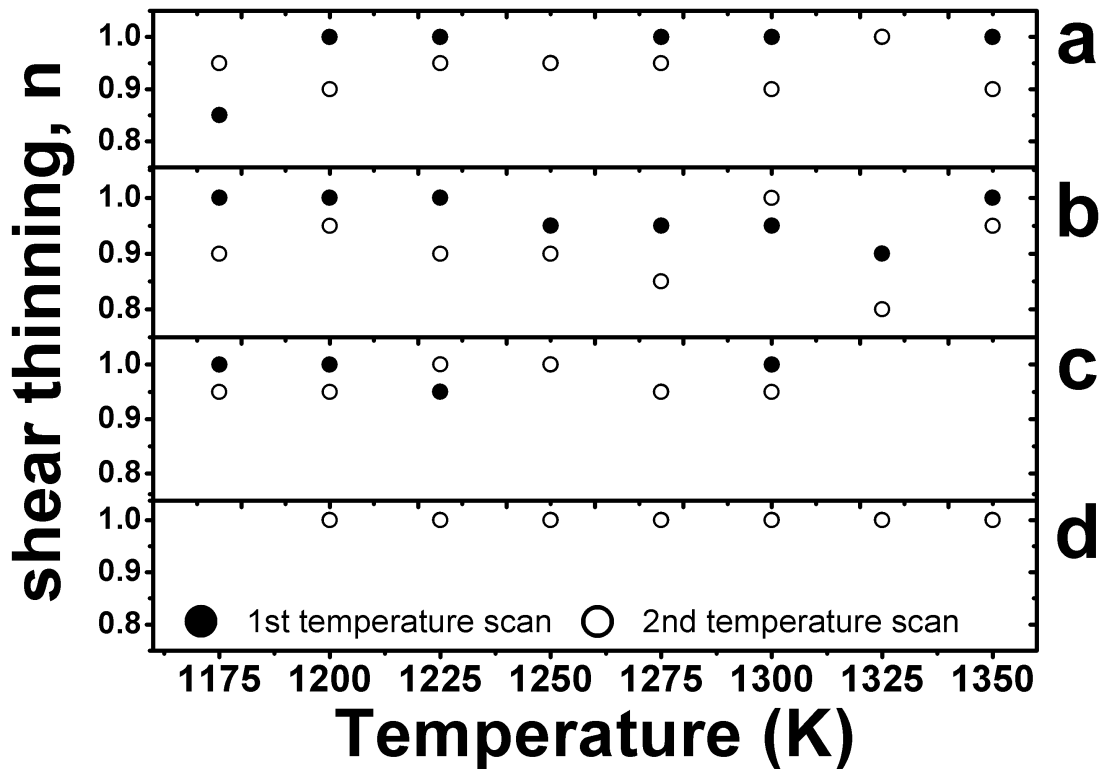


Figure 7.3: Shear thinning exponents, n , of (a) Vitreloy 106, (b) Vitreloy 106a, (c) Vitreloy 105 and (d) Vitreloy 101 determined at each of the measurement temperatures on heating shown in Fig. 7.2. The 1st temperature scan data (filled circles) correspond to the first series of isothermal measurements taken. The 2nd temperature scan data (open circles) were collected after completion of the first series of measurements. No appreciable shear thinning is noticed in any of the compositions investigated. For both data sets, all values of n for Vitreloy 101 (d) were determined to be 1.0 ± 0.3 [209].

7.2 Viscous behavior of the melt

The pronounced shear rate and temperature dependence of the viscosity observed in the Vitreloy 1 melt was attributed to the presence of short- and medium-range order above T_{liq} [123]. Simple structural models of BMG-forming melts based on icosahedral clusters have been proposed by Miracle [102, 103] and Ma et al. [105] and were discussed in Sec. 3.2. The destruction of the MRO, due to a combination of mechanical shearing and temperature increase, is thought to give rise to the shear thinning and strong-to-fragile transition observed in Vitreloy 1 [123].

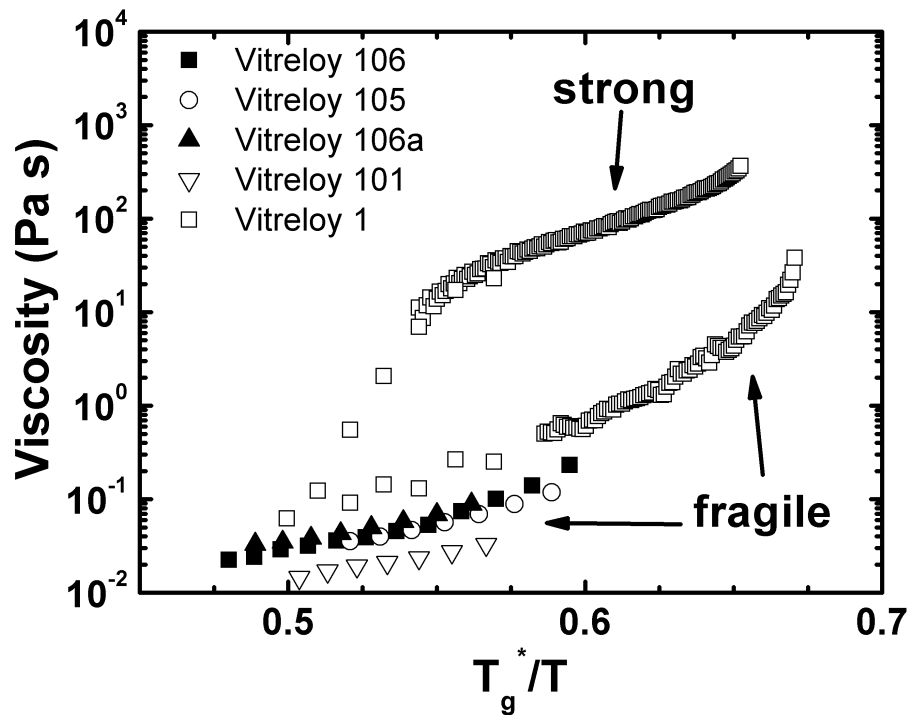


Figure 7.4: Angell-plot showing the experimentally determined melt viscosities of each alloy investigated here [209]. Included are the viscosity data from Vitreloy 1 (open squares) taken from Ref. [123].

Figure 7.4 shows an Angell-plot of the measured melt viscosities of the alloys investigated here. Included as a comparison are the measured data from Vitreloy 1 (open squares), taken from Ref. [123]. The isothermal viscosity data were taken as the average of the 1st and 2nd temperature scans upon heating. Furthermore, even though zero to negligible shear thinning was observed for any of these alloys, only viscosity data corresponding to the

highest shear rates were considered, as to minimize the precision error inherent in measuring with low shear rates.

An overview of the experimentally determined viscosities of each composition over a wide temperature range is shown in the extended Angell-plot in Fig. 7.5. To highlight the distinct difference in fragilities between the low and high-temperature regimes, VFT-fits of the three-point beam-bending (solid curve) and concentric shear cell (dashed lines) viscosity data for Vitreloy 106a are provided. In contrast to the value of $D^* = 21$ determined in three-point beam-bending experiments, a value of $D^* = 10$ was obtained here by fitting the high-temperature data while assuming a T_g at $\eta = 10^{12}$ Pa s. Using the same fitting procedure, the high-temperature values of D^* were determined to be 9.6 for Vitreloy 106, 9.1 for Vitreloy 105 and 7.9 for Vitreloy 101. Comparing these values with those determined in three-point beam-bending experiments in the vicinity of T_g (see Table 7.1), one sees that the high-temperature liquid state is decidedly more fragile than that of the low-temperature regime. A transition from a kinetically fragile to a kinetically strong liquid must therefore take place in the liquid melt.

The data presented in Figs. 7.2d and 7.4 show that the melt viscosities determined for the Vitreloy 101 alloy are in accordance with those published in Ref. [270] using the noncontact oscillating drop technique above T_{liq} . However, the melt viscosity of the Cu-based Vitreloy 101 alloy was measured here to be $\sim 50\%$ lower than that of the Zr-based alloys. This result certainly appears reasonable, given that the diffusivity of Cu in its molten state is almost an order of magnitude greater than Zr, which is considered to act as the slow moving "backbone" of many Zr-based BMG systems [19]. Additionally, as shown in Fig. 7.3d, virtually no shear thinning behavior was observed in Vitreloy 101 ($n = 1$). This might suggest the absence of pronounced medium-range order in this particular system, as compared to that of the Zr-based BMGs. It should be pointed out though, that a fragility parameter of $D^* \sim 10$, which is more or less representative of all the BMG compositions studied here in their molten states, still corresponds to a kinetically stronger system than what is expected for simple metallic liquids with a value of $D^* \sim 2$ [86, 123, 278]. This suggests that there might still exist a high degree of short-range order in the high-temperature state of these molten BMG-forming systems.

During undercooling from the melt, the shear viscosity and temperature of the molten sample can be monitored simultaneously, as is shown in Fig. 7.6. Here the shear viscosity was determined at a constant shear rate of 50 s^{-1} while at the same time the temperature of the melt was recorded during undercooling

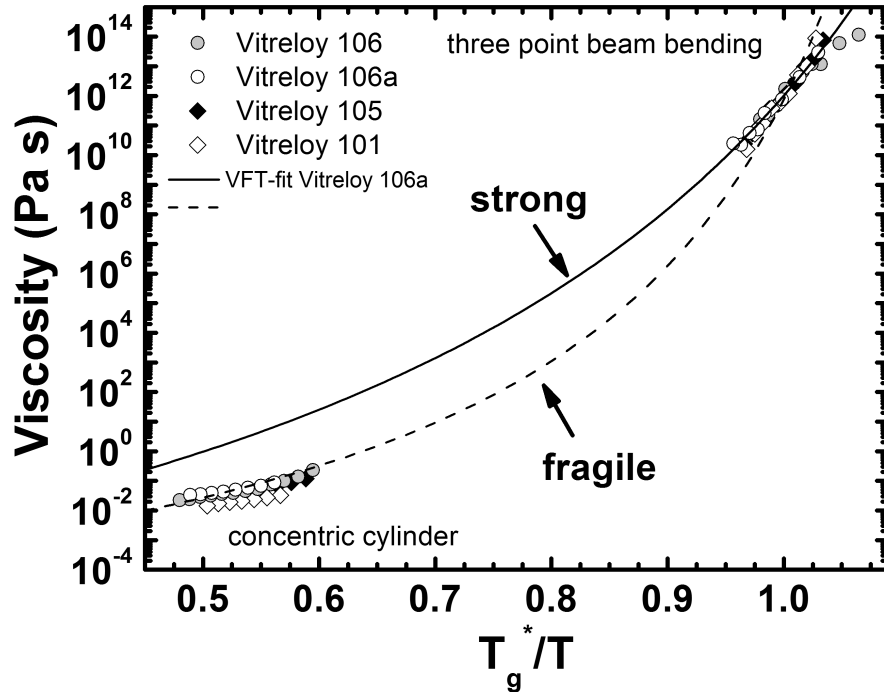


Figure 7.5: Angell-plot over the entire temperature range of measured viscosities for the alloys under investigation here. At low temperatures, near T_g , the isothermal equilibrium viscosities were measured using three-point beam-bending. Separate VFT-fits to the low and high temperature viscosity data of, e.g. Vitreloy 106a, are included here as solid and dashed curves, respectively. A VFT-fit of the low-temperature three-point beam-bending viscosity data yields a fragility parameter, D^* , of 21. From fitting the Vitreloy 106a viscosity data taken at temperatures above T_{liq} , D^* was determined to be ~ 10 [209].

from 1350 K with a cooling rate of $\sim 3 \text{ K s}^{-1}$. Beginning from T_{liq} the shear viscosity showed a slight increase during the first 10 seconds of undercooling, from ~ 0.3 to $\sim 0.6 \text{ Pa s}$, reflecting the decrease in atomic mobility as the melt was undercooled. At $\sim 1075 \text{ K}$ the shear viscosity increased abruptly almost two orders of magnitude to $\sim 30 \text{ Pa s}$, where the measurable limit of the torque sensor was exceeded. In the temperature signal, recalescence due to melt crystallization was measured to occur at the same time. Similar undercooling experiments carried out on each of the other alloy systems investigated showed analogous behavior; namely, the shear viscosity was observed to rise sharply around two orders of magnitude, coinciding with recalescence.

In each of the undercooling experiments during which a constant shear rate was applied, a sharp rise in the viscosity was observed at a particular degree of

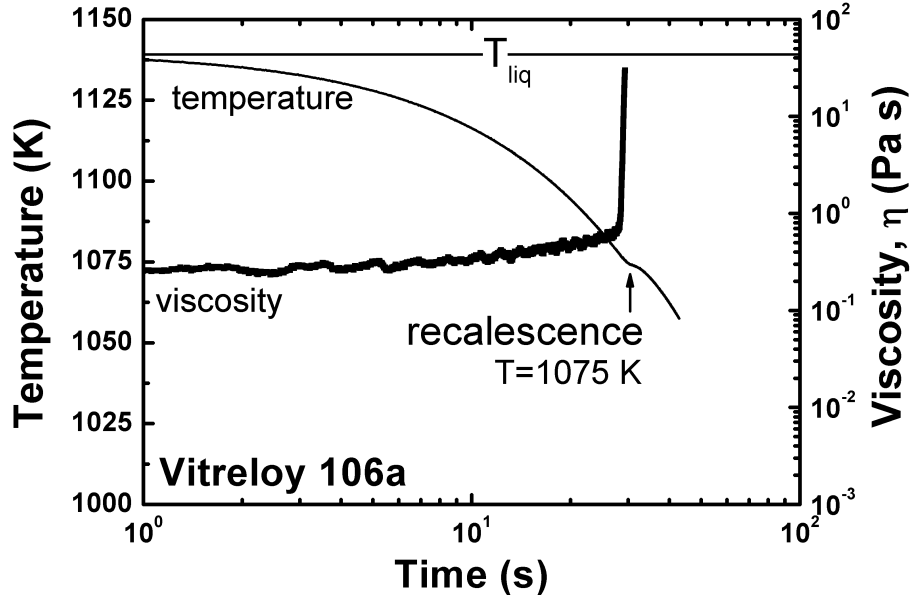


Figure 7.6: Measured viscosity at a shear rate of 50 s^{-1} during undercooling (filled squares) and temperature profile (solid curve) vs. time of Vitreloy 106a. The onset of recalcescence due to crystallization of the melt occurs at approximately the same temperature (1075 K) at which the viscosity exceeds the measurable range of the torque sensor [209].

undercooling. Since the viscosity rise occurs at the same temperature where recalcescence is measured, this can be interpreted as being due to the bulk crystallization of the melt. This is in contrast to Vitreloy 1, where the onset of recalcescence occurs a full 60 K below the temperature at which the viscosity exceeds the torque sensor's measurement capabilities.

It should be noted, however, that even when no shearing was applied, the recalcescence of Vitreloy 106a, for example, was still observed to occur after only $\sim 30 \text{ s}$ of undercooling at a rate of $\sim 3 \text{ K s}^{-1}$. This is in contrast to the previously published data of Hays et al. [201], showing the Vitreloy 106a alloy as having a critical cooling rate of 1.75 K s^{-1} as measured using containerless electrostatic levitation (ESL). Solidification experiments on Vitreloy 1, on the other hand, show that undercooling experiments performed using ESL [129] give the same time-temperature-transformation diagram as those performed in high-purity graphite [279]. The alloy melts investigated here apparently do not show the same degree of resistance to heterogeneous nucleation as Vitreloy 1.

Although the measured viscosity rise during undercooling (Fig. 7.6) can be

attributed to crystallization of the melt, the experimental results shown in Figs. 7.4 and 7.5 nevertheless give evidence of a distinctively more fragile liquid state at temperatures above T_{liq} than close to T_g . Furthermore, in contrast to Vitreloy 1, no transition from the strong to fragile state could be directly observed in any of the alloys investigated here. In Vitreloy 1, the transition from the ordered, kinetically strong to the disordered, kinetically fragile liquid state was observed to begin at ~ 1100 K, which is ~ 75 K above T_{liq} (see e.g. Fig. 7.4). After 1300 K the Vitreloy 1 melt is completely disordered and upon cooling observed to re-order into the strong liquid state at 907 K and later crystallize.

Since none of the investigated compositions showed a direct transition from the strong to the fragile liquid above T_{liq} , it is conceivable that such a transition takes place in the undercooled liquid itself. However, since each of the investigated alloys was observed to already be in its fragile state upon completion of melting at T_{liq} , the hysteretic viscosity behavior seen in Vitreloy 1 (Fig. 7.4) can therefore not be observed in these cases.

7.3 Fragile-to-strong transition

Very recently, further experimental evidence of fragile-to-strong transitions in BMG-forming liquids was published by Zhang et al. [271], where it was revealed that a variety of Gd-, Pr-, Sm-, La-, Al- and Ce-based BMG-forming systems exhibited distinctively more fragile liquid behavior in the high-temperature melt than at low temperatures near T_g . Additionally, experimental evidence of a fragile-to-strong transition was also found by Ito et al. in supercooled water [280], while simulation data show that the archetypically strong liquids SiO_2 [281–283] and BeF_2 [284] also undergo a fragile-to-strong transition at high temperatures.

It has been proposed that the underlying nature of this fragile-to-strong transition is due to the existence of two compositionally identical amorphous phases in the liquid state [123, 271]. Such a phenomenon, known as *polyamorphism*, has already been experimentally observed in water [285] and Al_2O_3 - Y_2O_3 melts [286–288]. Furthermore, recent experimental evidence has also shown that pressure-induced polyamorphic transitions can occur in the vitreous state of the $\text{Ce}_{55}\text{Al}_{45}$ metallic glass as well [289]. Analogous to crystalline polyamorphism, in which the same material can exist with more than one crystal structure, polyamorphism is characterized by the existence of two or more amorphous states. Such a transition occurring in the liquid state is usually described as a liquid-liquid transition. These polyamorphic transitions are

7.3 Fragile-to-strong transition

thought of as being density-driven; that is, the two coexisting liquid phases differ from each other only in density [285, 286].

In the $\text{Al}_2\text{O}_3\text{-Y}_2\text{O}_3$ system, this liquid-liquid transition occurs during quenching from the melt, resulting in two coexisting glassy phases with different densities [286]. In contrast to conventional phase separation, where demixing results in two compositionally different phases, the two amorphous phases discussed here are of the same composition. These low-density and high-density liquid states (LDL and HDL, respectively) can be characterized by having different coordination numbers. In liquid SiO_2 , for example, the pressure-induced transition from the LDL to the HDL states is thought to be related to the change from four-fold to five- or six-fold coordination [282]. In $\text{Al}_2\text{O}_3\text{-Y}_2\text{O}_3$, the structural changes with temperature have been proposed to occur mainly through the change from corner- to edge-shared AlO_4 and YO_6 structural units [287].

Additionally, liquid-liquid transitions are thought to be driven by a reduction in entropy and accompanied by a change from fragile liquid to strong liquid behavior [290, 291]. In the SiO_2 [282] and $\text{Al}_2\text{O}_3\text{-Y}_2\text{O}_3$ [287, 292] systems, as well as in water [293], the strong liquid state is characterized by having a low density (LDL), while the fragile liquid has the higher density (HDL). In each of these systems, the strong LDL that is present at low-temperatures exhibits a more open, usually tetrahedrally bonded network, while the fragile HDL that is present at higher temperatures has much weaker local organization [23, 282, 294].

In metallic glass systems, whose structural models are based on the dense and efficient packing of icosahedral clusters (see e.g. Refs. [102, 103, 105]), the presence of pronounced short- and medium-range order is associated with the strong, high viscosity liquid state, while destruction of this order at higher temperatures (or through mechanical shearing) is thought to cause a polyamorphic transition to a more kinetically fragile liquid with lower viscosity [123]. However, the mechanism by which the degree of order in the melt exactly affects the fragility, is still largely unclear. The melt viscosity of Vitreloy 1, for example, is close to three orders of magnitude larger than for simple metallic systems [19, 278], suggesting an efficient and dense packing scheme amongst its atomic constituents. Moreover, the addition of more elements to certain BMG-forming systems has been shown to cause an increase in the kinetic fragility parameter, D^* , of the supercooled liquid near T_g [86]. It would therefore seem reasonable to think that, by increasing the alloy complexity, a higher degree of packing is introduced, resulting in a more viscous and kinetically stronger melt. Yet, in the cases of the fragile-to-strong

7.3 Fragile-to-strong transition

transition in the non-metallic glass-formers discussed above, the strong liquid has the lower density (LDL), and it is the fragile liquid that is denser (HDL). In these cases, it appears that the determining factor for the fragility is the interaction potential and organization of the liquid's structural units. While the strong liquid phase may be structurally more open and less dense, it also exhibits a more developed and directional bond network. In SiO_2 and water the strong LDL phase is characterized by a fully developed, tetrahedrally coordinated network [293]. In contrast, the fragile HDL phase is formed by a disruption of this network – either through an increase in pressure or temperature – resulting in an increase in entropy and decrease in longer range structure; e.g., the medium-range order.

It should be recognized, however, that the relationship between density and fragility examined in these network-forming liquids does not necessarily extend to all such cases. Comparison of experimental data on the physical properties of various chalcogenide glasses, for example, shows that the kinetically strongest might also correspond to those with the highest density [295, 296]. Those results highlight the important role played by the bonding of the liquid's local structural elements in determining its kinetic and physical properties. Furthermore, there does seem to exist some evidence for a fragile-to-strong transition in Ge-Se liquids [297], as well as anomalous density variations, due to a change in the local bonding configuration, in high-temperature melts of Ge-As-Se [298].

In examining the case of the BMG-forming melts discussed here, it was speculated that the MRO present in the strong liquid consists of a highly organized network of SRO clusters. In the structural models of Refs. [102, 103, 105], this organization is thought to occur by placing the SRO clusters on fcc-lattice sites, or by arranging them onto larger icosahedral or icosahedral-like extended clusters. With regard to the MRO, simulation studies indicate that a percolating network of SRO clusters can form the "backbone" of metallic glasses [299]. Furthermore, the medium-range correlation was studied in certain simulated Cu-Zr glasses in Ref. [300], and it was found that strongly correlated icosahedral SRO clusters can form an interpenetrating, solid-like backbone network with a string-like topology.

Regardless of the exact structure of the MRO, it can nevertheless be inferred by the data presented in Figs. 7.4 and 7.5, that the fragile liquid should consist of less order than the strong liquid. In his model of glass-forming liquids, Tanaka [222] shows that strong short-range bond ordering positively correlates with a decrease in fragility. Extending this argument, it can be assumed that the highly medium-range ordered liquid should be stronger than

the liquid in which only SRO dominates. It should however be noted that the case for metallic liquids is quite different than that for molecular and network-forming liquids, in that the metallic liquid structure is denser and the atoms are more homogeneously distributed throughout the liquid [94]. Furthermore, it is difficult to predict whether the strong BMG-forming liquid should correspond to the higher or lower density state, as there is no reason to expect these metallic systems to behave like the network-forming, non-metallic glass-formers discussed above. Nevertheless, these cases could still provide a useful link to the phenomenology of the fragile-to-strong transition in BMG-forming liquids.

Finally, recent experimental studies on the kinetic arrest of B2 ordering in the crystalline $\text{Fe}_{50}\text{Co}_{50}$ superlattice [301] have shown parallels between that system's lambda (order-disorder) transition and the liquid-liquid transitions found in many glass-forming systems. In $\text{Fe}_{50}\text{Co}_{50}$, the kinetics of disordering are much slower than usual, such that a kinetic arrest occurs long before the ordering process is completed upon cooling from above the lambda transition. As such, when re-heated, the partially disordered $\text{Fe}_{50}\text{Co}_{50}$ system will exhibit enthalpic behavior consistent with that of a perfectly strong ($m = 16$) glass-forming liquid. These similarities seem to imply that fragile and strong liquids can be thought of as occupying opposite ends of an underlying order-disorder transition [301, 302].

7.4 Summary and Conclusions

The shear viscosities of the Vitreloy 106, 106a, 105 and 101 BMG alloys were determined at temperatures above T_{liq} using a Couette concentric cylinder viscometer. In contrast to the Vitreloy 1 alloy, no appreciable shear thinning or hysteretic viscosity behavior was observed for any of these compositions in their molten state. The measured melt viscosities for Vitreloy 106, 106a and 105 were on the order of 10^{-1} Pa s, while Vitreloy 101 was observed to be less viscous, having a melt viscosity closer to $\sim 10^{-2}$ Pa s.

Using a three-point beam-bending technique, viscosity measurements in the vicinity of T_g revealed that each of the investigated alloys showed distinctively stronger liquid kinetic behavior than in the melt above T_{liq} . These results are in agreement with others published on metallic glass-forming systems [123, 271]. However, after the completion of melting at T_{liq} , each investigated melt was observed to already be in its fragile state. Therefore, a transition between these two states must take place in the undercooled liquid between T_g and T_{liq} . Undercooling experiments during constant shearing showed a sharp

rise in viscosity, around two orders of magnitude, accompanied simultaneously by a noticeable recalescence, signifying bulk crystallization of the melt.

In experiments on the Vitreloy 1 liquid, it was determined that the observed hysteretic viscosity behavior above T_{liq} (see Fig. 7.4) was indeed due to a polyamorphic transition, and was not the result of phase separation and decomposition, since previous three-dimensional atom probe (3DAP), transmission electron microscopy (TEM) and small-angle X-ray scattering (SAXS) studies confirmed the existence of a chemically homogeneous glass, with no evidence of prior decomposition during cooling [303]. Studies on Vitreloy 105 and 106 also show that no chemical decomposition occurs during quenching from the melt [193], while decomposition is already present in as-cast Vitreloy 101 [244]. Since these data are unavailable for Vitreloy 106a, it cannot be conclusively determined if this alloy undergoes decomposition during quenching.

The Vitreloy 106a liquid crystallizes significantly earlier when undercooled in a graphite crucible, than when cooled using non-contact ESL techniques. This is in contrast to Vitreloy 1, whose crystallization times are relatively unaffected by the crucible's presence. Nevertheless, the high-temperature viscosity experiments described in Sec. 7.1 were performed relatively close to T_{liq} and still no appreciable shear thinning was noticed (Fig. 7.3). The fragile-to-strong transition must then take place in the undercooled melt, as postulated in Ref. [271]. In the case of the experiments presented in this chapter, rapid crystallization of the melt intervenes, due to the potent heterogeneous influence of the crucible wall, and precludes the direct observation of the fragile-to-strong transition as seen in Vitreloy 1.

The fragile-to-strong transition reported on in this chapter can be viewed as a polyamorphic transition from a kinetically fragile to a kinetically strong liquid state with identical composition. This interpretation is supported by short- and medium-range order icosahedral cluster models, possibly involving an order-disorder transition at a liquid-liquid critical point.

Chapter 8

Summarizing remarks and outlook

The overall aim of this work was to present a detailed assessment of the thermodynamics and kinetics of BMG-forming liquid systems. The analyses given here highlighted various topics, such as fragility, free volume and structure, that surround the unique thermophysical phenomena observed in BMG systems.

The fragility concept plays a crucial role in the classification of BMGs according to their equilibrium kinetic properties. The distinction between "strong" and "fragile" BMGs is, however, only a relative assessment. In the bigger picture, the fragilities of BMGs lie in a somewhat narrow range between the archetypically strong SiO_2 and GeO_2 network-forming liquids, and the extremely fragile molecular liquids like *o*-terphenyl [23, 168]. From outright observations, it appears that the addition of more elements to a BMG-forming system decreases the fragility of the melt, making it stronger. However, this notion is challenged by a few other BMG-forming systems, in which the further addition of elements does not appear to significantly affect the fragility, as observed in Zr-based systems. Namely, the noble metal BMG-forming systems [91, 147] exhibit a kinetically more fragile nature, while those based on alkaline earth metals, such as Mg and Ca [104, 304, 305], tend to remain quite strong. Even within the same BMG system the fragility parameter should not be expected to remain the same. In Zr-Cu-Ni-Al-Nb, for example, the fragility parameter varies significantly from $D^* = 21.0$ for Vitreloy 106a to $D^* = 35.2$ for Vitreloy 106. This is one indication that the origin of fragility in BMG-forming melts cannot be solely attributed to the hard-sphere topology; i.e., the extent of atomic packing, but rather the unique electronic structure of each atomic species and their chemical interactions with each other must be considered as well.

In the absence of direct structural investigations using electron microscopy or scattering techniques, one of the greatest challenges faced by experimentalists is to accurately explain the observed macroscopic phenomena in terms of microscopic or atomistic models. The classic free volume model based on hard spheres [58] is conceptually appealing and easy to employ from measurements on macroscopic quantities (e.g. volume change). However, metals tend to deviate from hard-sphere-like behavior, and this is one of the pitfalls concerning the application of the classic free volume theory to BMG systems [255]. Nevertheless, the success of structural models incorporating efficient cluster packing schemes [102, 103, 105], while mainly topological in nature, does seem to validate some of these assumptions. Despite its limitations, the free volume model has been employed by many researchers in the area of metallic glasses. As demonstrated by Argon [267] and Spaepen [268, 306], flow and deformation of metallic glasses are described well by a free volume approach. In fact, quite a number other models based on free volume descriptions have been successful in reproducing some of the key features of flow and viscoplastic deformation in BMGs [307–309]. Furthermore, the results presented in this work also showed that relaxation below the glass transition temperature is accompanied by some changes in excess volume, and that these changes are consistent with the amount of viscous flow expected from the free volume theory. However, while these free volume models haven proven themselves to be useful descriptors for certain macroscopic phenomena and can generally be used to fit a wide range of experimental data, their overall applicability to metallic glass systems may be somewhat limited.

Building on the ideas of Gibbs and DiMarzio [180] and later Adam and Gibbs [67], Goldstein [215] proposed a picture of viscous liquid flow being dominated by potential energy barriers that are high in comparison with the thermal energy, $\sim kT$. Later, Stillinger [216, 310] would begin to formalize the concept of what is now known as the potential energy landscape (PEL). Envisioned as a multi-dimensional surface in configurational space, the PEL can be used to give insight into the dynamical differences between fragile and strong liquids during undercooling. Fragile liquids, marked by deviation in Arrhenius behavior of the viscosity or relaxation time, are thought to possess a heterogeneous, or "rugged" landscape, consisting of multiple deep, well-separated megabasins. Relaxation at temperatures close to the glass transition may consist of the cooperative rearrangement of many molecules, reflected by the increase in activation energy as T_g is approached. In contrast, strong liquids are thought to consist of only a single megabasin [217]. Each single basin located within the megabasin has roughly the same height, reflecting the constant activation energy with changing temperature observed for strong liquids.

Applied to metallic glass systems, the PEL has been used as a framework for describing inelastic deformation, as well as certain rheological behavior based on mechanical properties, such as the shear modulus [269, 311]. As of yet, however, investigations into the PEL of metallic glass-forming systems appear to be restricted to shear and flow events observed in the glassy state [312, 313].

The mode-coupling theory (MCT) by Götze [314, 315] has found success as an attempt to understand the initial features of the slowing down of the liquid-like processes in glass-forming liquids. MCT predicts structural arrest at a critical temperature, T_c , below which liquid-like motion is frozen out. At this critical temperature, the diffusivity is predicted to vanish and the structural relaxation time would accordingly diverge [314]. It is now understood that the T_c predicted by MCT occurs at a higher temperature than T_g [241], and in some systems $\sim 20\%$ below the liquidus temperature [316]. Since dynamical divergence experimentally does not occur at T_c , modifications of the theory incorporate additional relaxation mechanisms such that, at T_c , the transport mechanism changes from liquid-like flow for $T > T_c$, to activated hopping processes for $T < T_c$ [317].

A recognized weakness of MCT are its deficiencies in describing real systems below the crossover at T_c ; its usefulness in describing experimental data typically only spans around 2-4 orders of magnitude [241, 318, 319]. From a theoretical standpoint, however, its appeal lies in the fact that the model parameters can be calculated *a priori* and it succeeds in making detailed predictions about relaxation dynamics in the high- T regime [217]. Furthermore, the critical temperature predicted by MCT appears to be compatible with that predicted by Goldstein in his potential energy barrier description [215, 320].

As for applications to metallic systems, recent experimental diffusion data on Pd-Cu-Ni-P melts show a distinct change in transport mechanism from the power-law asymptotic predicted by MCT at high temperatures, to an Arrhenius activated hopping process in the supercooled liquid near the glass transition [316]. Furthermore, the T_c predicted for this system by MCT is in excellent agreement with the temperature, at which these two transport modes were experimentally observed to merge [252]. Other successful applications of MCT to high-temperature dynamics of metallic liquids have been performed on binary Zr-Ni [321] and $\text{Zr}_{46.8}\text{Ti}_{8.2}\text{Cu}_{7.5}\text{Ni}_{10}\text{Be}_{27.5}$ [322].

The topic of the fragile-to-strong transition in Chapter 7 reintroduced the fragility concept and highlighted its role in the question of structure in BMG-forming melts. The observation of two kinetically distinct viscous states of the liquid; i.e., fragile and strong, can certainly be explained within the proposed

short and medium-range order structural model of metallic glasses. Indeed, it was already shown that the local structure preference drives the polyamorphic fragile-to-strong transition in water [285, 294, 323], SiO₂ [282] and Al₂O₃-Y₂O₃ liquids [287, 292]. It should therefore be reasonable to assume that a similar structure-driven transformation occurs in BMG liquids, in which pronounced order has already been experimentally affirmed [112, 114, 324, 325]. The fact that a variety of kinetically strong, BMG-forming liquids show similar viscous behavior [271] implies that the fragile-to-strong transition might be a universal phenomenon amongst BMGs, if not glass-forming liquids in general [301].

Although not addressing metallic systems in particular, Angell [139] has put forth the idea that the polyamorphic transition observed in many glass-forming liquids is a manifestation of the system being able to sample more than one type of PEL. This viewpoint places the fragile and strong states of the liquid onto separate megabasins, with the strong liquid megabasin being located at lower potential energies. The fragile liquid can then relocate into the strong liquid megabasin (and vice versa) through a first-order phase transition at a certain temperature. There has also apparently been success in describing some of the features of the fragile-to-strong transition in water with an extended version of the MCT [326, 327].

Returning now to the free volume model, it is interesting to consider the role of the free volume in the fragile-to-strong transition. Since the free volume theory was originally developed to describe the viscous slowdown of glass-forming liquids during cooling, it is not surprising that free volume assessments are usually absent from the subject of polyamorphic phase transitions in liquids. In describing the difference between each amorphous phase, one only needs to consider parameters like entropy or density; it appears that a free volume description in this case would be superfluous. However, free volume is a useful concept to describe flow processes, as it can be intimately related with the viscosity. Considering that the fragile and strong versions of a given polyamorphic liquid can be readily distinguished from each other by differences in viscosity (see Chapter 7), it stands to reason that the free volume could, nevertheless, become a useful descriptor of the two liquid states.

However, the question of how exactly the free volume is distributed in the liquid still remains open and needs to be answered before drawing any conclusions about its role in the fragile-to-strong transition. Pressure-induced polyamorphism in network-forming gallo-germanosilicate [328] and B₂O₃ [329, 330] glasses have shown that, at least in these systems, the case is relatively straightforward – increased pressure results in densification and topological

distortion of the tetrahedral network, and accordingly reduces the free volume. The case for BMG-forming liquids, on the other hand, might not be that clear. Indeed, as was discussed in this work, the free volume in BMGs appears to be quite different from that in network-forming and molecular glasses. As of yet, however, only viscometric data have provided evidence of a fragile-to-strong transition in BMG melts; therefore, without accompanying structural data, interpretations of this phenomenon based on free volume models would be mostly speculative.

Although, it may in fact be the case that free volume models will ultimately offer no new information about the dynamics of BMG-forming liquids. It would appear that a physically more satisfying, while albeit somewhat more abstract, approach to the thermodynamics and kinetics of metallic glass-forming liquids is a configurational entropy description using the Adam-Gibbs formulation, as carried out here in Chapter 5. This was advocated by Goldstein in the 1960s over the classic free volume theory [215, 238]. Since then, the picture of viscous liquids has been continuously adapted to include the ideas of cooperative dynamics and the potential energy landscape [23, 49, 139, 173, 214, 216, 217, 331]. The incorporation of BMG liquids into this picture has taken place not only through the development of new compositions, improved microscopy and scattering techniques, but also through novel methods of gleaning new information from thermodynamic and kinetic properties, such as diffusion [220, 252, 253, 332], viscosity [123, 271] and heat capacity [301].

Appendix A

Alloy properties

Zr_{41.2}Ti_{13.8}Cu_{12.5}Ni_{10.0}Be_{22.5}

Trade name: Vitreloy 1

$T_g = 620$ K ($q_H = 0.333$ K/s) [13]

$T_x = 629$ K ($q_H = 0.333$ K/s) [13]

$T_K = 560$ K [13]

$T_K = 387$ K [91]

$\Delta H_x = -5.6$ kJ g-atom⁻¹ ($q_H = 0.333$ K/s) [13]

$T_{eut} = 937$ K [13]

$T_{liq} = 1026$ K [123]

$\Delta H_f = 8.2$ kJ g-atom⁻¹ [13]

$\Delta S_f = 8.0$ J g-atom⁻¹ K⁻¹

$\rho = 6087$ kg m⁻³

$\mu = 60.03$ g g-atom⁻¹

Specific heat fitting constants

a	b	c	d
(J g-atom ⁻¹ K ⁻²)	(J K g-atom ⁻¹)	(J g-atom ⁻¹ K ⁻²)	(J g-atom ⁻¹ K ⁻³)
9.2197×10^{-3}	7.5841×10^6	-8.5970×10^{-3}	2.1611×10^{-5}

Table A.1: Ref. [91]

Zr_{44.0}Ti_{11.0}Cu_{10.0}Ni_{10.0}Be_{25.0}

Trade name: Vitreloy 1b

$$T_g = 620 \text{ K } (q_H = 0.416 \text{ K/s})$$

$$T_x = 774 \text{ K } (q_H = 0.416 \text{ K/s})$$

$$T_K = 541 \text{ K}$$

$$T_0 = 367 \text{ K}$$

$$\Delta H_x = -7.5 \text{ kJ g-atom}^{-1} (q_H = 0.416 \text{ K/s})$$

$$T_{eut} = 921 \text{ K}$$

$$T_{liq} = 1102 \text{ K}$$

$$\Delta H_f = 9.30 \text{ kJ g-atom}^{-1}$$

$$\Delta S_f = 8.44 \text{ J g-atom}^{-1} \text{ K}^{-1}$$

$$\rho = 6047 \text{ kg m}^{-3}$$

$$\mu = 59.88 \text{ g g-atom}^{-1}$$

Specific heat fitting constants

a	b	c	d
(J g-atom ⁻¹ K ⁻²)	(J K g-atom ⁻¹)	(J g-atom ⁻¹ K ⁻²)	(J g-atom ⁻¹ K ⁻³)
6.530×10^{-3}	7.090×10^6	-7.990×10^{-3}	1.94×10^{-5}

Table A.2: This work

Zr_{57.0}Cu_{15.4}Ni_{12.6}Al_{10.0}Nb_{5.0}

Trade name: Vitreloy 106

$$T_g = 673 \text{ K } (q_H = 0.25 \text{ K/s})$$

$$T_x = 736 \text{ K } (q_H = 0.25 \text{ K/s})$$

$$T_K = 664 \text{ K [270]}$$

$$T_0 = 348 \text{ K}$$

$$\Delta H_x = -5.5 \text{ kJ g-atom}^{-1} (q_H = 0.333 \text{ K/s})$$

$$T_{eut} = 1091 \text{ K [270]}$$

$$T_{liq} = 1115 \text{ K [270]}$$

$$\Delta H_f = 9.40 \text{ kJ g-atom}^{-1} [270]$$

$$\Delta S_f = 8.43 \text{ J g-atom}^{-1} \text{ K}^{-1}$$

$$\rho = 6689 \text{ kg m}^{-3}$$

$$\mu = 76.52 \text{ g g-atom}^{-1}$$

Specific heat fitting constants

a	b	c	d
(J g-atom ⁻¹ K ⁻²)	(J K g-atom ⁻¹)	(J g-atom ⁻¹ K ⁻²)	(J g-atom ⁻¹ K ⁻³)
1.330×10^{-2}	6.320×10^6	-3.020×10^{-3}	8.370×10^{-6}

Table A.3: Ref. [270]

Zr_{58.5}Cu_{15.6}Ni_{12.8}Al_{10.3}Nb_{2.8}

Trade name: Vitreloy 106a

$$T_g = 671 \text{ K } (q_H = 0.25 \text{ K/s})$$

$$T_x = 752 \text{ K } (q_H = 0.25 \text{ K/s})$$

$$T_K = 548 \text{ K [164]}$$

$$T_0 = 437 \text{ K}$$

$$\Delta H_x = -6.38 \text{ kJ g-atom}^{-1} (q_H = 0.333 \text{ K/s}) [164]$$

$$T_{eut} = 1080 \text{ K}$$

$$T_{liq} = 1140 \text{ K}$$

$$\Delta H_f = 8.70 \text{ kJ g-atom}^{-1} [164]$$

$$\Delta S_f = 7.75 \text{ J g-atom}^{-1} \text{ K}^{-1}$$

$$\rho = 6642 \text{ kg m}^{-3}$$

$$\mu = 76.17 \text{ g g-atom}^{-1}$$

Specific heat fitting constants

a	b	c	d
(J g-atom ⁻¹ K ⁻²)	(J K g-atom ⁻¹)	(J g-atom ⁻¹ K ⁻²)	(J g-atom ⁻¹ K ⁻³)
5.650×10^{-3}	5.697×10^6	-7.10×10^{-3}	1.365×10^{-5}

Table A.4: Ref. [164]

Zr_{52.5}Cu_{17.9}Ni_{14.6}Al_{10.0}Ti_{5.0}

Trade name: Vitreloy 105

$$T_g = 675 \text{ K } (q_H = 0.333 \text{ K/s}) \text{ [270]}$$

$$T_x = 727 \text{ K } (q_H = 0.333 \text{ K/s}) \text{ [270]}$$

$$T_K = 638 \text{ K [270]}$$

$$T_0 = 443 \text{ K}$$

$$\Delta H_x = -6.76 \text{ kJ g-atom}^{-1} (q_H = 0.333 \text{ K/s})$$

$$T_{eut} = 1044 \text{ K}$$

$$T_{liq} = 1125 \text{ K}$$

$$\Delta H_f = 8.20 \text{ kJ g-atom}^{-1} \text{ [270]}$$

$$\Delta S_f = 7.52 \text{ J g-atom}^{-1} \text{ K}^{-1}$$

$$\rho = 6568 \text{ kg m}^{-3}$$

$$\mu = 72.93 \text{ g g-atom}^{-1}$$

Specific heat fitting constants

<i>a</i>	<i>b</i>	<i>c</i>	<i>d</i>
(J g-atom ⁻¹ K ⁻²)	(J K g-atom ⁻¹)	(J g-atom ⁻¹ K ⁻²)	(J g-atom ⁻¹ K ⁻³)
2.120×10^{-2}	6.430×10^6	-8.61×10^{-3}	1.680×10^{-5}

Table A.5: Ref. [270]

Cu_{47.0}Ti_{34.0}Zr_{11.0}Ni_{8.0}

Trade name: Vitreloy 101

$$T_g = 673 \text{ K } (q_H = 0.333 \text{ K/s}) \text{ [270]}$$

$$T_x = 717 \text{ K } (q_H = 0.333 \text{ K/s}) \text{ [270]}$$

$$T_K = 537 \text{ K [270]}$$

$$T_0 = 479 \text{ K}$$

$$\Delta H_x = -7.50 \text{ kJ g-atom}^{-1} (q_H = 0.333 \text{ K/s})$$

$$T_{eut} = 1083 \text{ K}$$

$$T_{liq} = 1164 \text{ K}$$

$$\Delta H_f = 11.30 \text{ kJ g-atom}^{-1} \text{ [270]}$$

$$\Delta S_f = 10.01 \text{ J g-atom}^{-1} \text{ K}^{-1}$$

$$\rho = 6775 \text{ kg m}^{-3}$$

$$\mu = 60.87 \text{ g g-atom}^{-1}$$

Specific heat fitting constants

<i>a</i>	<i>b</i>	<i>c</i>	<i>d</i>
(J g-atom ⁻¹ K ⁻²)	(J K g-atom ⁻¹)	(J g-atom ⁻¹ K ⁻²)	(J g-atom ⁻¹ K ⁻³)
1.560×10^{-2}	2.830×10^6	-8.90×10^{-4}	6.82×10^{-6}

Table A.6: Ref. [270]

Au_{49.0}Cu_{26.9}Si_{16.3}Ag_{5.5}Pd_{2.3}

Trade name: *none*

$$T_g = 396 \text{ K } (q_H = 0.333 \text{ K/s})$$

$$T_x = 456 \text{ K } (q_H = 0.333 \text{ K/s})$$

$$T_K = 348 \text{ K}$$

$$T_0 = 268 \text{ K}$$

$$\Delta H_x = -3.59 \text{ kJ g-atom}^{-1} (q_H = 0.333 \text{ K/s})$$

$$T_{eut} = 615 \text{ K}$$

$$T_{liq} = 650 \text{ K}$$

$$\Delta H_f = 5.30 \text{ kJ g-atom}^{-1}$$

$$\Delta S_f = 8.14 \text{ J g-atom}^{-1} \text{ K}^{-1}$$

$$\rho = 13120 \text{ kg m}^{-3}$$

$$\mu = 126.57 \text{ g g-atom}^{-1}$$

Specific heat fitting constants

<i>a</i>	<i>b</i>	<i>c</i>	<i>d</i>
(J g-atom ⁻¹ K ⁻²)	(J K g-atom ⁻¹)	(J g-atom ⁻¹ K ⁻²)	(J g-atom ⁻¹ K ⁻³)
1.395×10^{-2}	2.200×10^6	-1.43×10^{-2}	4.62×10^{-5}

Table A.7: This work

Appendix B

Copyright Permissions

A portion of the figures located in this work were reprinted with the kind permissions of: *Elsevier Limited*, *The American Institute of Physics*, *The American Association for the Advancement of Science*, *The Materials Research Society* and *Nature Publishing Group*.

Figure	Reference	License #
2.8	[23]	2901331055768
3.1, 3.2	[85]	2920220835353
3.3	[86]	2901251203693
3.4	[92]	2920221232676
3.5	[96]	2920221423556
3.7	[101]	2920230311925
3.8, 3.9	[123]	2920230487586
3.11	[129]	2920230834329
3.12	[14]	2920231093898
3.13	[139]	2920231331014
3.14	[142]	2920240496687
2.9, 5.1-5.6	[75]	2901250938064
5.8, 5.11, 5.12, 5.30, 5.32-5.34, 6.1, 6.5-6.11	[177]	2901250307353
5.23, 5.27, 6.2, 6.4	[208]	2901250600185
5.24, 7.2-7.6	[209]	3014110230673

References

- [1] Raedersdorf, S., *Master thesis*, Master thesis, Saarland University, 2007.
- [2] Schmitt, T., *Viscosity measurements on Zr-based bulk metallic glass forming liquids above the melting point*, Diploma thesis, Saarland University, 2008.
- [3] Hembree, W., *Master thesis*, Master thesis, Saarland University, 2010.
- [4] Turnbull, D., *The Journal of Chemical Physics* **18** (1950) 198.
- [5] Turnbull, D., *Journal of Applied Physics* **21** (1950) 1022.
- [6] Turnbull, D. and Cech, R. E., *Journal of Applied Physics* **21** (1950) 804.
- [7] Klement, W., Willens, R., and Duwez, P., *Nature* **187** (1960) 896.
- [8] Drehman, A. J., Greer, A. L., and Turnbull, D., *Applied Physics Letters* **41** (1982).
- [9] Inoue, A., Nakamura, T., Sugita, T., Zhang, T., and Masumoto, T., *Materials Transactions-JIM* **34** (1993) 351.
- [10] Inoue, A., Zhang, T., Nishiyama, N., and Ohba, K., *Materials Transactions-JIM* **34** (1993) 1234.
- [11] Inoue, A., Nakamura, T., Nishiyama, N., and Masumoto, T., *Materials Transactions-JIM* **33** (1992) 937.
- [12] Peker, A. and Johnson, W. L., *Applied Physics Letters* **63** (1993) 2342.
- [13] Busch, R., Kim, Y. J., and Johnson, W. L., *Journal of Applied Physics* **77** (1995) 4039.
- [14] Waniuk, T. A., Busch, R., Masuhr, A., and Johnson, W. L., *Acta Materialia* **46** (1998) 5229.
- [15] Masuhr, A., Busch, R., and Johnson, W. L., *Journal of Non-Crystalline Solids* **250-252** (1999) 566.
- [16] Tang, X., Busch, R., Johnson, W. L., and Wu, Y., *Physical Review Letters* **51** (1998) 24.
- [17] Geyer, U. et al., *Physical Review Letters* **75** (1995) 2364.

REFERENCES

- [18] Fielitz, P., Frohberg, G., Macht, M.-P., and Naundorf, V., *Journal of Non-Crystalline Solids* **250-252** (1999) 674.
- [19] Masuhr, A., Waniuk, T. A., Busch, R., and Johnson, W. L., *Physical Review Letters* **82** (1999) 13.
- [20] Busch, R., *JOM* **52** (2000) 39.
- [21] Kelton, K. F. and Greer, A. L., *Nucleation in Condensed Matter*, Elsevier, 2010.
- [22] Lu, I., Wilde, G., Görler, G. P., and Willnecker, R., *Journal of Non-Crystalline Solids* **250-252** (1999) 577.
- [23] Angell, C. A., *Science* **267** (1995) 1924.
- [24] Kim, Y., Lin, H., and Kelly, T., *Acta Metallurgica* **37** (1989) 247.
- [25] Turnbull, D., *Contemporary Physics* **10** (1969) 473.
- [26] Cahn, R. W. and Haasen, P., *Physical Metallurgy*, North-Holland, 4th edition, 1996.
- [27] Porter, D. A. and Easterling, K. E., *Phase Transformations in Metals and Alloys*, Chapman & Hall, 2nd edition, 2001.
- [28] Uhlmann, D. R., *Journal of Non-Crystalline Solids* **7** (1972) 337.
- [29] Kolmogorov, A. N., *Izv. Akad. Nauk. SSR* **3** (1937) 355.
- [30] Johnson, W. A. and Mehl, R. F., *Trans. AIME* **135** (1939) 416.
- [31] Avrami, M., *The Journal of Chemical Physics* **7** (1939) 1103.
- [32] Avrami, M., *The Journal of Chemical Physics* **8** (1940) 212.
- [33] Avrami, M., *The Journal of Chemical Physics* **9** (1941) 177.
- [34] Matsuo, T., *Pure and Applied Chemistry* **70** (1998) 599.
- [35] Bai, H. Y., Luo, J. L., Chen, Z. J., and Wang, W. H., *Applied Physics Letters* **78** (2001) 2697.
- [36] Bai, H. Y., Luo, J. L., Zhang, J., and Chen, Z. J., *Journal of Applied Physics* **91** (2002) 9123.
- [37] Hodge, I. M., *Journal of Non-Crystalline Solids* **169** (1994) 211.
- [38] Matyushov, D. V. and Angell, C. A., *The Journal of Chemical Physics* **126** (2007) 094501.
- [39] Nemilov, S. V., *Glass Physics Chemistry* **21** (1995).
- [40] Eyring, H., *The Journal of Chemical Physics* **4** (1936) 283.
- [41] Busch, R. and Johnson, W. L., *Applied Physics Letters* **72** (1998) 2695.

REFERENCES

- [42] Busch, R., Liu, W., and Johnson, W. L., *Journal of Applied Physics* **83** (1998) 4134.
- [43] Legg, B., Schroers, J., and Busch, R., *Acta Materialia* **55** (2007) 1109.
- [44] Schroers, J., *Acta Materialia* **56** (2008) 471.
- [45] Jiang, M. and Dai, L., *Physical Review B* **76** (2007) 1.
- [46] Nemilov, S. V., *Journal of Non-Crystalline Solids* **352** (2006) 2715.
- [47] Douglas, R. W., *J. Soc. Glass Technol.* **33** (1949).
- [48] Doremus, R. H., *Journal of Applied Physics* **92** (2002) 7619.
- [49] Angell, C. A., *Journal of Non-Crystalline Solids* **131-133** (1991) 13.
- [50] Vogel, H., *phys. Z.* **22** (1921) 645.
- [51] Fulcher, G., *Journal of the American Ceramic Society* **8** (1925) 339.
- [52] Tammann, G. and Hesse, W., *Z. anorg. u. allg. Chem.* **156** (1926) 245.
- [53] Hecksher, T., Nielsen, A., Olsen, N. B., and Dyre, J., *Nature Physics* **4** (2008).
- [54] Scott, G. D., *Nature* **188** (1960) 908.
- [55] Bernal, J. D. and Mason, J., *Nature* **188** (1960) 910.
- [56] Fox, T. G. and Flory, P. J., *Journal of Applied Physics* **21** (1950) 581.
- [57] Doolittle, A. K., *Journal of Applied Physics* **22** (1951) 1471.
- [58] Cohen, H. and Turnbull, D., *Journal of Chemical Physics* **31** (1959).
- [59] Fox, T. G. and Flory, P. J., *Journal of the American Chemical Society* **70** (1948) 2384.
- [60] Fox, T. G. and Flory, P. J., *The Journal of Physical Chemistry* **55** (1951) 221.
- [61] Fox, T. G. and Flory, P. J., *Journal of Polymer Science* **14** (1954) 315.
- [62] Bueche, F., *The Journal of Chemical Physics* **21** (1953) 1850.
- [63] Williams, M., Landel, R., and Ferry, D., *Journal of the American Chemical Society* **77** (1955) 3701.
- [64] Kovacs, A., *Rheologica Acta* **5** (1966) 262.
- [65] Turnbull, D. and Cohen, M. H., *The Journal of Chemical Physics* **34** (1961) 120.
- [66] Grest, G. and Cohen, H., *Adv. Chem. Phys* **48** (1981) 455.
- [67] Adam, G. and Gibbs, J. H., *Journal of Chemical Physics* **43** (1965) 139.
- [68] Hirai, N. and Eyring, H., *Journal of Applied Physics* **29** (1958) 810.

REFERENCES

- [69] Hirai, N. and Eyring, H., *Journal of Polymer Science* **131** (1959) 174502.
- [70] Angell, C. A., *Pure and Applied Chemistry* **63** (1991) 1387.
- [71] Zarzycki, J., *Glass and the vitreous state*, Masson, Paris, 1982.
- [72] Angell, C. A., *Encyclopedia of Materials: Science and Technology* **4** (2001) 3565.
- [73] Moynihan, C. T., Easteal, A. J., Debolt, M. A., and Tucker, J., *Journal of the American Ceramic Society* **59** (1976) 12.
- [74] Tool, A. Q., *Journal of the American Chemical Society* **29** (1946) 240.
- [75] Evenson, Z., Gallino, I., and Busch, R., *Journal of Applied Physics* **107** (2010) 123529.
- [76] Lu, Z. P., Liu, Y., and Liu, C. T., Evaluation of Glass-Forming Ability, in *Bulk Metallic Glasses - An Overview*, edited by Miller, M. and Liaw, P., Springer, 2008.
- [77] Wang, W., Dong, C., and Shek, C., *Materials Science and Engineering: R: Reports* **44** (2004) 45.
- [78] Fan, G. J., Choo, H., and Liaw, P., *Journal of Non-Crystalline Solids* **353** (2007) 102.
- [79] Inoue, A., Zhang, T., and Masumoto, T., *Journal of Non-Crystalline Solids* **156-158** (1993) 473.
- [80] Waniuk, T. A., Schroers, J., and Johnson, W. L., *Applied Physics Letters* **78** (2001) 1213.
- [81] Cohen, M. H. and Turnbull, D., *Nature* (1961).
- [82] Greer, A. L. and Highmore, R. J., *Nature* **339** (1989) 363.
- [83] Greer, A. L., *Nature* **366** (1993) 303.
- [84] Inoue, A., *Acta Materialia* **48** (2000) 279.
- [85] Busch, R., Schroers, J., and Wang, W. H., *MRS Bulletin* **32** (2007) 620.
- [86] Shadyspeaker, L. and Busch, R., *Applied Physics Letters* **85** (2004) 2508.
- [87] Men, H., Kim, W. T., and Kim, D. H., *Journal of Non-Crystalline Solids* **337** (2004) 29.
- [88] Ma, H. and Fecht, H.-J., *Journal of Materials Research* (2008) 8.
- [89] Senkov, O. N., Miracle, D. B., and Scott, J., *Intermetallics* **14** (2006) 1055.
- [90] Senkov, O. N. and Miracle, D. B., *Metallurgical and Materials Transactions A* **41** (2009) 1677.
- [91] Gallino, I., Schroers, J., and Busch, R., *Journal of Applied Physics* **108** (2010) 063501.
- [92] Fan, G. J., Löffler, J. F., Wunderlich, R. K., and Fecht, H.-J., *Acta Materialia* **52** (2004) 667.

REFERENCES

- [93] Li, Y., Guo, Q., Kalb, J. A., and Thompson, C. V., *Science* **322** (2008) 1816.
- [94] Cheng, Y. and Ma, E., *Progress in Materials Science* **56** (2011) 379.
- [95] Frank, F., *Proceedings of the Royal Society of London. Series A* **215** (1952) 43.
- [96] Herlach, D. M., *Materials Science* **12** (1994) 177.
- [97] Hayes, T., Allen, J., Tauc, J., Giessen, B., and Hauser, J., *Physical Review Letters* **40** (1978) 1282.
- [98] Gaskell, P. H., *Nature* **276** (1978) 484.
- [99] Gaskell, P. H., *Journal of Non-Crystalline Solids* **32** (1979) 207.
- [100] Miracle, D. B., Sanders, W. S., and Senkov, O. N., *Philosophical Magazine* **83** (2003) 2409.
- [101] Miracle, D. B., *Nature Materials* **3** (2004) 697.
- [102] Miracle, D. B., *Acta Materialia* **54** (2006) 4317.
- [103] Miracle, D. B., Greer, A. L., and Kelton, K. F., *Journal of Non-Crystalline Solids* **354** (2008) 4049.
- [104] Senkov, O. N. et al., *Physical Review B* **82** (2010) 1.
- [105] Sheng, H. W., Luo, W. K., Alamgir, F. M., Bai, J. M., and Ma, E., *Nature* **439** (2006) 419.
- [106] Holland-Moritz, D., Herlach, D. M., and Urban, K., *Physical Review Letters* **71** (1993) 1196.
- [107] Ohsaka, K. et al., *Applied Physics Letters* **70** (1997) 726.
- [108] Schenk, T., Holland-Moritz, D., Simonet, V., Bellissent, R., and Herlach, D. M., *Physical Review Letters* **89** (2002) 1.
- [109] Kelton, K. F. et al., *Physical Review Letters* **90** (2003) 19.
- [110] Takagi, T. et al., *Applied Physics Letters* **79** (2001) 485.
- [111] Nagahama, D., Ohkubo, T., and Hono, K., *Scripta Materialia* **49** (2003) 729.
- [112] Li, J., Gu, X., and Hufnagel, T. C., *Microscopy and Microanalysis* **9** (2003) 509.
- [113] Kumar, G., Nagahama, D., Ohnuma, M., Ohkubo, T., and Hono, K., *Scripta Materialia* **54** (2006) 801.
- [114] Hirata, A., Hirotsu, Y., Ohkubo, T., Tanaka, N., and Nieh, T. G., *Intermetallics* **14** (2006) 903.
- [115] Na, J., Sohn, S., Kim, W., and Kim, D., *Scripta Materialia* **57** (2007) 225.
- [116] Egami, T., *Annals New York Academy of Sciences* (1981) 238.

REFERENCES

- [117] Mulder, A. L., van der Zwaag, S., and van den Beukel, A., *Acta Metallurgica* **32** (1984) 1895.
- [118] Radelaar, S. and van den Beukel, A., *Acta Metallurgica* **31** (1983) 419.
- [119] van den Beukel, A., Huizer, E., van der Zwaag, S., and Mulder, A. L., *Scripta Materialia* **18** (1984) 515.
- [120] van den Beukel, A. and Huizer, E., *Acta Metallurgica* **35** (1987) 2843.
- [121] van den Beukel, A. and Sietsma, J., *Acta Metallurgica* **38** (1990) 383.
- [122] Tuinstra, P., Duine, P., Sietsma, J., and van Den Beukel, A., *Acta Metallurgica* **43** (1995) 2815.
- [123] Way, C., Wadhwa, P., and Busch, R., *Acta Materialia* **55** (2007) 2977.
- [124] Way, C., *Viscosity of the Zr_{41.2}Ti_{13.8}Cu_{12.5}Ni_{10.0}Be_{22.5} Bulk Metallic Glass Forming Alloy Above the Liquidus Temperature*, Ph.d. thesis, Oregon State University, 2005.
- [125] Shechtman, D., Blech, I., Gratias, D., and Cahn, J. W., *Physical Review Letters* **53** (1984) 1951.
- [126] Köster, U., Meinhardt, J., Roos, S., and Liebertz, H., *Applied Physics Letters* **69** (1996) 179.
- [127] Wang, R., *Nature* **278** (1979) 700.
- [128] Schroers, J., Holland-Moritz, D., Herlach, D. M., Grushko, B., and Urban, K., *Materials Science and Engineering: A* **A215** (1997) 43.
- [129] Kim, Y. J., Busch, R., Johnson, W. L., Rulison, A. J., and Rhim, W. K., *Applied Physics Letters* **68** (1996) 1057.
- [130] Schneider, S., Thiyagarajan, P., and Johnson, W. L., *Applied Physics Letters* **68** (1996) 493.
- [131] Busch, R., Schneider, S., Peker, A., and Johnson, W. L., *Applied Physics Letters* **67** (1995) 1544.
- [132] Kim, Y. J., Busch, R., Johnson, W. L., Rulison, A. J., and Rhim, W. K., *Applied physics letters* **65** (1994) 2136.
- [133] Hays, C. C., Kim, C. P., and Johnson, W. L., *Applied Physics Letters* **75** (1999) 1089.
- [134] Waniuk, T., Schroers, J., and Johnson, W. L., *Physical Review B* **67** (2003) 184203.
- [135] Greer, A. L., *Science* **10** (1995) 88.
- [136] Schroers, J., Johnson, W. L., and Busch, R., *Applied Physics Letters* **76** (2000) 2343.
- [137] Schroers, J., Busch, R., and Johnson, W. L., *Acta Materialia* **49** (2001) 2773.

REFERENCES

- [138] Schroers, J., Masuhr, A., Johnson, W. L., and Busch, R., *Physical Review B* **60** (1999) 11855.
- [139] Angell, C. A., *MRS Bulletin* **33** (2008) 544.
- [140] Kui, H. W., Greer, A. L., and Turnbull, D., *Applied Physics Letters* **45** (1984) 615.
- [141] Sun, L., Wu, Q., Xu, Y., and Wang, W., *Physica B Condensed Matter* **240** (1997) 205.
- [142] Schroers, J., Wu, Y., and Johnson, W. L., *Philosophical Magazine A* **82** (2002) 1207.
- [143] Schroers, J., Johnson, W. L., and Busch, R., *Applied Physics Letters* **77** (2000) 1158.
- [144] Reed, T. B., *Free energy of formation of binary compounds*, 1971.
- [145] Inoue, A. and Nishiyama, N., *Materials Transactions-JIM* **38** (1997) 179.
- [146] Nishiyama, N. and Inoue, A., *Applied Physics Letters* **80** (2002) 568.
- [147] Haruyama, O. et al., *Physical Review B* **83** (2011) 1.
- [148] Masuhr, A., Busch, R., and Johnson, W. L., *Materials Science Forum* **269-272** (1998) 779.
- [149] Choi-Yim, H. and Busch, R., *Acta Materialia* **47** (1999) 2455.
- [150] Lin, X. H. and Johnson, W. L., *Materials Transactions-JIM* **38** (1997) 473.
- [151] Liu, C. T., Chisholm, M. F., and Miller, M. K., *Intermetallics* **10** (2002) 1105.
- [152] Höhne, G., Hemminger, W., and Flammersheim, H.-J., *Differential Scanning Calorimetry: An Introduction for Practitioners*, Springer-Verlag, Berlin, 1996.
- [153] Brown, M. E., *Introduction to Thermal Analysis: Techniques and Applications*, Kluwer Academic Publishers, New York, 2nd edition, 2001.
- [154] Brown, M. E., *Handbook of thermal analysis and calorimetry: Recent advances, techniques and applications*, Elsevier, 2007.
- [155] Gere, J. M., *Mechanics of Materials*, Brooks/Cole Thomson Learning, 5th edition, 2001.
- [156] Trouton, F. and Others, *Proceedings of the Royal Society of London. Series A* **77** (1906) 426.
- [157] Hagy, H. E., *Journal of the American Ceramic Society* **46** (1963) 93.
- [158] NIST, *Nist Special Publication* **96** (2010) 2008.
- [159] Moynihan, C. T., Easteal, A. J., and Wilder, J. A., *Journal of Physical Chemistry* **78** (1974).
- [160] Böhmer, R. and Angell, C. A., *Physical Review B* **45** (1992) 10091.
- [161] Brüning, R. and Samwer, K., *Physical Review B* **46** (1992) 11318.
- [162] Busch, R., Bakke, E., and Johnson, W. L., *Acta Materialia* **46** (1998) 4725.

REFERENCES

- [163] Yue, Y., von der Ohe, R., and Jensen, S. L., *The Journal of Chemical Physics* **120** (2004) 8053.
- [164] Gallino, I., Shah, M., and Busch, R., *Acta Materialia* **55** (2007) 1367.
- [165] Plazek, D. J. and Bero, C. A., *Journal of Physics: Condensed Matter* **15** (2003) S789.
- [166] Choi-Yim, H., Xu, D., and Johnson, W. L., *Applied Physics Letters* **82** (2003) 1030.
- [167] Gallino, I., Shah, M., and Busch, R., *Journal of Alloys and Compounds* **434-435** (2007) 141.
- [168] Böhmer, R., Ngai, K. L., Angell, C. A., and Plazek, D. J., *Journal of Chemical Physics* **99** (1993) 4201.
- [169] Wang, L.-M., Velikov, V., and Angell, C. A., *The Journal of Chemical Physics* **117** (2002) 10184.
- [170] Macedo, P. B., *The Journal of Chemical Physics* **49** (1968) 1887.
- [171] Laughlin, W. T. and Uhlmann, D. R., *Journal of Physical Chemistry* **76** (1972).
- [172] Breitling, S. M. and Magill, J. H., *Journal of Applied Physics* **45** (1974) 4167.
- [173] Angell, C. A., *Nuclear Physics B* **5A** (1988) 69.
- [174] Angell, C. A., *Chemical Reviews* **90** (1990) 523.
- [175] Angell, C. A., *Polymer Papers* **38** (1997).
- [176] Kittel, C., *Introduction to Solid State Physics*, John Wiley & Sons, Inc., 8th edition, 2005.
- [177] Evenson, Z. and Busch, R., *Acta Materialia* **59** (2011) 4404.
- [178] Kubaschewski, O., Alcock, C., and Spencer, P., *Materials Thermochemistry, 6th Ed.*, Pergamon Press, New York, 1993.
- [179] Kauzmann, W., *Chemical Reviews* **43** (1948) 219.
- [180] Gibbs, J. H. and DiMarzio, E. A., *Journal of Chemical Physics* **28** (1958) 373.
- [181] Greet, R. J. and Turnbull, D., *The Journal of Chemical Physics* **47** (1967) 2185.
- [182] Takahara, S., Yamamuro, O., and Suga, H., *Journal of Non-Crystalline Solids* **171** (1994) 259.
- [183] Huang, D., Simon, S. L., and McKenna, G. B., *The Journal of Chemical Physics* **119** (2003) 3590.
- [184] Simon, S. L. and McKenna, G. B., *Journal of Non-Crystalline Solids* **355** (2009) 672.
- [185] Johari, G. P., *Journal of Non Crystalline Solids* **288** (2001) 148.

REFERENCES

- [186] Hillert, M., *Acta Metallurgica* **1** (1953) 764.
- [187] Christian, J. W., *The Theory of Transformations in Metals and Alloys*, Pergamon Press, Oxford, UK, 2nd editio edition, 2002.
- [188] Palumbo, M. and Battezzati, L., *Calphad* **32** (2008) 295.
- [189] Schroers, J., *Advanced Materials* **22** (2010) 1566.
- [190] Gonser, U. and Wagner, H.-G., *Metall* **8** (1982).
- [191] Willnecker, R., Wittmann, K., and Görler, G. P., *Journal of Non-Crystalline Solids* **156-158** (1993) 450.
- [192] Shen, T. D. and Schwarz, R. B., *Applied Physics Letters* **75** (1999) 99.
- [193] Löffler, J. F. et al., *Applied Physics Letters* **77** (2000) 525.
- [194] Heinrich, J., Busch, R., Müller, F., Grandthyll, S., and Hüfner, S., *Applied Physics Letters* **100** (2012) 071909.
- [195] Lu, Z. P. and Liu, C. T., *Acta Materialia* **50** (2002) 3501.
- [196] Wang, Y. et al., *Scripta Materialia* **48** (2003) 1525.
- [197] Suryanarayana, C., Seki, I., and Inoue, A., *Journal of Non-Crystalline Solids* **355** (2009) 355.
- [198] Fiore, G., Rizzi, P., and Battezzati, L., *Journal of Alloys and Compounds* **509** (2011) S166.
- [199] Lohwongwatana, B., *Development, characterization, and applications of gold and platinum bulk metallic glasses*, Ph.d. thesis, California Institute of Technology, 2007.
- [200] Mukherjee, S., Schroers, J., Zhou, Z., Johnson, W. L., and Rhim, W.-K., *Acta Materialia* **52** (2004) 3689.
- [201] Hays, C. C. et al., *Applied Physics Letters* **79** (2001) 1605.
- [202] Kissinger, H., *Analytical Chemistry* **29** (1957) 1702.
- [203] Fiore, G., Ichim, I., and Battezzati, L., *Journal of Non-Crystalline Solids* **356** (2010) 2218.
- [204] Gale, W. F. and Totemeier, T. C., editors, *Smithells Metal Reference Book*, Elsevier, Oxford, 8th edition, 2004.
- [205] Gao, Y. et al., *Materials Letters* **57** (2003) 2341.
- [206] Gun, B., Laws, K., and Ferry, M., *Journal of Non-Crystalline Solids* **352** (2006) 3887.
- [207] Huang, L., Li, L., Liang, G., Guo, Y., and Wu, D., *Journal of Non-Crystalline Solids* **354** (2008) 1048.
- [208] Evenson, Z., Raedersdorf, S., Gallino, I., and Busch, R., *Scripta Materialia* **63** (2010) 573.

REFERENCES

- [209] Evenson, Z., Schmitt, T., Nicola, M., Gallino, I., and Busch, R., *Acta Materialia* **60** (2012) 4712.
- [210] Schroers, J., Lohwongwatana, B., Johnson, W. L., and Peker, A., *Materials Science and Engineering A* **449-451** (2007) 235.
- [211] Moynihan, C. T. et al., *Annals New York Academy of Sciences* **279** (1976) 15.
- [212] Moynihan, C. T., *Journal of the American Ceramic Society* **76** (1993) 1081.
- [213] Khonik, V. A., Mitrofanov, Y. P., Khonik, S. V., and Saltykov, S. N., *Journal of Non-Crystalline Solids* **356** (2010) 1191.
- [214] Martinez, L. M. and Angell, C. A., *Nature* **410** (2001) 663.
- [215] Goldstein, M., *Journal of Chemical Physics* **51** (1969) 3728.
- [216] Stillinger, F. H., *Science* **225** (1984).
- [217] Debenedetti, P. G. and Stillinger, F. H., *Nature* **410** (2001) 259.
- [218] Johari, G. P., *The Journal of Chemical Physics* **112** (2000) 7518.
- [219] Wang, L.-M., Angell, C. A., and Richert, R., *The Journal of Chemical Physics* **125** (2006) 074505.
- [220] Faupel, F. et al., *Reviews of Modern Physics* **75** (2003) 237.
- [221] Tanaka, H., *Physical Review Letters* **90** (2003) 5.
- [222] Tanaka, H., *Journal of Non-Crystalline Solids* **351** (2005) 678.
- [223] Spaepen, F., *Acta Metallurgica* **23** (1975) 729.
- [224] Yeh, J.-W. et al., *Advanced Engineering Materials* **6** (2004) 299.
- [225] Yeh, J.-W., Chen, Y. L., Lin, S. J., and Chen, S. K., *Materials Science Forum* **560** (2007) 1.
- [226] Zhou, Y. J., Zhang, Y., Wang, Y. L., and Chen, G. L., *Applied Physics Letters* **90** (2007) 181904.
- [227] Cunliffe, A., Plummer, J., Figueroa, I., and Todd, I., *Intermetallics* **23** (2012) 204.
- [228] Slipenyuk, A. and Eckert, J., *Scripta Materialia* **50** (2004) 39.
- [229] Haruyama, O. et al., *Acta Materialia* **58** (2010) 1829.
- [230] Ruitenberg, G., De Hey, P., Sommer, F., and Sietsma, J., *Physical Review Letters* **79** (1997) 4830.
- [231] van den Beukel, A., Sietsma, J., and De Hey, P., *Acta Metallurgica* **46** (1998) 5873.
- [232] Wen, P. et al., *Physical Review B* **69** (2004) 8.

REFERENCES

- [233] Launey, M., Busch, R., and Kruzic, J., *Scripta Materialia* **54** (2005) 483.
- [234] Launey, M., Kruzic, J., Li, C., and Busch, R., *Applied Physics Letters* **91** (2007) 051913.
- [235] Launey, M., Busch, R., and Kruzic, J., *Acta Materialia* **56** (2008) 500.
- [236] Zhang, W. et al., *Scripta Materialia* **61** (2009) 744.
- [237] Geyer, U. et al., *Applied Physics Letters* **69** (1996) 2492.
- [238] Goldstein, M., *The Journal of Chemical Physics* **39** (1963) 3369.
- [239] Kohlrausch, R., *Annalen der Physik und Chemie* **91** (1854) 179.
- [240] Williams, G. and Watts, C., *Transactions of the Faraday Society* **66** (1969) 80.
- [241] Ediger, M. D., Angell, C. A., and Nagel, S. R., *Journal of Physical Chemistry* **100** (1996) 13200.
- [242] Vilgis, T. A., *Physical Review B* **47** (1993) 2882.
- [243] Einstein, A., *Annalen der Physik* **34** (1911) 591.
- [244] Glade, S. C., Löffler, J. F., Bossuyt, S., Johnson, W. L., and Miller, M. K., *Journal of Applied Physics* **89** (2001) 1573.
- [245] Friedrichs, H. and Neuhäuser, H., *Journal of Physics: Condensed Matter* **1** (1989) 8305.
- [246] Ali, M. S. and Sheldon, R. P., *Journal of Applied Polymer Science* **14** (1970) 2619.
- [247] Straff, R. and Uhlmann, D. R., *Journal of Polymer Science: Polymer Physics Edition* **14** (1976) 1087.
- [248] O'Reilly, J. M., *Journal of Applied Physics* **50** (1979) 6083.
- [249] Bacq, O. L. and Willaime, F., *Physical Review B* **59** (1999) 8508.
- [250] Haruyama, O. and Inoue, A., *Applied Physics Letters* **88** (2006) 131906.
- [251] Spaepen, F. and Taub, A. I., *Acta Metallurgica* **28** (1980) 1781.
- [252] Bartsch, A., Rätzke, K., Meyer, A., and Faupel, F., *Physical Review Letters* **104** (2010) 1.
- [253] Brillo, J., Pommrich, A., and Meyer, A., *Physical Review Letters* **107** (2011) 1.
- [254] Johari, G. P. and Aji, D. P. B., *The Journal of Chemical Physics* **129** (2008) 056101.
- [255] Egami, T., *JOM* **62** (2010) 70.
- [256] Hasegawa, M. and Young, W. H., *J. Phys F: Metal Phys* **8** (1978).
- [257] Canales, M. and Padró, J. A., *Physical Review E* **60** (1999) 551.
- [258] Egami, T., *Intermetallics* **14** (2006) 882.

REFERENCES

- [259] Egami, T., Poon, S., Zhang, Z., and Keppens, V., *Physical Review B* **76** (2007) 1.
- [260] Haruyama, O., Kohda, M., Nishiyama, N., and Egami, T., *Journal of Physics: Conference Series* **144** (2009) 012050.
- [261] Egami, T., Levashov, V. A., Morris, J. R., and Haruyama, O., *Metallurgical and Materials Transactions A* **41** (2010) 1628.
- [262] Egami, T., *Progress in Materials Science* **56** (2011) 637.
- [263] Nagel, C. et al., *Physical Review B* **57** (1998) 224.
- [264] Schmidtke, E., Faupel, F., Nagel, C., and Rätzke, K., *Physical Review B* **60** (1999) 9212.
- [265] Ishii, A. et al., *Materials Transactions-JIM* **49** (2008) 1975.
- [266] Bennett, C. H., Chaudhari, P., Moruzzi, V., and Steinhardt, P., *Philosophical Magazine A* **40** (1979) 485.
- [267] Argon, A. S., *Acta Metallurgica* **22** (1979) 145.
- [268] Spaepen, F., *Scripta Materialia* **54** (2006) 363.
- [269] Ye, J. C., Lu, J., Liu, C. T., Wang, Q., and Yang, Y., *Nature Materials* **9** (2010) 619.
- [270] Glade, S. C. et al., *Journal of Applied Physics* **87** (2000).
- [271] Zhang, C., Hu, L., Yue, Y., and Mauro, J. C., *The Journal of Chemical Physics* **133** (2010) 014508.
- [272] Glade, S. C. and Johnson, W. L., *Journal of Applied Physics* **87** (2000) 7249.
- [273] Mukherjee, S., Schroers, J., Johnson, W. L., and Rhim, W.-K., *Physical Review Letters* **94** (2005) 1.
- [274] Polk, D. E. and Turnbull, D., *Acta Metallurgica* **20** (1972) 493.
- [275] Tsang, K. H., Lee, S. K., and Kui, H. W., *Journal of Applied Physics* **70** (1991) 4837.
- [276] Assael, M. J. et al., *Journal of Physical and Chemical Reference Data* **35** (2006) 285.
- [277] Barnes, H. A., Hutton, J. K., and Walters, K., *An Introduction to Rheology*, Elsevier Science, Amsterdam, 1989.
- [278] Iida, T. and Guthrie, R. I. L., *The Physical Properties of Liquid Metals*, Clarendon Press, Oxford, 1988.
- [279] Schroers, J., Busch, R., Masuhr, A., and Johnson, W. L., *Applied Physics Letters* **74** (1999) 2806.
- [280] Ito, K., Moynihan, C. T., and Angell, C. A., *Nature* **398** (1999).

REFERENCES

- [281] van Beest, B. W. H., Kramer, G. J., and van Santen, R. A., *Physical Review Letters* **64** (1990) 1955.
- [282] Barrat, J.-L., Badro, J., and Gillet, P., *Molecular Simulation* **20** (1997) 17.
- [283] Saika-Voivod, I., Poole, P. H., and Sciortino, F., *Nature* **412** (2001) 514.
- [284] Hemmati, M., Moynihan, C. T., and Angell, C. A., *The Journal of Chemical Physics* **115** (2001) 6663.
- [285] Angell, C. A., *Annual Review of Physical Chemistry* **55** (2004) 559.
- [286] Aasland, S. and McMillan, P. F., *Nature* **369** (1994) 633.
- [287] Wilding, M. C., Mcmillan, P. F., and Navrotsky, A., *Physica A* **314** (2002) 379.
- [288] Greaves, G. N. et al., *Science* **322** (2008) 566.
- [289] Sheng, H. W. et al., *Nature Materials* **6** (2007) 192.
- [290] Angell, C. A., Richards, B. E., and Velikov, V., *Journal of Physics: Condensed Matter* **11** (1999) A75.
- [291] Angell, C. A. and Moynihan, C. T., *Metallurgical and Materials Transactions B* **31** (2000).
- [292] Wilding, M. C. and Mcmillan, P. F., *Journal of Non-Crystalline Solids* **295** (2001) 357.
- [293] Liu, L., Chen, S.-H., Faraone, A., Yen, C.-W., and Mou, C.-Y., *Physical Review Letters* **95** (2005) 1.
- [294] Angell, C. A., *Journal of Physical Chemistry* **97** (1993) 6339.
- [295] Sreeram, A., Varshneya, A., and Swiler, D., *Journal of Non-Crystalline Solids* **128** (1991) 294.
- [296] Tatsumisago, M., Halfpaf, B. L., Green, J. L., Lindsay, S. M., and Angell, C. A., *Physical Review Letters* **64** (1990) 1549.
- [297] Stø len, S., Grande, T., and Johnsen, H.-B., *Physical Chemistry Chemical Physics* **4** (2002) 3396.
- [298] Krebs, H. and Ruska, J., *Journal of Non-Crystalline Solids* **16** (1974) 329.
- [299] Shi, Y. and Falk, M., *Scripta Materialia* **54** (2006) 381.
- [300] Li, M., Wang, C., Hao, S., Kramer, M., and Ho, K., *Physical Review B* **80** (2009) 1.
- [301] Wei, S., Gallino, I., Busch, R., and Angell, C. A., *Nature Physics* **5** (2010) 1.
- [302] Angell, C. A., *Journal of Non-Crystalline Solids* **354** (2008) 4703.
- [303] Martin, I., Ohkubo, T., Ohnuma, M., Deconihout, B., and Hono, K., *Acta Materialia* **52** (2004) 4427.

REFERENCES

- [304] Zheng, Q., Cheng, S., Strader, J., Ma, E., and Xu, J., *Scripta Materialia* **56** (2007) 161.
- [305] Zheng, Q., Xu, J., and Ma, E., *Journal of Applied Physics* **102** (2007) 113519.
- [306] Spaepen, F., *Acta Metallurgica* **25** (1977) 407.
- [307] Falk, M. L. and Langer, J. S., *Physical Review E* **57** (1998) 7192.
- [308] Johnson, W. L., Lu, J., and Demetriou, M. D., *Intermetallics* **10** (2002) 1039.
- [309] Demetriou, M. D., *Journal of Applied Physics* **95** (2004) 2857.
- [310] Stillinger, F. H., *Science* **267** (1995) 1935.
- [311] Johnson, W. L., Demetriou, M. D., Harmon, J. S., Lind, M. L., and Samwer, K., *MRS Bulletin* **32** (2007) 644.
- [312] Rodney, D. and Schuh, C., *Physical Review Letters* **102** (2009) 1.
- [313] Liu, Y., Wang, K., Inoue, A., Sakurai, T., and Chen, M., *Scripta Materialia* **62** (2010) 586.
- [314] Götze, W. and Sjögren, L., *Reports on Progress in Physics* **55** (1992) 241.
- [315] Götze, W., *Complex Dynamics of Glass-Forming Liquids: A Mode Coupling Theory*, Oxford University Press, New York, 2009.
- [316] Meyer, A., *Physical Review B* **66** (2002) 1.
- [317] Götze, W., *Journal of Physics: Condensed Matter* **11** (1999) A1.
- [318] Binder, K. and Kob, W., *Glassy materials and disordered solids : An introduction to their statistical mechanics*, World Scientific Publishing Co. Pte. Ltd., London, 2005.
- [319] Domschke, M., Marsilius, M., Blochowicz, T., and Voigtmann, T., *Physical Review E* **84** (2011).
- [320] Angell, C. A., *Journal of Physical Chemistry of Solids* **49** (1988) 863.
- [321] Voigtmann, T. et al., *Europhysics Letters* **82** (2008) 66001.
- [322] Meyer, A., Wuttke, J., Petry, W., Randl, O., and Schober, H., *Physical Review Letters* **80** (1998) 4454.
- [323] Jagla, E. A., *Journal of Physics: Condensed Matter* **11** (1999) 10251.
- [324] Mechler, S., Schumacher, G., Zizak, I., Macht, M.-P., and Wanderka, N., *Applied Physics Letters* **91** (2007) 021907.
- [325] Hirata, A. et al., *Nature materials* **10** (2011) 28.
- [326] Chong, S.-H., Chen, S.-H., and Mallamace, F., *Journal of Physics: Condensed Matter* **21** (2009) 504101.

REFERENCES

- [327] Chen, S.-H. et al., *Journal of Physics: Condensed Matter* **21** (2009) 504102.
- [328] Cormier, L. et al., *Physical Review B* **76** (2007) 1.
- [329] Nicholas, J., Sinogeikin, S., Kieffer, J., and Bass, J., *Physical Review Letters* **92** (2004).
- [330] Huang, L., Nicholas, J., Kieffer, J., and Bass, J., *Journal of Physics: Condensed Matter* **20** (2008) 075107.
- [331] Angell, C. A., *Journal of Research of the National Institute of Standards and Technology* **102** (1997) 171.
- [332] Yang, F., Kordel, T., Holland-Moritz, D., Unruh, T., and Meyer, A., *Journal of Physics: Condensed Matter* **23** (2011) 254207.